Stony Brook University

The Role of Thermodynamic Processes in the Evolution of Single and Multi-banding within Winter Storms

A Dissertation Presented

by

Sara Anne Ganetis

to

The Graduate School

in Partial Fulfillment of the

Requirements

for the Degree of

Doctor of Philosophy

in

Marine and Atmospheric Science

Stony Brook University

May 2017

Stony Brook University

The Graduate School

Sara Anne Ganetis

We, the dissertation committee for the above candidate for the

Doctor of Philosophy degree, hereby recommend

acceptance of this dissertation.

Dr. Brian A. Colle – Dissertation Advisor
Professor – School of Marine and Atmospheric Sciences

Dr. Edmund Chang - Chairperson of Defense
Professor – School of Marine and Atmospheric Sciences

Dr. Minghua Zhang
Professor – School of Marine and Atmospheric Sciences

Dr. Sandra E. Yuter
Professor – Department of Marine, Earth, and Atmospheric Sciences
North Carolina State University

Dr. David M. Schultz
Professor – School of Earth and Environmental Sciences
The University of Manchester

This dissertation is accepted by the Graduate School

Charles Taber

Dean of the Graduate School

Abstract of the Dissertation

The Role of Thermodynamic Processes in the Evolution of Single and Multi-banding within Winter Storms

by

Sara Anne Ganetis

Doctor of Philosophy

in

Marine and Atmospheric Science

Stony Brook University

2017

Mesoscale precipitation bands within Northeast U.S. (NEUS) winter storms result in heterogeneous spatial and temporal snowfall. Several studies have provided analysis of snowbands focusing on larger, meso-α scale bands with lengths (L) > 200 km known as single bands. NEUS winter storms can also exhibit multiple bands with meso-β scale (L < 200 km) and similar spatial orientation and when ≥ 3 occur are termed multi-bands; however, the genesis and evolution of multi-bands is less well understood. Unlike single bands, there is no multi-bands climatological study. In addition, there has been little detailed thermodynamic analysis of snowbands. This dissertation utilizes radar observations, reanalyses, and high-resolution model simulations to explore the thermodynamic evolution of single and multi-bands.

Bands are identified within 20 cool season (October–April) NEUS storms. The 110-case dataset was classified using a combination of automated and manual methods into: single band only (SINGLE), multi-bands only (MULTI), both single and multi-bands (BOTH), and non-banded (NONE). Multi-bands occur with the presence of a single band in 55.4% of times used in

this study, without the presence of a single band 18.1% of the time, and precipitation exhibits no banded characteristics 23.8% of the time. Most MULTI events occur in the northeast quadrant of a developing cyclone poleward of weak-midlevel forcing along a warm front, whereas multi-bands associated with BOTH events mostly occur in the northwest quadrant of mature cyclones associated with strong mid-level frontogenesis and conditional symmetric instability. The non-banded precipitation associated with NONE events occur in the eastern quadrants of developing and mature cyclones lacking mid-level forcing to concentrate the precipitation into bands.

A high-resolution mesoscale model is used to explore the evolution of single and multi-bands based on two case studies, one of a single band and one of multi-bands. The multi-bands form in response to intermittent mid-level frontogenetical forcing in a conditionally unstable environment. The bands within their genesis location southeast of the single band move northwest towards the single band by 700-hPa steering flow. This allows for the formation of new multi-bands within the genesis region, unlike the single band that remains fixed to a 700-hPa frontogenesis maximum. Latent heating within the band is shown to increase the intensity and duration of single and multi-bands through decreased geopotential height below the heating maximum that leads to increased convergence within the band.

Dedication Page

This dissertation is dedicated to any girl who finds wonder in the natural world but fears they may not be smart enough to pursue a career studying it. Believe in yourself and go for it!

Table of Contents

List of Tables

Chapter 2 **Page**

Chapter 3

Chapter 4

Chapter 5

List of Figures

Chapter 1 **Page**

Chapter 2

Chapter 4

Chapter 5

Chapter 6

List of Abbreviations

BMJ: Betts–Miller–Janjic cumulus parameterization scheme
BOTH: Both single and multi-bands
CFSR: Climate Forecast System Reanalysis
CFSv2: Climate Forecast System version 2
CI: Conditional instability
CSI: Conditional symmetric instability
DEV: Developing cyclone stage
DTC: Developmental Testbed Center
FH: Forecast hour from initialization time
GFS: Global Forecast System
IC: Initial condition
MAT: Mature cyclone stage
MET: Model Evaluation Tools
MODE: Method for Object-based Diagnostic Evaluation Tool
MORR: Morrison double-moment microphysics scheme
MPV*: Saturated equivalent potential vorticity
MULTI: Multi-bands only
MYJ: Mellor-Yamada-Janjic PBL scheme
NAM: North American Mesoscale model
NARR: North American Regional Reanalysis
NCAR: National Center for Atmospheric Research
NCEP: National Centers for Environmental Prediction
NEUS: Northeast United States
NOAA: National Oceanic and Atmospheric Administration
NOAH-MP: Noah-multiparameterization land surface model
NOLC: No latent cooling simulation
NOLH: No latent heating simulation
NONE: Non-banded
PBL: Planetary Boundary Layer
RRTM: Rapid Radiative Transfer Model
RUC: Rapid Update Cycle model
SBU: Stony Brook University
SINGLE: Single band only
THOM: Thompson single-moment microphysics scheme
WRF: Weather Research and Forecasting model
WSM6: WRF Single Moment 6-class microphysics scheme
YSU: Yonsei University PBL scheme

Acknowledgments

I would like to thank my advisor, Dr. Brian A. Colle, for his patience, encouragement, guidance and thoughtful discussions over the years. He taught me how to "slice and dice" even if you do not always know exactly what you are looking for. I would like to thank Dr. Sandra Yuter for acting as a committee member and mentor and for being so patient and honest during our many conversations. I am very grateful for the time and effort shared with me by my committee members both external, Dr. David Schultz, and internal, Drs. Edmund Chang and Minghua Zhang.

This work was not completed in a bubble. I am incredibly grateful for the work on the observational side of the project by the students and staff in Dr. Yuter's group, particularly Nicole Hoban, Nicole Corbin, Laura Thomkins, Dr. Matthew Miller, and anyone else who helped create the stitched radar reflectivity product. A huge thank you to both Nathan Korfe and Zhenhai Zhang who provided 6-hourly cyclone track data from the CFSR and CFSv2 when they were with the Coastal Meteorology and Atmospheric Prediction (COMAP) group at SBU. None of this work could have been possible without the technical assistance of Mark Lang and Dr. Ping Liu who helped with cluster management and maintenance and put up with so many of my emails over the years. A huge thank you to the staff of ITPA and SoMAS for always having quick answers ready for my questions. I am incredibly grateful for the sharing of code and wisdom by past and present students of the COMAP group, especially Dr. Michael Erickson, David Stark, and Dr. Kelly Lombardo.

I would like to thank my family and friends for their support and encouragement along this journey. I need to thank my parents who put up with so much including watching The Perfect Storm no less than a million times, letting me stay near windows during thunderstorms, driving across the country with me for an internship, and always being there to provide shelter during the many storms. Finally, I owe so much to my supportive fiancé, Matthew Sienkiewicz. I am grateful for his good coding practices he shared while a member of the COMAP group, for being a fantastic officemate, and for showing that everything (including writing a dissertation) is best when you find the humor in it.

Chapter 1:

Introduction

1.1 Background

Mesoscale banding within United States (U.S.) East Coast winter storms can lead to localized heavy snowfall rates, snowfall amounts, and high winds that can negatively impact the lives and property within the heavily populated urban corridors of the Mid-Atlantic and New England states. For example, the recent blizzard of 8–9 February 2013 exhibited an intense mesoscale snowband and resulted in over 600,000 people who lost power, over 6,000 cancelled flights, and 18 fatalities (Krekeler 2013; Picca et al. 2014). Winter storms exhibit bands with a variety of sizes, motions, and intensities (Novak et al. 2004; Kenyon 2013), but most studies have investigated the primary band, or a single snowband with length (L) > 200 km largely ignoring analysis of groups of smaller, multiple bands with L < 200 km that are similarly impactful. For example, the 26–27 December 2010 East Coast winter storm produced over 10 finescale (5–20-km wide and 10–100-km long) bands that led to over 6,000 cancelled flights and regional train service (Soltow 2011) and was attributed to several deaths mainly due to impassable snow-covered roadways in New York City (Kocin et al. 2011). Detailed analysis and comparison of the multi-band environment with that of the single band within winter storms is needed to enhance understanding and prediction of the similarly impactful bands.

The identification of mesoscale bands associated with extratropical cyclones was initially done via ground-based radar (Houze et al. 1976; Sanders and Bosart 1985b). By observing radar data from 11 landfalling West Coast occluded cyclones, Houze et al. (1976) created the first classification scheme based on band size and location relative to the cyclone center that included categories such as narrow cold frontal (width < 5 km), warm frontal (widths ~ 50 km), and wave bands (widths 10–20 km). The physical mechanisms resulting in the various banding types was also investigated (Hobbs 1978; Keyser and Anthes 1982; Parsons and Hobbs 1983). For example, narrow cold frontal bands were determined to result from boundary layer convergence at the leading edge of the cold frontal boundary and could exhibit wave-like structure. These

early studies of banding within mature West Coast extratropical cyclones provided foundational work of mesoscale band classification and dynamics and highlighted the prevalence of small bands.

Mesoscale bands found within the comma head of developing and mature extratropical cyclones impacting the U.S. East Coast have been the subject of studies also employing conventional radar data for classification (e.g., Novak et al. 2004; 2010; Kenyon et al. 2013). The primary band, or a single snowband with $L > 200$ km typically found to the northwest of a surface low pressure center in a region of strong geostrophic confluence, coincides with the ascending branch of the ageostrophic frontogenetical circulation that is dramatically narrowed and enhanced on the warm side of a mid-level frontal boundary in an environment with conditional symmetric instability (CSI) or weak moist symmetric stability (Emanuel 1985; Thorpe and Emanuel 1985; Xu 1989). Although single snowbands are usually the focus of many winter mesoscale precipitation studies (e.g. Sanders and Bosart 1985a,b; Wolfsberg et al. 1986; Novak et al. 2004, 2008, 2009, 2010, 2012; Moore et al. 2005; Picca et al. 2014; Colle et al. 2014; Baxter and Schumacher 2017) smaller multi-bands, or multiple parallel bands with $L <$ 200 km, are found embedded within the comma head region of an extratropical cyclone and are less understood. One reason most studies did not investigate multi-bands was the lack of access to fine scale observations or gridded reanalysis data (Novak 2009).

This study investigating single bands and multi-bands in East Coast winter storms will use a combination of the examination of radar data and gridded reanalysis data from over 100 storms and in-depth case studies using a high-resolution mesoscale model. The rest of this chapter provides additional background on previous climatological studies of banded structures in winter storms, the forcing, stability, and microphysical properties of single bands, multi-banded processes, and concludes with a discussion of the research goals and approach.

a. Climatology of banded structures in winter storms

Although comparisons of case studies of banding within individual winter storms are prevalent in the literature (e.g. Nicosia and Grumm 1999; Jurewicz and Evans 2004), multiyear climatological studies consisting of >5 storms are less numerous. Novak et al. (2004) used mosaic radar reflectivity data to identify 88 cases from 1996 to 2001. Their study employed a

subjective classification scheme to manually apply to the reflectivity data that included single bands, narrow cold-frontal rainbands, and multi-bands, but only the compared the environments between single bands and non-banded cases. There were 48 single-banded events and 13 non-banded events classified. To determine the differences in forcing and stability between both single-banded and non-banded cases, both the NCEP–NCAR reanalysis (2.5°) and the NCEP ETA model (80-km) gridded datasets were used to make cyclone-relative composites. The main results of their study was that single bands typically formed to the northwest of the surface cyclone center with a closed mid-level (~700-hPa) circulation providing strong low-to-mid-level deformation and frontogenesis in the presence of weaker conditional stability than non-banded cases shown in Figure 1.1.

Single bands result from specific environmental ingredients of moisture, instability and lift, but little was known how those quantities change throughout the lifetime of a band outside of case studies. The climatological study by Novak et al. (2010) aimed to isolate the role of moist processes in the evolution of the single-banded environment. Using the methodology from Novak et al. (2004), they identified 144 heavy precipitation cases from 2002 to 2008 but out of the 75 that exhibited a closed 700-hPa low, 30 single-banded cases were examined. In this study there were single, transitory and null categories in the classification scheme with no separation of multi-bands. Band-relative composites were created using three-hourly 32-km grid spacing North American Regional Reanalysis (NARR; Mesinger et al. 2006) and composite cross-sections and stability time series were created using hourly 20-km grid spacing Rapid Update Cycle (RUC; Benjamin et al. 2004) analyses to characterize the environmental evolution of the banded and null events. The main results of their study were that mid-level frontogenesis was stronger for banded events than null and found CI more prevalent than CSI. The lifecycle of single bands was examined in the context of frontogenetical ascent within a layer of CI (Figs. 1.2a–d). Bands dissipated when upstream diabatic PV anomalies and geopotential height falls shifted the location of maximum frontogenetical forcing away from the existing primary band (Figs. 1.2e–f).

Not all single bands associated with NEUS winter storms have the same lifecycle, consisting of intensity, duration, and motion. Kenyon et al. (2013) provided a climatology of band motion within East Coast winter storms. They analyzed archived WSR-88D radar data from 71 cases from 2005–2010 to classify snowband motion into four modes: laterally

translating, laterally quasi-stationary, hybrid, and pivoting. Composite environments for each type of geographic-centric band movement were created from the 0.5° resolution NCEP Climate Forecast System Reanalysis (CFSR; Saha et al. 2010). Their main results are that low- to mid-tropospheric temperature advection, flow confluence/diffluence, curvature, and horizontal shear in the near-band environment can be used to distinguish between the different modes. This study lacked any discussion of multi-bands and how they may affect the movement of primary snowbands.

Most band classification studies have relied on the human eye for band identification and classification (e.g., Novak et al. 2004; 2010; Kenyon et al. 2013). The first automated CONUS-wide study of banded precipitation was created by Fairman et al. (2016). Using image processing methods on composite radar imagery, one result was that for Dec–Feb from 2003–2014 the Northeast U.S. experiences relative peaks in the banded precipitation in the Tug Hill Plateau of upstate NY and lee of Lake Erie in western NY (likely associated with lake-effect precipitation bands) and within the Ohio Valley extending across the Appalachians to the coast of NJ (likely associated with banding within extratropical cyclones). This was a large-scale study focusing on banded features with a major axis ≥ 100 km, therefore smaller-scale bands, especially those embedded within the comma head of extratropical cyclones, were not addressed.

Climatological studies of bands have been conducted for storms impacting the West Coast and East Coast of the United States, but questions remain with how banding within continental cyclones compared. A recent climatology of single-banded snowfall in Central U.S. cyclones (between the Rocky and Appalachian Mountains) was conducted by Baxter and Schumacher (2017) using 1-km composite radar imagery for 66 cyclones exhibiting ≥ 4 in of accumulated snowfall during 5 cool seasons from 2006–2011. Their study manually identified single bands that were ≥ 250 km long and defined events every 3 hours within a storm. Out of the 66 cyclones, there were 98 banded events and 38 non-banded events. The average snowband lasted 5.2 h, was 45 km wide and 428 km long. Out of the banded events, 54 occurred in the northeast (NE) quadrant relative to the cyclone center, 29 in the northwest (NW) quadrant, and 15 within both northern quadrants. Out of the 38 non-banded events, the precipitation coverage occurred in both northern quadrants for 28 events. This study differed from that of the East Coast winter storm analysis of Novak et al. (2004) in that this study found nearly twice as many non-banded events and more single bands formed in the NE rather than the NW quadrant. Cyclone-

relative composite analysis of the atmospheric state (i.e., mid-level trough/ridge and upper-level jet streak location and magnitude) and key banding ingredients (i.e., mid-level frontogenesis, mid-level saturation equivalent potential vorticity, and sufficient mid-level relative humidity) compared single bands that formed in the NE and NW quadrants. Single bands that formed in either the NE and NW quadrants exhibited coincident mid-level frontogenesis maxima with decreased mid-level instability which acted to enhance and concentrate the ascent, but the bands in the NE quadrant were associated with a zonally elongated warm front resulting from a weaker downstream ridge and jet streak. Non-banded events were associated with weaker mid-level frontogenesis, less amplified mid-level flow, and a lack of juxtaposition between frontogenesis maxima and layers of weakened stability. This study did not address bands < 250 km in length and may see slightly different cyclone structure than that of Northeast U.S. cyclones for reasons such as the enhanced baroclinicity produced by the Gulf Stream.

b. Forcing, stability, and microphysical properties of the single band environment

Sufficient moisture, weak stability or available instability, and a lifting or forcing mechanism are necessary banding ingredients resulting in single-banded mesoscale structures in the comma head of extratropical cyclones (Novak et al. 2004; 2009). For NEUS winter storms, most single bands occur to the northwest of the surface low pressure center in a region of enhanced mid-level frontogenesis and weak mid-level stability (Novak et al. 2010).

The single band typically coincides with the ascending branch of the ageostrophic frontogenetical circulation in an environment with conditional symmetric instability (CSI) or weak moist symmetric stability (Sanders and Bosart 1985; Shields et al. 1991). Theoretical work by Emanuel (1985), Thorpe and Emanuel (1985), Xu (1989a,b, 1992) showed that intense single cores of ascent can form through a coupled relationship between frontogenesis and moist symmetric stability, whereby the ascending branch of a frontal circulation is dramatically narrowed and enhanced when there is weak moist symmetric stability on the warm side of a frontal boundary. CSI can coexist with conditional instability (CI) therefore the banded environment may result in moist gravitational and moist symmetric convection (Schultz and Schumacher 1999). Novak et al. (2010) found that CI occurred more often than CSI for single bands within mature cyclones. This suggests that single bands may form from the release of a

variety of instabilities and even in weakly stable environments to moist gravitational and moist symmetric motions due to forced ascent (Schultz and Schumacher 1999).

Many of the aforementioned studies have highlighted the single mesoscale snowband within the comma head of extratropical cyclones, but the focus has been on the structure and intensity of the band, not the detailed microphysical characteristics and thermodynamic reasons for these changes. Snow crystal habit is highly sensitive to vertical thermal and moisture profiles (Magono and Lee 1966; Pruppacher and Klett 1997). Stark et al. (2013) examined the microphysical evolution of two mesoscale snowbands crossing Long Island, NY using vertically-pointing radar data and surface observations including snow crystal habit and degree of riming. Their study highlighted the rapid frontogenetical ascent in an environment favorable for dendritic growth coincident with a mature band, and an increased snow density indicative of colder-type crystals in a post-band environment. Colle et al. (2014) examined cyclone-centric snow characteristics and environments for 12 cyclones over three winter seasons for developing and mature East Coast cyclones. Overall, their study acknowledged that the snow habit observed at a location is dependent on the location and intensity of the cyclone and that there is a large amount of spatial variability as a result of the heterogeneous thermal profiles and the magnitude of vertical motion throughout the comma head. Questions still remain about how thermodynamic processes directly impact the observed microphysical character of hydrometeors and the resultant evolution of single and multi-bands.

Picca et al. (2014) provided evidence that the blizzard of 8–9 February 2013 exhibited dramatic changes in snow habit and degree of riming. The thermodynamic analysis using a mesoscale model to investigate the band evolution showed that prolonged diabatic heating maintained an above-freezing layer within the band that resulted in mixed-phase precipitation while the surrounding environment was cooling due to cold air advection (Ganetis and Colle 2015). Although a mesoscale model has been used to examine the evolution of a single band (Novak et al. 2008; 2012; Ganetis and Colle 2015), the methodology has not been applied in such detail to multi-bands.

c. Multi-banding within the comma head of extratropical cyclones

There are few studies of multi-bands from real events using conventional observations

and gridded model data (Shields et al. 1991; Schultz et al. 2004; Schumacher et al. 2010). The climatology of Novak et al. (2004) included a multi-bands classification category but it was not included in the in-depth analysis. One of the three events studied in Nicosia and Grumm (1999) exhibited multiple bands that they attributed to weaker frontogenesis when compared to the other two cases that exhibited single bands. Examination of the multi-band environment has primarily been done using theoretical and idealized modeling (e.g., Xu 1992; Morcrette and Browning 2006; Pizzamei et al. 2005).

The banding ingredients resulting in multi-bands are hypothesized to be different than larger, single bands perhaps resulting from greater available instability with similar frontogenetical forcing (Xu 1992). Shields et al. (1991) studied the 10–11 February 1988 multi-banding event and discussed possible multi-banding mechanisms that included frontogenetical forcing leading to an enhanced temperature gradient which would lead to thermal wind imbalance. This would incite a thermally direct transverse circulation that would increase the winds aloft. The increased winds would mean an increase in absolute ageostrophic momentum and thus a decrease in gravitational and inertial resistance to sloping ascent which would allow for the development and release of CSI after which the atmosphere would return to a near-neutral state with respect to CSI. An uneven rate in these processes could cause multiple bands because they would occur in so-called pulses but requires an examination of high-resolution data.

A second possible multi-banding mechanism could be the concept of mesoconvective ascent along the warm front as described by Neiman et al. (1993). Mesoconvective ascent can be described by the analogy of air rising in either an escalator or elevator method. The escalator is the warm-frontal ascent as the warm southerly airstream rises over the cold easterly polar airstream in a slantwise fashion. The elevator is the mesoconvective ascent where small-scale convective updrafts are embedded within the warm frontal boundary. Chagnon and Gray (2009) examined the link between potential vorticity (PV) dipoles and the linear structure of warm-season convection. Relative vorticity can be generated in a sheared environment by an updraft prior to condensational heating and hence prior to PV generation. If the updraft is moist and produces diabatic PV. PV dipoles are formed as vertical dipoles via the stretching of planetary vorticity and horizontal dipoles via the tilting of horizontal vorticity of background shear (Fig. 1.3). They found that linear features were associated with elongated horizontal PV dipoles,

whereas cellular convection was not. The relationship between such PV dipoles and multi-bands forming in a sheared environment remains to be determined.

A third possible multi-banding forcing mechanism is atmospheric waves traveling within a stable ducted layer. Uccellini and Koch (1987) reviewed several cases of both singular and wave packet disturbances and concluded that the source of gravity waves is likely the geostrophic adjustment process to an upper-tropospheric jet streak and they are maintained by a ducting layer defined by a lower-tropospheric inversion. Plougonven and Zhang (2014) provide a review of internal gravity waves from atmospheric jets and fronts. Gravity waves have also been linked to the generation of wide cold-frontal rainbands in landfalling wintertime cyclones along the West Coast of the United States. Kawashima (2016) linked wide cold-frontal rainbands to the superposition between upward-propagating gravity waves generated by melting-induced cooling within an environment of strong frontal ascent. Rauber et al. (2017) found evidence of wave activity above the boundary layer and at mid-levels along a sloping warm frontal zone that resulted in multiple bands of snowfall using the National Center for Atmospheric Research (NCAR) High-Performance Instrumented Airborne Platform for Environmental Research (HIAPER) Cloud Radar flown at an altitude at 12.8 km. Observations of gravity wave activity may be difficult to obtain, which may motivate such analysis of this forcing mechanism be completed with a mesoscale model.

1.2 Research goals and approach

The availability of radar data has provided the technology to observe the presence of multiple snowbands that appear to characterize many snowstorms (Kocin and Uccellini p. 206). Although Novak et al. (2004) produced a climatology of the banded structures in Northeast U.S. extratropical cyclones for 5 years and included multi-bands defined as >3 finescale (5–20-km width) bands with periodic spacing and similar spatial orientation, comparing the environmental forcing and stability of multi-bands to single bands was beyond the scope of their published study. Further work by Novak et al. (2010) completed additional analysis of the evolution of different band environments but did not include a multi-bands category. It is unclear whether multi-bands also form in a region of confluence around 700 hPa, from gravity waves, an upper-level jet-induced ageostrophic circulation, or another mechanism which motivates an extended

climatology of these features. Available gridded analyses of environmental banding ingredients combined with a higher-resolution mesoscale model provide the necessary spatial and temporal resolution for the analysis of multi-bands. This study builds upon the limited existing work of the thermodynamic evolution of single bands and adds the investigation of multi-bands.

This work aims to answer the following fundamental questions regarding single and multi-bands in the comma head region of extratropical cyclones in the Northeast U.S.:

- What are the differences in available moisture, instability and lift among multi-bands and single bands as well stratiform precipitation areas in the comma head?
- What is the relative role of frontogenesis, gravity waves, or shear-induced circulations on snow band development?
- What are the roles of diabatic processes including latent heating (condensation/deposition/freezing) and cooling (evaporation/sublimation/melting) on the evolution of these bands?
- What are the formation and maintenance mechanisms of multi-bands as revealed by a detailed case study?

These questions will be addressed using a combination of available observations during NEUS winter storms, reanalysis data, and case studies using the Weather Research and Forecasting (WRF) model.

One goal of this research is to create a multi-year dataset consisting of cool season (October through April) banding events that are identified and classified using predominately objective methods. This dataset can be compared with that of previous climatological studies that relied on manual classification methods. A potential caveat of using a solely objective method is that various fields, specifically radar reflectivity, can contain a wide range of values during one time in a single storm. The method can be tuned to produce minimal error when compared with subjective methods for one single storm, but may fail when applied to a different storm. The objective methodology applied to the data in this study is discussed, including the many tests that were conducted before a single method was chosen. Ultimately, subjective methods were also employed for the final banding classification steps in this work in order to implement consistent classification among diverse storms.

The environmental ingredients of multi-bands will be investigated to complement previous work completed for single bands. By comparing data for both single bands and multi-bands, differences in the environmental stability and forcing can be determined. For example, it is hypothesized that multi-bands form in a region of greater instability than single bands and may be forced from gravity waves in a ducted layer or a widespread region of deformation and frontogenesis at low-levels.

Another goal of this research is to complete a process-oriented analysis using a mesoscale model run down to ~1-km grid spacing for a subset of case studies to compare the thermodynamics and microphysics of single bands and multi-bands. The case studies will be used to determine the roles of diabatic processes including latent heating (condensation, deposition, freezing) and cooling (evaporation, sublimation, melting) on the evolution of single and multi-bands. The condensational warming acts to enhance the vertical ageostrophic circulation which maintains the region of enhanced frontogenesis, banding, and gravity waves but the roles of evaporative cooling (if the environment is sub-saturated) and heating from freezing or cooling from melting have yet to be fully assessed in either a single or multi-banding case. Additional questions such as how multi-bands impact any pre-existing single bands will also be determined. For example, Novak et al. (2009; 2010) determined that upstream convection/PV anomalies acted to weaken the pre-existing single band but if the pre-existing convection is multi-banded in nature and merges with the primary band it is unknown whether that would have the same dissipative effect.

The research questions investigating single bands and multi-bands in East Coast winter storms will be addressed by a combination of a climatological study of over 100 storms and in-depth case studies using a high resolution mesoscale model and will be organized as follows. Chapter 2 describes the methods used to identify and classify precipitation bands in Northeast U.S. winter storms. Chapter 3 discusses the thermodynamic environment of the various classifications of precipitation bands with a focus on contrasting known banding environmental ingredients (i.e., moisture, instability, lift). Chapter 4 provides a detailed case study of the thermodynamic and microphysical evolution of an intense single band within the 8 - 9 Feb 2013 blizzard. Chapter 5 discusses a case study of both a single band and multi-bands within the 26–27 Dec 2010 Northeast U.S. winter storm; through the analysis of this case, multi-banding genesis and maintenance hypotheses are tested and contrasted with that of a single band. Chapter

6 provides a summary of the results of this study including unique contributions to mesoscale snowband research and offers some insight into future research avenues on this topic.

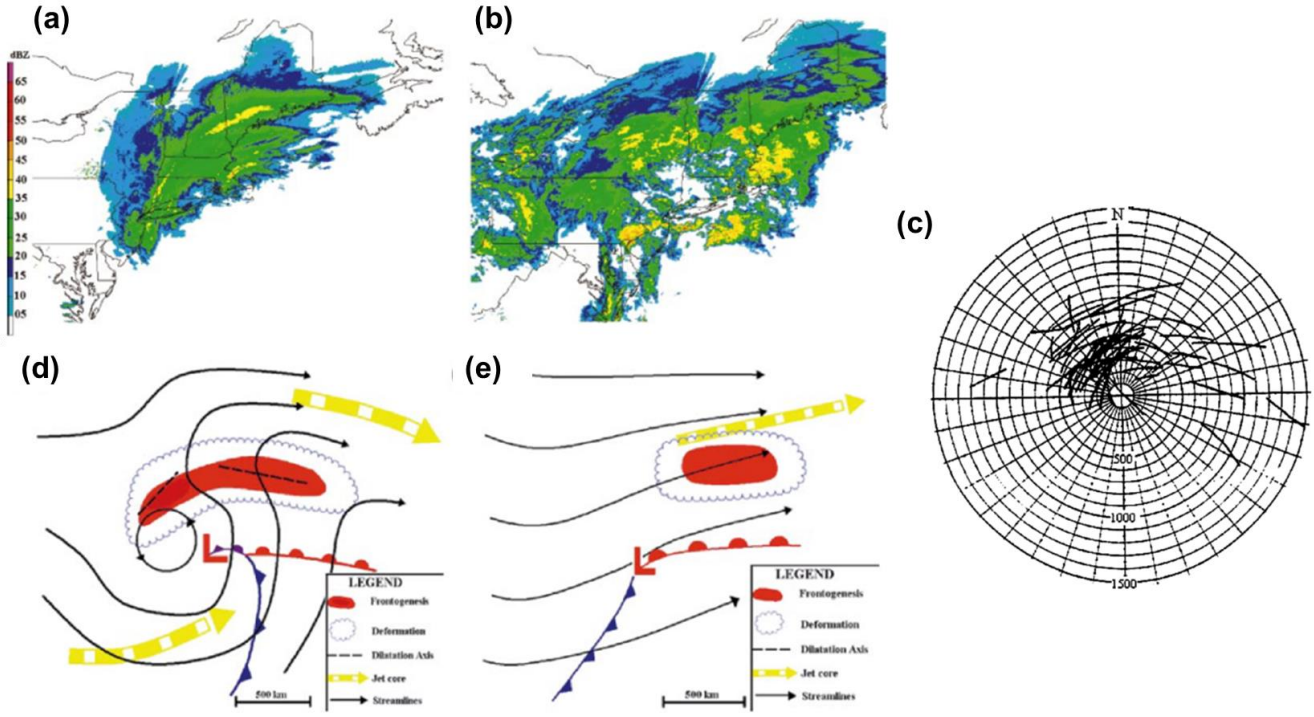

Figure 1.1. Observed regional composite radar reflectivity of (a) a single-banded event of 0000 UTC 6 Feb 2001 from Novak et al. (2004, Fig. 2a), (b) non-banded event of 1200 UTC 14 Feb 2000 from Novak et al. (2004, Fig. 2b). (c) The distribution of single bands relative to the surface cyclone center from Novak et al. (2004, Fig. 4). Conceptual model showing the synoptic and mesoscale environmental ingredients attributed to (d) the presence of a single band (Novak et al. 2004, Fig. 15a) and (e) non-banded case (Novak et al. 2004, Fig. 15b).

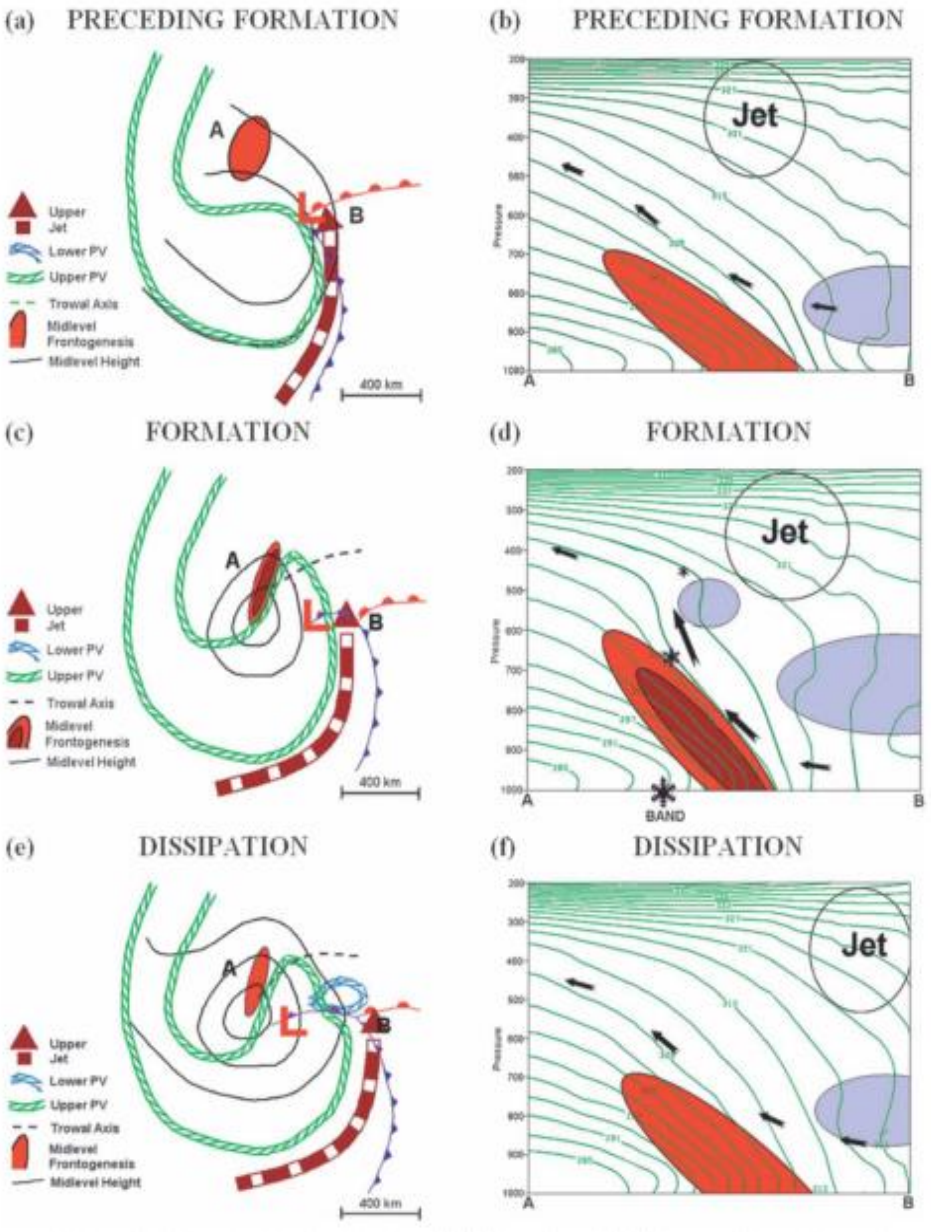

Figure 1.2. Schematic evolution of a single band environment northwest of the surface cyclone from Novak et al. (2010, Fig. 15) illustrating the juxtaposition of mid-level forcing (i.e., frontogenesis), mid-level instability (i.e., conditional instability) northwest of the surface cyclone. Representative northwest-southeast cross sections through the single band environment showing these features with height are also provided.

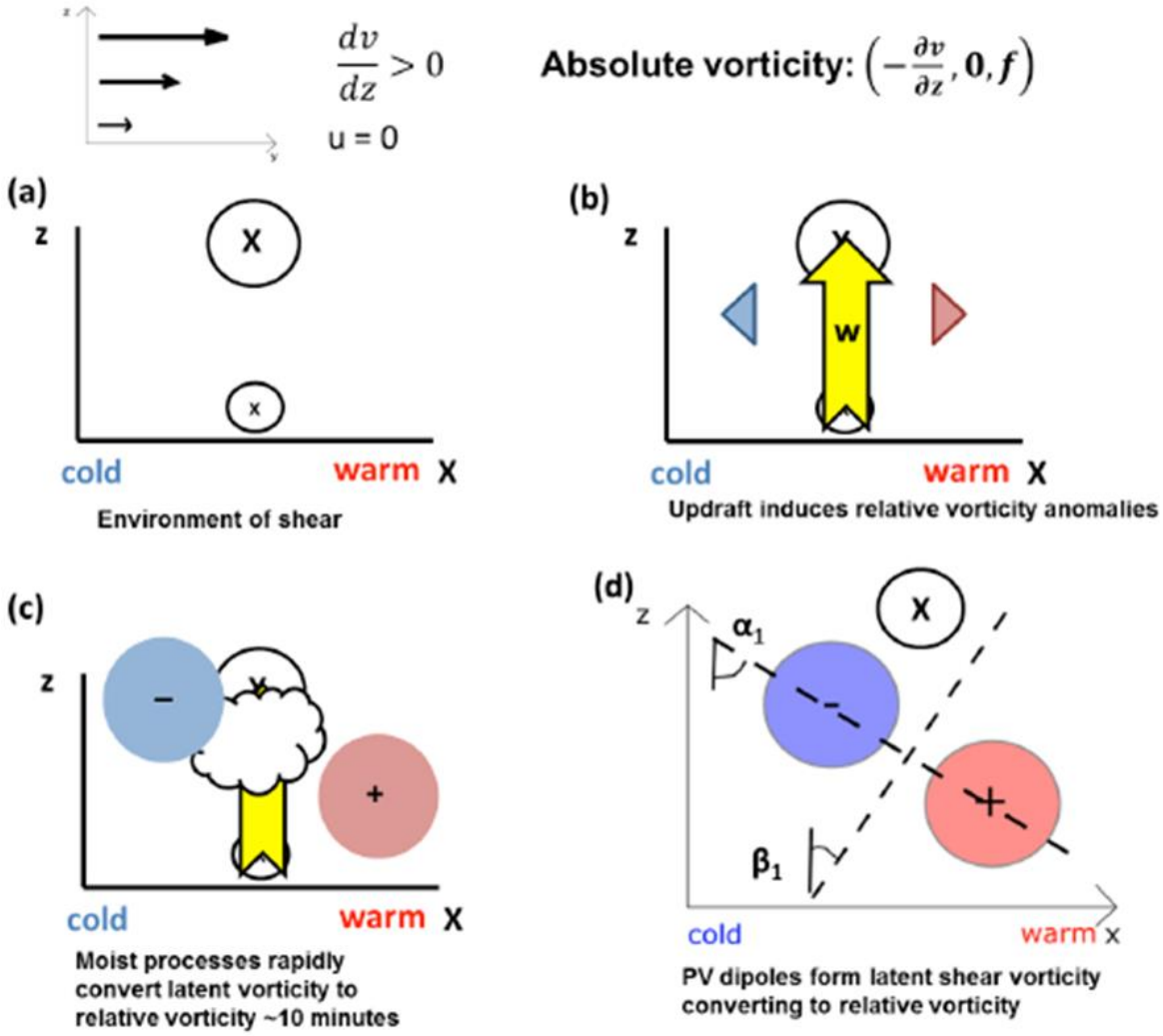

Figure 1.3. Summary schematic of the idealized formation of horizontal PV dipoles in the presence of a moist updraft from the description of mechanisms developed by Chagnon and Gray (2009). Here panel d is adapted from their Figure 1b.

Chapter 2:

Classification of Banded Structures within Northeast U.S. Winter Storms

2.1 Introduction

Cool season extratropical cyclones can exhibit snowbands, which are linear (identifiable long axis and short axis) regions of enhanced snowfall as interpreted via a linear region of enhanced reflectivity embedded within weaker radar reflectivity (Sanders and Bosart 1985b). Climatologies of snowbands in East Coast winter storms can provide knowledge of the dynamics and processes responsible in these high-impact mesoscale features. By creating a dataset of multiple cases that exhibited similar mesoscale precipitation structures, more insight into the representativeness of a single case can be obtained.

Cases are identified for inclusion within a climatological study by various criteria. Storms are identified by surface precipitation thresholds (e.g., Novak et al. 2004; Novak et al. 2010) and specifically surface snowfall thresholds (e.g., Kenyon et al. 2013; Baxter and Schumacher 2017). Once cases are determined, snowbands can be identified within the broader precipitation of a storm. Previous studies have imposed band classification schemes that depend on band attributes such a size, duration, and magnitude (e.g., Novak et al. 2004, 2010; Fairman et al. 2016; Baxter and Schumacher 2017) and even motion (Kenyon 2013). Bands have been identified according to subjective classification schemes (e.g., Novak et al. 2004; Novak et al. 2010; Kenyon et al. 2013; Baxter and Schumacher 2017) and objective classification schemes (Fairman et al. 2016).

Banding characteristics such as size and duration can be obtained from climatological studies. Relating these attributes to band location relative to the cyclone center can provide additional insight into which quadrant of a cyclone is more conducive to banding than others which can be used to make inferences about the environment supportive of bands. The ultimate goal of banding classification is that once storms are classified and grouped together by their similarities, composites can be created of synoptic and mesoscale fields to compare and contrast

banding ingredients (i.e., forcing, instability, and lift) of the various banding types or to compare with that of storms that exhibit no bands.

This study uses a combination of automatic, or objective, and manually, or subjective, snowband identification methods from cases of winter storms that track within the NEUS domain. A comparison of this study domain with that of previous climatological banding studies is provided in Figure 2.1. This domain was centered on Long Island, NY and selected to incorporate data available from 6 coastal NEUS radars east of the Appalachian Mountains in order to minimize analysis of terrain-influenced precipitation bands. Section 2.2 details the data and methods used to identify storms and classify snowbands by size. Section 2.3 highlights the results from the identification and classification of snowbands within the dataset. Section 2.4 summarizes the main findings from creating this climatology and how the distribution of observed banding types compares with that of previous studies.

2.2 Data and methods

a. Case identification

Different approaches have been used to identify snow band events in the past. For example, Novak et al. (2004) looked for 1.0 in of rainfall or 0.5 in liquid equivalent snowfall over a 24 h period to obtain a 5 cool season (i.e., October–April) dataset with 111 cases over the Northeast United States. Novak et al. (2010) performed the same methodology by for 6 cool seasons in a later set of years that identified 144 cases. Both of the aforementioned studies did not discriminate between precipitation features producing rain or snow at the surface. Meanwhile, Kenyon et al. (2013) identified cases in the Northeast US that exhibited heavy snow accumulation defined as accumulation ≥ 6 in. (15.2 cm) during a calendar day. This resulted in 136 identified heavy snow days that were then subjectively examined for evidence of lake effect snow activity, which accounted for 40 of these dates. Ultimately, 96 heavy snow dates were determined to arise from 70 separate cases during 6 cool seasons. Baxter and Schumacher (2017) focused their study on the Central US and also restricted their identified cases to being associated with snowfall. They did this by using the National Centers for Environmental Information (NCEI) Cooperative Summary of the Day (COOP) to search for days with > 4 inches (10.2 cm)

of snowfall during the 1200 UTC – 1200 UTC 24-h period. The Automated Surface Observing System (ASOS) temperature data was used to further determine if the precipitation type was snow. This methodology produced 105 cases within 5 cool seasons.

A recent study by Fairman et al. (2016) identified cases using 1-km horizontal grid spacing composite radar data for the entire CONUS from 12 years, with no special focus on winter storms. This study did not identify cases but rather treated each 5-minute radar file independently to examine bulk statistics of bands defined as reflectivity objects having a major axis ≥ 100 km and a ratio of major axis length to minor axis length of 3:1 or greater. Such bands were examined in separate geographical regions and during all seasons. For example, they were able to highlight lake effect systems and the East Coast storm track in winter without reference to the number of cases that comprised the climatological maxima.

The five climatological banding studies highlighted here had varied study domains (Fig. 2.1), data, and methods. All were used to inform the data and methodology used in this study. In this study, cases were identified as cool season (October - April) low pressure systems that tracked through the Northeast U.S. between 1996/97 - 2015/16 with ≥ 1.00 in (2.54 cm) of liquid equivalent snowfall measured at ≥ 2 of 7 Automated Surface Observing System (ASOS) stations across the northeast United States which consisted of Portland, ME, Islip, NY, Boston, MA, Philadelphia, PA, Bridgeport, CT, Providence, RI, and Newark, NJ (Hoban 2016). Over 150 cases were initially identified using this metric over 20 cool seasons, but 110 were ultimately used based on radar data availability from six coastal radars (Fig. 2.2). Each case could span multiple days, depending on the speed and extent of the affecting cyclone, but such days were consolidated into a single case within the database. This resulted in a total of 110 cases which are provided in Table 2.1.

b. Cyclone tracking

The band location relative to the parent surface cyclone center (i.e., nearest sea level pressure minimum) is used in this study in order to compare with recent studies that highlight single bands form in the northwest quadrant for NEUS storms (Novak et al. 2004) or the northeast quadrant for continental US storms (Baxter and Schumacher 2017). Cyclone tracks were calculated from the from the 6 hourly 0.5° NCEP Climate Forecast System Reanalysis

(CFSR; Saha et. al. 2010) for years it is available (1996–2010) and then from the 6 hourly 0.5° NCEP Climate Forecast System version 2 (CFSv2; Saha et al. 2014) analyses (2011–2016). Other reanalysis data were considered, especially the North American Regional Reanalysis (NARR). Charles and Colle (2009) showed that the NARR had a weak bias for cyclones along the U.S. East Coast that was not shown with the CFSR (Colle et al. 2013). The CFSR was used in favor of the NARR for additional reasons discussed more in-depth in Chapter 3.

In order to track the extratropical cyclones on a common grid, the Hodges (1995) cyclone tracking scheme was implemented according to the methodology provided in Colle et al. (2013) and reproduced here. A spectral bandpass filter was used to preprocess the data. The wavelength is set to 1000 km for planetary scale removal and 600 km for the high frequency cutoff. The cyclone tracking involves four: (1) Segmentation identifies the objects in the MSLP fields, which are the regions around minima in the MSLP field. This requires thresholding the data into object and background points and then the partitioning of the points into distinct objects that are stored for further processing. (2) Feature detection identifies suitable points, such as local minimum in MSLP field within each object. The minimum is found by comparing each object point with its neighbors. If clusters of local minima occur with points having the same local extreme value, the centroid of these points is found for each cluster. (3) To determine the correspondence between feature points, a constrained optimization using a cost function is applied. Those feature points connected as one cyclone are labeled with a unique storm ID. All of these feature points are stored in records that have four fields for a 2-D domain: two for the coordinates (latitude and longitude), one for the strength of the feature point, and one for the track number for the feature point. (4) Those identified storms are filtered to retain only those that last at least 24 hours and move farther than 1000 km. The minimum lifetime and minimum moving distance are set to remove the feature points exist for too short time or remain too stationary.

Cyclone tracks were identified for each case in the study. If there were multiple cyclones in the NEUS domain for a particular case, the cyclone subjectively determined to be more associated with the observed precipitation as shown by the radar reflectivity regional composite discussed in Section 2.2c was manually selected. If a cyclone track did not appear for a particular case because the cyclone was too weak to be identified then the NOAA Weather Prediction Center (WPC) surface analyses for that date and time were used to subjectively track the manually-identified low pressure center every 6-h.

Comparisons of sea level pressure minimum (i.e., cyclone position) for the raw 0.5° gridded CFSR data and the cyclone position from the tracker derived from the SBU methodology for various times along the track for the 26–27 Dec 2010 case shows good agreement (Fig. 2.3). There was also good agreement of the magnitude of the cyclone for this example case between the SBU tracker, WPC surface analyses, the raw CFSR grid and additional gridded datasets including the North American Regional Reanalysis (NARR; Mesinger et al. 2006) and the ECMWF European Reanalysis (ERA-Interim; Dee et al. 2011) as shown in Table 2.2. The SBU tracking method is within ± 10 hPa of the WPC analyses, which are consistently stronger along the track of this cyclone than resolved by the reanalysis datasets. Several additional cases were examined and the WPC analyses were at least ±5 hPa of the SBU tracking method, with < 50 km of between track locations. The cyclone tracks from the CFSR (1996-2010) and CFSv2 analyses (2011-2016) calculated via the Hodges tracking scheme for each of the 110 cases in the study are provided in Figure 2.4.

c. Regional composite radar dataset

Radar data was "stitched together" or composited according to methodology developed by our collaborators at NCState University (Dr. Sandra Yuter) from six Northeast U.S. coastal radar sites (KGYX, KENX, KBOX, KOKX, KDIX, KDOX) in Figure 2.5. The methods are described in detail in Hoban (2016) and Corbin (2016) and are summarized in this section. Level-II radar data was interpolated to a constant elevation of 2 km AGL from each of the six radar sites. Clutter maps were employed to quality-control the data for non-meteorological echoes, or noise due to radar beam interferences specifically close to the radar (within a radius of 2 km). Data extending approximately 200 km from all radar sites were calibrated to the KOKX radar. In the case of overlapping data between two radars (KBOX, KENX, KDIX overlap with KOKX), data was only taken from the KOKX radar for that time. The approximately 5-minute data was interpolated into a 2 km by 2 km horizontal grid and available as one file for all times within each case.

d. Objective identification of bands

Bands of precipitation are classified from automatically-detected objects from the gridded reflectivity data. The Method for Object-Based Diagnostic Evaluation (MODE) tool within the Model Evaluation Tools (MET) version 5.1 developed at the Developmental Testbed Center (DTC) at the Research Applications Laboratory (RAL) at the National Center for Atmospheric Research (NCAR) was used to objectively identify precipitation structures in the stitched regional composite radar data (Developmental Testbed Center 2015; Davis 2006a,b; Brown et al. 2007; Bullock et al. 2016).

MODE typically works on both an observational dataset and a forecast dataset by identifying objects in each independent dataset, quantifying object attributes within each independent dataset, and then applying a fuzzy logic algorithm to compare objects within the two datasets. In this study, objects were identified and attributes were provided for the observational dataset only as a method of objective identification rather than verification.

MODE identifies objects within a gridded field in three steps: 1) convolution thresholding, 2) masking and creating a field object, 3) returning objects and their attributes in the raw data field. The first convolution thresholding step is meant to smooth the raw data field. A simple filter function is applied (Eq. 2.1) that smooths the data before masking is applied.

$$C(x,y) = \sum_{u,v} \phi(u,v)\, f(x-u)(y-v) \qquad \text{Eq. 2.1}$$

$$\phi(x,y) = \begin{cases} H \text{ if } x^2 + y^2 = R^2 \\ 0 \; otherwise \end{cases} \qquad \text{Eq. 2.2}$$

$$\pi R^2 \, \mathrm{H} = 1 \qquad \text{Eq. 2.3}$$

In Equation 2.1, f is the raw data field, ϕ is the filter function and C is the resulting convolved field with the variables (x,y) and (u,v) being grid coordinates (Developmental Testbed Center 2015). The filter function (Eq. 2.2) is a simple circular filter determined by the radius of influence, R, and a height H which are related by Equation 2.3. The stitched regional composite reflectivity data has a grid unit length of 2 km. To keep smoothing from being performed on the raw field, the convolution radius (R) was set to 0 grid units. Masking is then used to create a

binary field from the convolved data that equals 1 where the convolution filter function (C) returns the threshold value, T, and 0 elsewhere, as in Equation 2.4.

$$M(x,y) = \quad = \begin{cases} 1 \text{ if } C(x,y) \geq T \\ 0 \; otherwise \end{cases} \qquad \text{Eq. 2.4}$$

The threshold value for the reflectivity field varies for each case is the most important quantity in the method of determining objects in the precipitation field. Lawson and Gallus (2016) found that objective identification and verification of reflectivity data using a similar method exhibited "substantial sensitivity" to the reflectivity threshold chosen for summertime convection. They found that using too low of a reflectivity value (5 dBZ) yielded too small of a sample size of objects, but using too high of a value (40 dBZ) lost other features, i.e., stratiform precipitation. They concluded that the threshold chosen should be done so to focus on the signal of interest. In a study of banding throughout all four seasons, Fairman et al. (2016) chose a static threshold value of 20 dBZ for their similar method.

In this study, the threshold is computed based on a series of tests on example cases. Statistics were computed upon the regional composite reflectivity data by first converting the data from a 3-dimensional array with dimensions in time, latitude, and longitude to a one-dimensional array. The following quantities were calculated on this 1-D array: minimum, lower-dectile, lower-octile, lower-quartile, median, mean, upper-quartile, upper-octile, upper-dectile, and maximum. Data were used throughout the entire regional radar composite domain and also tested on a sub-region centered over Long Island, NY (Fig. 2.5).

The results of this thresholding test are shown as an example for a singular time for one case in Figure 2.6, but were tested in 10 cases listed in Table 2.3 to determine broader applicability for a range of storms. The median value of reflectivity within the whole domain and the subdomain for each case proved to be too low when used as the threshold value for masking the data (Figs. 2.6b,c). The resulting object field encompassed almost all of the existing reflectivity echoes with no isolation of individual structures. The upper-octile and upper-dectile resulted in the opposite effect, i.e. too few structures were identified because the threshold was too high (Figs. 2.6h,i). Using the upper-quartile reflectivity value proved to be the best measure from the available statistics when calculated from the subdomain versus the whole domain (Figs. 2.6e,f). When reflectivity is plotted above this threshold, objects could be identified that matched

objects identified using subjective identification methods, i.e. with the naked eye looking for local maxima in the data comparing Figures 2.6a,d,g with Figure 2.6f. However, relying on this subdomain method is not prudent because there is less likelihood of always having reflectivity within the small box versus the whole domain during a storm.

The previous thresholding methods calculated the quantities using one value per case, or calculating one single threshold to represent the entire duration of a storm. This method failed when a storm exhibited brief periods of higher reflectivity while most bands occurred with lower reflectivity values (e.g., a region of rain within the domain that cooled to an all-snow event for the remainder of the storm). To counter this limited static threshold, the previous statistics were calculated for each instantaneous data time step for the duration of each case to produce a dynamic threshold value. This was computed over the entire data domain. The threshold that was found to work best through manual verification of 10 cases (Table 2.3) when dynamically calculated was the upper-sextile of the reflectivity throughout the Northeast U.S. domain at each time within a storm. That meant that 17% of the reflectivity data is at or above this value, therefore highlighting the enhancements of snowbands within the weaker, smaller reflectivity values. Many sensitivity tests were conducted for this thresholding method including comparing the upper-sextile with the upper-quartile and upper-octile of reflectivity calculated over the entire region. The upper-quartile was found to be too low and failed to separate individual bands of higher reflectivity embedded within widespread precipitation. The upper-octile was found to be too high of a threshold that trimmed bands down, therefore underestimating their spatial characteristics. This upper-sextile threshold (T) was used to create the masked field (Eq. 2.4) at each time available during each case.

Once the masked field (M) is computed, objects are identified with the MODE tool as regions that are continuous in space. If there is even one grid point separating the objects, they are counted as separate objects. Attributes are computed for each object and include the object area which is the number of grid squares an object occupies and the centroid, or geometric center, of an object. The length, width, aspect ratio, and axis angle are computed by fitting a rectangle around each object. The aspect ratio is the ratio of the short axis to the long axis. The axis angle is the angle of the long axis of the rectangle relative to 90° (east). A schematic of the spatial attributes of an idealized snowband object that are used in this study is provided in Figure 2.7.

The MODE software output in this study was gridded NetCDF files and ASCII text files. The NetCDF files contain the raw data, the raw data overlaid on object locations, and the object numbers in a gridded format. The text files contain all of the object attributes for each object identified for that time. MODE was run in such a way that it looped through each available time in each case. There is no need for consistency between time steps as each time step is processed independently. Therefore, files were created for each time during each case.

There is a large variation of storm (and reflectivity) intensity between all 110 storms that ultimately motivated a dynamic threshold. However, this instantaneously-calculated threshold was not without its limitations. There were times when a weaker band existed during a stronger storm with too high a reflectivity threshold that resulted in a failure of the method. The threshold was often skewed higher by offshore rain in several storms, which might be unique to this study of Northeast U.S. winter storms due to their proximity to the warm Gulf Stream waters. This method did not work well for 8 out of 110 storms during which manual methods had to be employed to subjectively identify (i.e., use the human eye on the raw observed reflectivity field) instead of relying on the objective methods. All objective and subjective data was then classified according to the criteria that will be discussed in Section 2.2e.

e. Classification of bands

Previous climatologies of bands used predominantly subjective classification schemes. Novak et al. (2004) classified "events" within each case as either a single band, multi-bands, narrow cold-frontal band, non-banded, transitory, and undefined from 5-minute composite reflectivity data. They defined a single band event as a linear structure 20–100 km in width (minor axis), ≥ 250 km in length (major axis), with an intensity ≥ 30 dBZ maintained for at least 2 h. Multi-band events were defined as ≥ 3 finescale (5–20-km width) bands with periodic spacing and similar spatial orientation, with intensities ≥ 10 dBZ over the background reflectivity maintained for at least 2 h. Narrow cold-frontal band events were defined as a narrow (10–50 km), long (≥ 300 km) band found along surface cold front or in the warm sector, with an intensity ≥ 40 dBZ maintained for at least 2 h. Transitory events was a structure that meets all respective criteria in a given category, except one (usually the lifetime), while non-banded met none of the aforementioned criteria. Undefined events were those that could not be classified due

to, for example, incomplete radar data.

The subjective classification by Kenyon et al. (2013) highlighted the behavior, or movement, of snowbands from 5-minute composite reflectivity data. They defined a band as having an aspect ratio (length-to-width) ≥ 4:1 with reflectivity ≥ 25 dBZ along ≥ 50% of the band axis and ≥ 10 dBZ over the background reflectivity that persisted for ≥ 3 h around a 6-hourly analysis time. To confirm that bands were snowbands, the additional criterion of observed snow at the surface (per hourly surface observations) at any time within the event was required. Non-banded or weakly banded events were classified as any time of observed reflectivity that did not fit all of the aforementioned criteria. They then applied the following scheme based on band motion: (1) laterally translating, exhibited predominantly cross-axis motion, thereby favoring quasi-uniform snowfall accumulation along their paths, (2) laterally quasi-stationary, characterized by near-zero cross- axis motion, favoring heavy snowfall accumulation along a narrow corridor that may extend for several hundred kilometers, (3) pivoting, exhibited pronounced rotation such that heavy snowfall accumulation is particularly favored near the center of rotation, and (4) hybrid, dominated by along-axis motion, but with a concurrent cross-axis component of motion.

The recent study by Baxter and Schumacher (2017) used a simple subjective classification scheme on 1-km grid spacing composite reflectivity data with 5-dBZ binning for continental cyclones. Their classification scheme consisted of two categories: single snowbands and non-banded. Single snowbands were identified if they featured radar reflectivity of ≥ 25 dB, a length (major axis) ≥ 250 km, and an aspect ratio (length to width) of 3:1 that spatially and temporally coincided with ASOS and COOP snowfall reports. If snowfall reports coincided with a region of reflectivity that did not meet the aforementioned criteria then it was classified as non-banded. Their study acknowledged the existence of multiple bands at one time within a storm, but treated each band as an independent single snowband.

In this study, the classification was a multi-step process that combined subjective classification used in the aforementioned climatologies but for objectively identified bands. Classification was first completed by post-processing the text data output by MODE. Objects were determined to be snowbands if their aspect ratios (length of minor axis divided by the length of major axis) was ≤ 0.5. The bands were additionally classified into primary bands, mid-sized bands, or undefined according to the length and width criteria provided in Table 2.4. An

example of each of the classified objects, the raw objects determined from MODE, and the observed reflectivity field from each of the three threshold tests discussed in Section 2.2d is provided in Figure 2.8.

Next, both the classified field and the raw reflectivity field were looped to subjectively classify dominant banding types within one region of the storm at each 6-hourly analysis time during a case (i.e., 0000, 0600, 1200, 1800 UTC). The classifications were one of four different categories based on the types of objects that were identified within one boxed region extending 150 km from each of the 6 sounding locations in Figure 2.9 (i.e., KGYX, KALB, KCHH, KOKX, KIAD, KWAL) every 6 h during a case. Initially, the most representative classification for a particular case was subjectively determined during the time of peak banding activity to allow for only one classification per case, even though most storms exhibited an evolution of banding types so each 6-h event was retained. The use of 6-hourly events is consistent with what had been done in previous studies (e.g., Novak et al. 2004; Baxter and Schumacher 2017). The four categories were adapted from Novak et al. (2004). The first category is for a storm that exhibits a primary band ($L \geq 200$ km) and no other identified structures and is termed the single band category (SINGLE). The second category is for a storm that exhibits ≥ 2 mid-sized bands that are parallel to each other and move with a similar velocity and is the multi-band category (MULTI). The third category is for a storm that exhibits a large, primary band accompanied by mid-sized bands that exhibit similar motions and is termed the both single band and multi-bands category (BOTH). The fourth and final category is for storms that exhibit none of the previous linear precipitation structure classification criteria and is termed the non-banded category (NONE). The method of classifying a time during a storm is provided in Figure 2.10. Examples of cases in each of the four categories are found in Figure 2.11.

f. Subjective classification of banding events for cyclone stage and movement

There was a large amount of variability in the stage of the cyclone responsible for ≥ 1.0 in (2.54 cm) liquid equivalent snowfall in the study domain as well as band motion manually observed within the storms of this study. This motivated the additional sub-classification based on both cyclone stage and band motion. Cyclone maturity has been used in refining climatological studies such as by Novak et al. (2010) who used the presence of a closed 700-hPa

circulation to differentiate comma head cases (i.e., stronger cyclones that would likely have precipitation wrapping around the center to form a comma head) from non-comma head cases within their 6-year study. Kenyon et al. (2013) looked into band motion with a special focus on both laterally translating and radially pivoting single bands.

Cyclone maturity during each 6-hour time was classified as either developing (DEV) or mature (MAT) determined manually using the NWS's WPC surface analyses following the Norwegian and Shapiro and Keyser cyclone models (Bjerknes and Solberg 1922; Shapiro and Keyser 1990; Colle et al. 2014). Specifically, DEV storms were defined as having an open wave frontal structure while mature cyclones were at the start of the occluded stage defined as when circulations around a cyclone create an occluded front that separates the cold air behind the cold front from the warm air ahead of the cold front (Schultz and Vaughan 2010). An idealized schematic of the different cyclone stages is provided in Figure 2.12. The location of the precipitation band relative to the cyclone center can depend on cyclone maturity, such as forming north of a warm front in a DEV cyclone versus northwest of the occluded front in a MAT cyclone (Schultz and Vaughan 2010). The observed microphysics of snowbands in NEUS winter storms was found to vary in qualities such as the degree of riming depending on the cyclone phase which indicates the sensitivity of microphysics to the strength of vertical motions (Colle et al. 2014). The four initial classification categories were classified into DEV and MAT cyclones resulting in eight categories shown in the chart in Figure 2.13.

The 5-minute interval loops of raw reflectivity and classified bands were used to classify geographic-centric band motion by animating ± 1 h on either side of the 6-hourly analysis time. The two classification categories used were radial (RAD) and lateral (LAT). One or more bands were classified as moving radially if their motion was perpendicular to their long axis or axes. Multi-bands were classified as having similar orientations so their long axes were always oriented in the same direction, by definition. An idealized schematic of the two classifications of band motion is provided in Figure 2.14. This radial classification is comparable to the laterally translating and pivoting classifications used by Kenyon et al. (2013). The other classification is lateral, defined as band motion parallel to the long axis. This classification is comparable to the laterally quasi-stationary classification used by Kenyon et al. (2013). The results from their study showed that various band motions resulted from different synoptic and mesoscale environments, so therefore were taken into account within this study for comparison. The eight classifications

of band type and cyclone strength were further sub-classified into RAD and LAT moving bands, resulting in 12 different classification categories. The non-banded (NONE) classification was classified into DEV or MAT cyclones, but no motion criteria were applied because there were no defined bands to base the classification on. The sub-classification using band motion criteria are shown in the schematic within Figure 2.13.

One of the primary goals of this study is to elucidate the differences in banding ingredients within the synoptic and mesoscale mass fields between single bands and multi-bands. The classification criteria contain the BOTH category for when mid-sized bands are coincident with primary bands at an analysis time. While this category was treated independently and useful conceptual information was gained for forecasting uses of storms producing both precipitation structures, all storms containing the BOTH category were qualified with a single or multi-banding dominance criteria. The spatial extent and duration of single or multi-bands within the same region of a storm was determined from the animations of raw reflectivity and object classification data from ± 1 h of the classified time. If a single band was present with < 3 multi-bands (recall that the multi-band definition is ≥ 2 mid-sized bands) with shorter durations than the single band, then the single band type was dominant. If there were > 3 multi-bands that persisted as long as the single band with similar magnitudes (as measured in dBZ) then that time was classified as multi-bands dominant. If a single band coincides with multi-bands at the classification time but forms from or breaks down into multi-bands within the two-hour window then that time was classified as multi-bands dominant. This final sub-classification was applied to all cases of both a single band and multi-bands (BOTH) in order to compare three scenarios of single bands (SINGLE), multi-bands (MULTI) and non-banded (NONE) that can be further broken down into cyclone strength and band movement, if the sample sizes allow. An example of a BOTH case that was predominantly single banded versus predominantly multi-banded is provided in Figure 2.15.

2.3 Results

a. Distribution by case

The most common category exhibited from the 110 storms in the study was the both single and multi-bands classification with a total count of 55 storms (Table 2.5). It turns out that multi-bands accompany a single band at some point during its life cycle, solely single bands detected in 2 storms. The location of the clusters of each classification can be seen relative to the cyclone center in Figure 2.16. All three classifications of individual and combined single bands and multi-bands tend to occur in the northern quadrants relative to a cyclone center, whereas the non-banded classification tend to occur in the eastern and southern quadrants. Storms were also analyzed to compare 56 stronger, MAT storms with 54 weaker, DEV storms. It was found that DEV storms mostly exhibited the non-banded precipitation classification (22) and the both single band and multi-band classification (26), whereas MAT storms were mostly associated with the classification of both single band and multi-bands (33).

The results of the band motion classification on the cyclone strength classified times (one per case only) are provided in Table 2.5. Band motion was predominantly in the radial or perpendicular direction to the band(s), with 49 of the 73 banded case classification exhibiting RAD movement, leaving the remaining 24 as parallel or laterally-moving (LAT). The most pronounced difference between RAD and LAT movement was for the BOTH classification for both the developing and mature cyclones. In this case, RAD was the preferred band motion, particularly for mature cyclones that exhibited over 5 times as many counts of RAD movement (28 storms) than LAT movement (5 storms).

b. Distribution by event

The results of the approximately 6-hourly event classifications produced a total of 193 events from the 110 cases. The distribution relative to the cyclone center is consistent with what was shown with the previous one classification per case analysis (Fig. 2.17). The initial classification into the four standard categories is as follows: 5 SINGLE, 35 MULTI, 107 BOTH, and 46 NONE. Applying the cyclone strength classification, all 5 SINGLE events were associated with a mature cyclone and most occurred in the northwest quadrant of a cyclone (Fig. 2.18a). MULTI events were approximately equitably distributed between developing (18) and mature (17) cyclones. BOTH events were less often observed with developing (43) than mature cyclones (64). NONE events were more often associated with developing (29) than mature

cyclones (17). The results of the final application of the geographic-centric band movement classification are provided in Table 2.6. While the distribution of counts of MULTI events was similar for both DEV and MAT cyclones, the bands favored lateral movement when associated with DEV cyclones versus a radial movement when associated with MAT cyclones with approximately twice as many counts in each classification. For both MAT and DEV cyclones, more multi-bands occurred in the northeast quadrant than the northwest quadrant (Fig. 2.18b). A similar relationship for band motion is evident when comparing the motion associated with BOTH events. Lateral band motion is favored when a cyclone is classified as DEV versus the radial motion for when a cyclone is classified as MAT. RAD classified events typically occurred in the northwest quadrant of a MAT cyclone, while LAT classified events typically occurred in the northeast quadrant of a DEV cyclone (Fig. 2.18c). Non-banded events were predominantly in the eastern quadrants, favoring the northeast quadrant (Fig. 2.18d).

Even with the approximately 6-hourly events, there are only 5 times at which there was only a primary or single band observed. However, a primary was present in all of the 106 BOTH events. The application of qualitative band dominance for the BOTH events as either being predominantly single-banded or multi-banded is conducted to re-merge the previous classification into three main categories: SINGLE, MULTI, NONE. This resulted in 52 SINGLE, 95 MULTI, and 46 NONE events for all cyclone strengths and band motions. Slightly more SINGLE events were associated with DEV (23) than MAT cyclones (29). Approximately two-thirds as many MULTI events were associated with DEV (38) than MAT cyclones (57). Applying the band motion classification, SINGLE events were almost equally likely to move radially (10) as laterally (13) while a storm was developing. However, SINGLE bands were more likely to move radially (24) than laterally (5) when a storm was mature. SINGLE bands in the northwest quadrant were most often associated with radially moving bands while the laterally moving bands were typically located in the northeast quadrant (Fig. 2.19b). MULTI events associated with DEV cyclones most often had bands moving laterally (27) than radially (11). However, when associated with a MAT cyclone, bands within MULTI events tended to move radially (51) rather than laterally (6). Most mature RAD MULTI events occurred in the northwest quadrant of the cyclone (Fig. 2.19c). The band motion characteristics combined with the cyclone strength information is used to inform the analysis of environmental ingredients

associated with these different banded and non-banded structures that will be discussed in Chapter 3.

c. Spatial band characteristics

The MODE object data from the 77 banded cases in this study was used to examine some spatial characteristics of the identified bands. From hourly data within 61 (71) cases, 208 primary bands (786 mid-sized bands) were analyzed. Using this hourly data, bands are likely sampled multiple times within a single case. The average length for single bands (multi-bands) was 345.05 km (72.85 km). The distribution of lengths of both mid-sized bands and primary bands are shown in Figure 2.20. The average width of single bands (multi-bands) was 102.96 km (24.52 km). The average aspect ratios was similar for single bands and multi-bands, 0.31 and 0.36, respectively. The relationship between length and width for both primary bands and multi-bands is provided in Figure 2.21 and shows that the majority of bands had lengths $\leq$ 500 km and widths $\leq$ 100 km. The average area of single bands was much larger than that of multi-bands, 38,743 km^2 compared to 2,349 km^2. This is evident when looking at the distribution of band area for both mid-sized bands and primary bands, which shows the largest number of counts at each of the edges of the distribution indicating that mid-sized bands are typically much smaller than primary bands (Fig. 2.22). When the area of every band was added up, multi-bands comprised 18.67% of the total banded precipitation area. With close to 20% of all banded precipitation area coming from multi-bands (1.85×10^6 km^2), the importance of these features related to cyclone impact (i.e., surface snowfall accumulations, rates, visibility) is apparent. A summary of the quantitative band characteristics is found in Table 2.7.

Band orientation in addition to the location relative to the cyclone center is shown for primary bands from SINGLE and BOTH events for DEV and MAT cyclones in Figure 2.23. There is a cluster in the northwest quadrant of bands oriented southwest-northeast which is hypothesized to match the orientation of enhanced baroclinic zones that will be analyzed in Chapter 3. More primary bands in the northeast quadrant are associated with DEV cyclones rather than MAT cyclones (Fig. 2.23). The more west-east orientation of these primary bands is hypothesized to be due to their collocation with the warm front which requires additional

analysis. The band orientations and clustering in the northern quadrants is consistent with similar analysis conducted by Novak et al. (2004) and Baxter and Schumacher (2017).

2.4 Summary and discussion

The methodology and results of a combination of objective and subjective band classification of 110 NEUS winter storms are discussed. The dataset was comprised of extratropical cyclones that produced ≥ 1.00 in (2.54 cm) liquid equivalent snowfall in the NYC metropolitan area. A regional composite of 2-km AGL radar reflectivity data from six coastal NEUS radars were used to identify and classify bands using MODE, specifically into primary bands ($L \geq 200$ km) and mid-sized bands ($L < 200$ km) both with aspect ratios (ratio of width to length) ≤ 0.5.

Several thresholding tests were conducted to conclude that using the upper-sextile of domain-calculated reflectivity produces the best band identification results. The identified bands were then classified within one of six regions of a cyclone within a sounding domain into one of four categories at a 6-hourly analysis time: single band only (SINGLE), multi-bands only (MULTI), both single and multi-bands (BOTH), and non-banded (NONE). The most common categories were BOTH (59) and NONE (37). The initial classification of one per case during peak band activity was modified to include classifications done approximately every 6 hours within an event for events that showed evolution in the banding characteristics (i.e., transitioned from non-banded to banded or from single-banded to multi-banded). This took the count of classified times from 110 to 193. The most common categories were BOTH (107) and NONE (46).

Additional information was used to further sub-classify the categories by their association with a DEV or MAT cyclone and the type of geographic-centric band movement exhibited as being either radially moving (perpendicular to long axis) or laterally moving (parallel to long axis). This analysis was done for both the initial 110 classification times and then extended to the 193 6-hourly events. Consistent results between both datasets showed that SINGLE bands most often form in the northwest quadrant, MULTI in the northeast, and BOTH in both northern quadrants. The NONE classification most often occurs in the eastern quadrants of a developing cyclone. Isolating the three main categories of SINGLE, MULTI, AND NONE, the existing 6-

hourly event dataset was re-examined to determine whether BOTH events were single band dominant or multi-band dominant. All BOTH events were then distributed to the SINGLE and MULTI classifications. This showed that SINGLE bands most often form in the northwest quadrant of cyclones whether they are accompanied by multi-bands or not. Additionally, MULTI bands tend to be located in the northeast quadrant of DEV cyclones but the northwest quadrants of MAT cyclones.

The results of this study are for snow-producing cyclones of all strengths that impact the NEUS. Previous studies over various study domains using similar methodologies produced somewhat consistent results. For example, Novak et al. (2004) determined that single bands most often occur in the northwest quadrant of a cyclone over the NEUS which is consistent with the results provided here. However, Baxter and Schumacher (2017) showed that for continental cyclones, single bands most often form in northeast quadrant along a pronounced warm frontal boundary. The results may vary between coastal storms and continental cyclones because of the enhanced baroclinicity provided by the warm waters of the Gulf Stream that would be most evident by enhanced gradients and stronger forcing to the northwest of the cyclone.

Novak et al. (2010) isolated single bands within strong storms as defined by a closed 700-hPa low indicative of a comma head that were all located in the northwest quadrant relative to the cyclone center. The results isolating mature SINGLE events agrees with this preferential location. The study by Kenyon et al. (2013) showed that different band movements were preferred depending on the location relative to the surface cyclone and mid-to-upper-level forcing. Specifically, their laterally-translating and pivoting categories which are similar to the radial (RAD) classification used in this study showed that this band movement was most often seen in both northern quadrants. Similarly, laterally quasi-stationary bands which are similar to the laterally moving (LAT) classification used in this study were most often found in the northeast quadrant of a developing cyclone. This is consistent with the movement and cyclone strength for both the developing cyclone exhibiting SINGLE LAT and MULTI LAT bands which were most often located in the northeast quadrant.

Both studies by Novak et al. (2004; 2010) examined a larger number of single bands (48 and 36 events, respectively, over 6 separate cool seasons). This could be due to their lack of an inclusion of surface snowfall observations therefore not confining their results to snowbands. A study over six cool seasons by Kenyon et al. (2013) that did discriminate by snowfall identified

34 total band events. This study consisted of 20 cool seasons and identified 147 banded snowfall events, which is similar to what one would expect if 34 events per six seasons were extrapolated to 20 seasons.

Comparisons of datasets that used different study domains, years, and classification schemes are useful in order to put the results of this study into context. Although there are some differences in the storm and band counts, the general results of the band location relative to the cyclone, the strength of the cyclone, and motion of the band(s) are consistent. For example, BOTH and SINGLE mostly occur to the northwest of a MAT cyclone (Novak et al. 2004; 2009). The studies used to compare did not examine multi-bands, but rather focused on larger bands (i.e., L > 200 km). The environments resulting in these banded structures will be compared with results of banding ingredients in Chapter 3. However, there will be no such comparison for multi-bands and therefore existing conceptual models will be adapted to incorporate these findings.

Table 2.1. Case dates used in the study that exhibited ≥ 1.00 in (2.54 cm) of liquid equivalent snow and had radar data available from all six of the radar sites. For cases lasting multiple days, a single date is listed corresponding to the most meteorologically-relevant.

Case Dates			
19960102	20031214	20090203	20130116
19960110	20040102	20090218	20130121
19960112	20040112	20090228	20130208
19970111	20040114	20091205	20130214
19970127	20040117	20091219	20130216
19970216	20040127	20091231	20130306
19970310	20040206	20100209	20130318
19970331	20040217	20100216	20131210
19971227	20040316	20100225	20131215
19990306	20040319	20100302	20131217
20000113	20050122	20101226	20140102
20000125	20050220	20110107	20140110
20000130	20050224	20110112	20140121
20000316	20050228	20110125	20140129
20001230	20050308	20110126	20140203
20010119	20051204	20110201	20140205
20010205	20051209	20110202	20140213
20011208	20060114	20110221	20140215
20020107	20060211	20110227	20140218
20020119	20060309	20110323	20150124
20021127	20070213	20110331	20150126
20021205	20070225	20111028	20150202
20021224	20070319	20120121	20150214
20030207	20081207	20120210	20150221
20030217	20081219	20120229	20150301
20030306	20081231	20121107	20160122
20030407	20090111	20121226	
20031205	20090128	20121229	

Table 2.2. Comparison of sea level pressure (SLP, hPa) for the case of 26–27 December 2010 from the SBU cyclone track dataset, the ERA-Interim, the CFSR, and the NARR.

DD/HH	SBU Track SLP (hPa)	WPC SLP (hPa)	CFSR SLP (hPa)	NARR SLP (hPa)	ERA-Interim SLP (hPa)
26/06	1002.26	1001.00	1002.52	1003.86	1002.00
26/12	995.47	992.00	995.24	997.13	995.00
26/18	988.36	986.00	986.84	991.10	987.00
27/00	981.79	977.00	978.33	985.23	980.00
27/06	976.05	970.00	973.60	979.13	973.00
27/12	969.60	962.00	968.488	972.00	968.00

Table 2.3. List of 10 cases used for MODE threshold tests for identification of objects. Cases may span multiple days but only the initial case date is listed.

19 Mar 2004	3 Feb 2009
14 Jan 2006	19 Dec 2009
11 Feb 2006	26 Dec 2010
13 Feb 2007	12 Jan 2011
19 Dec 2008	9 Feb 2013

Table 2.4. Criteria used to objectively classify objects output from the MET MODE tool applied to stitched regional composite reflectivity data.

	Length (L)	Width (W)	Aspect Ratio (W/L)
Primary Band	≥ 200 km	20 ≤ W ≤ 100 km	≤ 0.5
Mid-sized Band	< 200 km	10 ≤ W ≤ 50 km	≤ 0.5
Undefined/Cell	10 ≤ L ≤ 100 km	10 ≤ W ≤ 100 km	> 0.5

Table 2.5. Initial case classification by band type, cyclone stage, and band motion.

Classification	Cyclone Stage	Number of Storms Radial (Lateral) Movement to Cyclone Center
Single Band	Developing	0 (0)
	Mature	0 (2)
Multi-bands	Developing	2 (4)
	Mature	4 (2)
Both Single & Multi-bands	Developing	15 (11)
	Mature	28 (5)
Non-banded	Developing	22
	Mature	15

Table 2.6. As in Table 2.5 but for 6-hourly events during banded cases.

Classification	Cyclone Stage	Number of Storms Radial (Lateral) Movement to Cyclone Center
Single Band	Developing	0 (0)
	Mature	3 (2)
Multi-bands	Developing	6 (12)
	Mature	14 (3)
Both Single & Multi-bands	Developing	15 (28)
	Mature	58 (6)
Non-banded	Developing	29
	Mature	17

Table 2.7. Average spatial band characteristics from objectively identified band attributes.

	Single Bands	**Multi-bands**
# from # cases	208 bands from 61 cases	786 bands from 71 cases
Mean L	345.05 km	72.85 km
Mean W	102.96 km	24.52 km
Mean AR	0.31	0.36
Mean Area	38743 km^2	2349 km^2
Total Area	8.06 x 10^6 km^2 (81.33% of all banded precipitation area in 110 cases)	1.85 x 10^6 km^2 (18.67% of all banded precipitation area in 110 cases)

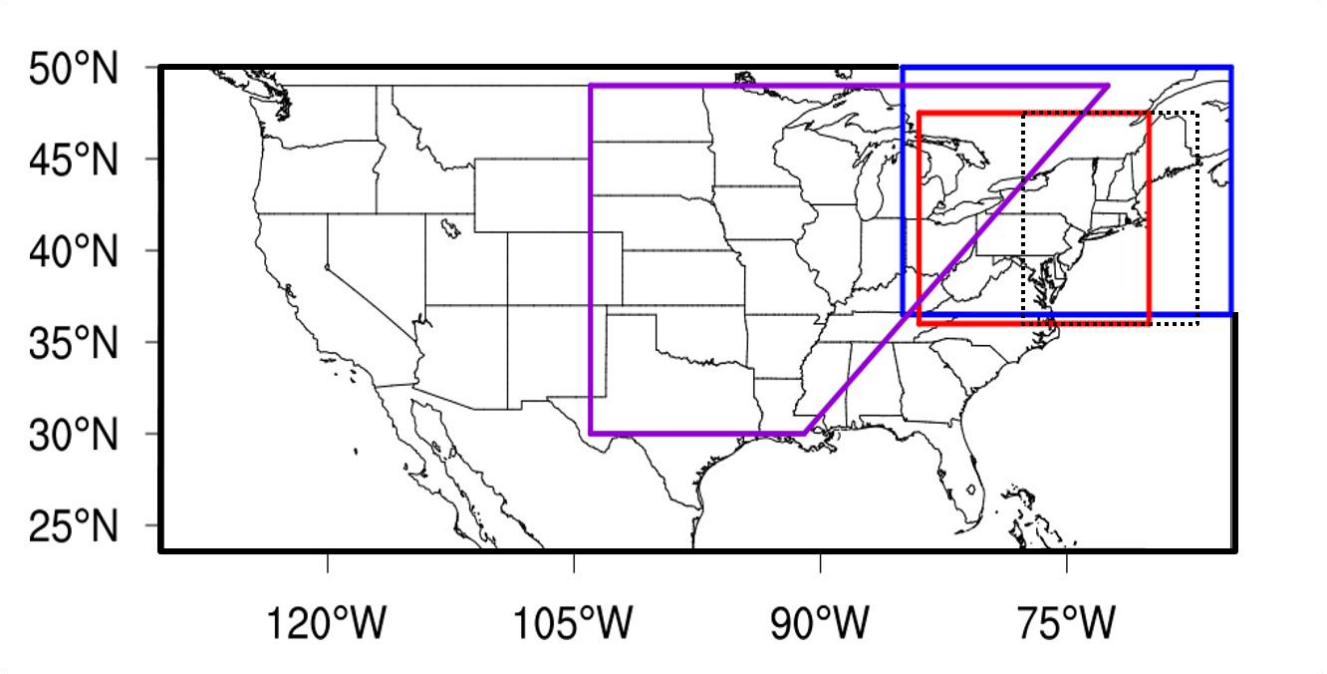

Figure 2.1. Comparison of previous banding climatological study domains with the current study domain. The outermost domain (solid black) is of CONUS study by Fairman et al. (2016). Baxter and Schumacher (2017) highlighted continental cyclones (purple) to contrast with the studies by Novak et al. (2004; 2010) of NEUS cyclones (blue). Kenyon et al. (2013) studied band motion in NEUS storms (red). The domain used in this study of NEUS storms is shown (dashed black).

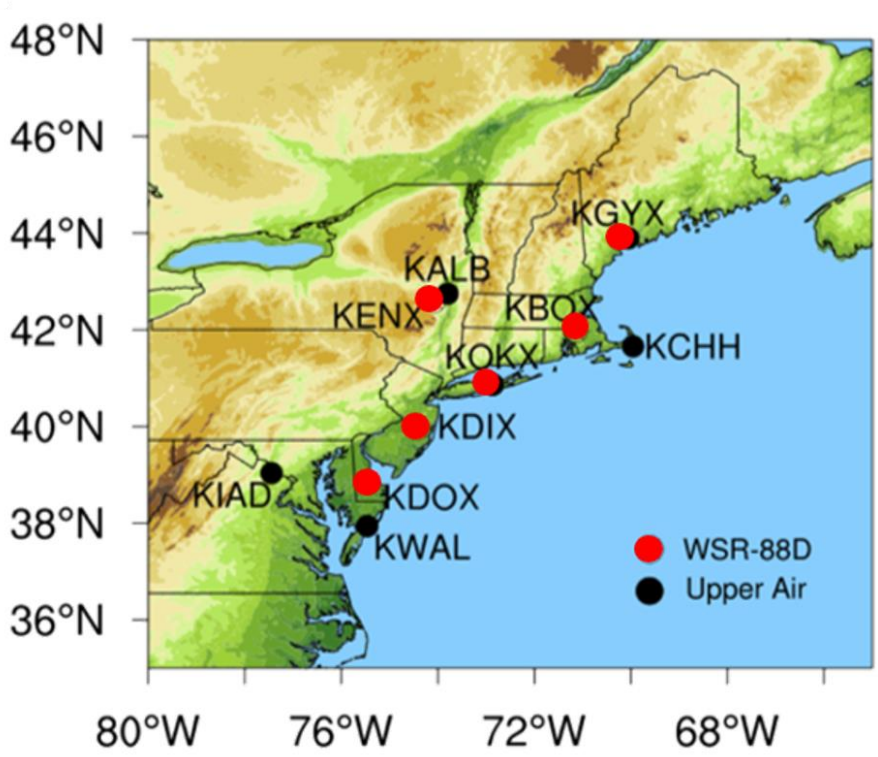

Figure 2.2. Map of six radar locations (red markers) used in the creation of the stitched radar composites. Sounding locations are also provided (black markers).

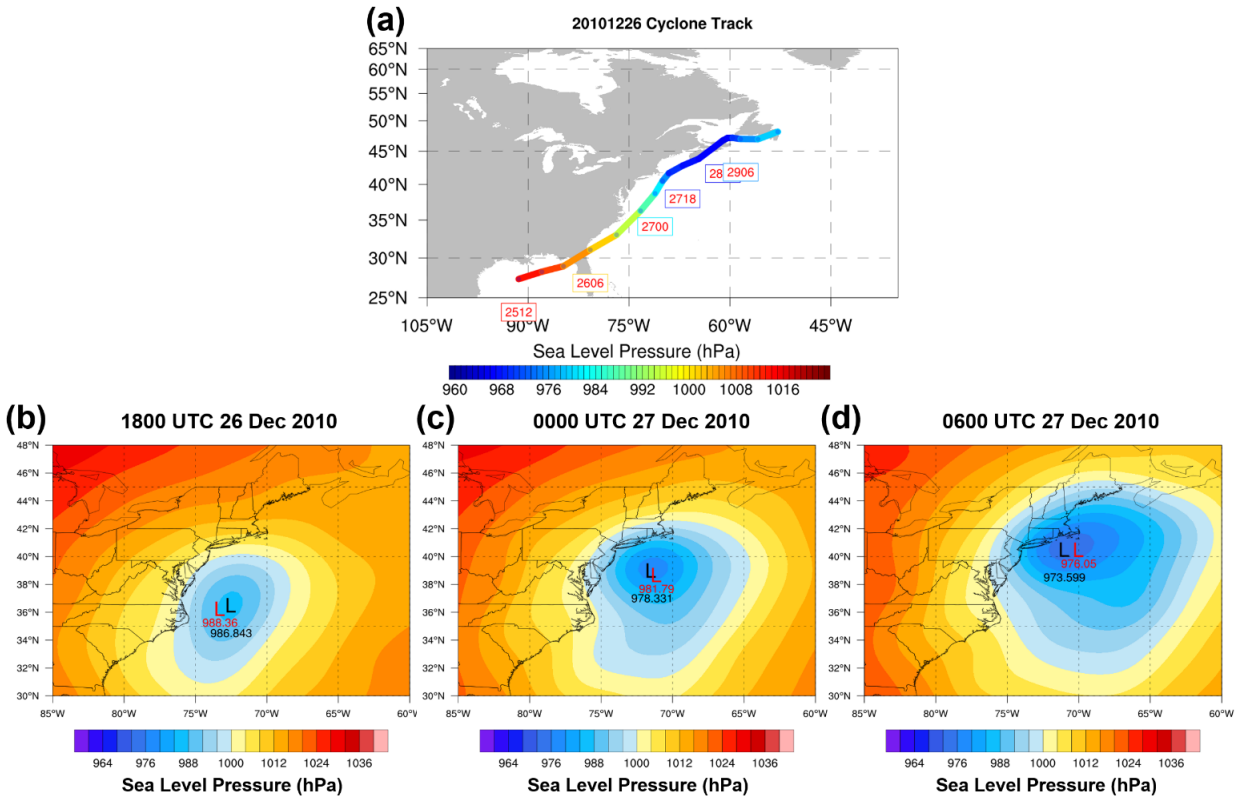

Figure 2.3. (a) The observed track shaded by sea level pressure of the 26–27 Dec 2010 cyclone. Comparisons of sea level pressure and minimum (i.e., cyclone position) indicated by the "L" marker for the gridded CFSR data (shaded, black "L") and the cyclone tracker derived from the SBU methodology (red "L").

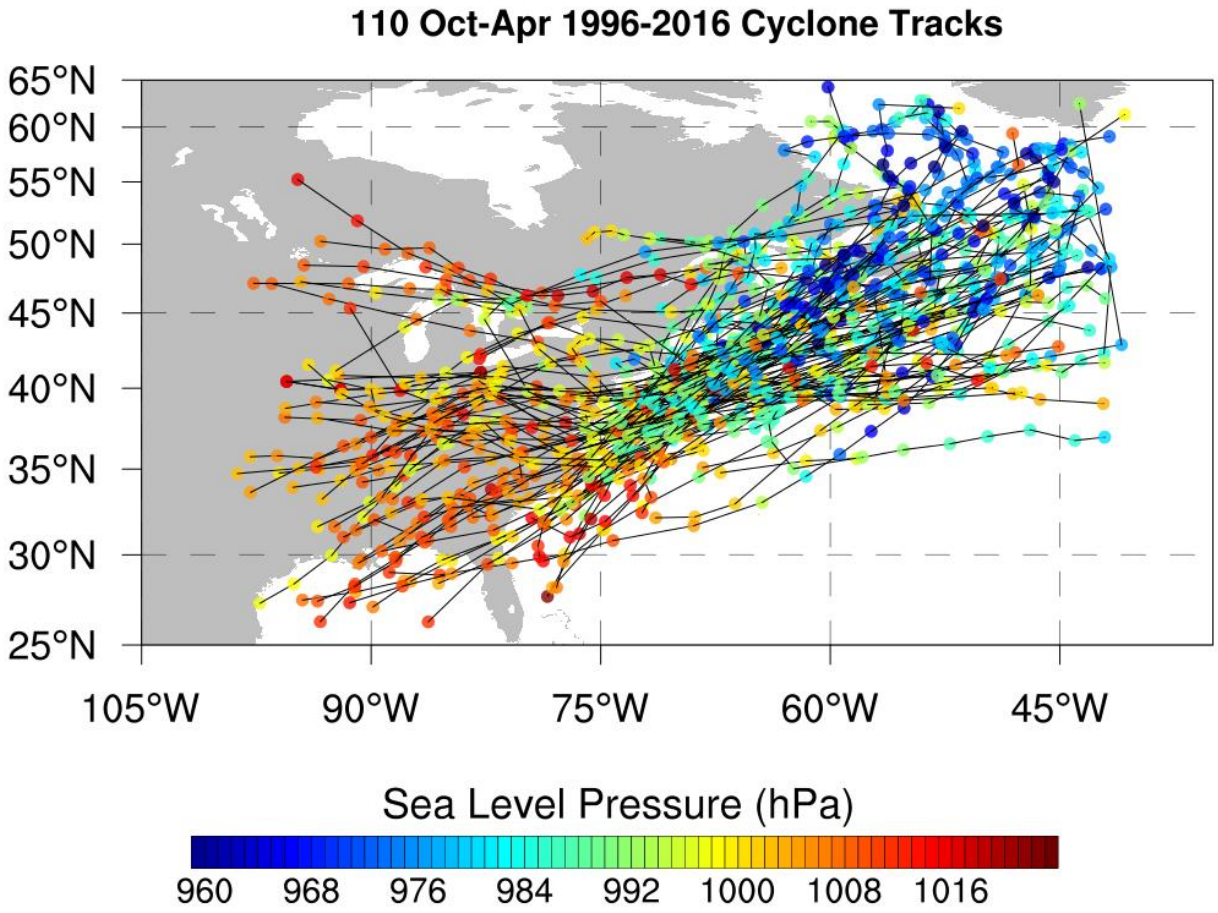

Figure 2.4. Sea level pressure along each of the 110 cyclone tracks in the study.

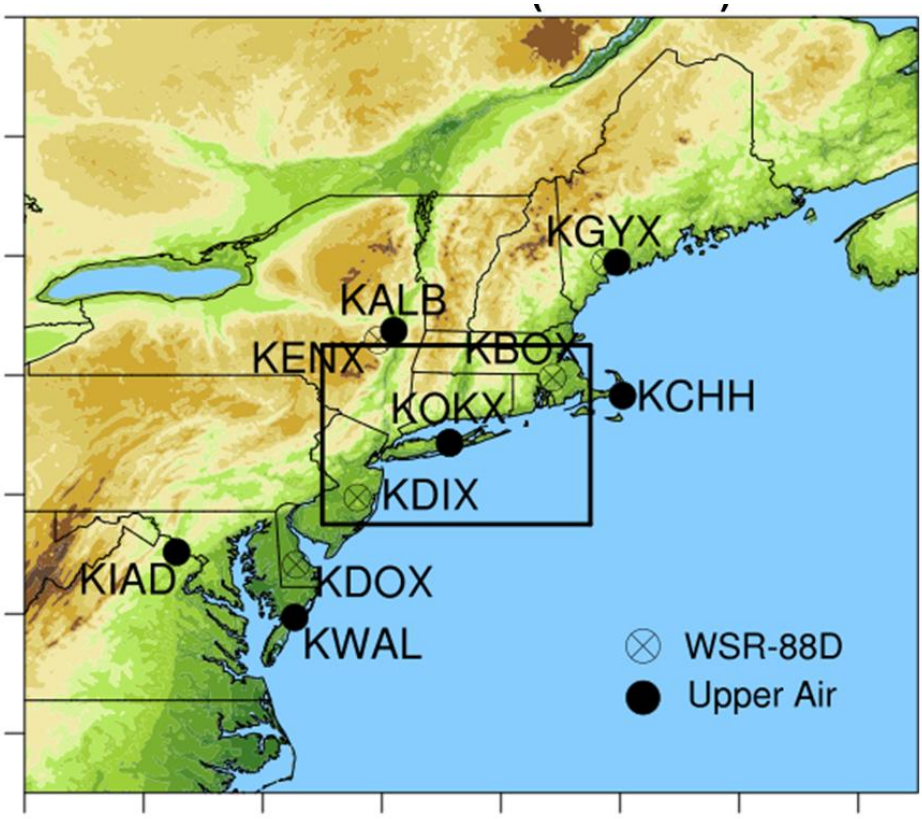

Figure 2.5. Whole domain (outer box) and location of subdomain (inner box) used to calculate statistics on the stitched reflectivity in order to obtain the convolution thresholding value used with the MODE tool.

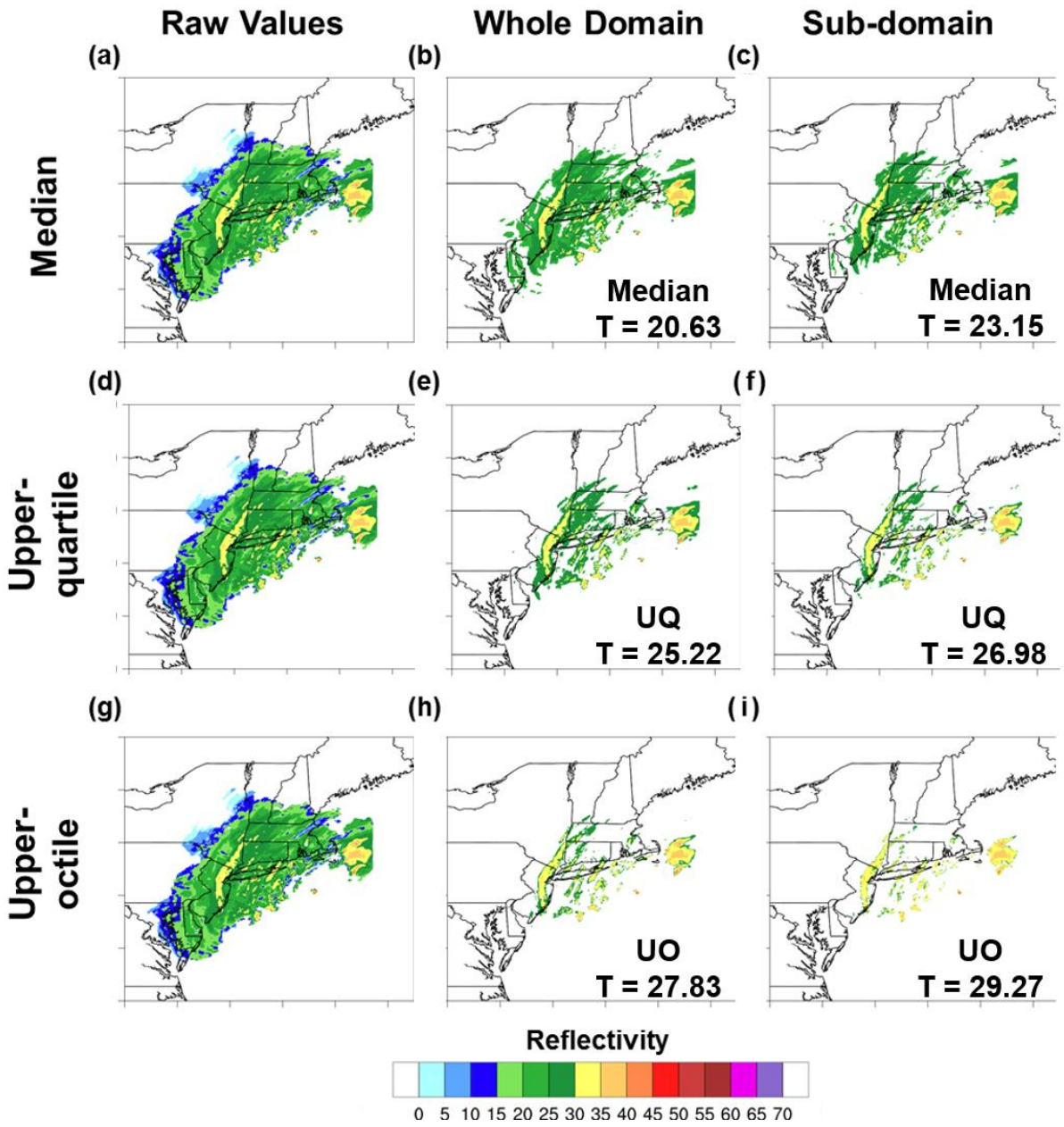

Figure 2.6. Stitched regional composite reflectivity data for 0008 UTC 27 Dec 2010 for the whole domain with no threshold subsetting (a,d,g), for reflectivity ≥ the median value for the whole domain (b, 20.65 dBZ) and the subdomain (c, 23.15 dBZ), for reflectivity ≥ the upper-quartile for the whole domain (e, 25.22 dBZ), and the subdomain (f, 26.98 dBZ), and for reflectivity ≥ the upper-octile for the whole domain (h, 27.83 dBZ) and for the subdomain (i, 29.27 dBZ).

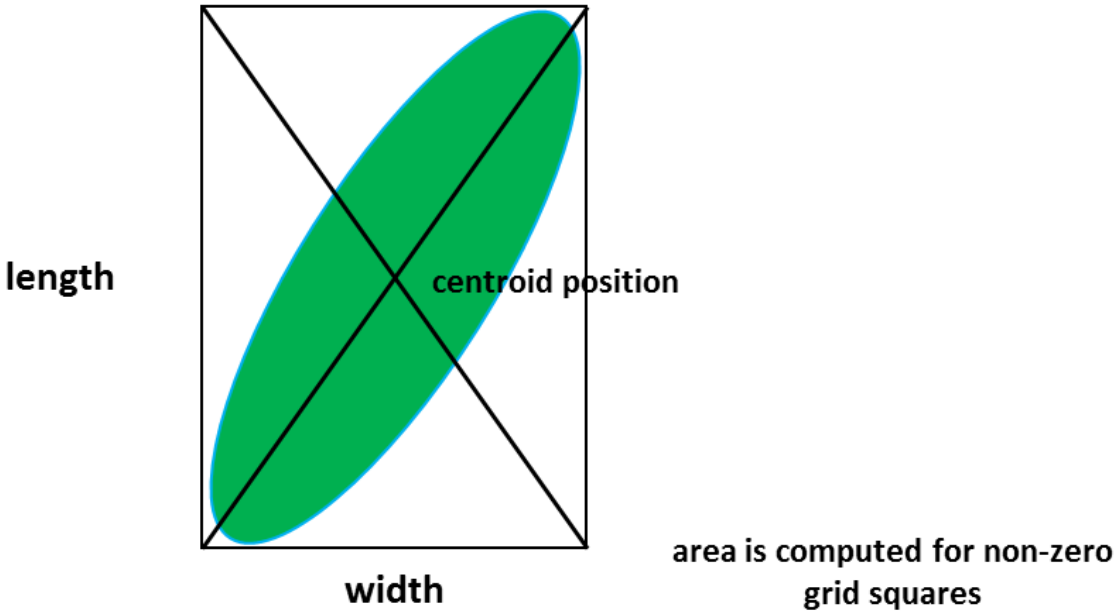

Figure 2.7. Schematic showing idealized object and its corresponding length, width, area, and centroid position attributes.

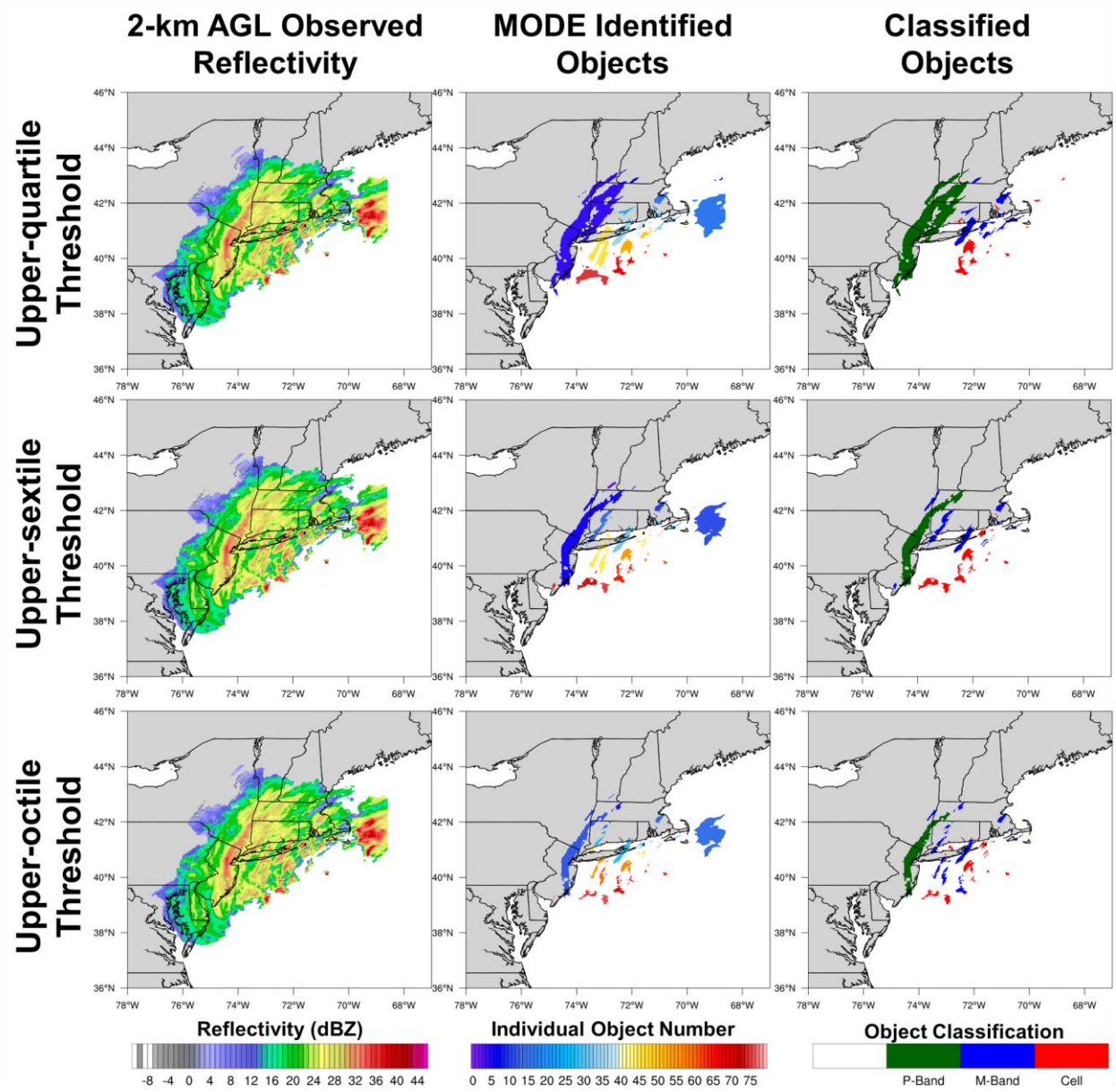

Figure 2.8. Instantaneously-calculated threshold tests for 0002 UTC 27 Dec 2010 for the (top row) upper-quartile of 25.98 dBZ, (center row) upper-sextile of 27.67 dBZ, (bottom row) upper-octile of 28.76 dBZ showing (left column) observed 2-km reflectivity (dBZ, shaded according to scale), (center column) individual objects produced by MODE (colored by object ID number), and (right column) objects shaded by classification into primary bands (green), mid-sized bands (blue) and cells/undefined (red) according to the criteria provided in Table 2.3.

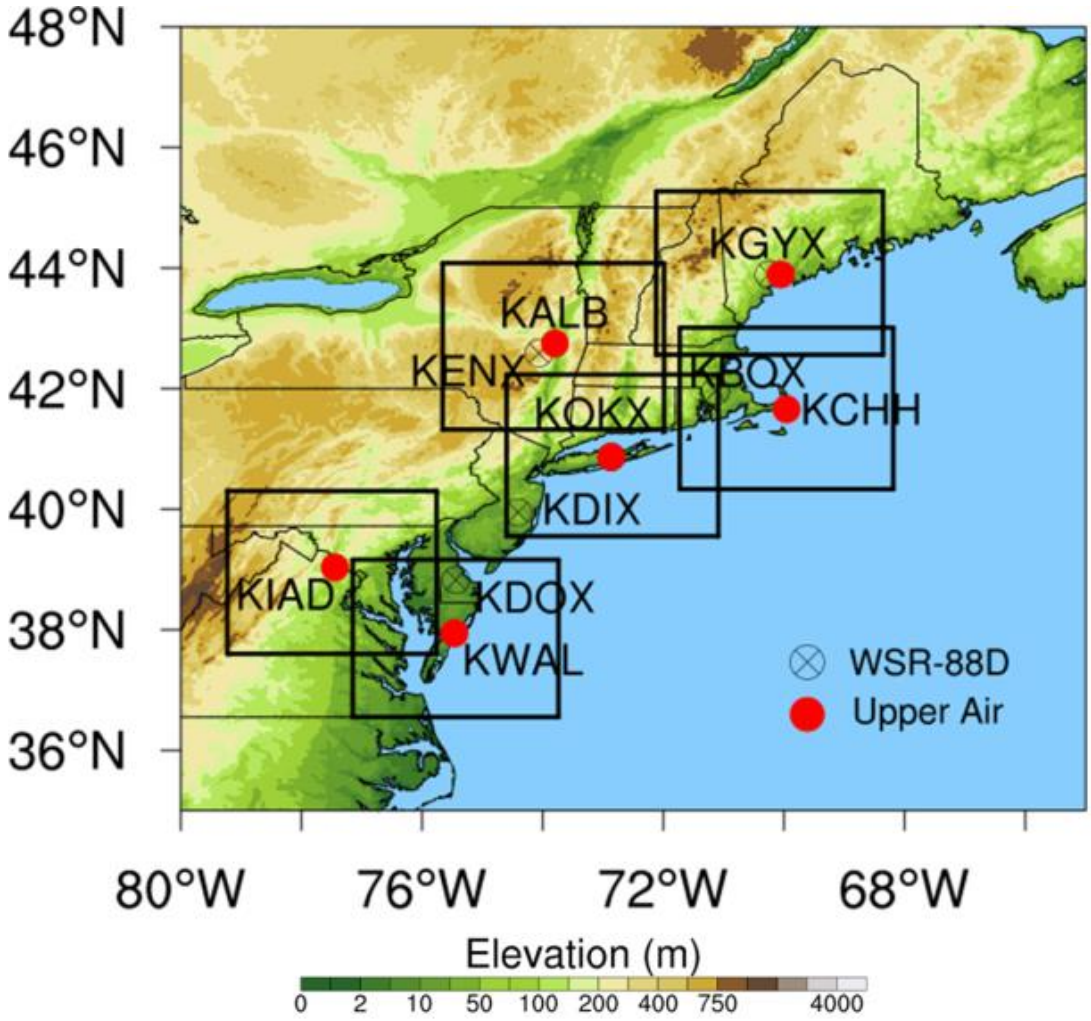

Figure 2.9. The radar (circle with cross) and upper air (filled red circle) locations for this study. Boxes extending 150 km in each direction around each upper air site are shown to indicate the regions used during both objective and subjective case classifications.

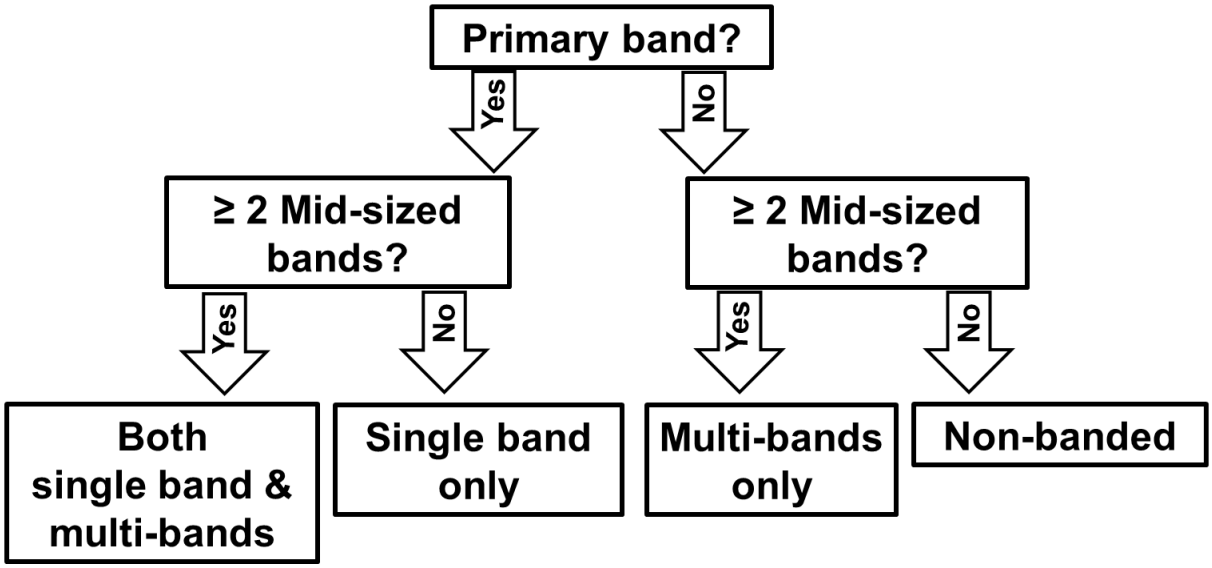

Figure 2.10. The method used to objectively classify each 6-hourly time during a case within each of the 6 sounding domains provided in Figure 2.9. This method was also employed for subjective analysis of the single most representative time during a case.

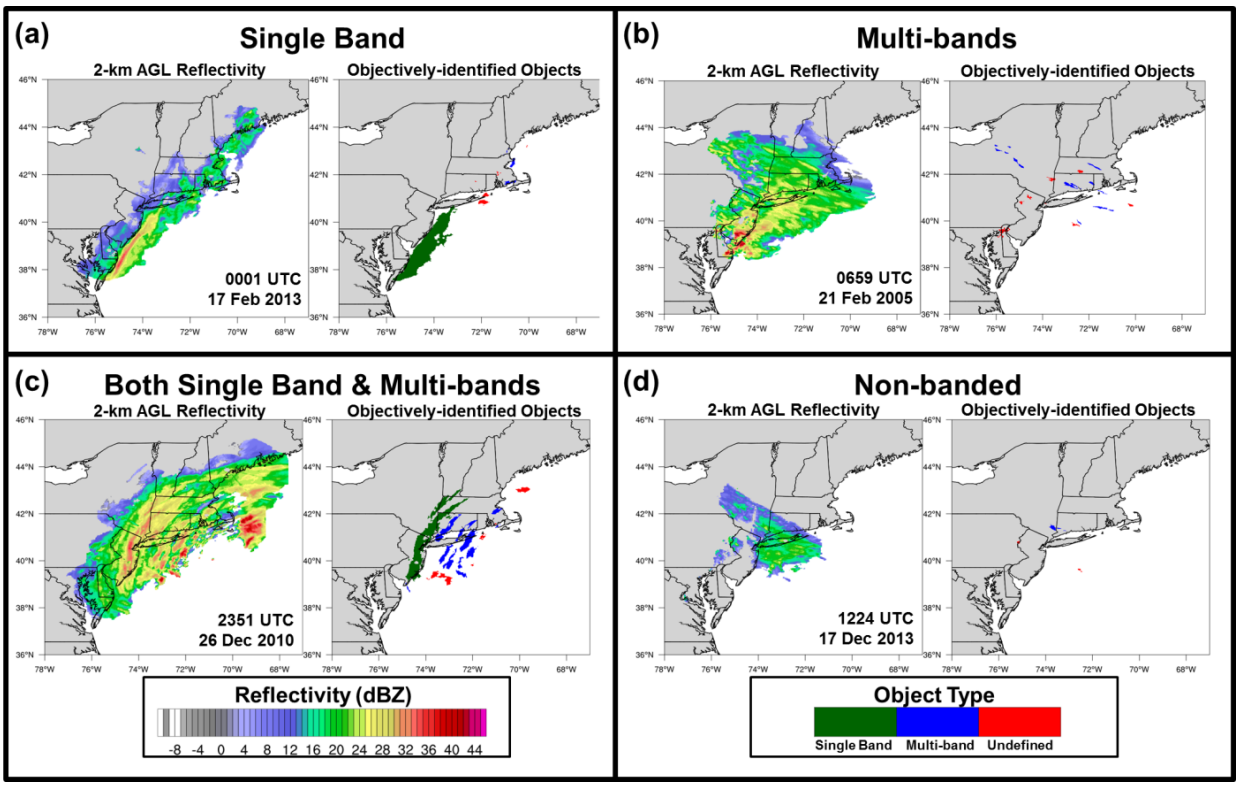

Figure 2.11. Examples of 2-km AGL stitched regional composite reflectivity and the resulting classified objects from the MET MODE tool output for the four banding classifications exhibited in Northeast U.S. winter storms, (a) a large, single band, (b) multi-bands, (c) both single and multi-bands, and (d) non-banded.

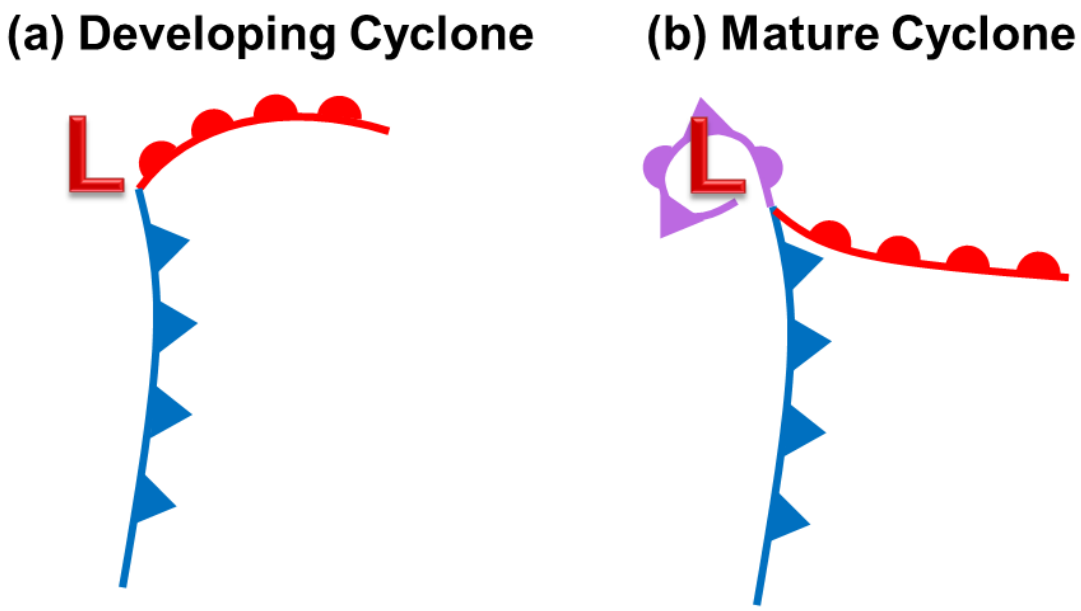

Figure 2.12. Conceptual model used to classify cyclones into either (a) developing or (b) mature adapted from the models provided by Bjerknes and Solberg (1922) and Shapiro and Keyser (1990).

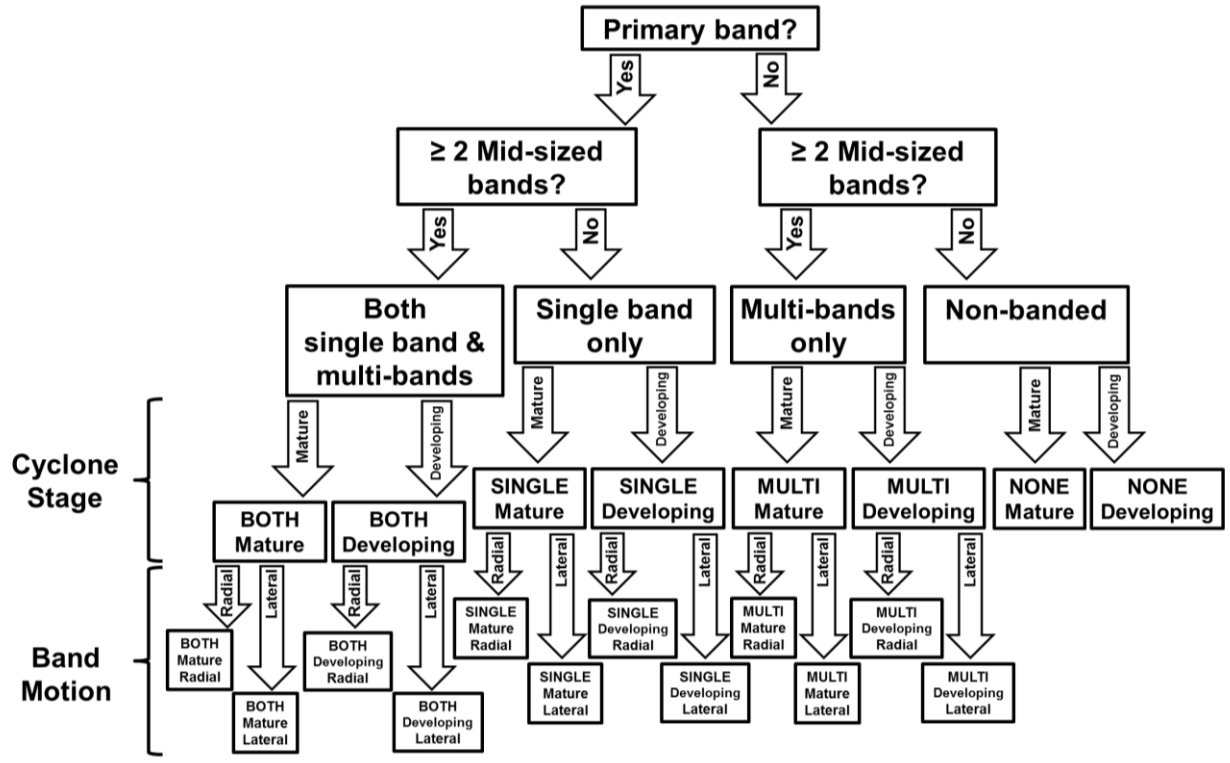

Figure 2.13. As in Fig. 2.10 but with additional classification schemes added including cyclone stage (mature or developing) and band motion (radial/perpendicular or lateral/parallel) that took the four initial classifications based solely on band existence and size and created 12 classification categories that incorporate the new criteria.

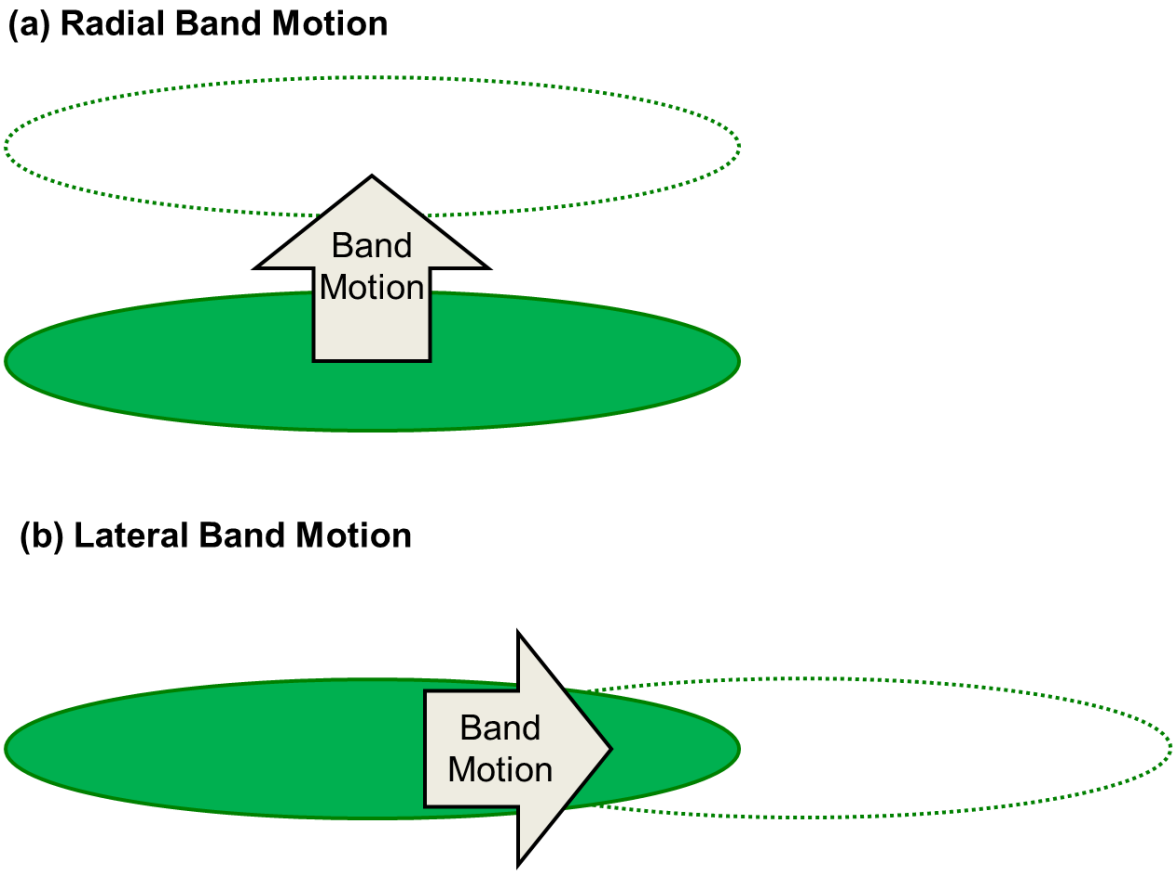

Figure 2.14. Schematics showing band motion as defined as (a) radial or perpendicular to the long axis of the band and (b) lateral or parallel to the long axis of a band as adapted from similar classifications by Kenyon et al. (2013) (their laterally translating, pivoting, and laterally quasi-stationary classifications).

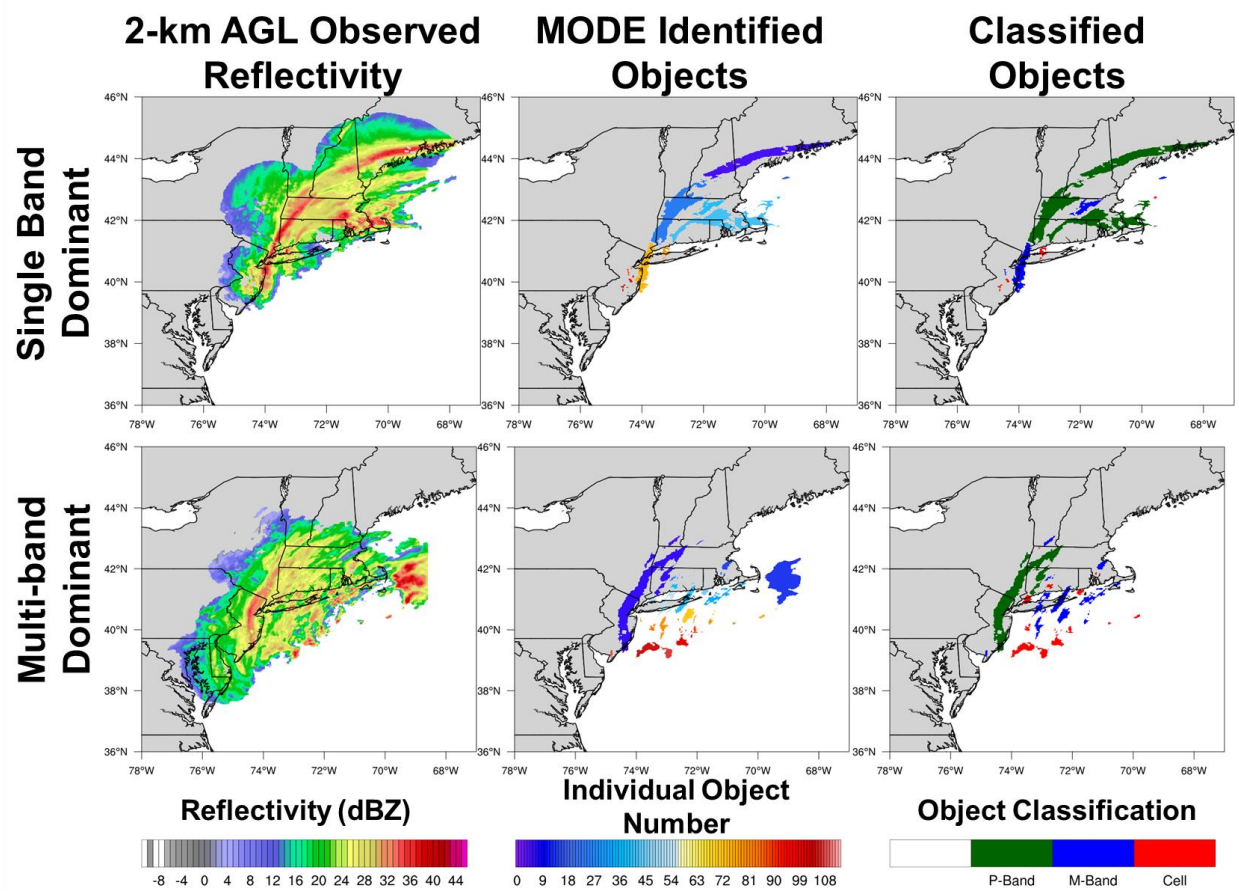

Figure 2.15. As in Figure 2.8 but for just the upper-sextile threshold showing a classification of BOTH re-classified as (top row) single band dominant for 0000 UTC 6 Feb 2001 and (bottom row) multi-band dominant for 0000 UTC 27 Dec 2010.

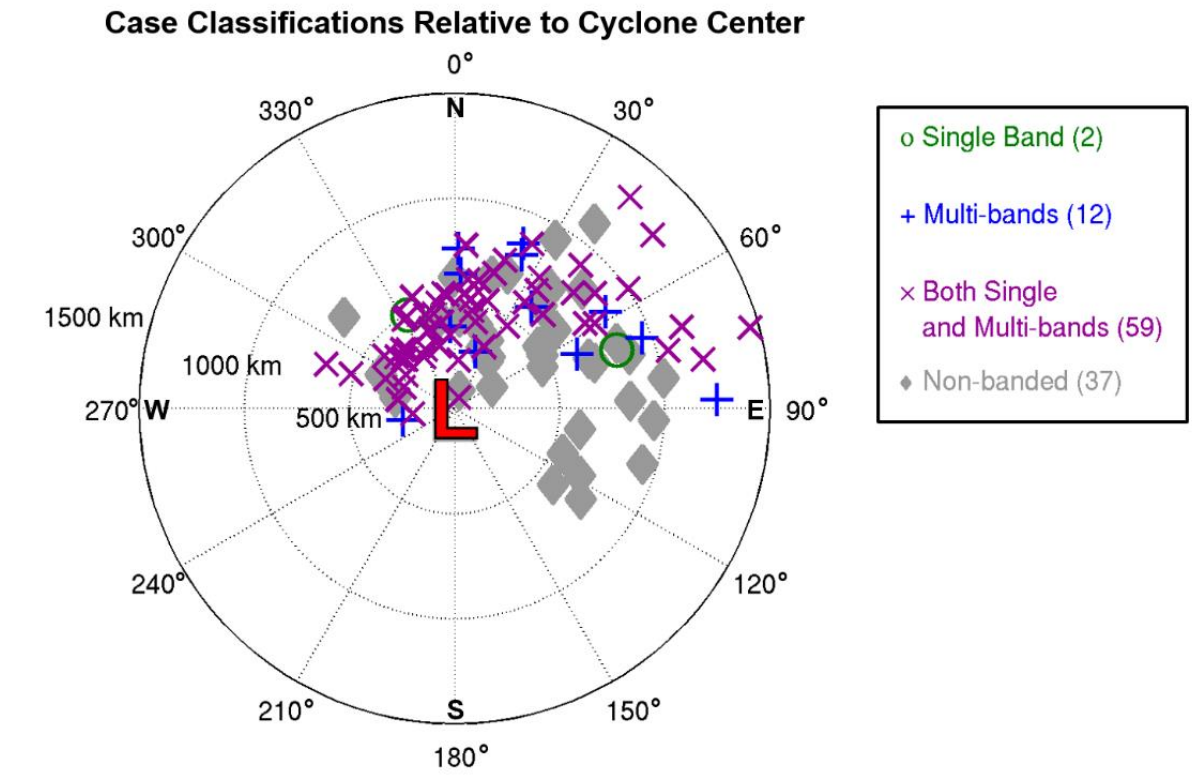

Figure 2.16. Case classifications for single band cases (green circle), multi-band cases (blue plus sign), both single and multi-band cases (purple cross), and non-banded (gray diamond) plotted by distance (km) and direction (angle) from cyclone center at time of peak banding activity or precipitation coverage for non-banded cases. Points correspond to the sounding location in the center of the classified domain.

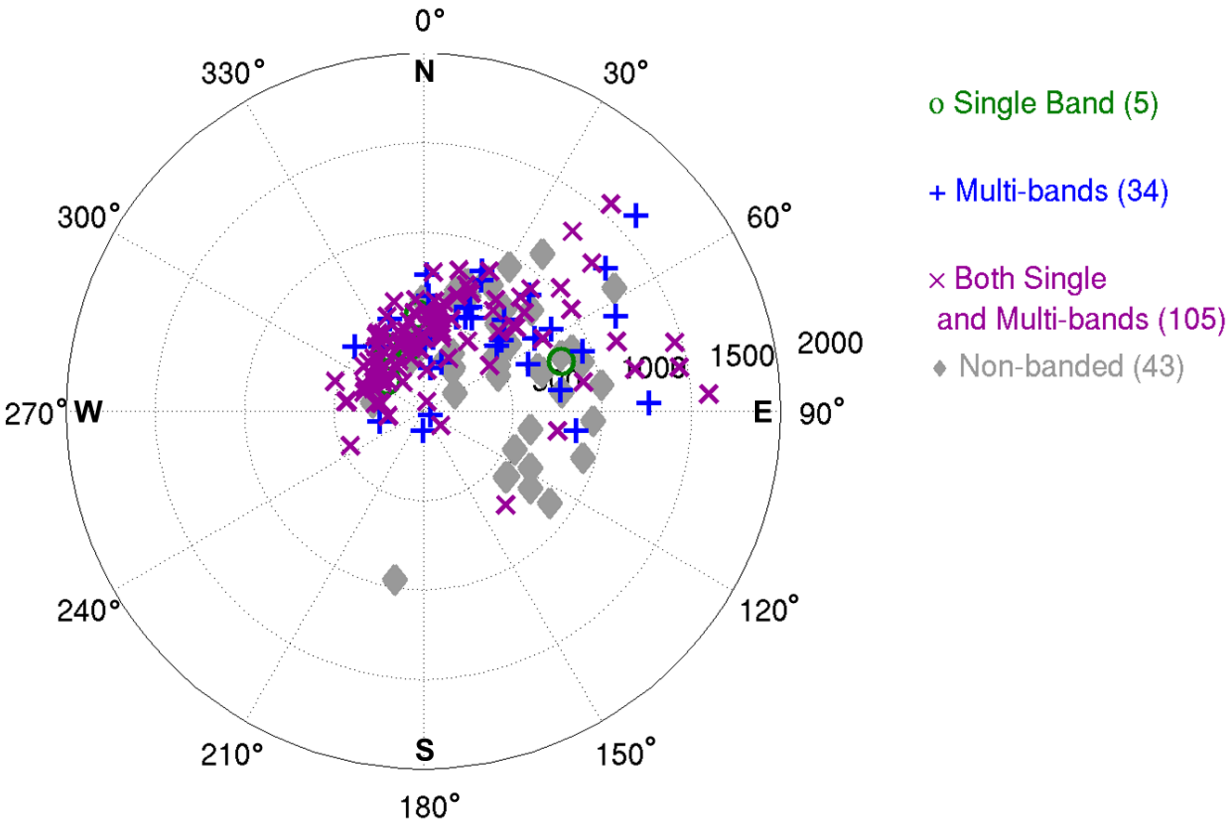

Figure 2.17. As in Figure 2.16 but for approximately 6-hourly events during all 110 cases. The radial distance is given in kilometers and the angle in degrees.

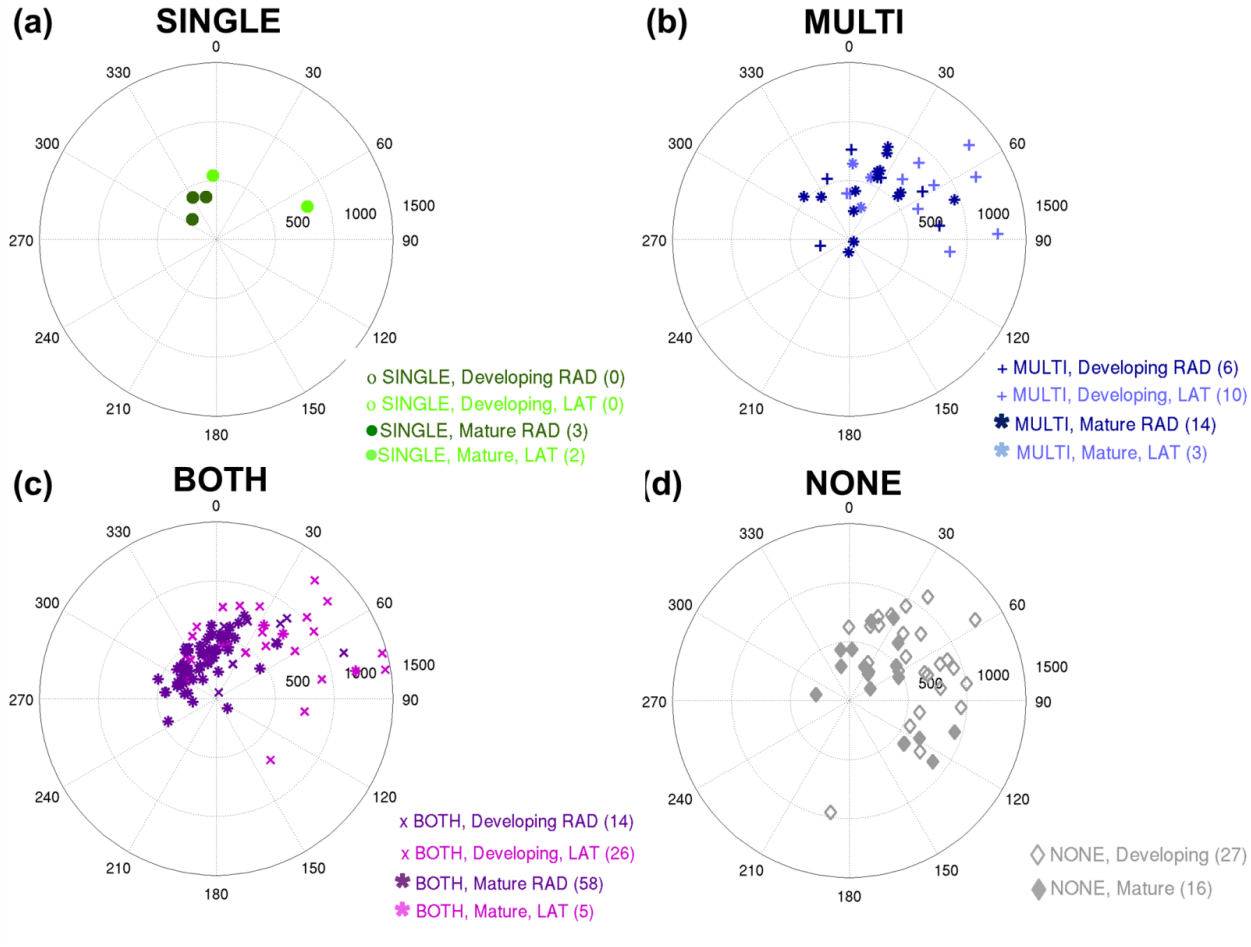

Figure 2.18. Distance and angle from cyclone center for 193 events for (a) SINGLE events for mature (filled circle) and developing (open circle) cyclones for LAT moving bands (light green) and RAD moving bands (dark green), (b) MULTI events for mature (asterisk) and developing (plus sign) cyclones for LAT moving bands (light blue) and RAD moving bands (dark blue), (c) BOTH events for mature (asterisk) and developing (cross) cyclones for LAT moving bands (light purple) and RAD moving bands (dark purple), (d) NONE events for mature (filled diamond) and developing (open diamond) cyclones. The radial distance is in kilometers and the angle from the cyclone to the classified event is in degrees.

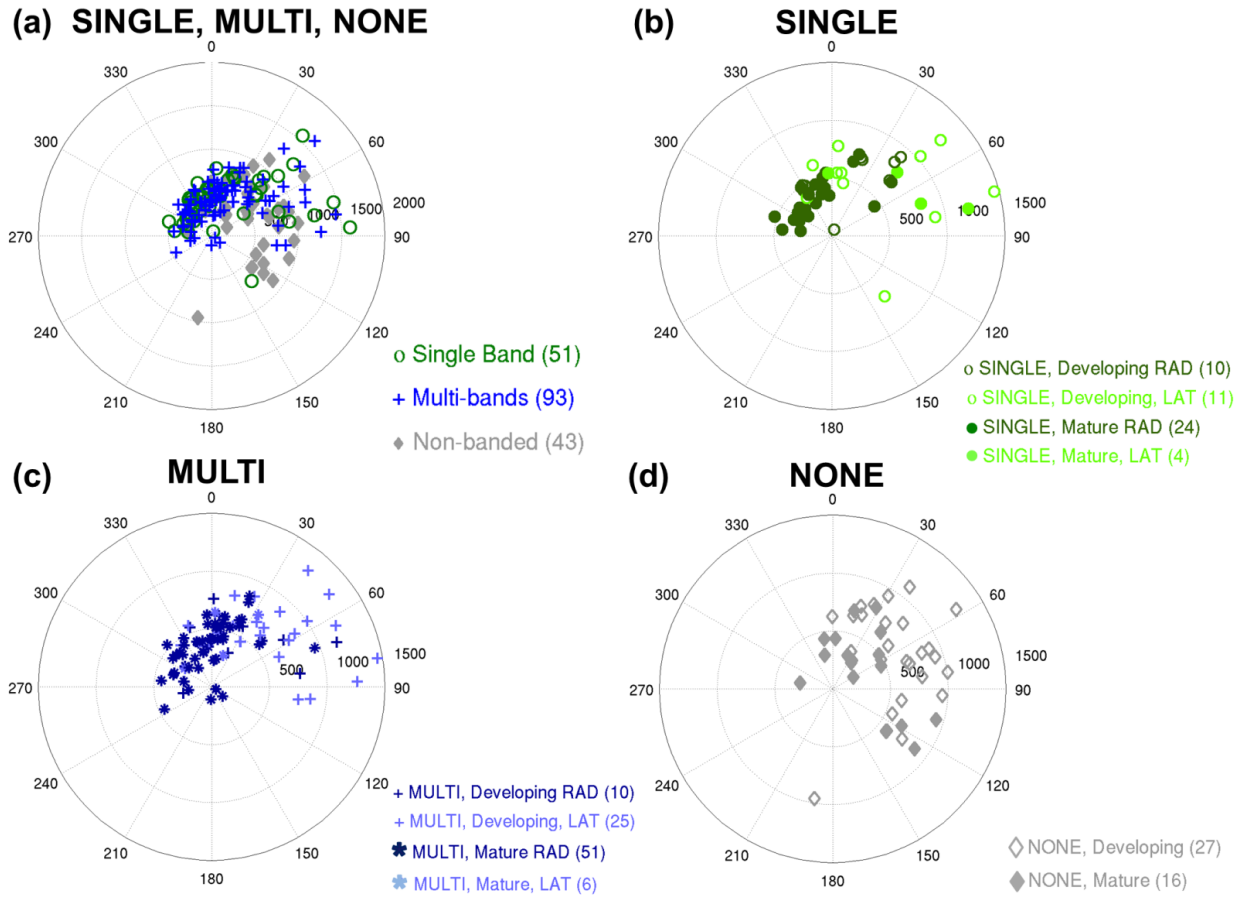

Figure 2.19. (a) As in Figure 2.17 but for only the three main classification categories of SINGLE (green circles), MULTI (blue plus sign), and NONE (grey diamond). (b–d) As in Figure 2.18.

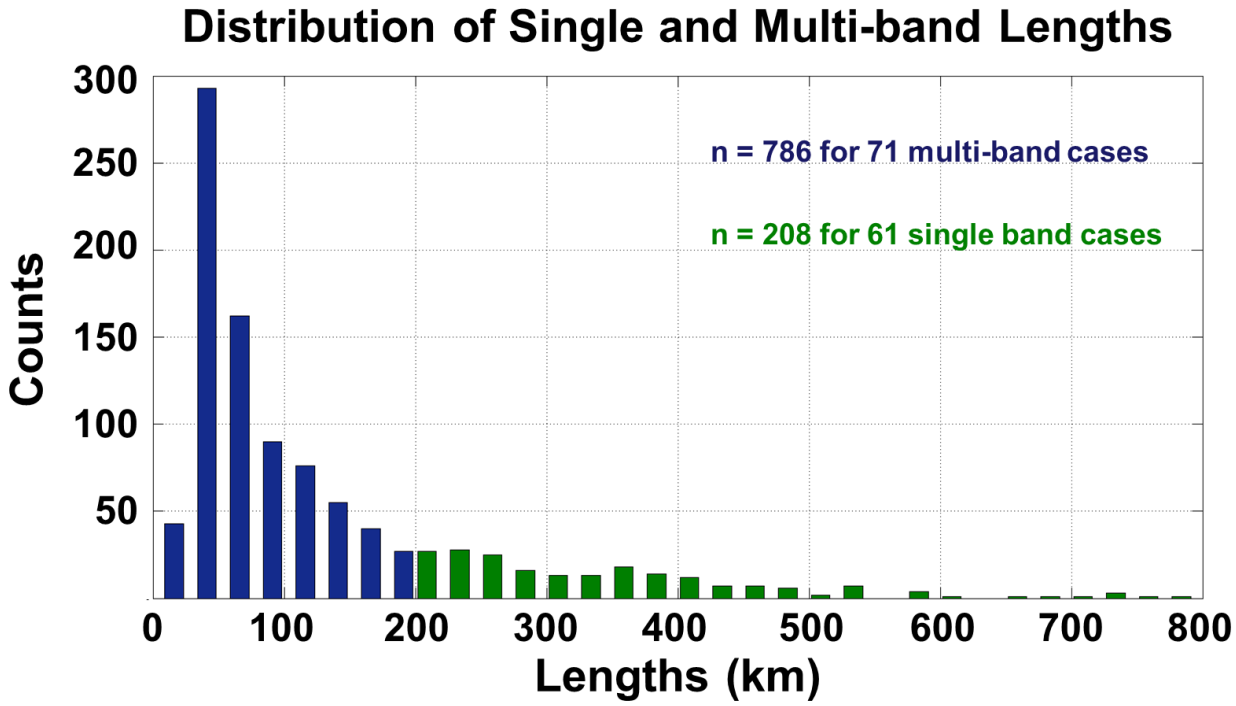

Figure 2.20. The distribution of the lengths of multi-bands (blue) and single bands (green) for each object classified as such from each hour of the ~5-minute MODE output from the 71 cases exhibiting multi-bands and 61 cases of single bands.

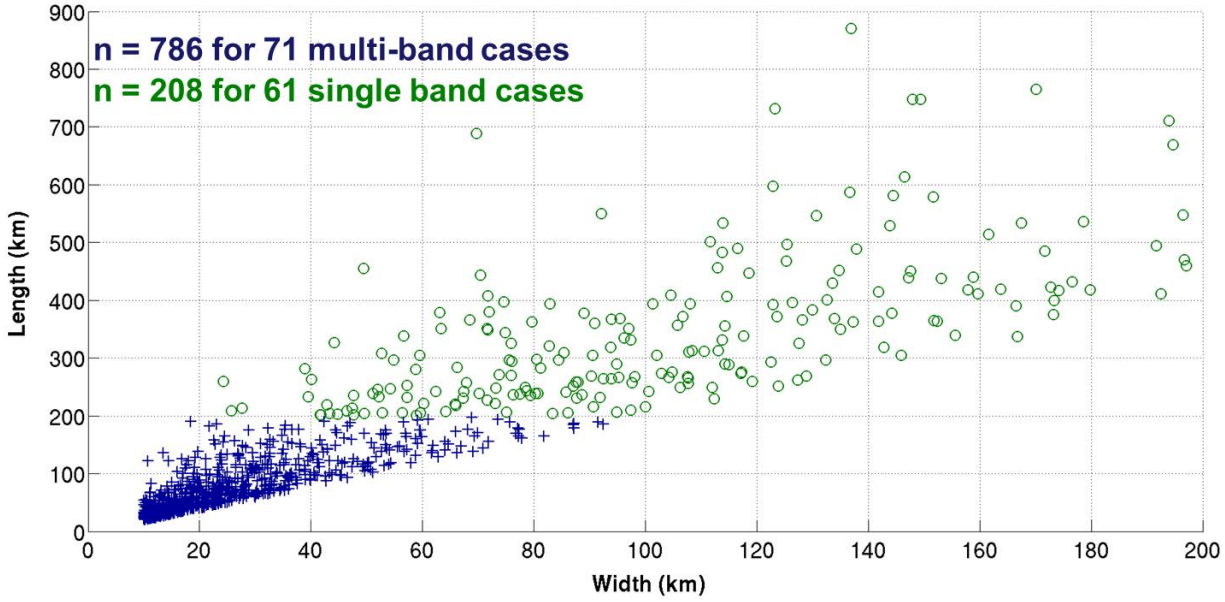

Figure 2.21. Scatterplot of width vs. length of each multi-band (blue cross) object and single band (green circle) object from hourly data from 71 cases exhibiting multi-bands and 61 cases of single bands.

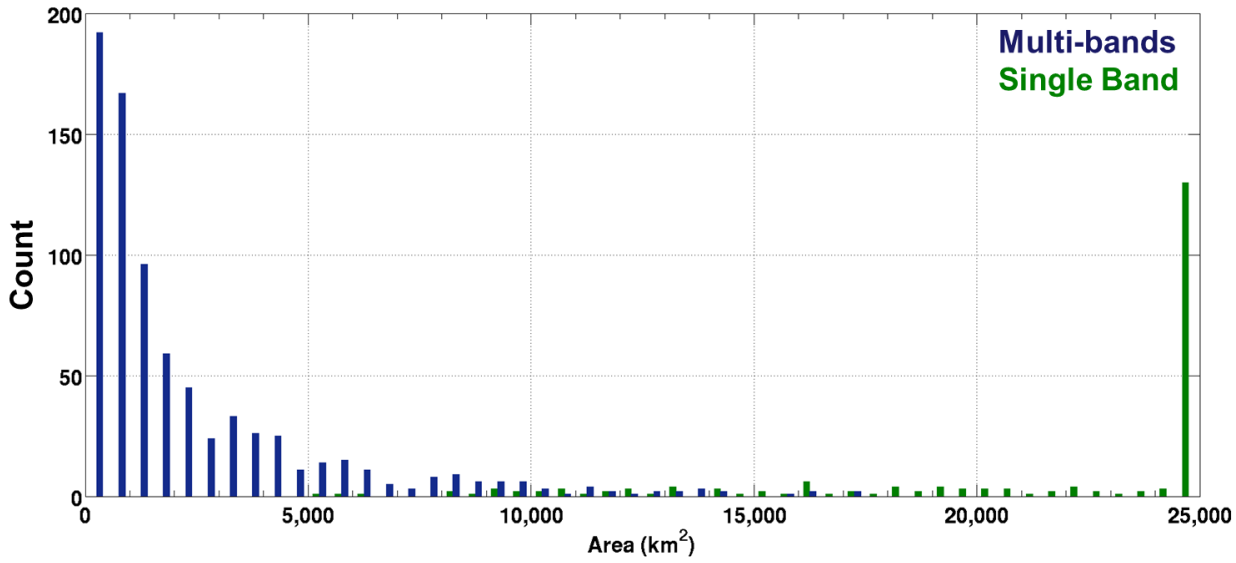

Figure 2.22. Distribution of number of counts of specific object area values for multi-bands (blue) and single bands (green).

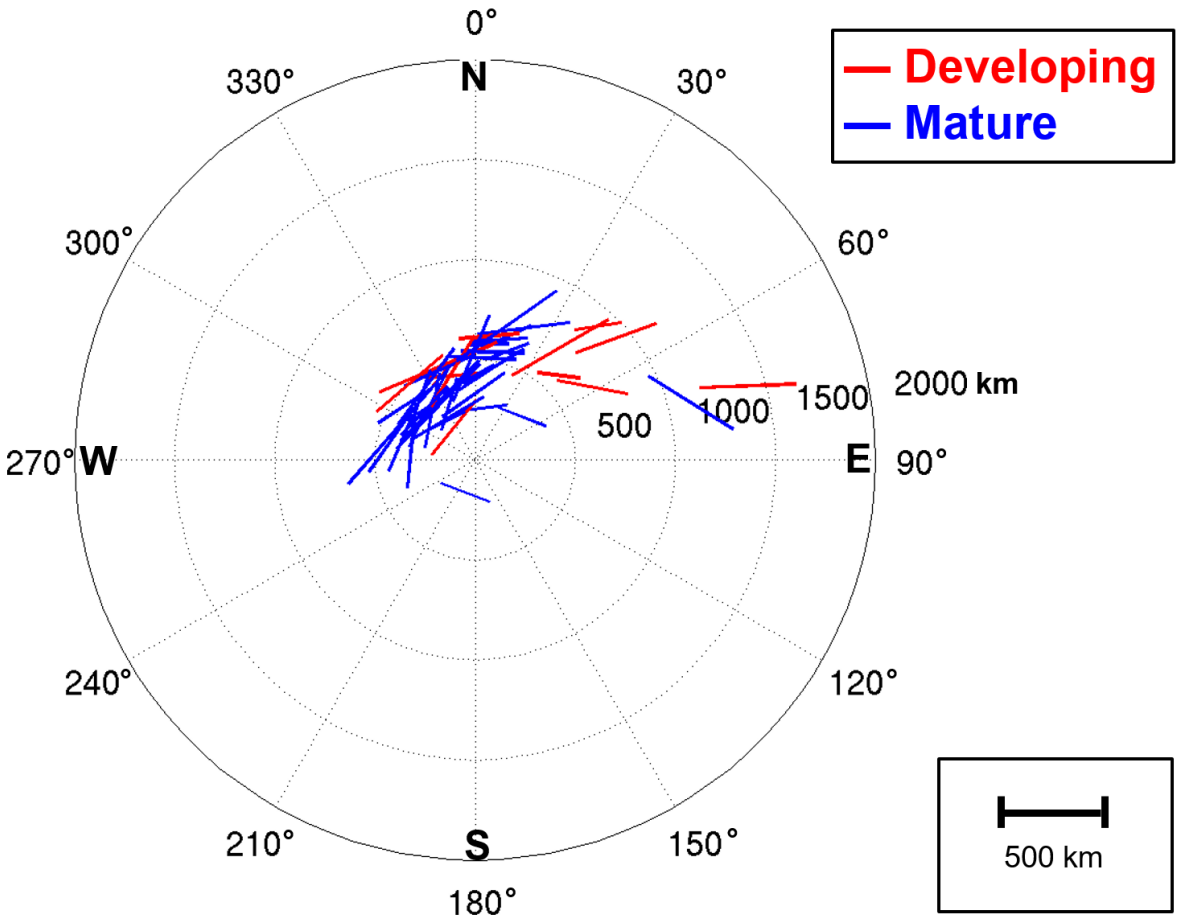

Figure 2.23. Primary band locations and orientations relative to the cyclone center (origin of plot) with the radius in km and angle in degrees. Bands associated with mature cyclones are in blue and developing cyclones are in red.

Chapter 3:

Analysis of the Environmental Conditions for Snowbands in Northeast U.S. Winter Storms

3.1 Introduction

This chapter analyzes the environments for banding classification types presented in Chapter 2 using observed soundings and gridded reanalysis data. The objective is to compare well-known banding ingredients including mid-level forcing for ascent via frontogenesis, available mid-level instability, and available moisture for the classifications of single band only (SINGLE), multi-band only (MULTI), both single and multi-bands (BOTH), and non-banded (NONE).

As discussed in Section 1.1b, there are well-known characteristics of the flow that are commonly associated with single bands. For example, Novak et al. (2004) found that a closed 700-hPa low was often associated with stronger mid-level deformation to the northwest of a surface cyclone center which can provide sufficient forcing for ascent to develop a single snowband. Baxter and Schumacher (2017) provided evidence that the location of the surface cyclone and low-level frontal boundaries could be either upstream or downstream of a mid-level trough and produce a single band. Kenyon et al. (2013) related these phasing differences of upper and lower levels to band motion, specifically that vertically stacked systems were mostly associated with pivoting single bands, whereas a surface low downstream of a mid-level trough would result in either a quasi-stationary laterally moving or a laterally-translating single band. The method by which these generalizations were determined was by analyzing composites of known features (i.e., mid-level flow, upper-level jet cores, surface temperature gradients) for cases of single banded snowfall. Previous studies have neglected any inclusion of a multi-banded category. This chapter provides composites of key banding ingredients in order to compare cases with multi-bands to single and non-banded cases. Highlights from a few example cases from each classification will further explore any synoptic and mesoscale differences.

Section 3.2 describes the observed sounding and gridded reanalysis data and methods used to create vertical profiles and cyclone-centric composites of banding ingredients. Section 3.3 presents the comparison of banding ingredients and synoptic and mesoscale environments that result in SINGLE, MULTI, BOTH, or NONE events. This analysis is done for both mature (MAT) and developing (DEV) cyclones, separately, as discussed in Chapter 2. Section 3.4 provides a summary of the findings of this chapter and compares them with what is known of banding ingredients for single band events from previous studies of coastal and continental cyclones.

3.2 Data and methods

a. Vertical profiles

Observed soundings from the six upper-air locations over the Northeast U.S. are available approximately every 12 h (Fig. 3.1). To increase the temporal frequency of available vertical profiles to every 6-h, vertical profiles were also derived at the nearest grid point to each observed sounding location from the 0.5° resolution NCEP Climate Forecast System Reanalysis (CFSR; Saha et al. 2010). This is the same analysis data used by Kenyon et al. (2013) for their environmental band analysis. The CFSR and the Climate Forecast System version 2 (CFSv2; Saha et al. 2014), which was used for dates later than 2010, have data approximately every 38 km horizontally with 64 vertical pressure levels (Saha et al. 2014). Figure 3.2 shows the grid points, which are spatially representative with the observed sounding sites, even despite the elevation differences at two locations near substantial terrain, KALB and KGYX. Most analysis is limited to above the boundary layer, thus minimizing the effect of terrain or surface type differences (e.g. proximity to the coast at KOKX and KCHH).

The accuracy of these CFSR grid point profiles was determined by comparing 1292 available soundings every 6 h during each of the 110 events from the 6 coastal sites (Figs. 3.2, 3.3). Mean values and $\pm 1\sigma$ are calculated for the mean error of several environmental variables. The mean error of temperature was typically within 2°C and relative humidity within 15%. The mean errors for mixing ratio above the boundary layer (> 2 km AGL) are typically within 1 g kg^{-1} and are within 2 K for potential temperature. Novak et al. (2010) utilized the 32-km North

American Regional Reanalysis (NARR; Mesinger et al. 2006) for their composite analysis. Spatial plots and vertical profiles from the NARR were compared to the CFSR for several cases and both were found to be very similar, although the NARR tended to exhibit weaker cyclones (not shown). Charles and Colle (2009) showed that the NARR had a weak bias for cyclones along the U.S. East Coast. Due to the aforementioned analysis and the immediate availability of CFSR cyclone track data from Colle et al. (2013), the CFSR was chosen as the preferred dataset for this study. The CFSR-derived soundings were considered representative to the observed atmosphere and were subsequently used for this study.

Six domains for the thermodynamic analysis formed the basis of the classification scheme described in Chapter 2. Each 6-h event corresponds to bands (or lack thereof) within a specific domain that is centralized to and extends ~150 km from a sounding site. The domain size was chosen to minimize overlap between neighboring sounding sites. That sounding, in the center of the domain, can then be associated with the band type, cyclone maturity, and band motion for that particular time in that domain. Profiles are point-locations and therefore are susceptible to discrepancies in band location. Soundings were grouped by classification into SINGLE, MULTI, BOTH, and NONE, and then additionally divided into developing or mature cyclones and whether the bands move radially or laterally. The profiles are meant to serve as a proxy for the banded environment, regardless of whether they correspond with the band location, the upstream band environment, or the post-band environment. The hypothesis is that the environments will vary among the classification types enough to provide representative differences regardless of band position, such as SINGLE AND BOTH exhibiting higher values of mid-level frontogenesis than NONE and MULTI, etc.

b. Gridded composite analysis

To address the issue of spatial variability of point-based soundings, the gridded CFSR data are used to calculate cyclone relative composites. For each classification time, the absolute SLP minimum in East Coast-centered box (25 by 27 grid points) was defined to be the cyclone center (Fig. 3.4). A similar method was employed by Baxter and Schumacher (2017). All variables available within the CFSR were then taken from grid points extending ~500 km in all four primary directions from that point (41 by 61 grid points), which therefore could extend

outside of the box in Figure 3.4 as necessary. This new grid was re-centered to a common point taken offshore the NYC metropolitan area (40.0°N, 72.0°W), which is the main focus of our study (Fig. 3.4). This allowed for cyclone-centered composites that retain some geographic context and is similar to the method of cyclone-centered re-centering employed by Novak et al. (2004), Baxter and Schumacher (2017), and the band-centered re-centering by Kenyon et al. (2013).

3.3 Results

a. Analysis of banding environments

Comparisons of the thermal, moisture, and kinematic variables from a representative profile from 1000 hPa to 300 hPa from each event were examined. Significance is assessed via bootstrapping (Wilks 2011); each classification dataset is resampled by replacing randomly 1,000 times. For all four datasets, the size for each resample is equivalent to the total number of events in the original dataset (5 SINGLE, 35 MULTI, 107 BOTH, 46 NONE).

It is hypothesized that atmospheric stability may be important for the development of banded precipitation in a warm frontal zone if gravity wave activity in a ducted stable layer (Wei and Zhang 2013) lift parcels and release any instability above this layer. Consistent with this hypothesis, 29% of MULTI and 21% of BOTH profiles show enhanced stability from the surface to 700 hPa with 10 and 23 profiles exhibiting a 50-hPa deep stable layer (≥ 0.05°C hPa^{-1}), respectively, while SINGLE and NONE events exhibited no stable layers (Fig. 3.5a–d). From 750-800 hPa, the MULTI events are significantly more stable than the NONE classification at the 2.5th and 97.5th percentiles with 95% confidence (not shown). In contrast, there is little variation in the temperature and humidity between the four classifications (Fig. 3.5).

Multi-bands are hypothesized to arise within a more conditionally unstable environment in which moist updrafts can break down into several smaller circulations (Xu 1992). Individual profiles of saturation equivalent potential temperature (θ_e*) show the presence of weak conditional instability indicated by a small decrease in θ_e* with height for all classifications with 20% (7 profiles) of MULTI exhibiting a 50-hPa deep conditionally unstable layer ($\leq$ -0.02 K hPa^{-1}), the highest percentage out of all classifications but not significantly different (Figs. 3.6a–

e). The MULTI events have larger average wind shear (1000–700 hPa) values, ~10.3 m s^{-1} (20 kts) compared to the ~2.6 m s^{-1} (5 kts) and ~5.1 m s^{-1} (10 kts) for SINGLE and BOTH, respectively (Fig. 3.6j). This supports the hypothesis that multi-bands may be associated with shear-induced waves traveling within a ducted stable layer which will be explored in Chapter 5.

Larger, single bands may be associated with stronger forcing for lift via frontogenesis than multi-bands, especially given their preferential location in the northwest quadrant of low pressure systems. Multi-bands may exist in an environment of weaker forcing for lift but greater instability, leading air to want to rise more frequently and robustly over a larger area than the single band. This is evident for the average profiles of 2-D Petterssen (1936) frontogenesis (Eq. 3.1; as in Novak et al. 2004, their Eq. 1) for SINGLE and BOTH events (Figs. 3.7a,c) when compared to MULTI (Fig. 3.7b).

$$F_{2D} = \frac{1}{|\nabla\theta|}\left(-\frac{\partial\theta}{\partial x}\left(\frac{\partial u}{\partial x}\frac{\partial\theta}{\partial x} + \frac{\partial v}{\partial x}\frac{\partial\theta}{\partial y}\right) - \frac{\partial\theta}{\partial y}\left(\frac{\partial u}{\partial y}\frac{\partial\theta}{\partial x} + \frac{\partial v}{\partial y}\frac{\partial\theta}{\partial y}\right)\right) \qquad \text{Eq. 3.1}$$

Equation 3.1 of frontogenesis (F_{2D}) includes the gradients in the zonal (x) and meridional (y) directions of potential temperature (θ), and the zonal and meridional components of the wind (u and v, respectively). Non-banded environments were hypothesized to be associated with weaker forcing (i.e., frontogenesis). The NONE classification was associated with low values of frontogenesis than other classifications (Fig. 3.7d). At 700-hPa, the mean value of frontogenesis for NONE is statistically different than the mean value for BOTH at the 95% confidence interval (Fig. 3.7e). Conditional symmetric instability (CSI) is indicated by negative values of saturation equivalent potential vorticity (MPV*; Eqs. 3.2-3.3; McCann 1995) in the absence of inertial and conditional instability (Schultz and Schumacher 1999).

$$MPV^* = \frac{1}{\rho}\eta \cdot \nabla\theta_{es} \qquad \text{Eq. 3.2}$$

$$MPV^* = g\left(\left(\frac{\partial\theta_{es}}{\partial x}\frac{\partial v}{\partial P}\right) - \left(\frac{\partial\theta_{es}}{\partial y}\frac{\partial u}{\partial P}\right) - \frac{\partial\theta_{es}}{\partial P}\left(\frac{\partial v}{\partial x} - \frac{\partial u}{\partial y} + Corl.\right)\right), \qquad \text{Eq. 3.3}$$

in which g is gravity, P is pressure, *Corl.*is the Coriolis parameter equal to $2\Omega sin\phi$ where ϕ is

latitude, ρ is the density, η is the absolute vorticity vector and θ_{es} is the saturation equivalent potential temperature (aka θ_e^*). Equation 3.3 follows from Equation 3.2 assuming the horizontal gradient of the vertical wind speed is small and can be neglected. Banded precipitation has been related to CSI via the following components of the conceptual model put forth by Clark et al. (2002): (1) a region of mid-troposphere frontogenesis over the banded precipitation region, (2) a saturated mesoscale updraft on the warm side of the frontogenesis region, (3) negative MPV production near the updraft dominated by differential vertical theta-e transport, and (4) release of CSI leading to banded precipitation. CSI is evident in the average profiles of all classification types below 600 hPa (Figs. 3.7f–i). Negative value of MPV* would indicate the presence of CSI in the absence of CI, a known instability responsible for enhancing circulations associated with some single bands (Novak et al. 2010). The most negative values in the average profiles of MPV* are found between 900-800-hPa for all classifications, with MPV* < 0 and statistically insignificant differences among the classifications between 700-550-hPa (Fig. 3.7j).

Looking at one particular level (e.g., 700 hPa), frontogenesis was calculated along with the stability in the 100-hPa layer extending to 600-hPa and the layer-averaged value of MPV* (Figs. 3.8, 3.9). The NONE events exhibit the weakest frontogenesis (< 2 K (100 km 1 h)$^{-1}$). BOTH events had the largest frontogenetical values with 21 of 107 (~20%) events associated with frontogenesis > 1.5 K (100 km 1 h)$^{-1}$ and no events exhibited 700–600-hPa conditionally unstable layers (θ_e^* decreasing with height) but 99 of 107 (93%) events were associated with moist symmetric instability (MPV* < 0). One (34) of the MULTI events exhibited conditional instability (conditional symmetric instability), and relatively weak frontogenesis values with 34 events < 1.5 K (100 km 1 h)$^{-1}$. For MULTI cases, frontogenesis is slightly larger at other levels (e.g., 850 hPa) but still smaller than that of BOTH and SINGLE, which suggests an alternative forcing source other than frontogenesis may be resulting in these bands.

Different snow crystal habits and densities result from variations in saturation, amount of cloud water present, and temperature (Magono and Lee 1966, Pruppacher and Klett 1997, Stark et al. 2013). The vertical motion within the vertical levels where -15°C ≤ T ≤ -10°C can promote the ice crystal growth of columns, sectors, and dendrites if the environment is supersaturated (Magono and Lee 1966). Figure 3.10 shows the relationship between the depth of this temperature range and the average value of vertical velocity in that layer. Note that if only one of the 50-hPa-spaced vertical levels fell within the range of temperatures, then the depth was taken

to be 0 m. Vertical motion is not necessary for ice crystal growth if cloud water is present, otherwise it is a useful indicator of other snow growth processes such as growth by aggregation or collection. There are more events exhibiting deeper growth layers > 2000 m for MULTI (Fig. 3.10b) and for BOTH (Fig. 3.10c) than for NONE (Fig. 3.10d) which may suggest that the deeper layer may promote more sectors or dendrites that can increase snowfall amounts within the snowbands.

The point-relative approach of the vertical profile analysis in this section must be supplemented with different methods such as the use of gridded composites or looking at representative cases for each classification for a variety of reasons. Each point is intended to represent the classification of SINGLE, MULTI, BOTH, or NONE exhibited at an analysis time within ~200 km of the point. There are a number of shortcomings of this approach especially that the point is chosen regardless of whether it is upstream or downstream of a classified band. Previous studies have shown great sensitivity to banding ingredients (i.e., frontogenesis, stability, moisture) depending on location relative to a specific band (e.g., Novak et al. 2004; Novak et al. 2010). The location of each vertical profile used are chosen with no normalization to cyclone stage (i.e., developing or mature) which can also affect the banding environmental conditions depending on what quadrant the profile is taken from (Colle et al. 2014). Therefore, additional approaches were taken to analyze the environmental differences between classifications, specifically cyclone-relative composites and spatial analysis of example cases which are provided in Section 3.2b and Section 3.2c.

b. Composites of banding environments

Spatial composites were created for each of the four classification types (SINGLE, MULTI, BOTH, NONE) for a variety of synoptic-scale mass and kinematic fields. Since the dataset contains extratropical cyclones with a variety of intensities and structures, the composites of sea level pressure and 700-hPa equivalent potential temperature (θ_e) showed little variation between the four classifications (Fig. 3.11). The SINGLE and BOTH composites showed a stronger cyclone by 4–6 hPa than those of the MULTI and NONE as well as higher values of θ_e extending poleward towards the cyclone center. The BOTH average minimum sea level pressure is statistically deeper than that of NONE by 2 hPa (2.5^{th} and 97.5^{th} percentiles of the mean of

1,000 resamples; 95% confidence). To account for the variety of cyclone intensity and structure, the four classifications were additionally classified into either developing (DEV) or mature (MAT) cyclones, and composites were calculated for each group. It should be noted that all 5 SINGLE cases were associated with a MAT cyclone rather than a DEV cyclone, and, although this sample size is too small to obtain robust results, it is retained in this study.

1) DEVELOPING CYCLONES

For the developing cyclone composites, all composites show a weak cyclone > 1000 hPa. The MULTI cyclone was the strongest at 1004 hPa and the NONE was the weaker by 1 hPa (Fig. 3.12). There is no significant difference between the cyclone strengths of these composites between the three classifications. Despite the similar cyclone strengths, there were differences in the northward extent of mid-level warm, moist air. The BOTH composite had larger values of 700-hPa θ_e extending poleward towards the cyclone center than either MULTI or NONE (Fig. 3.12b).

The baroclinic zones at 850-hPa may also indicate preferential band locations due to vertical frontal motions. The temperature gradient for DEV cyclones is strongest in the northwest quadrant of the cyclone for BOTH, whereas it is strongest in the northeast quadrant for MULTI and generally weak in both northern quadrants for NONE events (Fig. 3.13). This is consistent with the preferential locations relative to the cyclone center discussed in Chapter 2 for BOTH, MULTI, and NONE.

Low-to-mid-level (i.e., 700–500 hPa) flow amplification can be important for the genesis and maturation of primary bands, specifically when there is a closed 700-hPa low and amplified 500-hPa trough upstream to provide the necessary kinematic convergence in the primary band environment (Novak et al. 2010). At 700-hPa (Fig. 3.14), the DEV composite for all categories show an open wave or weaker trough pattern. This suggests that bands within these storms could be forming as a result of flow amplification at lower levels, such as the aforementioned 850-hPa baroclinic zone, or other mechanisms such as an upper-level jet streak. The mid-level (i.e., 500-hPa) geopotential height patterns for the DEV composites are also weakly amplified with weaker troughs, corresponding with weaker surface cyclones (Fig. 3.15).

Examination of the 250-hPa jet cores (i.e., wind speed maxima) shows that for DEV

composites, there is no upper-level jet present except for the BOTH classification which may suggest that bands could be forming through additional lifting via ageostrophic ascent present in the right entrance region of jet core or along the equatorward edge of the jet core (Baxter and Schumacher 2017).

The spatial pattern in vertical velocity relative to the cyclone can provide insight into where this large scale ascent can contribute to bands. The average vertical velocity was calculated for vertical levels of favorable snow growth defined as -15 °C $\leq T \leq$ -10 °C at each grid point in the CFSR. The resulting composites for the DEV cyclone events in Figure 3.16 show enhanced vertical motion to the northeast of the surface low (42.0°N, -72.0°W). The MULTI DEV composite shows larger values of upward vertical motion to the north and east of the surface low than the BOTH and NONE composites. This corresponds with the more widespread multi-bands located to the north of the surface low compared with the generally concentrated region of single and multi-bands typically confined to the northwest of the surface low presented in Chapter 2 (Fig. 2.18).

The DEV events had similar large-scale structures including weak mid-level flow amplification and > 1000 hPa surface cyclones. Within the DEV events, the MULTI events were similar to the NONE events in most cases with the exception of having larger values of upward vertical motion in the northeast quadrant. However, it is unclear what mechanisms are resulting in this region of widespread enhanced ascent which warrants further examination. The BOTH events were associated with the tightest 850-hPa temperature gradient in the northwest quadrant of a stronger composite cyclone with higher values of 700-hPa θ_e reaching the northern quadrants. Additional analysis is required to assess the forcing mechanisms that may result in bands in BOTH within an environment with more mid-level moisture.

2) MATURE CYCLONES

For the mature cyclones, all composites exhibited a significantly stronger cyclone than the respective DEV cyclones (2.5^{th} and 97.5^{th} percentiles with 95% confidence). The BOTH composite had the strongest cyclone with an average central pressure of 990 hPa (Fig. 3.17c). All composites except for the NONE composite showed evidence of high θ_e air at 700 hPa extending from the southeast towards the center of the cyclone and, in the cases of SINGLE and BOTH,

wrapping around the northeast towards the northwest quadrant relative to the cyclone center (Figs. 3.17a–d). This intrusion of high θ_e air contrasts with the low θ_e air to the west of the cyclone. The fact that this is evident in MAT and not in DEV cyclones, which lacks the high θ_e air in the northwest quadrant, further supports this hypothesis as there are more SINGLE and BOTH events associated with MAT cyclones than DEV cyclones.

The 700-hPa flow is more amplified for the MAT events. The MAT composites show an amplified trough for the NONE classification, with stronger closed 700-hPa lows for SINGLE, MULTI and BOTH (Figs. 3.19a–d). For the MAT cyclones, the BOTH and SINGLE 700-hPa closed low center is situated slightly upstream (i.e. northwest) of the corresponding surface low indicating that bands northwest of the surface low might be resulting from this favorable mid-level structure (Figs. 3.17a,c, 3.19a,c). For the MULTI composite, the weaker 700-hPa closed low is displaced farther upstream from the corresponding weaker surface low which may indicate a more widespread favorable region of precipitation bands than for SINGLE and BOTH (Figs. 3.17b, 3.19b).

The low-level baroclinic zones are more amplified with tighter gradients for MAT events than DEV events. For MAT cyclones, there is a well-defined back-bent front at 850-hPa for the SINGLE and BOTH composites extending into the northwest quadrant (Figs. 3.18a,c). This warm intrusion and enhanced temperature gradient is more focused in the northeast quadrant for MULTI and weaker in all quadrants for NONE (Figs. 3.18b,d).

All MAT composites show a longwave 500-hPa trough indicative of being associated with strong, well-developed cyclones. Weak coupled jet signatures are present for the MAT composites of SINGLE, MULTI, and BOTH, but the NONE composite shows a weak jet core to the southeast of the composite low (Figs. 3.17d, 3.20). Unlike the BOTH composite for DEV cyclones, the 250-hPa jet core may not provide additional ascent in the banded environment for the BOTH composite for MAT cyclones because the left exit region of the equatorward jet core is removed to the southeast from the preferential banding environment in the northwest quadrant (Figs. 3.15c, 3.20c).

For MAT cyclones, there are higher values of upward vertical motion in the growth zone for all classifications compared to that of DEV cyclones (Fig. 3.21). The areal extent of the vertical velocity maximum for MAT cyclones is a few hundred kilometers northwest of the surface low for SINGLE and BOTH, but extends to the northeast of the surface low for MULTI

and to the east of the surface low for NONE (Fig. 3.21). This is in spatial agreement with the analysis provided in Chapter 2 that most MULTI events occurred in the northeast quadrant of the cyclone and the precipitation associated with NONE events occurred in the eastern quadrants (Fig. 2.18).

The MAT events that exhibited bands (i.e., SINGLE, MULTI, BOTH) had similar large-scale structures including a well-defined back-bent 850-hPa front, closed 700-hPa lows embedded in higher-amplitude troughs, and higher values of 700-hPa θ_e reaching the northern quadrants. The NONE event composites had weaker 850-hPa baroclinic zones, weaker low-to-mid-level troughs, and the high 700-hPa θ_e air did not reach the northern quadrants. This suggests that in order to get bands in MAT cyclones, there needs to be a juxtaposition of moisture and mid-level forcing. Questions remain regarding the mesoscale differences between SINGLE, MULTI, and BOTH events, such as identifying the role of frontal circulations in band forcing and the importance of stable layers that this composite analysis could not answer. However, detailed case studies could look into such differences.

3) BAND MOTION

Composites were also created for laterally-moving bands (LAT) and radially-moving bands (RAD) for both DEV and MAT cyclones. For most classifications, there was little difference between LAT and RAD composites (not shown). However, there were some notable differences for the BOTH classification associated with MAT cyclones.

Composites of the 6 (58) BOTH-MAT-LAT (BOTH-MAT-RAD) events are examined (Figs. 3.22, 3.23). The composite surface lows are of comparable magnitudes (999 hPa). The BOTH-MAT-LAT, shows an elongated surface low with a pressure trough extending to the west (Fig. 3.22a). The BOTH-MAT-RAD shows structure similar to the conceptual model of a strong cyclone with the high values of θ_e mid-level wrapping around to the northwest quadrant (Fig. 3.23a). The low-to-midlevel flow is more amplified for the BOTH-MAT-RAD than BOTH-MAT-LAT (Figs. 3.22b,c, 3.23b,c). The composite jet cores show a strong (> 110 kts) coupled jet structure in a zonal orientation for BOTH-MAT-LAT and a weaker (~100 kts) coupled jet structure with a more amplified, or meridional, orientation for BOTH-MAT-RAD (Figs. 3.22c, 3.23c). The 850 hPa temperature gradients are also more amplified, or meridional, for BOTH-

MAT-RAD than for BOTH-MAT-LAT. There is also a lack of an 850-hPa cyclonic circulation for BOTH-MAT-LAT that is present for BOTH-MAT-RAD (Figs. 3.22d, 3.23d). This suggests that bands may travel in a single direction if the steering flow for BOTH-MAT-LAT is at 850 hPa but not for the more cyclonic flow of BOTH-MAT-RAD. There is an area of enhanced frontogenesis northeast of the surface low for the BOTH-MAT-LAT composite and northwest of the surface low for the BOTH-MAT-RAD composite, which shows where the forcing for lift was that supported the primary bands of this classification (Figs. 3.22d, 3.23d).

4) COMPOSITE CORRELATION ANALYSIS

In order to assess how representative the individual events are related to their corresponding composite, the linear spatial correlation was calculated (Baxter and Schumacher 2017; Gosselin et al. 2011; Moore et al. 2003). The equation for the linear spatial correlation (COR) is provided in Eq. 3.4.

$$COR = \frac{\frac{1}{N}\sum_{i=1}^{N}(X_i-\bar{X})(Y_i-\bar{Y})}{S_x S_y} \qquad \text{Eq. 3.4}$$

The individual (X) and composite (Y) fields are already re-centered with the surface low at the same point (42.0N, -72.0W) but are converted into one-dimensional arrays with N grid points (2501). $\bar{X}$ is the spatial average of X and $\bar{Y}$ is the spatial average of Y. $S_x(S_y)$is the standard deviation of the individual (composite) field. It has been shown that highly spatially varying mesoscale fields such as 700-hPa frontogenesis will produce a low correlation but larger-scale synoptic fields such as 700-hPa geopotential height will produce higher correlations (Baxter and Schumacher 2017; Gosselin et al. 2011).

Figure 3.24 shows the COR values comparing individual events to their respective composite. For all 193 events combined, the highest COR values with median values ≥ 0.90 were calculated for 500 hPa geopotential height, 700 hPa geopotential height, and 850 hPa temperature (Fig. 3.24a). When the COR values for these fields were compared for each classification and cyclone strength category (e.g., SINGLE and MAT, MULTI and DEV, etc.), median values remained ≥ 0.90 (Figs. 3.24b–h). The variable that is attributed to the smallest

correlation variable (average < 0.50) is 700 hPa frontogenesis. This is attributed to the large amount of spatial variability between events and the resultant composite. The remaining variables that were used (i.e., SLP, 250 hPa wind speed, 700 hPa relative humidity, and 650 hPa MPV*) exhibited median correlations between 0.5 and 0.9.

There were 9 events that are outliers for the highly-correlated fields of 500 hPa geopotential height, 700 hPa geopotential height and 850 hPa temperature, meaning that these individual events had less than a 0.70 correlation with the composite mean (Table 3.1). The individual fields were compared with the composite field (not shown). A few events associated with mature cyclones were actually found to be late-stage decaying cyclones. While these cyclones are in fact mature by definition, the structure of the low to mid-level height field, jet structure, and SLP fields vary to those of younger, yet mature, cyclones. For example, although the event of 0600 UTC 27 Dec 2010 is classified as BOTH and MAT, the cyclone is much deeper (974 hPa) than average (990 hPa) with the 700-hPa and 500-hPa lows nearly vertically stacked within high-amplitude longwave troughs above the surface low center which is different than the average upstream location of these mid-level lows within the composite likely resulting in lower COR values (not shown). This supports that bands can form under a broad spectrum of cyclone conditions. In spite of these outlier events, the composites are determined to be representative with most fields exhibiting median COR values > 0.5.

The composites analyzed in this section provided a comparison of large-scale synoptic ingredients such as the amplification of the upstream 700-hPa and 500-hPa troughs, presence of jet cores, and the surface cyclone magnitude and structure. Mesoscale environmental banding ingredients were not easily compared within the composites and can be examined on a case-by-case basis which follows in Section 3.2c.

c. Comparison of individual banding events

The vertical profile analysis of Section 3.2a and composite methodology of Section 3.2b compared several banding ingredients (e.g., frontogenesis, stability) and synoptic and mesoscale fields (e.g., 700-hPa trough amplitude) for the four classifications for both DEV and MAT cyclones. The composite methodology was not useful for mesoscale quantities that exhibited a lot of spatial variation such as frontogenesis and MPV* in order to compare those fields among

classified events (not shown). Individual example events that are subjectively chosen from each of the four classification categories are examined in more detail to compare frontogenesis and stability between the SINGLE, MULTI, BOTH, and NONE classifications (Fig. 3.25). Banding ingredients are compared for gridded fields and individual vertical profiles taken through the bands (or precipitation coverage for NONE) for each of the four events.

1) SINGLE

Previous analysis found that SINGLE events occurring within MAT cyclones form due to enhanced frontogenesis beneath in a layer of conditional symmetric instability in the northwest quadrant of the cyclone. The example SINGLE event occurred at 0600 UTC 17 Feb 2013 while a MAT low pressure system further developed off the coast of Virginia and exhibited a single band to the northwest of the 992 hPa surface cyclone center (Figs. 3.25a, 3.26a). The SINGLE event showed a highly amplified 700-hPa trough upstream of the surface low (Fig. 3.27a). The 850-hPa baroclinicity in the banded region is strong (~10°C 100 km^{-1}) with convergent 850-hPa winds in the frontal zone (Fig. 3.28a). There is a ~500 km region of 700-hPa frontogenesis in the northwest quadrant of the MAT cyclone values ≥ 2.0 K 100 km^{-1} h^{-1} near where the band exists in the reflectivity field (Fig. 3.28a). The SINGLE environment is associated with 700–600-hPa average MPV* ≥ -1.0 PVU (Fig. 3.29a). This suggests that there is CSI present near the primary band and agrees with previous analysis of this classification. The vertical velocity directly output from the CFSv2 averaged within the -15°C ≤ *T* -10°C snow growth zone is provided in Figure 3.31a. The vertical velocity minimum of -1.75 x 10^{-3} hPa s^{-1} indicating ascent is collocated with the band location.

The vertical profile through the primary band in the SINGLE event showed a weakly stable environment around 900 hPa and between 600–400 hPa with a strong veering wind profile (Fig. 3.32a). There was a ~600-hPa vertical velocity maximum of ~ -18 x 10^{-3} hPa s^{-1} (Fig. 3.33a). The profile of relative humidity showed that the column is approximately saturated to 400 hPa (Fig. 3.33e). A vertical profile of frontogenesis through the SINGLE band shows that it is maximized around 700 hPa at 2 K 100 km^{-1} h^{-1} (Fig. 3.34a). The region of most negative MPV* was found at 700 hPa, near the level of the frontogenesis maximum (Fig. 3.34i).

2) MULTI

MULTI events associated with DEV cyclones were found to be associated with strong stable layers, larger wind shear, and layers of stronger conditional instability. The example MULTI event of 0600 UTC 21 Feb 2005 was associated with a weaker 1006 hPa DEV cyclone tracking eastward from the Great Lakes, with the multi-bands situated in the northeast quadrant ahead of a warm front (Figs. 3.25b, 3.26b). The MULTI event exhibits a weak 700-hPa shortwave upstream of a weak ridge over the NEUS (Fig. 3.27b). This event corresponds with its 700-hPa geopotential height field composite with a linear spatial correlation of 0.97. The 850-hPa baroclinic zone in the northeast quadrant is weaker for MULTI (~2°C 100 km^{-1}) with winds at this level crossing the isotherms throughout the precipitation region indicative of warm air advection (Fig. 3.28b). There is a weak (< 1 K 100 km^{-1} h^{-1}) 700-hPa frontogenesis maximum in the northeast quadrant ~100 km southwest of the multi-banded region (Fig. 3.28b). This corresponds with MPV* ≤ -1.0 PVU in the multi-banded region (Fig. 3.29b). Compared with the SINGLE event, there is larger CSI for the MULTI event indicated by enhanced, smaller values of MPV*. The right entrance region of the poleward-most 250-hPa jet core of the two jet cores is near the region of multi-bands which might provide additional ageostrophic ascent for widespread precipitation (Fig. 3.30b). The vertical velocity averaged in the snow growth zone has the largest values of ascent compared to the other individual events over the region of the multi-bands of -2.25 x 10^{-3} hPa s^{-1} (Fig. 3.31b).

Three profiles through separate multi-bands were examined for the MULTI event which showed a strong stable layer between 900–800 hPa and 700–600 hPa with a shallow weaker stable layer in between (Fig. 3.32b). This supports the hypothesis that some multi-bands may form from gravity waves traveling within a ducted stable layer however more analysis is needed to investigate this. Maximum vertical velocity around -10 x 10^{-3} hPa s^{-1} at 600 hPa was found for the three MULTI profiles (Fig. 3.33b). Profiles of relative humidity show that the column is approximately saturated between 800 to 400 hPa (Fig. 3.33f). A vertical profile of frontogenesis through the MULTI bands show that it is maximized (2 K 100 km^{-1} h^{-1}) around 700 hPa (Fig. 3.34b). The profiles of MPV* through the multi-bands show enhanced values indicative of CSI between 850 and 550 hPa (Fig. 3.34j).

3) BOTH

BOTH events associated with MAT cyclones, like SINGLE events, form due to enhanced frontogenesis beneath in a layer of conditional symmetric instability in the northwest quadrant of the cyclone. The BOTH event of 0000 UTC 27 Dec 2010 exhibited both a primary band and multi-bands in the northwest quadrant of a strong 978 hPa MAT low offshore of Long Island, NY (Figs. 3.25c, 3.26c). The BOTH event shows a closed 700-hPa low slightly upstream of the surface low at this time (Fig. 3.27c). The 850-hPa baroclinicity in the banded region is strongest for the BOTH event (~12°C 100 km^{-1}) and shows convergent 850-hPa winds in the frontal zone (Fig. 3.28c). Strong frontogenesis (> 5 K 100 km^{-1} h^{-1}) is found in a ~300 km southwest-northeast-oriented maxima in the northwest quadrant of the MAT cyclone (Fig. 3.28c). There is 700-600-hPa average MPV* ≤ -1.0 PVU in the multi-banded region for the BOTH event (Fig. 3.29c). A region of negative values (< -2 PVU) is located ~100 km offshore of Long Island near where the multi-bands formed in addition to along the warm side of the frontogenesis maximum where the primary band was located at this time. The fact that the regions supporting both the primary band and multi-bands are exhibiting CSI suggests that this might be an important stability characteristic for bands in general. The 500-hPa circulation shows an amplified trough with a closed low indicative of the intense BOTH cyclone event (Fig. 3.30c). The 250-hPa jet may provide additional forcing for ascent for the BOTH event as the bands are located near the favorable left jet exit region (Fig. 3.30c). The BOTH event has a vertical velocity minimum of -2 x 10^{-3} hPa s^{-1} in the region of the primary band (Fig. 3.31c).

Vertical profiles through the primary band and three separate multi-bands are used to compare the two classes of bands within the same event. The primary band within the BOTH event shows a stable layer between 900–750 hPa and 650–550 hPa, with a layer of CI in between (Fig. 3.32c). The northernmost multi-band profile is similar, but the profiles through multi-bands farther south show a deep stable layer extending to 700 hPa followed by a layer of CI from 750–600 hPa with weak CI above. This layer of CI is located just above the low-level jet core ≥ 70 kts. These southernmost multi-band profiles, near the region of multi-band genesis, support that if the bands formed via shear-induced circulations, they could travel within the stable layer below 700 hPa for this particular case. Vertical velocity was maximized at 700-hPa with a value of ~ -18 x 10^{-3} hPa $s^{-1}$for the BOTH event (Fig. 3.33c). The dry intrusion above 600 hPa is

evident in vertical profiles of relative humidity for the BOTH profiles (Fig. 3.33g). The vertical profiles of frontogenesis through both the primary band and multi-bands show a few levels of maxima (> 5 K 100 km^{-1} h^{-1}) between 800 – 600 hPa (Fig. 3.34c). The profiles through the primary band and multi-bands show large negative values of MPV* between 800 and 600 hPa which is above each frontogenesis maximum (Figs. 3.34c,k).

4) NONE

NONE events associated with DEV cyclones have shown the weakest mid-level forcing (i.e., trough amplification, frontogenesis) out of all of the classifications. The example NONE event was associated with a weak pressure trough extending eastward from the Great Lakes with no clearly defined DEV cyclone in the East Coast domain (Figs. 3.25d, 3.26d). The NONE event, like MULTI, exhibits a weak 700-hPa shortwave upstream of a weak ridge over the NEUS (Fig. 3.27d). This event corresponds with its 700-hPa geopotential height field composite with a linear spatial correlation of 0.95. The 850-hPa baroclinic zone in the northeast quadrant is weak for (~2°C 100 km^{-1}) with winds at this level crossing the isotherms throughout the precipitation region indicative of broad warm air advection (Fig. 3.28d). There is no measurable 700-hPa frontogenesis for the NONE event (Fig. 3.28d). This supports the hypothesis that bands may require mesoscale convergences at low to mid-levels resulting from frontogenesis. The 700–600-hPa average MPV* was larger than -0.25 PVU in the NONE precipitation environment indicating weak CSI (Fig. 3.29d). The 250-hPa jet core is largely displaced from the precipitation area over Long Island which suggests that the jet does not provide additional large-scale upward motion (Fig. 3.30d). The NONE event has weak (-0.5 x 10^{-3} hPa s^{-1}) averaged vertical velocity within the snow growth layer in the precipitation region (Fig. 3.31d).

A vertical profile through the center of the non-banded precipitation region is examined. The NONE profile is associated with a low-level stable layer around 900 hPa with weak conditional stability extending to 550 hPa (Fig. 3.32d). A vertical velocity maximum at 800 hPa of -5 x 10^{-3} hPa s^{-1} was found for the NONE profile (Fig. 3.33d). The dry intrusion between 600 to 500 hPa is evident in the vertical profile of relative humidity (Fig. 3.33h). Frontogenesis values were small above a weak 0.5 K 100 km^{-1} h^{-1} maximum at 900 hPa (Fig. 3.34d). There is an MPV* minima between 900 and 850 hPa indicative of CSI which is above the layer of the

weak frontogenesis maximum (Fig. 3.34l).

3.4 Summary and discussion

An analysis of the environments and forcing mechanisms are examined using reanalyses for the 193 single band (SINGLE), multi-bands (MULTI), both single and multi-bands (BOTH) and non-banded (NONE) events within 110 NEUS winter storms. Most events were either BOTH (107), NONE (46) or MULTI (35) while only 5 events were SINGLE as discussed in Chapter 2. The environmental ingredients, including forcing and available instability, are analyzed for each of the four classifications. It was especially useful to sub-classify the classifications into being associated with either a developing (DEV) or mature (MAT) cyclone, given that the strength of the low pressure system is correlated with mid-to-upper-level patterns in geopotential height, wind speed and direction, etc.

The four classifications were compared using point-relative vertical profiles taken ±1 h of observed bands within 150 km of one of six sounding sites. The CFSR and CFSv2 data are used for all calculations, using the nearest grid point to the chosen sounding site. In addition to analysis at points fixed in space, cyclone-relative composites were calculated for several synoptic fields and band ingredients for classifications associated with DEV and MAT cyclones separately. In order to look into the differences found in the composite framework in greater detail, an example event from each of the four classifications was analyzed.

The vertical profiles and distributions from each individual event are analyzed to show subtle differences in available forcing and instability. On average, frontogenesis is stronger for BOTH events compared to MULTI and NONE, with more events exceeding 2 K 100 km^{-1} h^{-1}. However, MULTI and BOTH both typically exhibit a 200-hPa layer of conditional symmetric instability (CSI) more often than conditional instability (CI). NONE events show shallow near-surface layers of CSI, but precipitation is not forced via frontogenesis and concentrated into bands.

The comparison of the environmental ingredients for the four classifications for both DEV and MAT cyclones provided some subtle yet important differences. Bands are associated with larger low-level temperature gradients with deeper cyclones, more amplified mid-level troughs, and stronger upper-level jets than non-banded cases. For example, the location and

strength of the upper-level jet may produce enhanced ageostrophically-induced vertical motions interacting with mid-level convergent and baroclinic flow resulting in bands. Also, the strength of the surface low and mid-level trough may indicate how much warmer and higher moisture content (indicated by higher values of θ_e) may reach the northern quadrants of the cyclone where increased baroclinicity with the colder, drier to the north of the surface low may result in frontal ascent. A key difference between MULTI and SINGLE is that multi-bands can form in either a conditionally unstable environment with weak frontogenetical forcing or in the presence of strong stable layers with large vertical wind shear. Multi-bands can form in the northern quadrants of the cyclone where these conditions are met more often than the single bands that are concentrated in the northwest quadrant.

SINGLE events, all of which were within MAT cyclones, were associated with an average SLP of 974 hPa, a closed 700-hPa low located slightly upstream, an amplified 500-hPa trough and anticyclonically-curving 250-hPa jet with strong upward vertical motion within a preferred snow growth layer to the northwest of the cyclone center. An example SINGLE event was associated with a mature 992 hPa low, large amplitude 700-hPa and 500-hPa troughs upstream, with strong 700-hPa frontogenesis along a moderate north-to-south oriented 850-hPa baroclinic zone with CSI on the warm side of the frontogenesis maximum. This amplified flow pattern resulting in mature systems is consistent with the composite for SINGLE events in the NW quadrant of the surface low.

MULTI events associated with both DEV and MAT cyclones exhibited the largest frequency of stable layers and higher vertical wind shear values which motivates additional analysis into the role of gravity waves in a stable layer that will be discussed in Chapter 5. The MULTI events associated with DEV cyclones had an average SLP of 1004 hPa, higher values of 700-hPa θ_e air in the NE quadrant, and an amplified 700-hPa trough upstream of the surface low. An example MULTI event associated with a DEV 1006-hPa low is analyzed. An upstream 700-hPa trough is present and a moderate NW-SE-oriented 850-hPa baroclinic zone is located in the NE quadrant, possibly associated with a warm frontal boundary. There are multiple weak 700-hPa frontogenesis maxima in an environment of CSI on the warm, equatorward side of each. A shortwave trough is present at 500 hPa embedded within a large amplitude ridge. This event varies slightly from its composite partly due to the nature of the composite averaging out smaller-scale features, such as the shortwave trough at 700 hPa.

BOTH events associated with DEV cyclones had an average SLP of 1006 hPa, increased θ_e into the northwest quadrant, weak shortwave troughs at both 700-hPa and 500-hPa but a strong single jet core. This jet core could provide ageostrophic ascent on the warm, equatorward side indicated by a region of upward vertical motion that may be related to a low-level baroclinic zone that could result in the formation of single and multi-bands.

BOTH events associated with MAT cyclones had the deepest average sea level pressure of 990 hPa with the highest values of 700-hPa θ_e reaching the NW quadrant, the strongest 700-hPa closed low, and a weaker but clearly defined coupled jet and enhanced upward vertical motion in the preferred snow growth layer in the northwest quadrant. An example BOTH event for a MAT 978 hPa cyclone was analyzed. There is a closed low at 700 hPa with strong 700-hPa frontogenesis in the northwest quadrant in a strong 850-hPa baroclinic zone with CSI on the warm side of the frontogenesis maximum. Two 500-hPa lows are present embedded in the base of a large-amplitude 500-hPa trough. This event agrees with the composite for BOTH events for mature cyclones because of the presence of favorable environmental ingredients present in the NW quadrant.

The NONE events for DEV cyclones were associated with the weakest average SLP of 1007 hPa, weakly amplified 700 hPa and 500 hPa geopotential heights and a weak coupled jet. NONE events associated with MAT cyclones had an average SLP of 996 hPa, a 700-hPa trough upstream, a single jet, and increased vertical motion in the preferred snow growth layer to the SE of the surface low. The composites were deemed representative of each classification after the linear spatial correlation, a measure of the representativeness of an individual event to its composite, was calculated for several variables. Less than 10 events exhibited values < 0.70 for the highly correlated variables of 500 hPa and 700 hPa geopotential height and 850 hPa temperatures. Therefore, the composites were taken to be representative. An example NONE event associated with a weak developing cyclone was found to lack low-to-mid-level forcing (i.e., 700-hPa frontogenesis) but precipitation may have been occurring due to the interaction of a shortwave 500-hPa trough interacting with a 850-hPa baroclinic zone. The lack of available banding ingredients (frontogenesis, CSI, stronger low-level baroclinic zone) allows for this event to agree with its composite.

Previous studies have examined the environments of single bands (Novak et al. 2004; Baxter and Schumacher 2017) and even single bands solely from mature cyclones (Novak et al.

2010). While this study only produced 5 SINGLE events, there were 107 BOTH events, or events that exhibited both a single band and multi-bands to compare with previous studies. Comparing our BOTH and NONE events to the single band and non-banded classifications of Novak et al. (2004), there is general agreement. Specifically that banded events are associated with cyclogenesis and development of a closed midlevel (i.e., 700 hPa) circulation, deformation and strong midlevel frontogenesis NW of surface cyclone center in an environment of weaker conditional stability or CSI. Also that non-banded events are associated with weaker cyclones with no closed midlevel circulation and weaker frontogenesis. One notable difference between Novak et al. (2010) and this study is that CSI was present in only about one third of banding events, whereas in this study CSI was more common than CI. Baxter and Schumacher (2017) found that for some of their single band events, the important factor was the presence of a jet streak and upper-wave ageostrophic circulations which was found to be evident for the BOTH classification for DEV events in this study.

There are numerous known issues with the methods employed in this chapter. The first being that mesoscale environments are being analyzed using a coarse gridded dataset. It might be useful to re-calculate composites using a higher-resolution dataset but given the time period of this study (1996–2016), such high-resolution datasets are not available for all events such as the Rapid Refresh (RAP), formerly the Rapid Update Cycle (RUC), which was used in Novak et al. (2010). Another issue of looking at point-based data, is the threat of mis-matching point locations with pre-banding or post-banding environments which would show considerably different stability profiles, namely the environment may stabilize during the formation and maturation of a band (Novak et al. 2009). A related issue using point-based analyses is the aggregating of times for events that could be either before or after peak banding intensity. General differences between multi-bands and non-banded environments are provided in this chapter. The following two chapters utilize a high-resolution mesoscale model to analyze the evolution of both single and multi-bands, separately, to examine differences in more detail.

Table 3.1. Events that exhibited small linear spatial correlations (COR ≤ 0.70) for 500 hPa geopotential height, 700 hPa geopotential height and 850 hPa temperature. Event classification and cyclone strength is listed along with notes analyzing why the particular event resulted in small correlations relative its respective composite.

Event	Classification	Cyclone Stage	Notes
12 UTC 11 Jan 1997	MULTI	DEV	Amplified 700-hPa shortwave trough with strong jet, more comparable to BOTH-DEV composites
06 UTC 15 Jan 2006	NONE	MAT	Mature (981 hPa) occluded system
06 UTC 26 Feb 2010	MULTI	MAT	Very mature vertically-stacked cyclone
12 UTC 26 Feb 2010	BOTH	MAT	Vertically-stacked cyclone decaying
18 UTC 26 Feb 2010	MULTI	MAT	Vertically-stacked cyclone decaying
00 UTC 27 Feb 2010	MULTI	MAT	Vertically-stacked cyclone decaying
06 UTC 27 Dec 2010	BOTH	MAT	Very deep (974 hPa) system
06 UTC 23 Mar 2011	BOTH	MAT	More comparable to MULTI-DEV composites
12 UTC 7 Mar 2013	MULTI	MAT	Mature (991 hPa) cyclone, composite comparable to BOTH-MAT

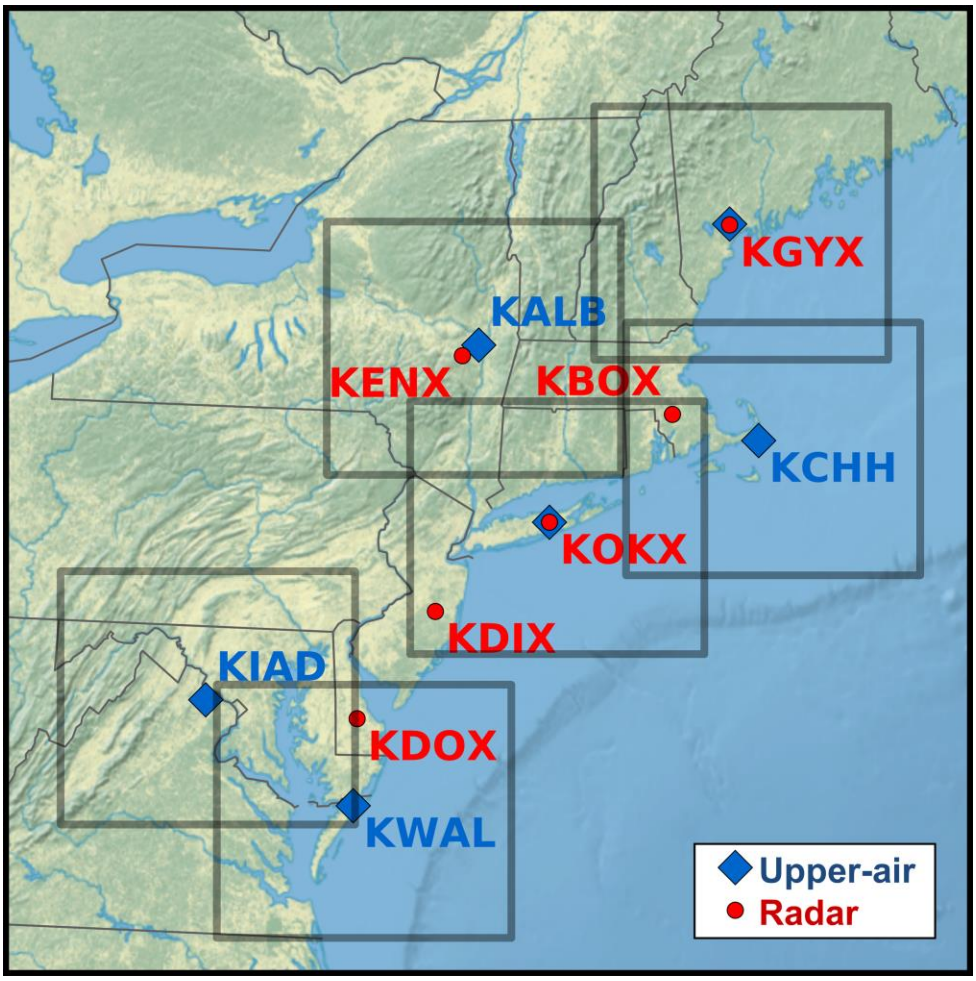

Figure 3.1. Map showing locations of six upper-air sites (red circles) used for vertical profiles through regional classification given by each box bounding ~150-km around the upper-air site.

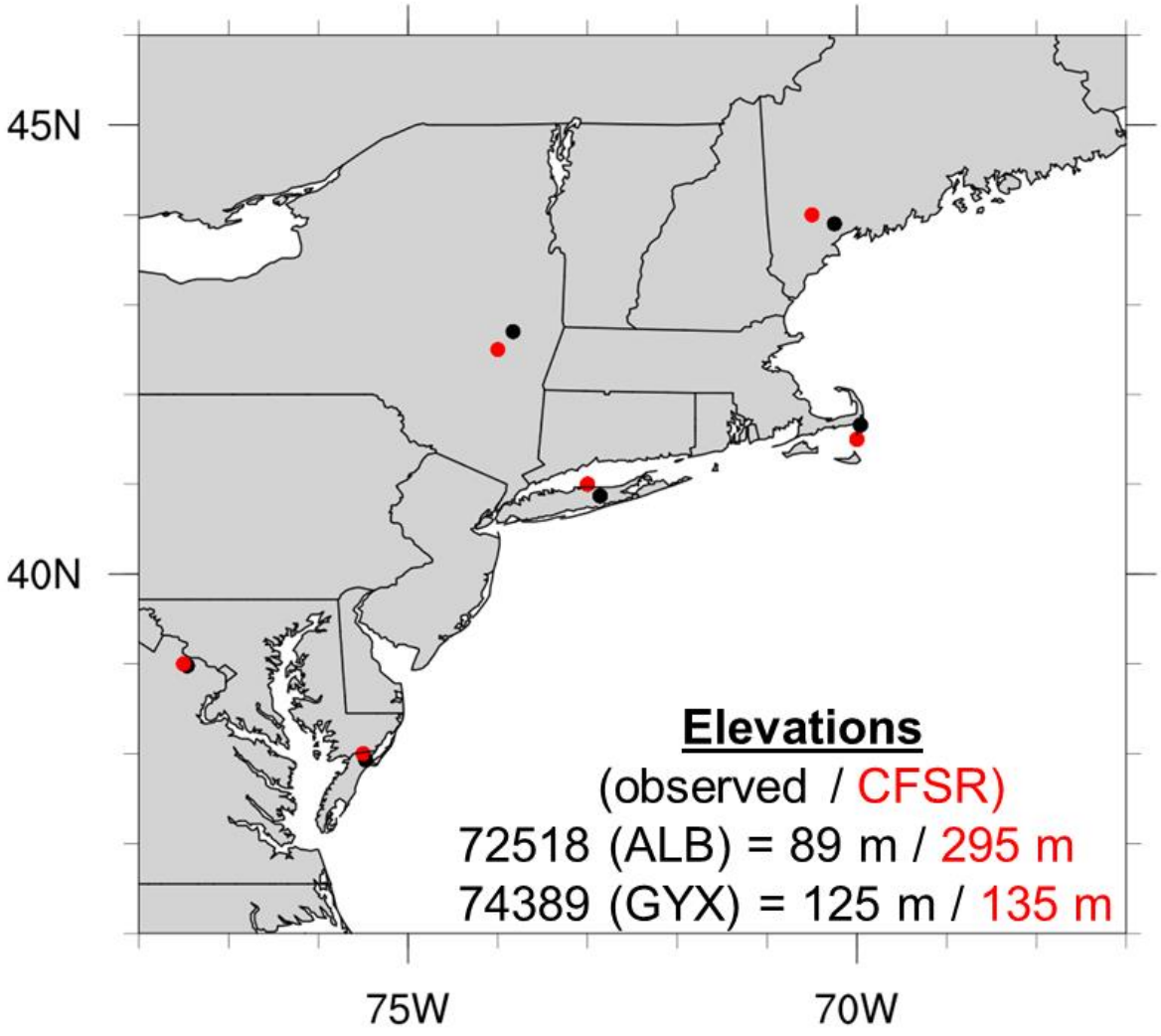

Figure 3.2. Map showing upper-air locations (black) and nearest CFSR grid point used for profiles (red) in Figure 3.3.

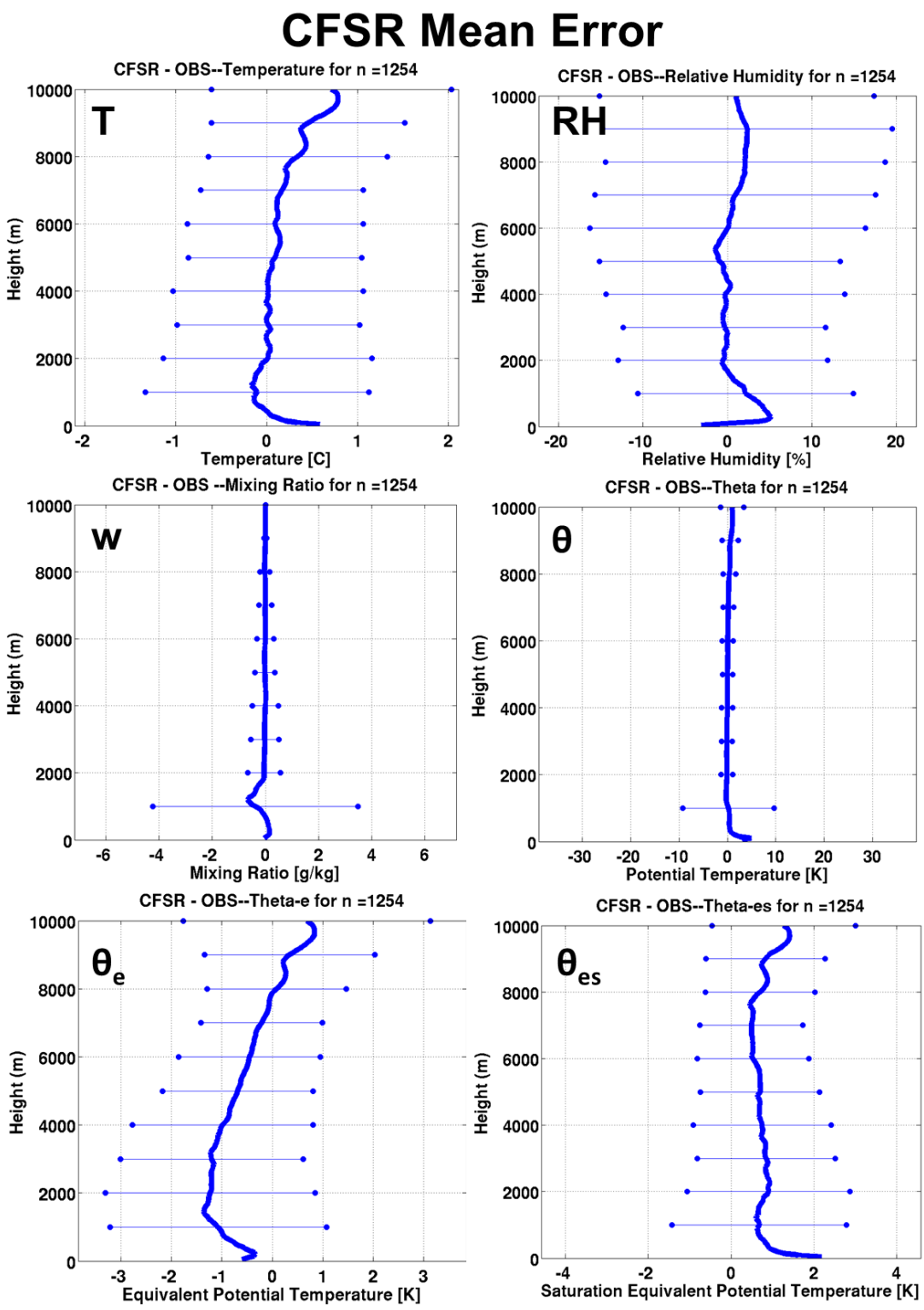

Figure 3.3. Mean error (CFSR - Observed) for 1292 vertical profiles for (clockwise from top-left) temperature (°C), relative humidity (%), mixing ratio (g kg^{-1}), saturation equivalent potential temperature (K), equivalent potential temperature (K), and potential temperature (K). Error bars indicate $\pm 1\sigma$.

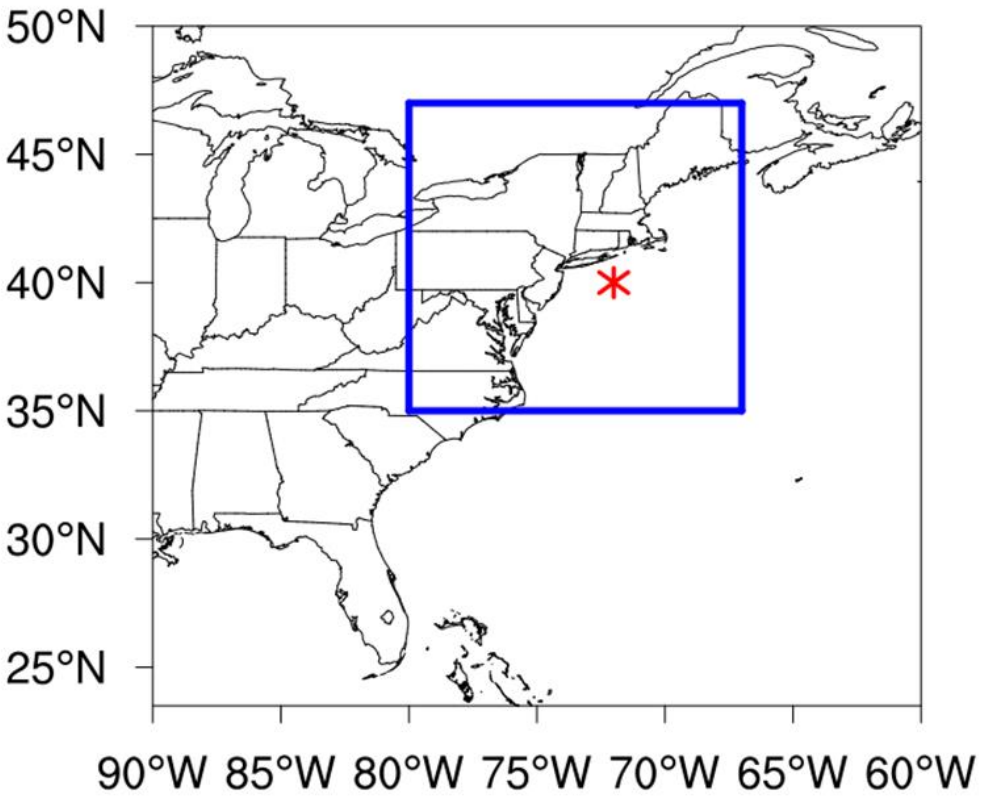

Figure 3.4. Bounds of box within which the sea level pressure minimum was found and taken to be the cyclone center. This point was then re-centered to 40.0, -72.0 (indicated by red asterisk) to create a ~1100 km domain with the ten grid points on either side in the meridional direction and 11 grid points on either side in the zonal direction.

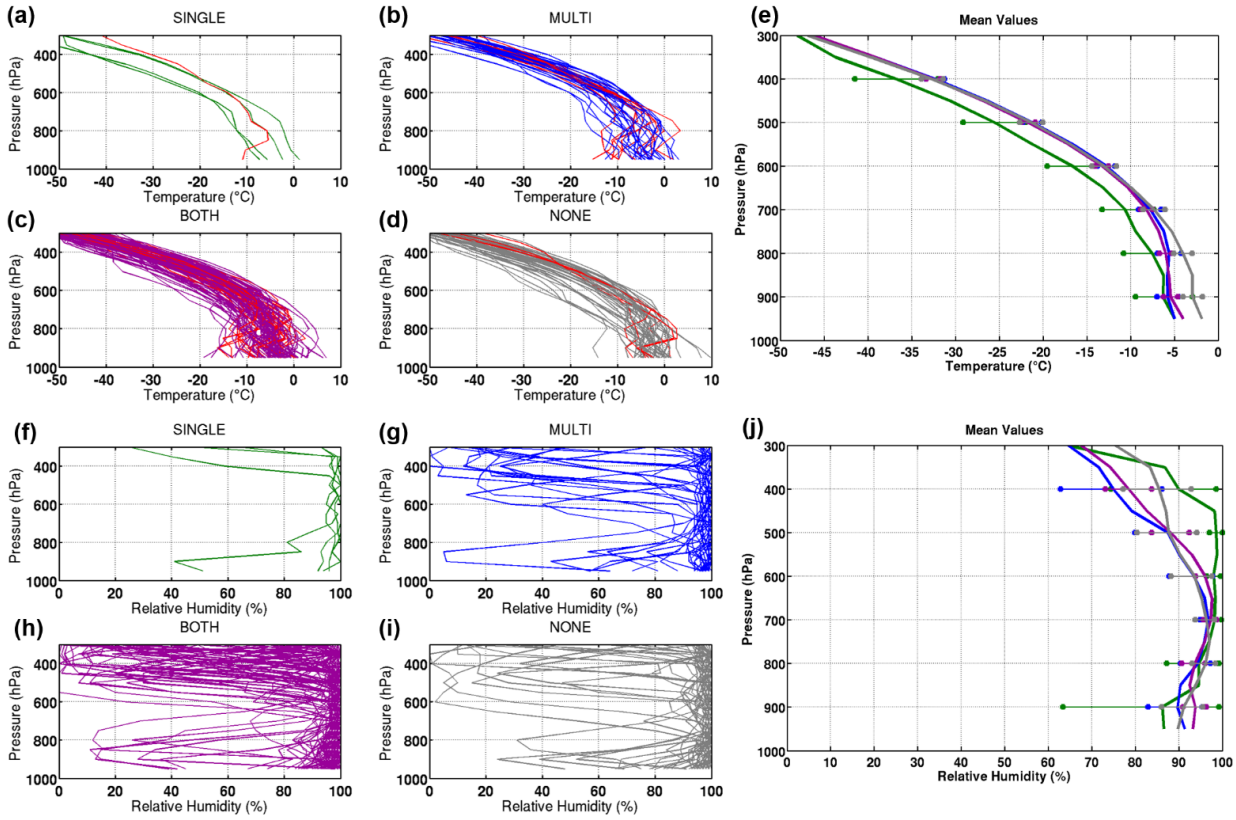

Figure 3.5. Vertical profiles of (a–e) temperature (°C) and (f–j) relative humidity (%) for events classified as (a,f) SINGLE in green, (b,g) MULTI in blue, (c,h) BOTH in purple, (d,i) NONE. Red profiles in (a-d) indicate those that exhibit a stable 50-hPa layer ($dT/dP \geq 0.05$°C hPa^{-1}). (e,j) Bold lines denote the average profile for each classification with markers indicating 2.5th and 97.5th percentiles of the mean with 95% confidence.

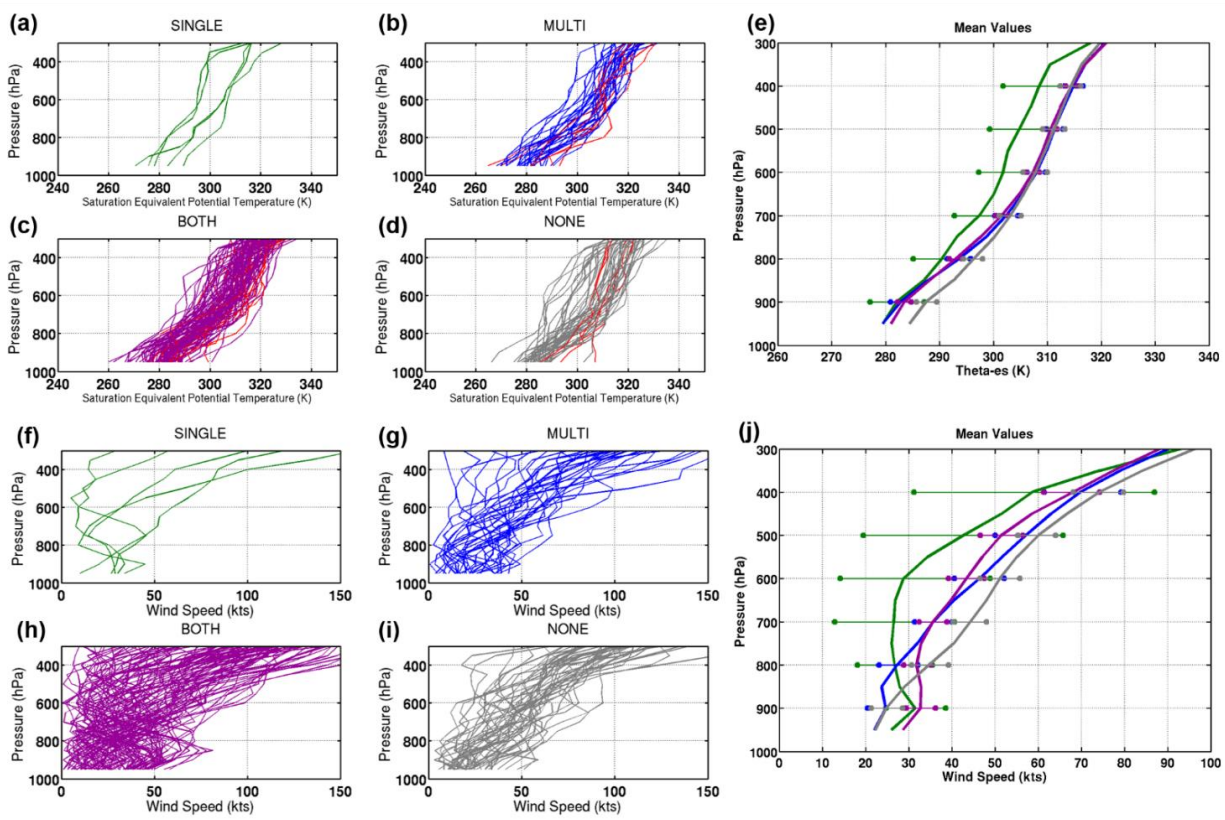

Figure 3.6. As in Figure 3.5 but for (a–e) saturation equivalent potential temperature (K) and (f–j) wind speed (kts). Red profiles in (a–d) indicate those that exhibit a conditionally unstable 50-hPa layer ($d\theta_e^*/dP \leq 0.02$ K hPa^{-1}).

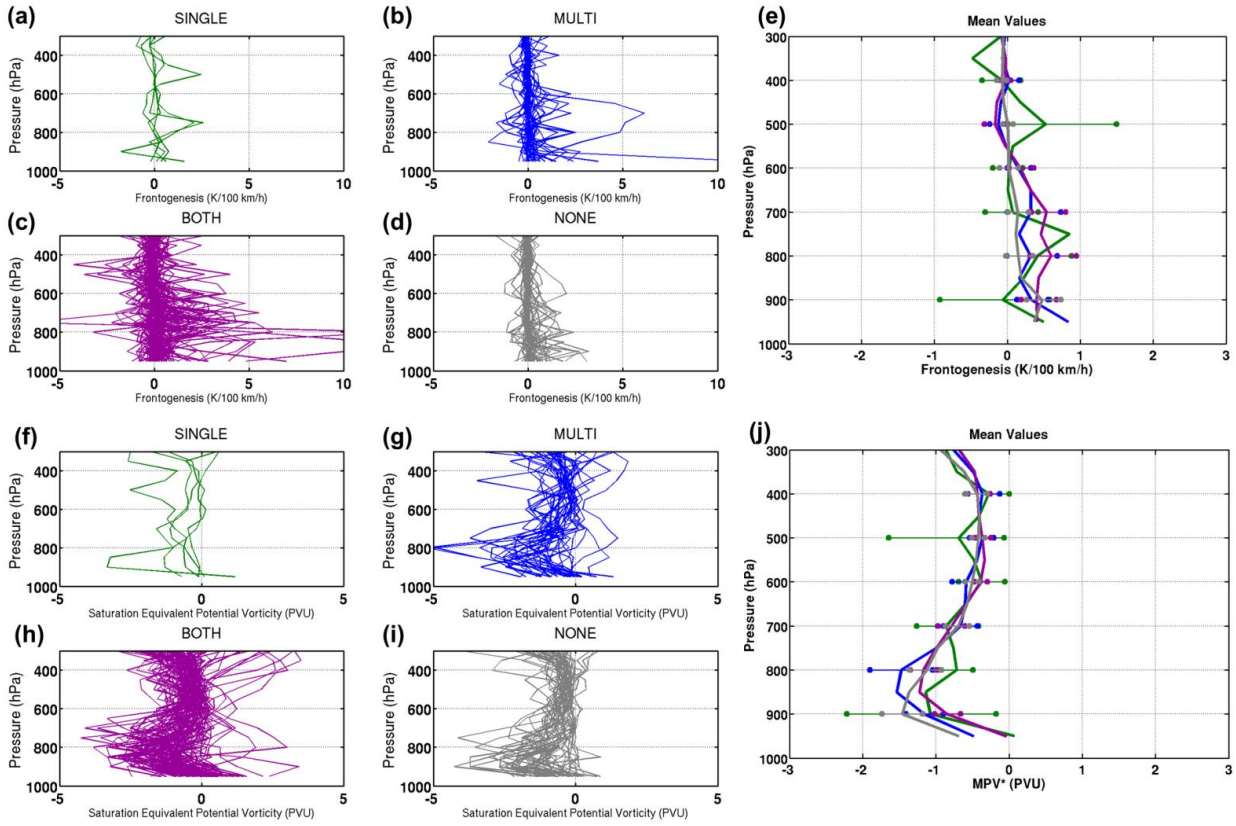

Figure 3.7. As in Figure 3.5 but for (a–e) frontogenesis (K 100 km^{-1} h^{-1}) and (f–j) saturation equivalent potential vorticity (MPV*, PVU).

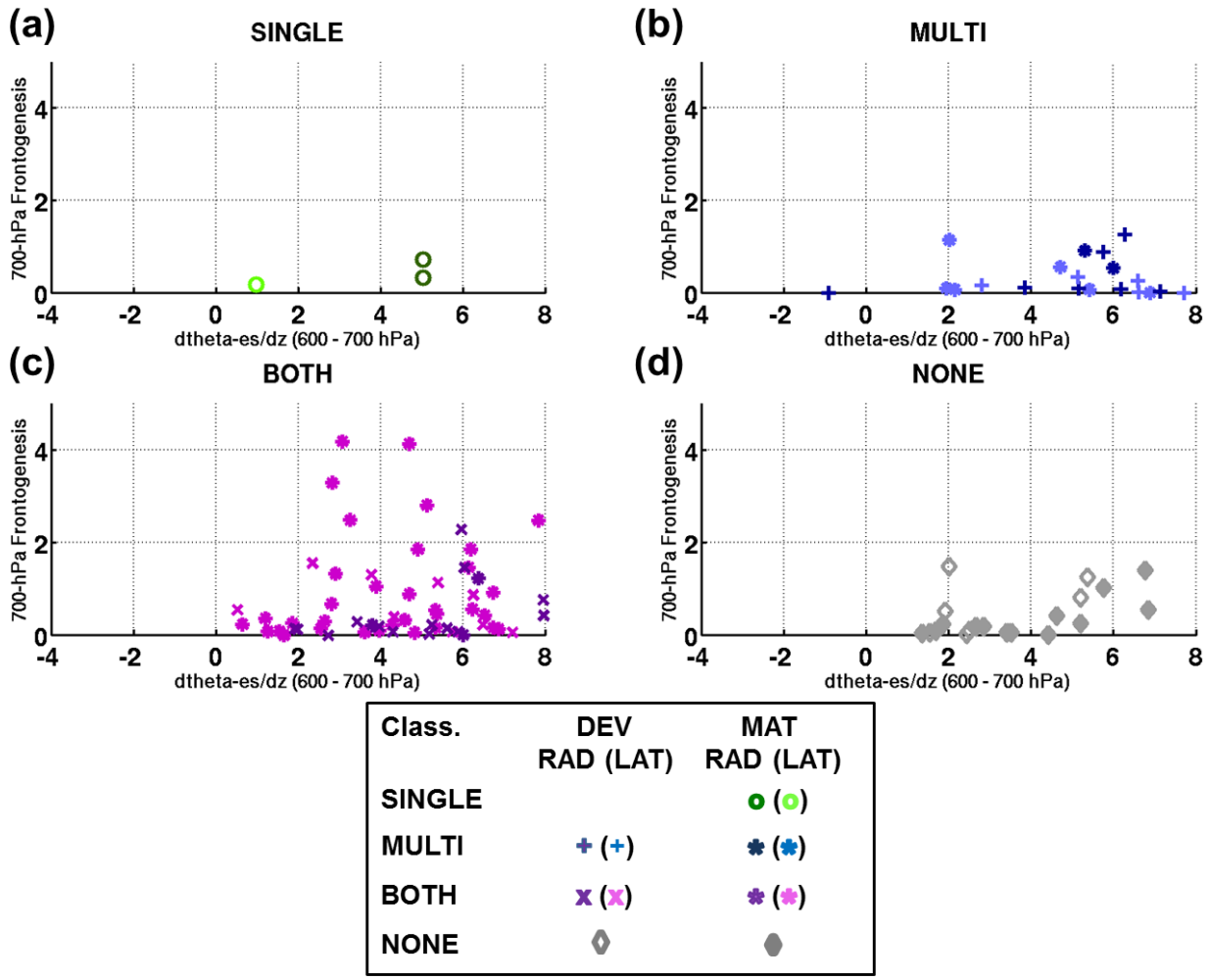

Figure 3.8. The distribution of the difference in saturation equivalent potential temperature with height between 700 hPa and 600 hPa along the abscissa (K km^{-1}) and 700-hPa frontogenesis (K 100 km^{-1} h^{-1}). Each marker style denotes cyclone strength and is colored by band motion type as shown in the legend.

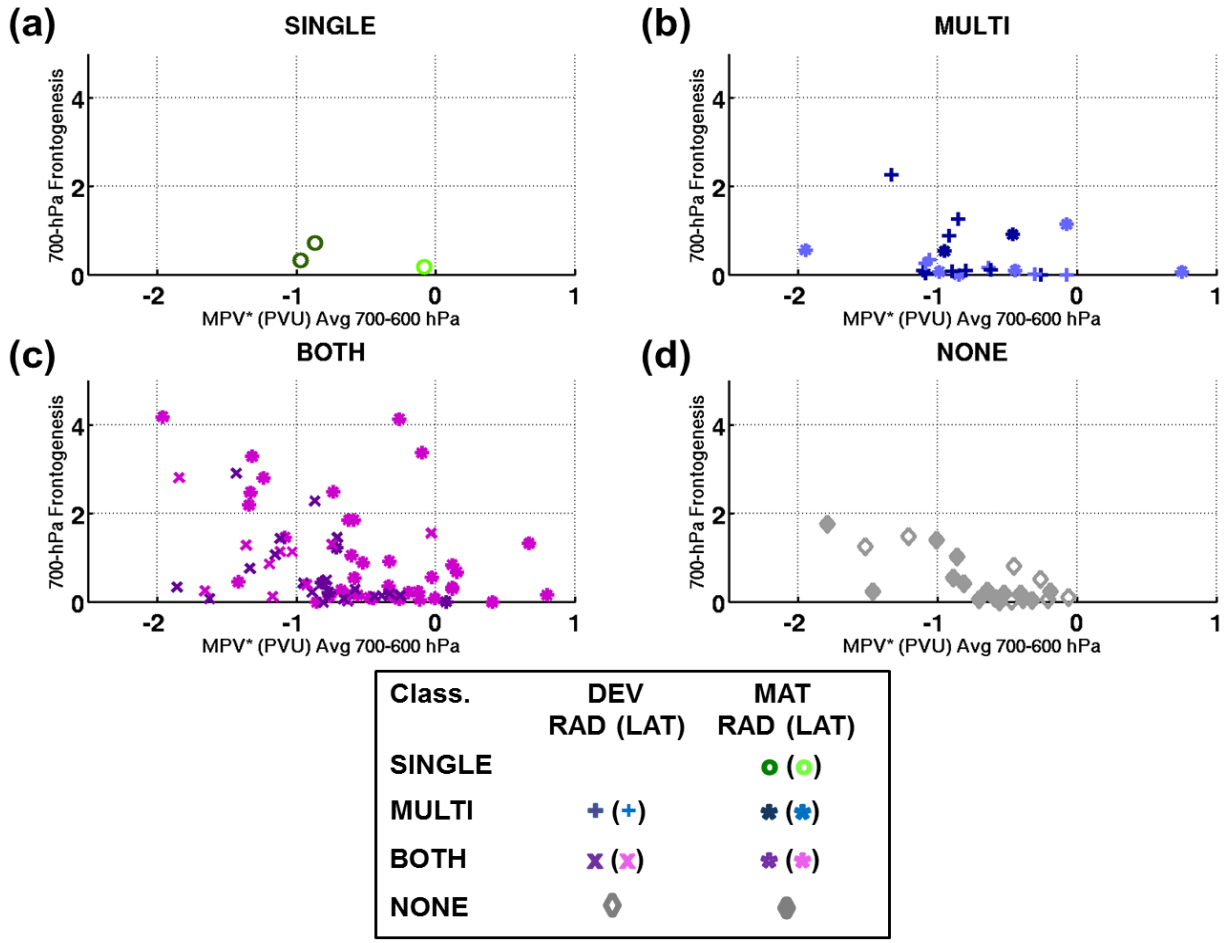

Figure 3.9. As in Figure 3.8 but for the relationship between 700–600-hPa averaged saturation equivalent potential vorticity (MPV*, PVU) on the abscissa and 700-hPa frontogenesis (K 100 km^{-1} h^{-1}) on the ordinate for (a) SINGLE, (b) MULTI, (c) MULTI, (d) NONE classified events.

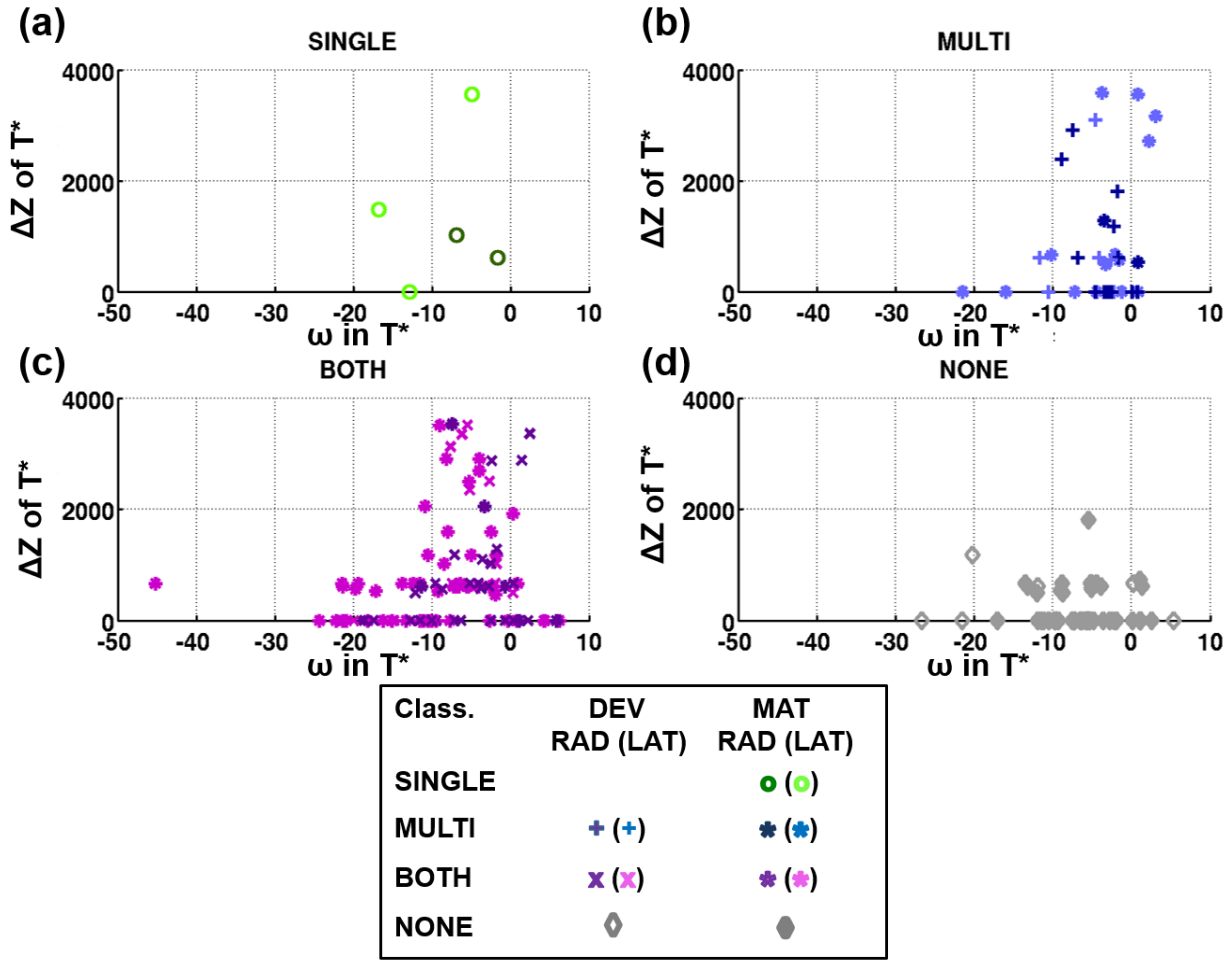

Figure 3.10. As in Figure 3.8 but for vertical velocity (omega, x 10^{-3} hPa s^{-1}) within the layers of T^* (-15°C ≤ T ≤ -10°C) along the abscissa and the vertical depth of the layer of T^* (m) along the ordinate.

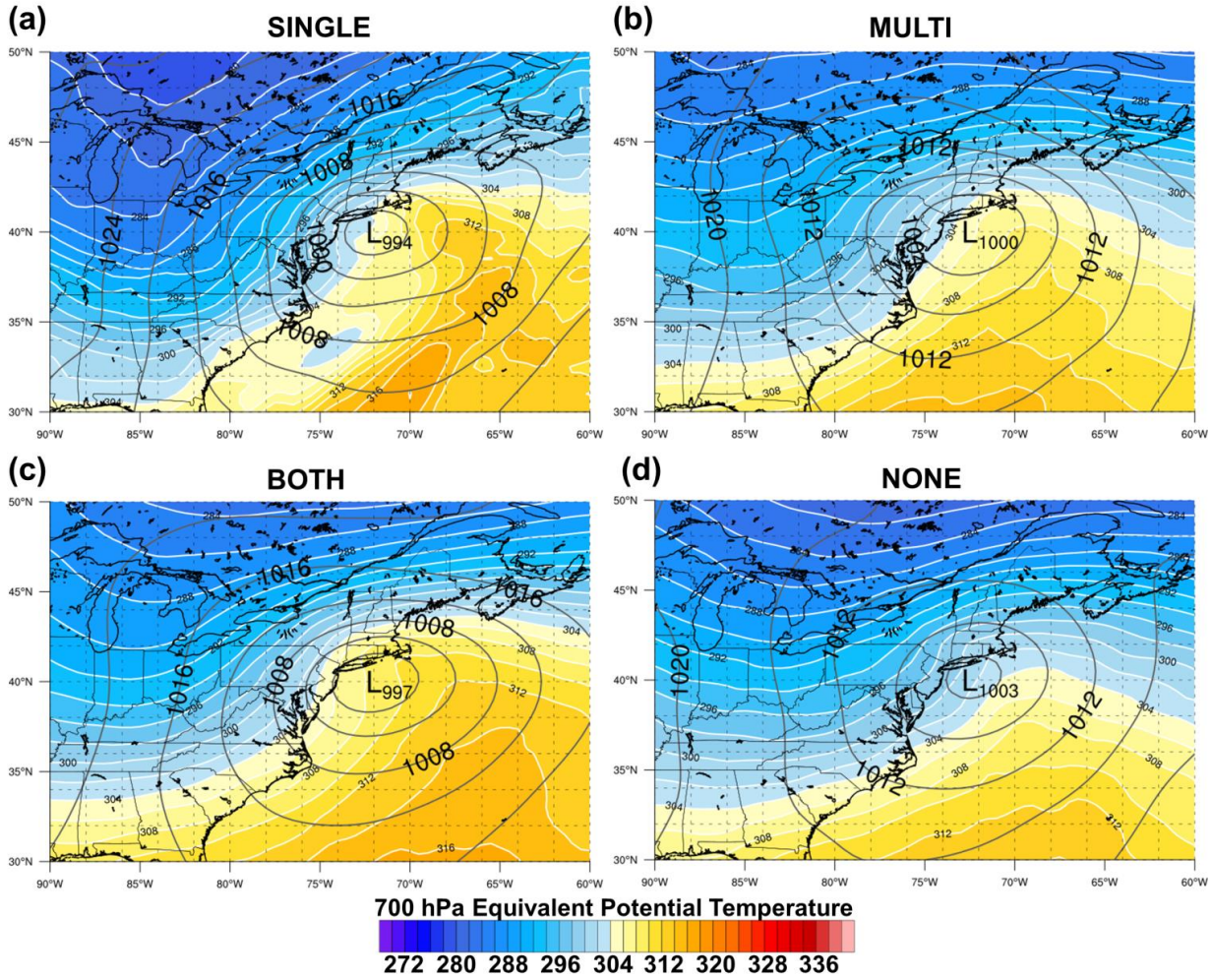

Figure 3.11. Composites of all (a) 5 SINGLE, (b) 35 MULTI, (c) 107 BOTH, and (d) 46 NONE events showing sea level pressure (contoured in black every 4 hPa) and 700 hPa equivalent potential temperature (shaded according to scale and contoured in white every 2 K).

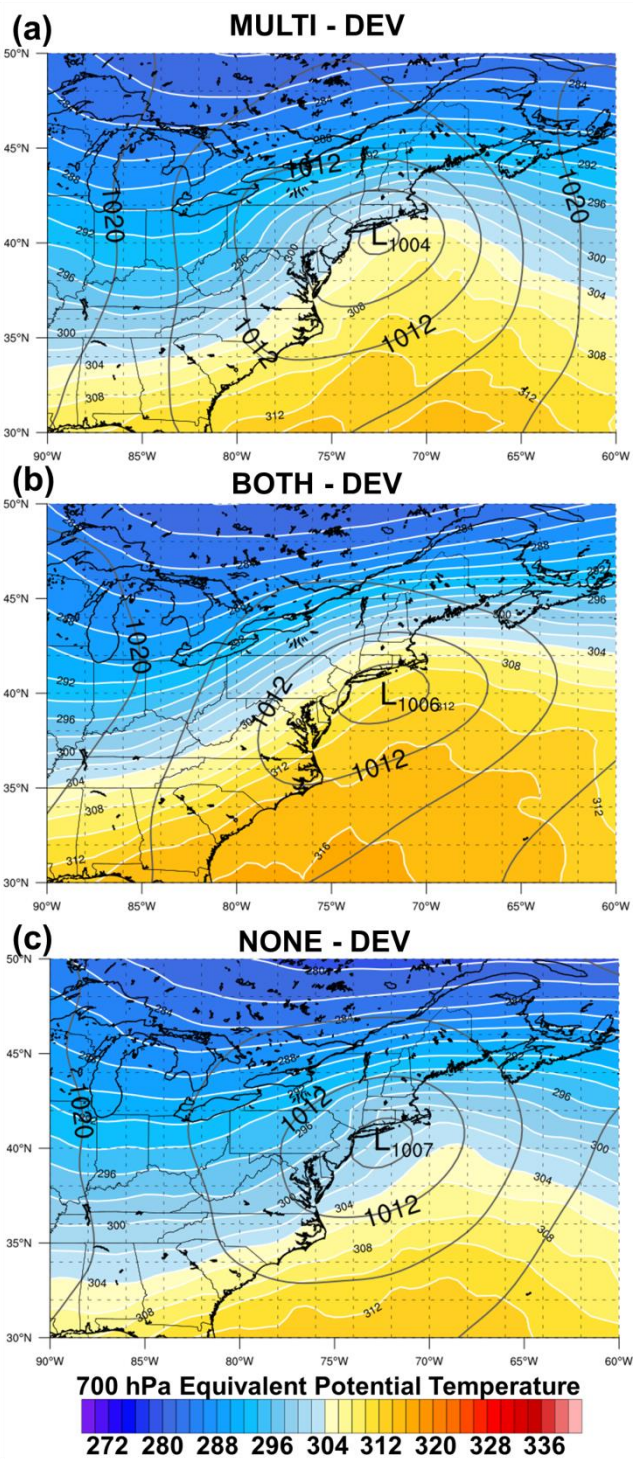

Figure 3.12. Composites of all (a) 18 MULTI, (b) 43 BOTH, (c) 29 NONE events associated with a developing cyclone (DEV) showing sea level pressure (contoured in black every 4 hPa) and 700 hPa equivalent potential temperature (shaded according to scale and contoured in white every 2 K).

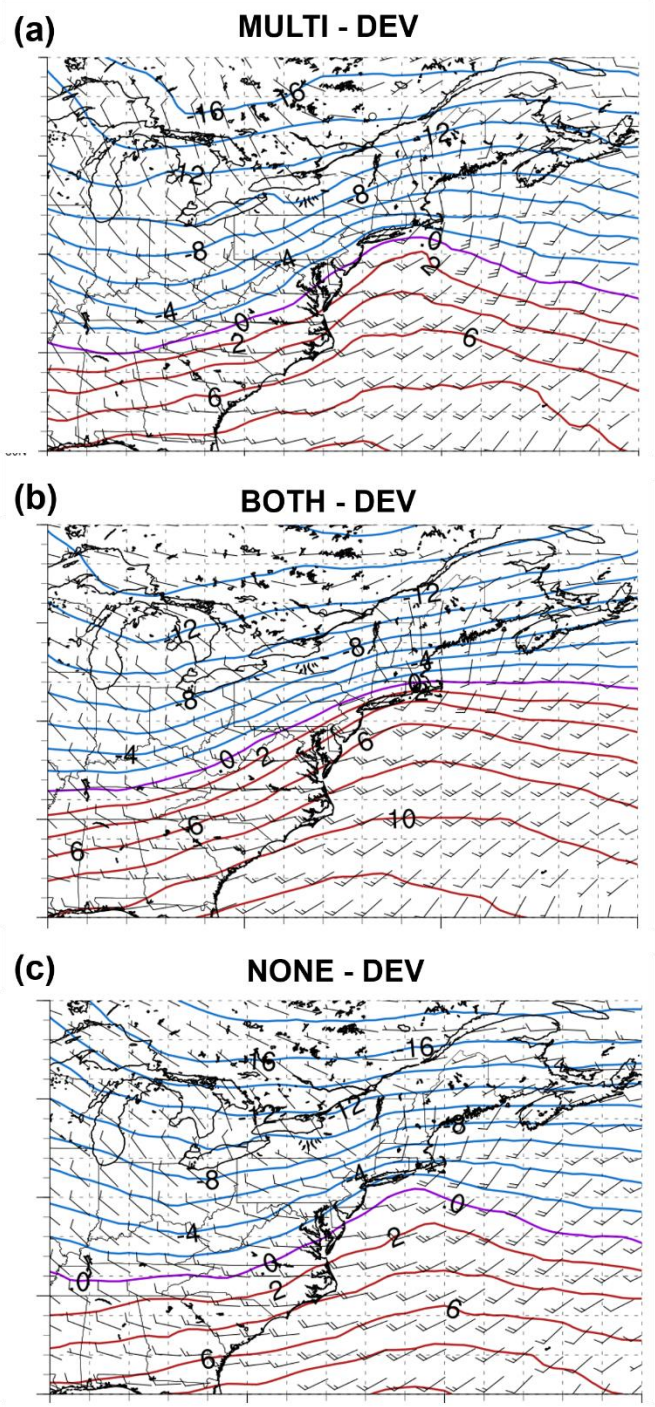

Figure 3.13. As in Figure 3.12 but for 850 hPa temperature (°C, contoured) and winds (kts, barbs).

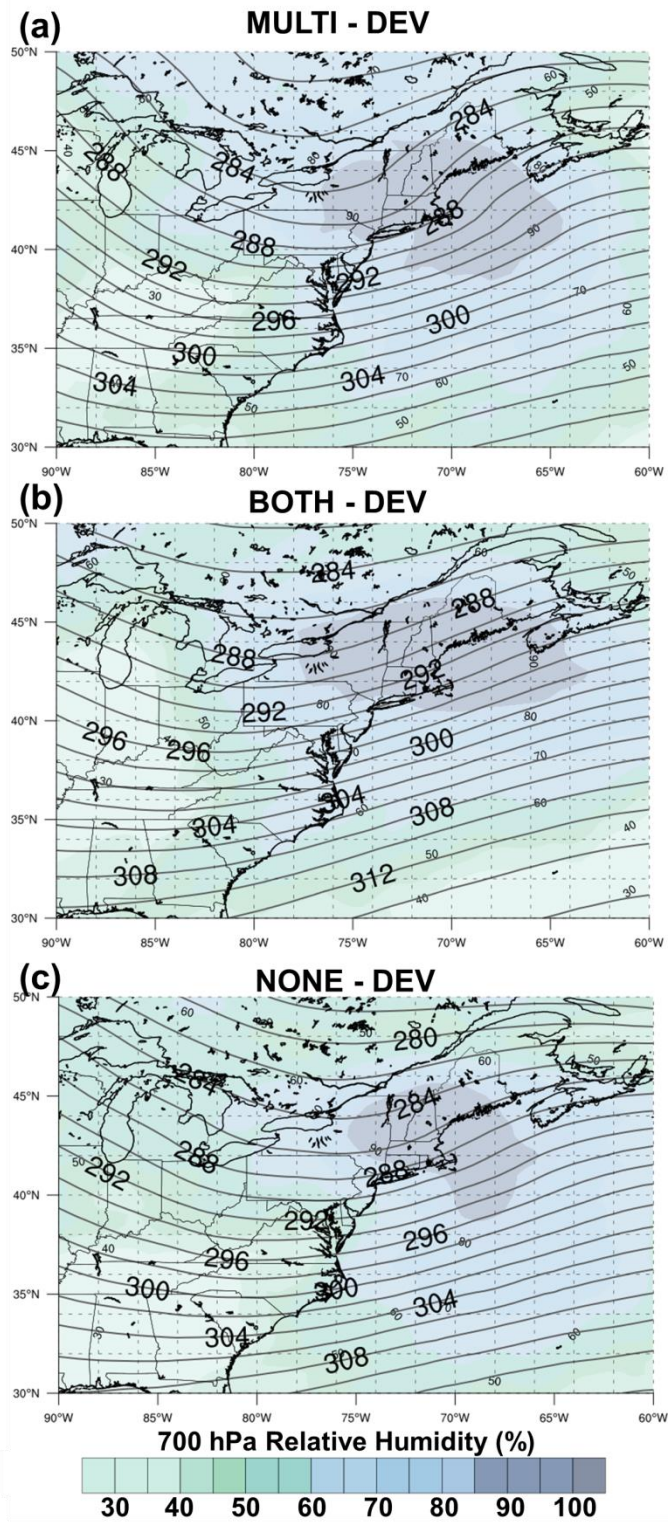

Figure 3.14. As in Figure 3.12 but for composites of 700-hPa geopotential height (contoured every 4 dam) and 700-hPa relative humidity (shaded according to scale every 5%).

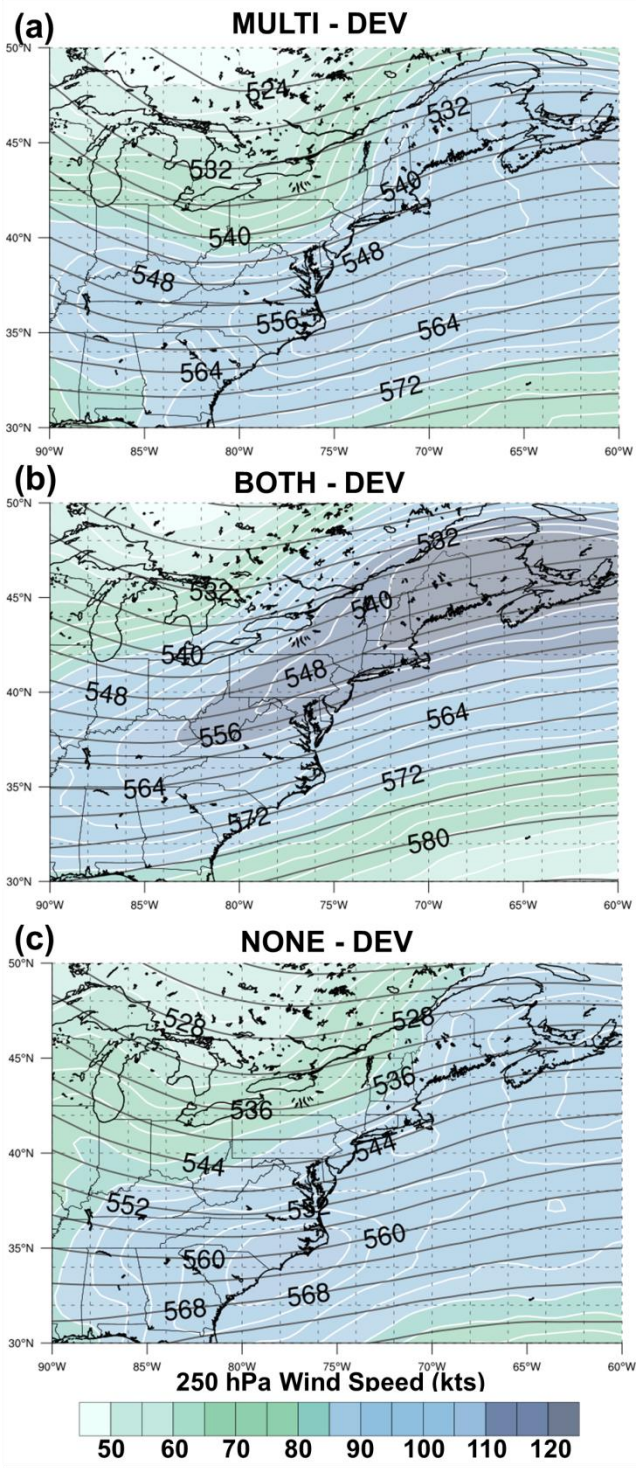

Figure 3.15. As in Figure 3.12 but for composites of 500-hPa geopotential height (contoured every 4 dam) and 250-hPa wind speed (shaded according to scale every 5 kts).

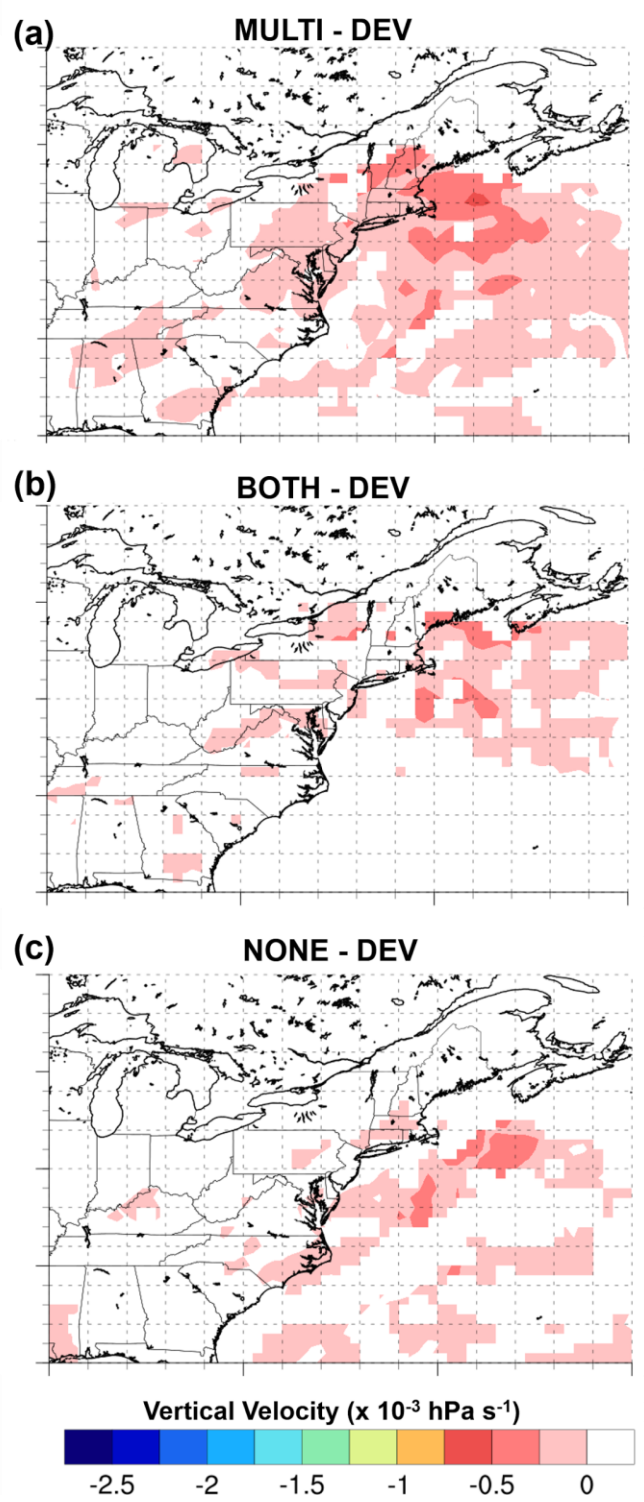

Figure 3.16. As in Figure 3.12 but for composites of vertical velocity (shaded according to scale every 0.5 x 10^{-3} hPa s^{-1}).

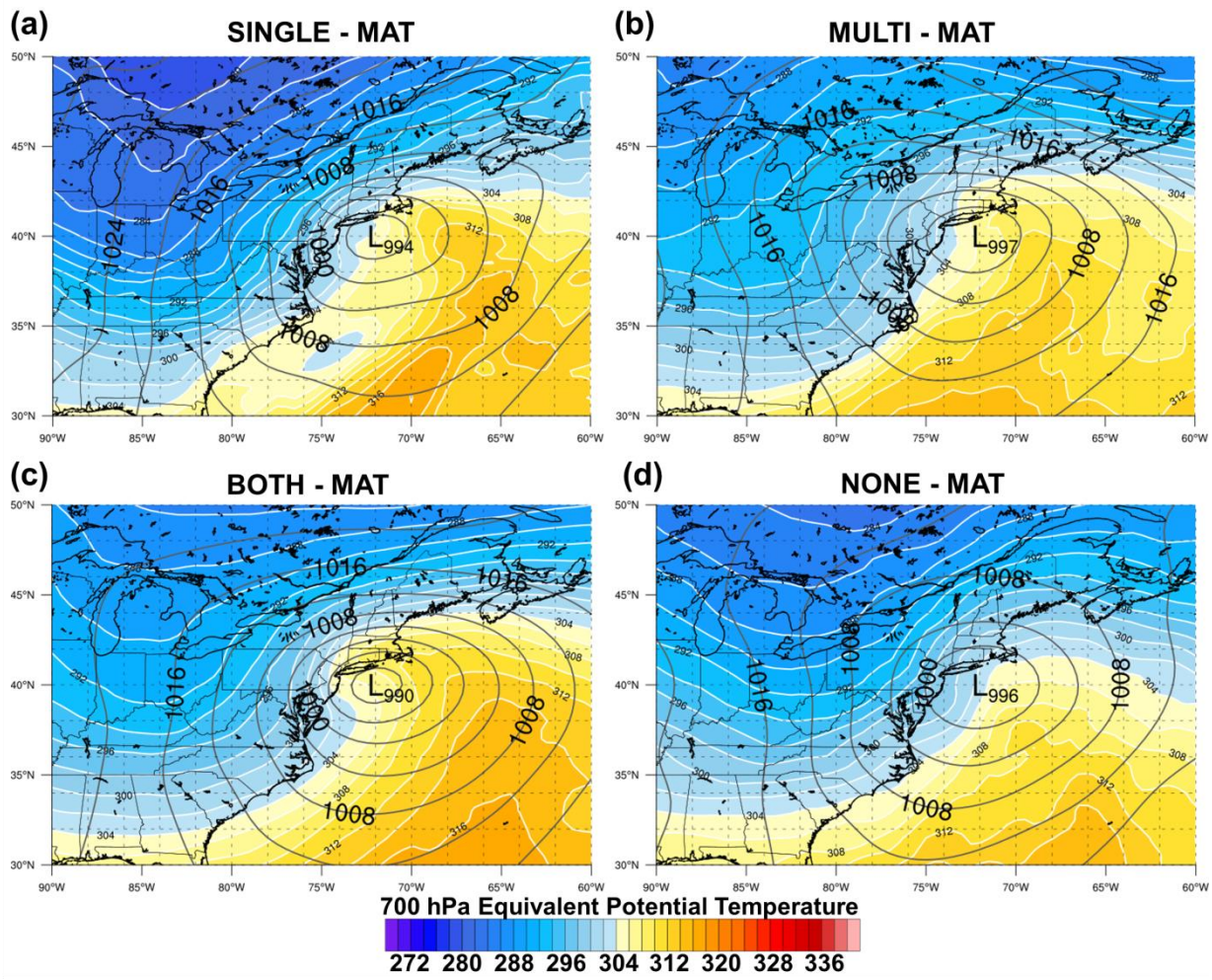

Figure 3.17. As in Figure 3.12 but for (a) 5 SINGLE, (b) 17 MULTI, (c) 64 BOTH, and (d) 17 NONE events associated with MAT cyclones.

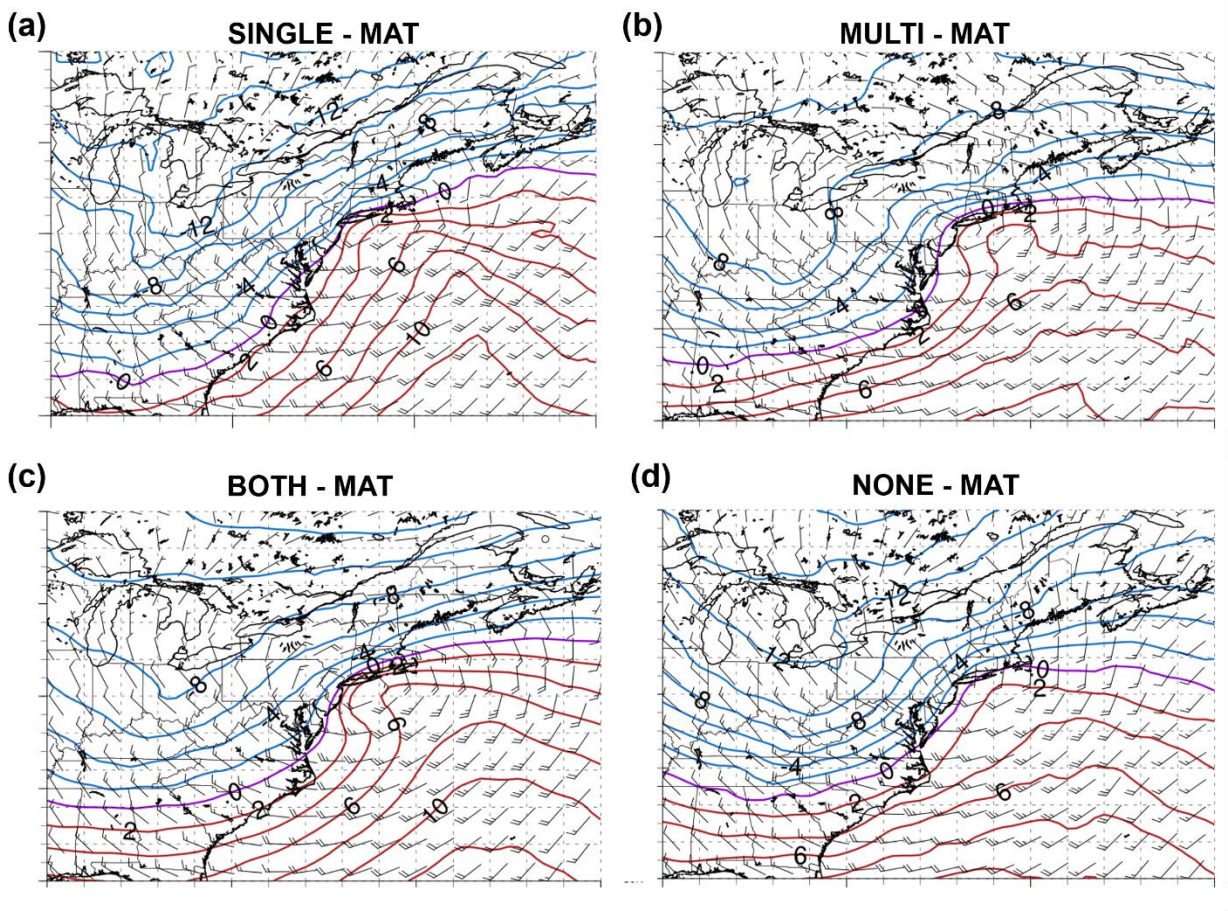

Figure 3.18. As in Figure 3.13 but for 850 hPa temperature (°C, contoured) and winds (kts, barbs).

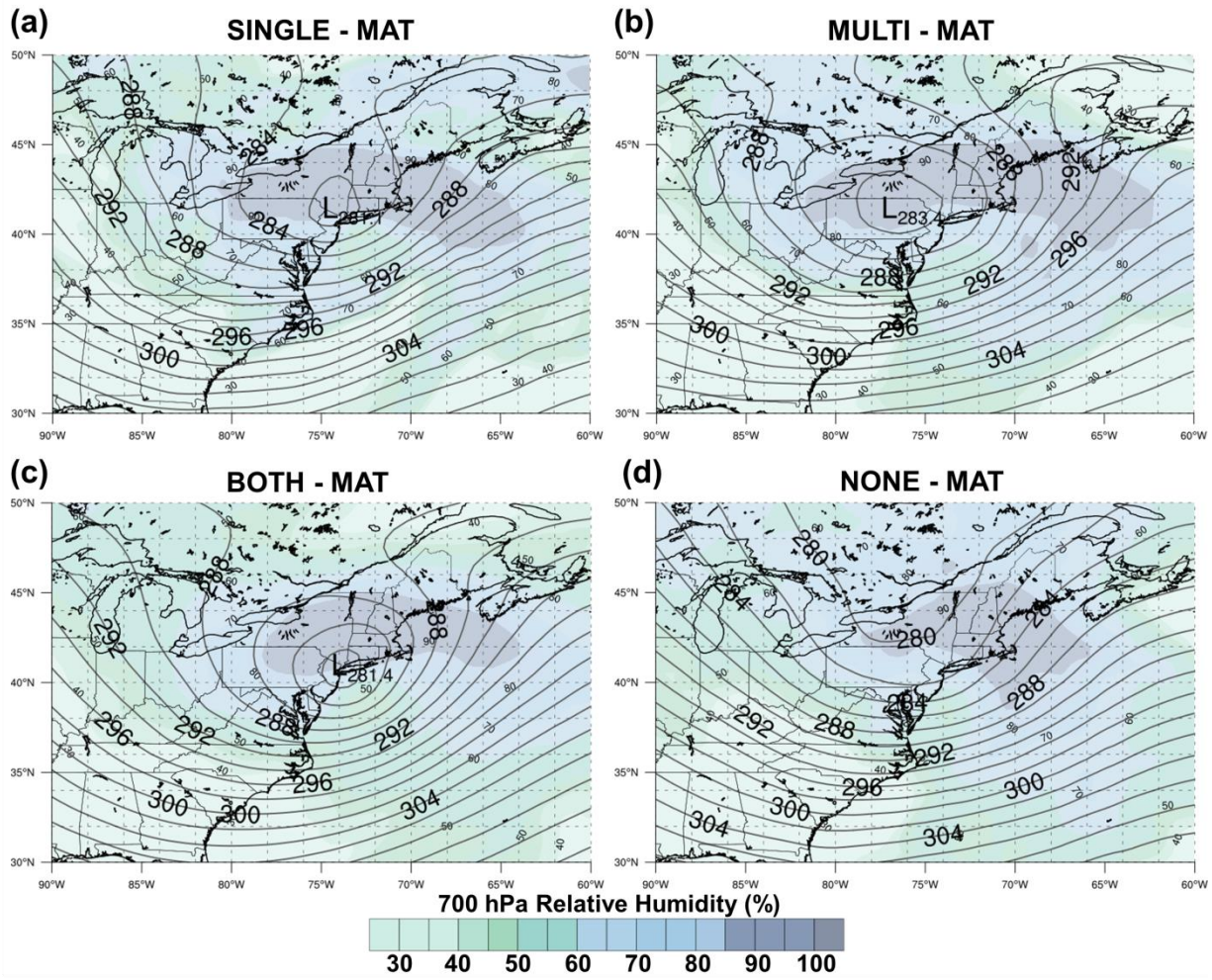

Figure 3.19. As in Figure 3.17 but for composites of 700-hPa geopotential height (contoured every 4 dam) and 700-hPa relative humidity (shaded according to scale every 5%).

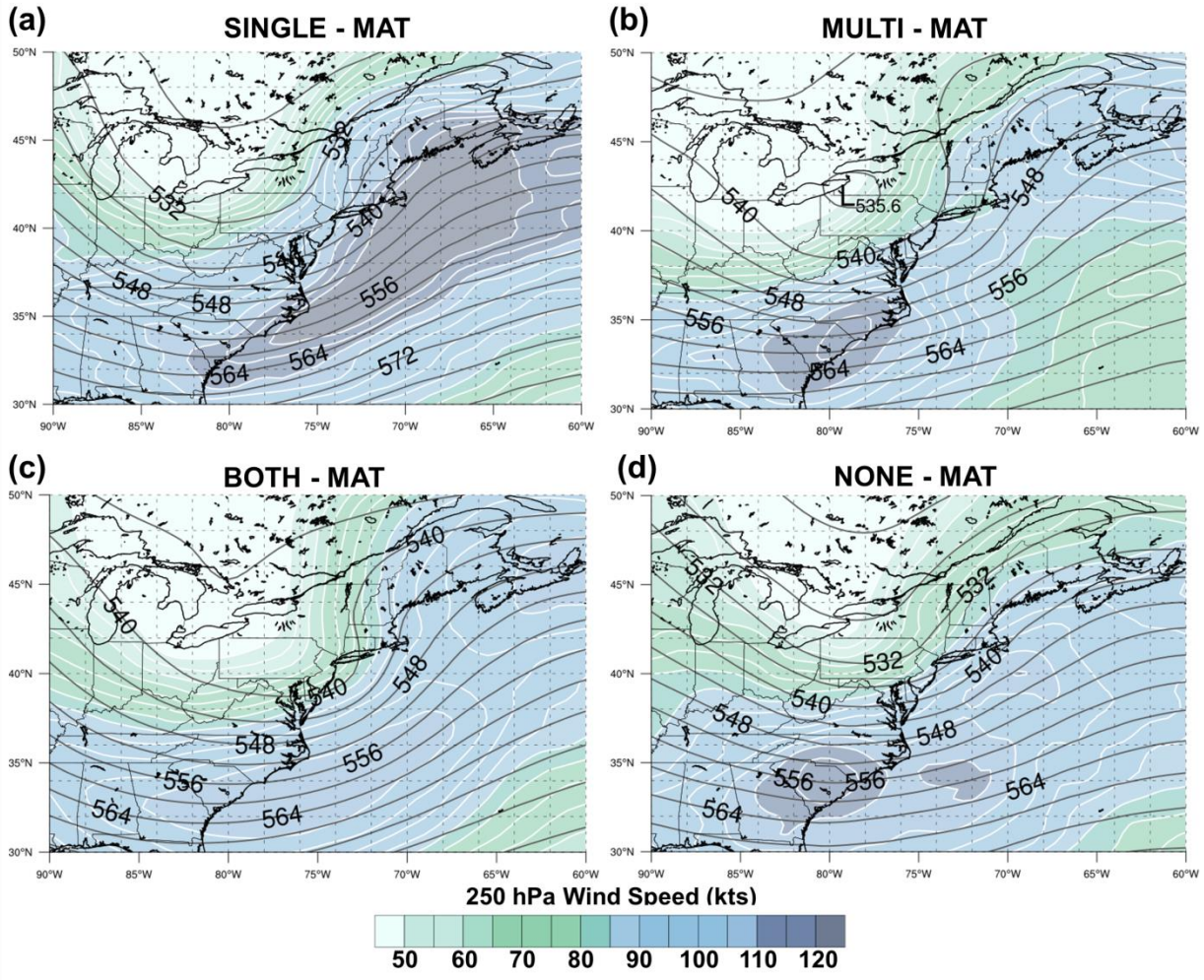

Figure 3.20. As in Figure 3.17 but for composites of 500-hPa geopotential height (contoured every 4 dam) and 250-hPa wind speed (shaded according to scale every 5 kts).

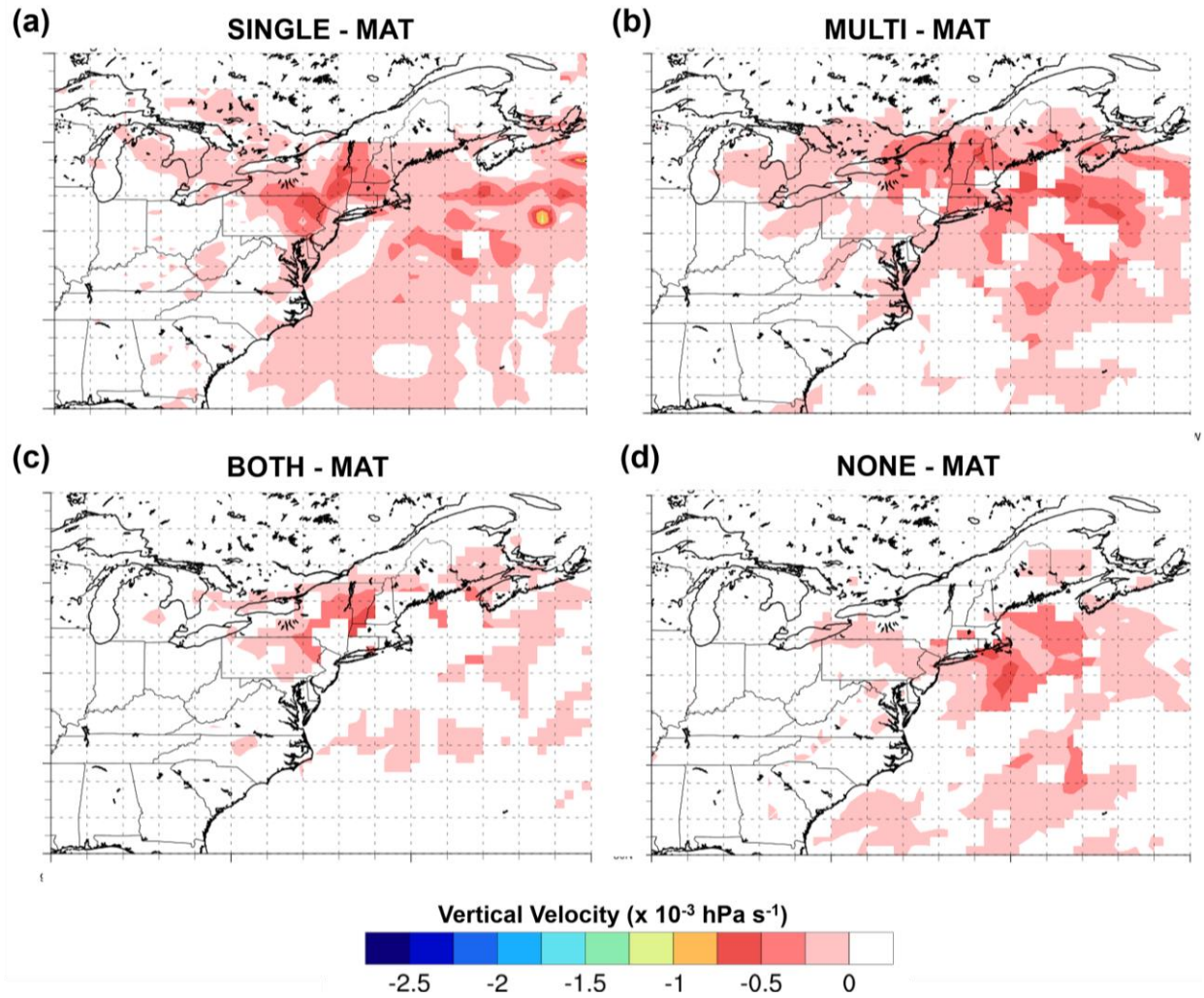

Figure 3.21. As in Figure 3.13 but for composites of vertical velocity (shaded according to scale every 0.5 x 10^{-3} hPa s^{-1}).

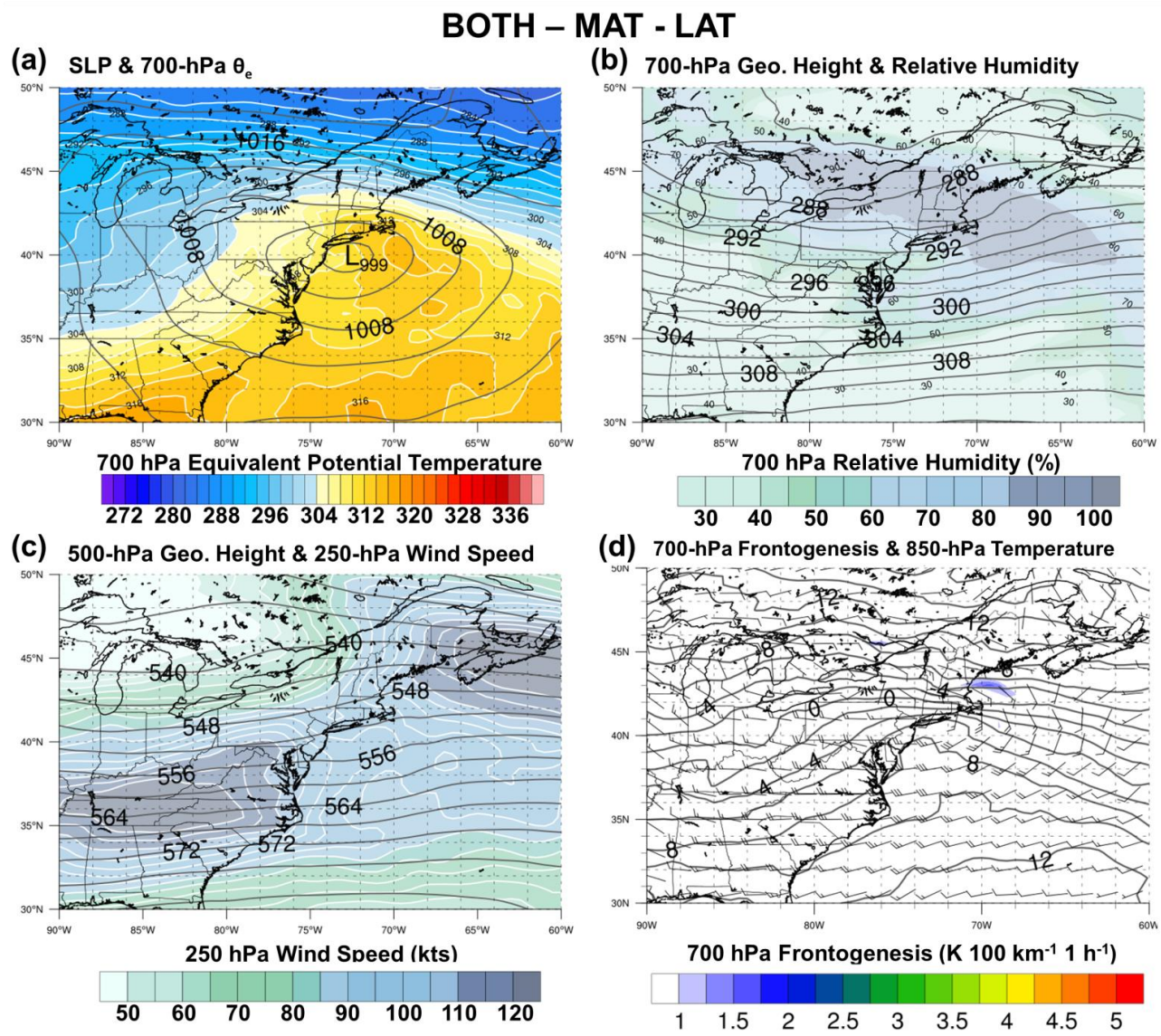

Figure 3.22. Composites for 6 LAT motion BOTH events associated with mature cyclones of (a) SLP (hPa, black contours) and 700-hPa θ_e (K, shaded), (b) 700-hPa geopotential height (dam, black contours) and 700-hPa relative humidity (%, shaded), (c) 500-hPa geopotential height (dam, black contours) and 250-hPa wind speed (kts, shaded), and (d) 850-hPa temperature (°C, black contours) and 700-hPa frontogenesis (K 100 km^{-1} 1 h^{-1}, shaded).

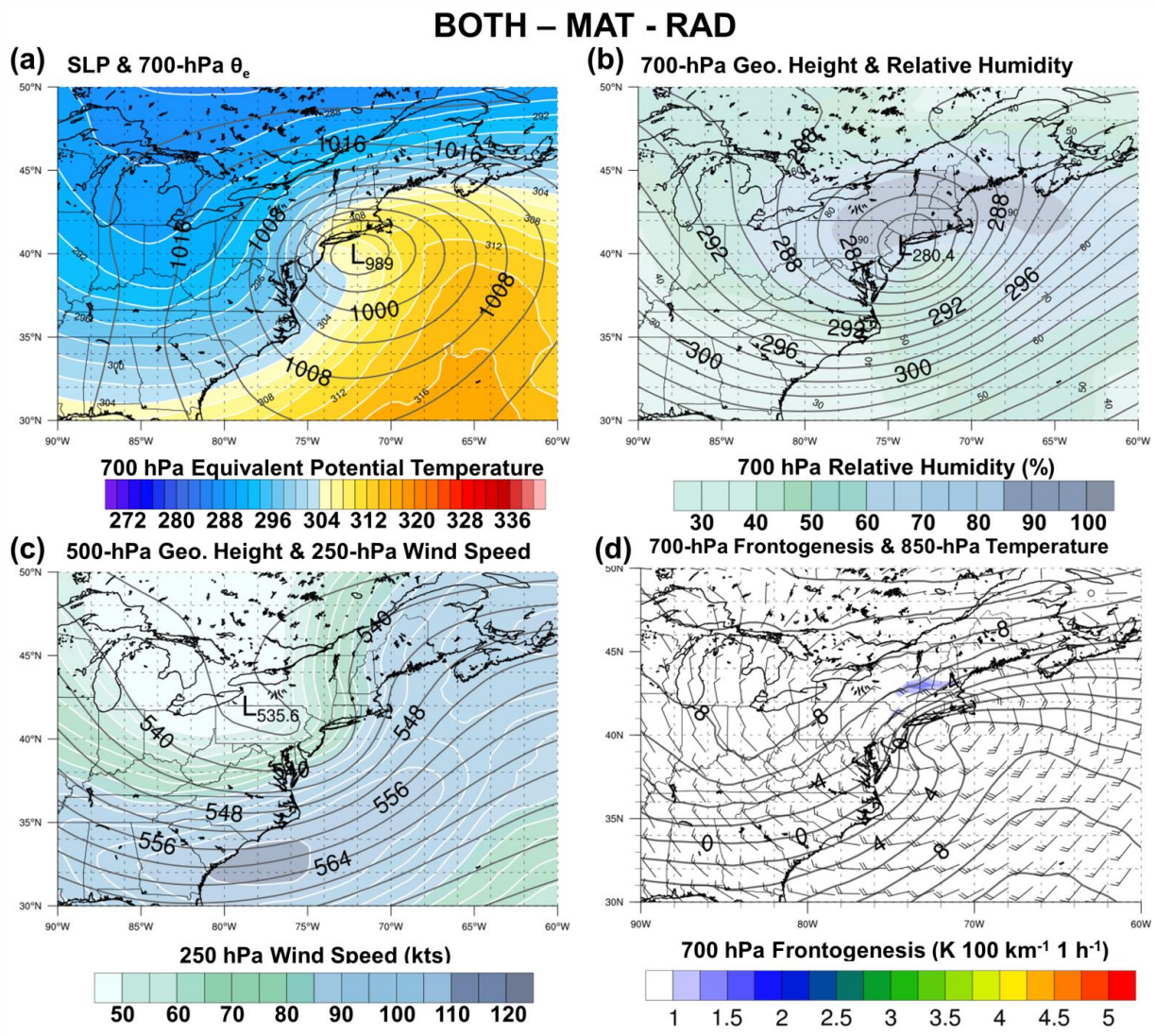

Figure 3.23. As in Figure 3.22 but for 58 RAD motion BOTH events.

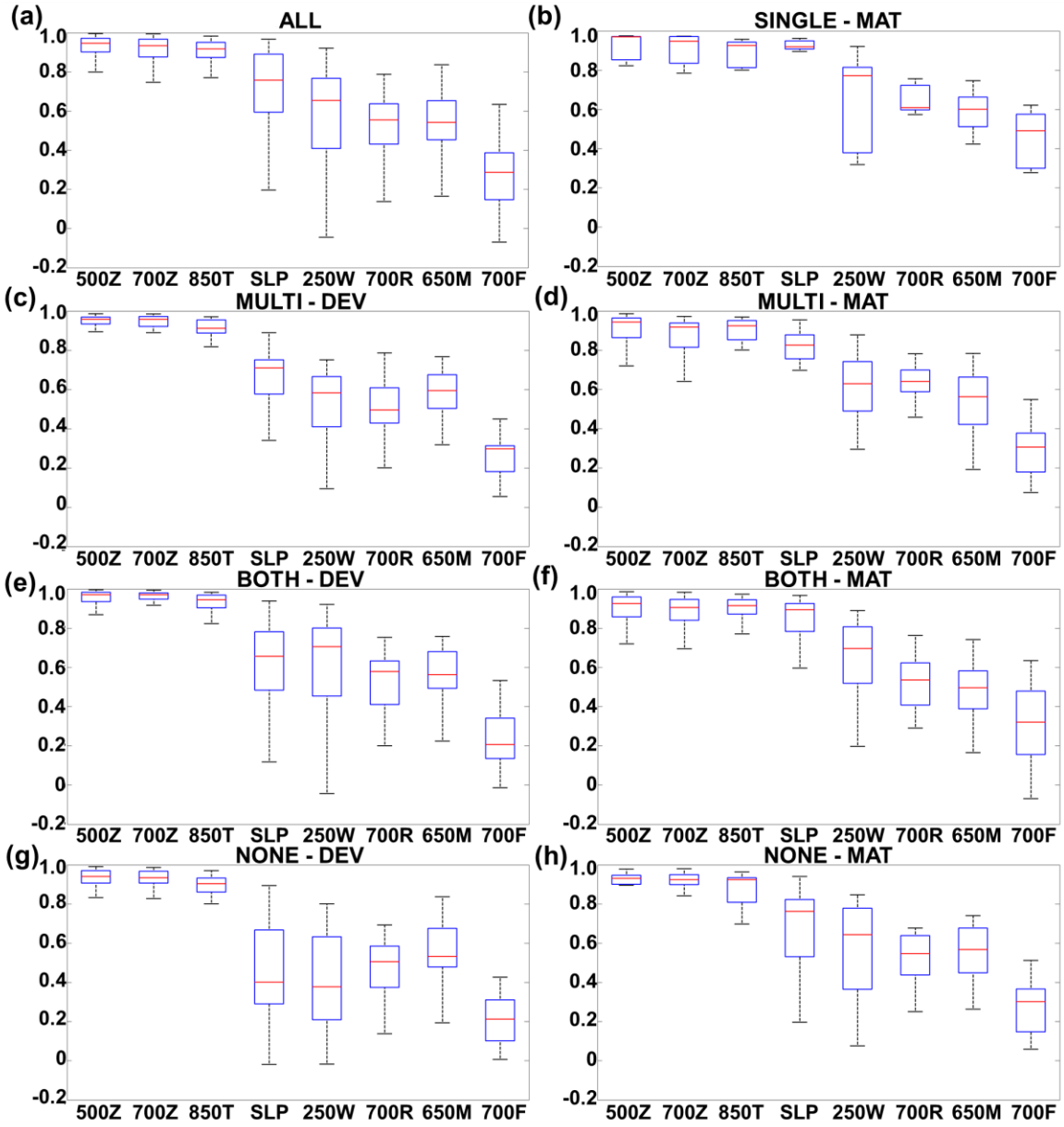

Figure 3.24. Box-and-whisker plots of linear spatial correlations (along the ordinate axis) as calculated from Equation 3.4 for 500-hPa geopotential height ("500Z"), 700-hPa geopotential height ("700Z"), 850-hPa temperature ("850T"), mean sea level pressure ("SLP"), 250-hPa wind speed ("250W"), 700-hPa relative humidity ("700R"), 650-hPa saturation equivalent potential vorticity ("650M"), and 700-hPa frontogenesis ("700F") for (a) all 193 events, (b) SINGLE events from mature cyclones, (c) MULTI events from developing cyclones, (d) MULTI events from mature cyclones, (e) BOTH events from developing cyclones, (f) BOTH events from mature cyclones, (g) NONE events from developing cyclones, (h) NONE events from mature cyclones. The horizontal line within each box represents the 50th percentile (median), the top (bottom) line of the box is the 75th (25th) percentile, and the top (bottom) line outside the box is the 90th (10th) percentile.

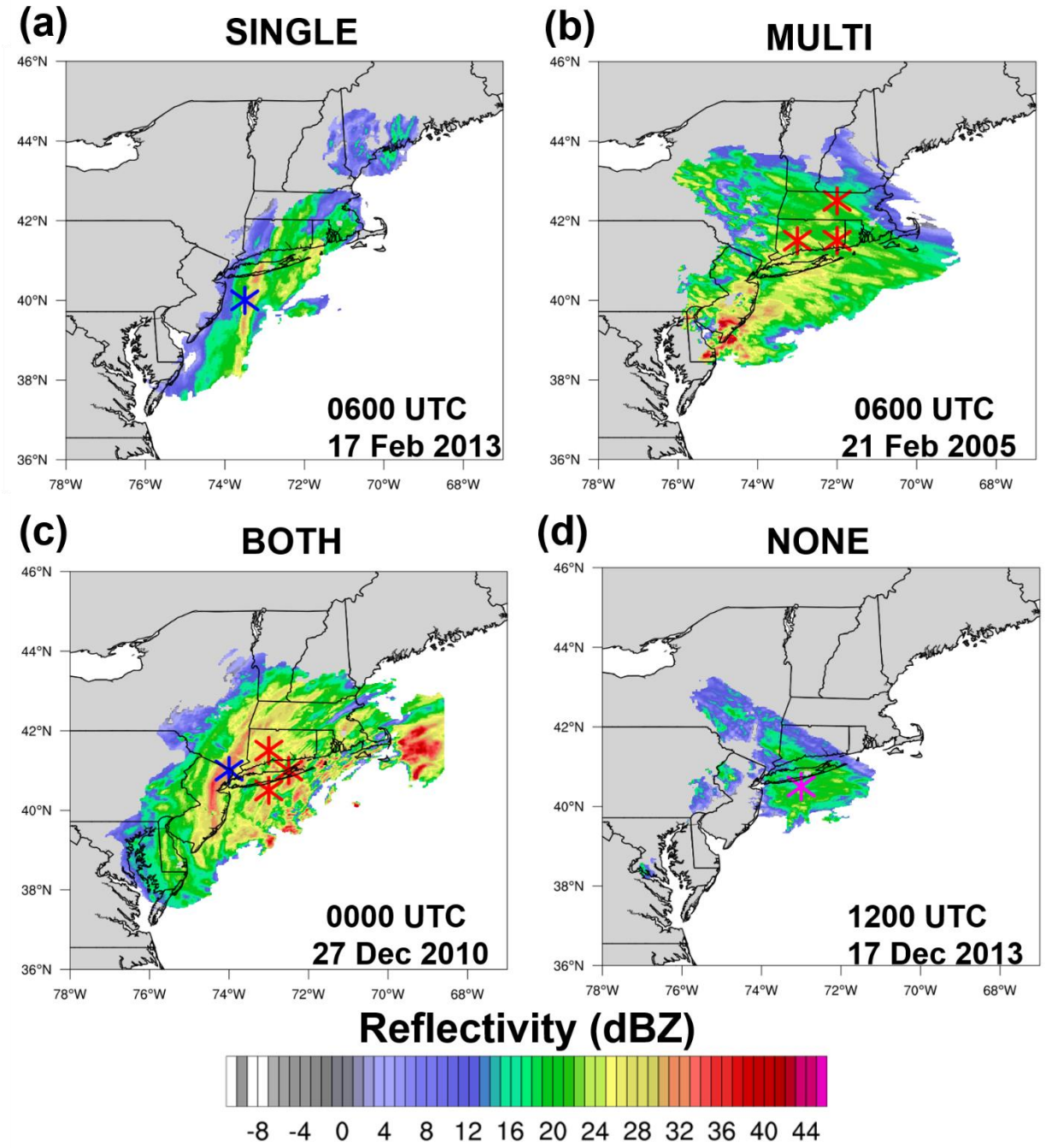

Figure 3.25. Example radar reflectivity times for each of the four classifications with markers showing the location of vertical profiles through individual (blue) primary bands, (red) multi-bands, and (purple) non-banded precipitation for a (a) SINGLE event of 0600 UTC 17 Feb 2013, (b) MULTI event of 0600 UTC 21 Feb 2005, (c) BOTH event of 0000 UTC 27 Dec 2010, and (d) NONE event of 1200 UTC 17 Dec 2013.

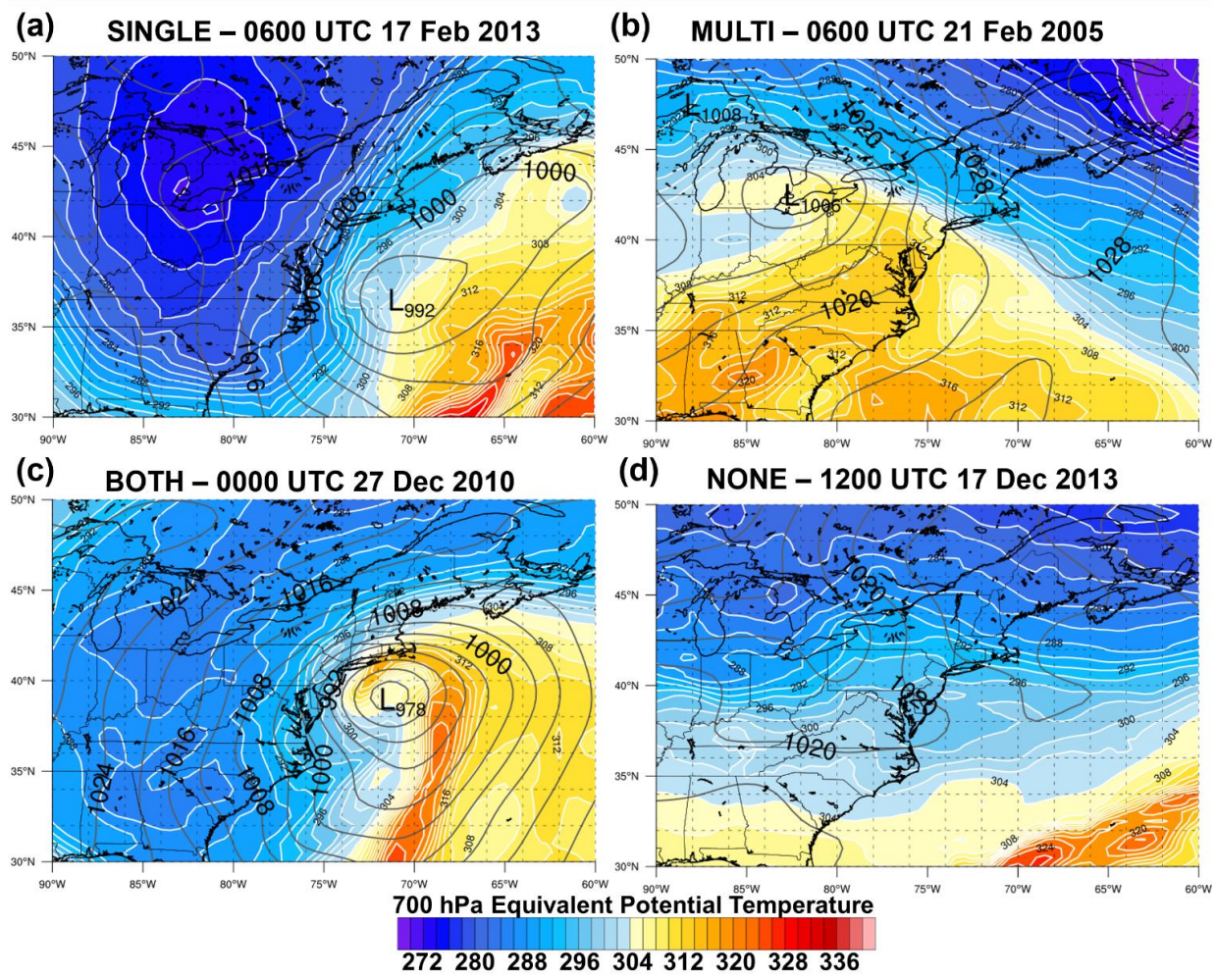

Figure 3.26. Individual event maps of sea level pressure (contoured in black every 4 hPa) and 700 hPa equivalent potential temperature (shaded according to scale and contoured in white every 2 K) for a (a) SINGLE, (b) MULTI, (c) BOTH, and (d) NONE event.

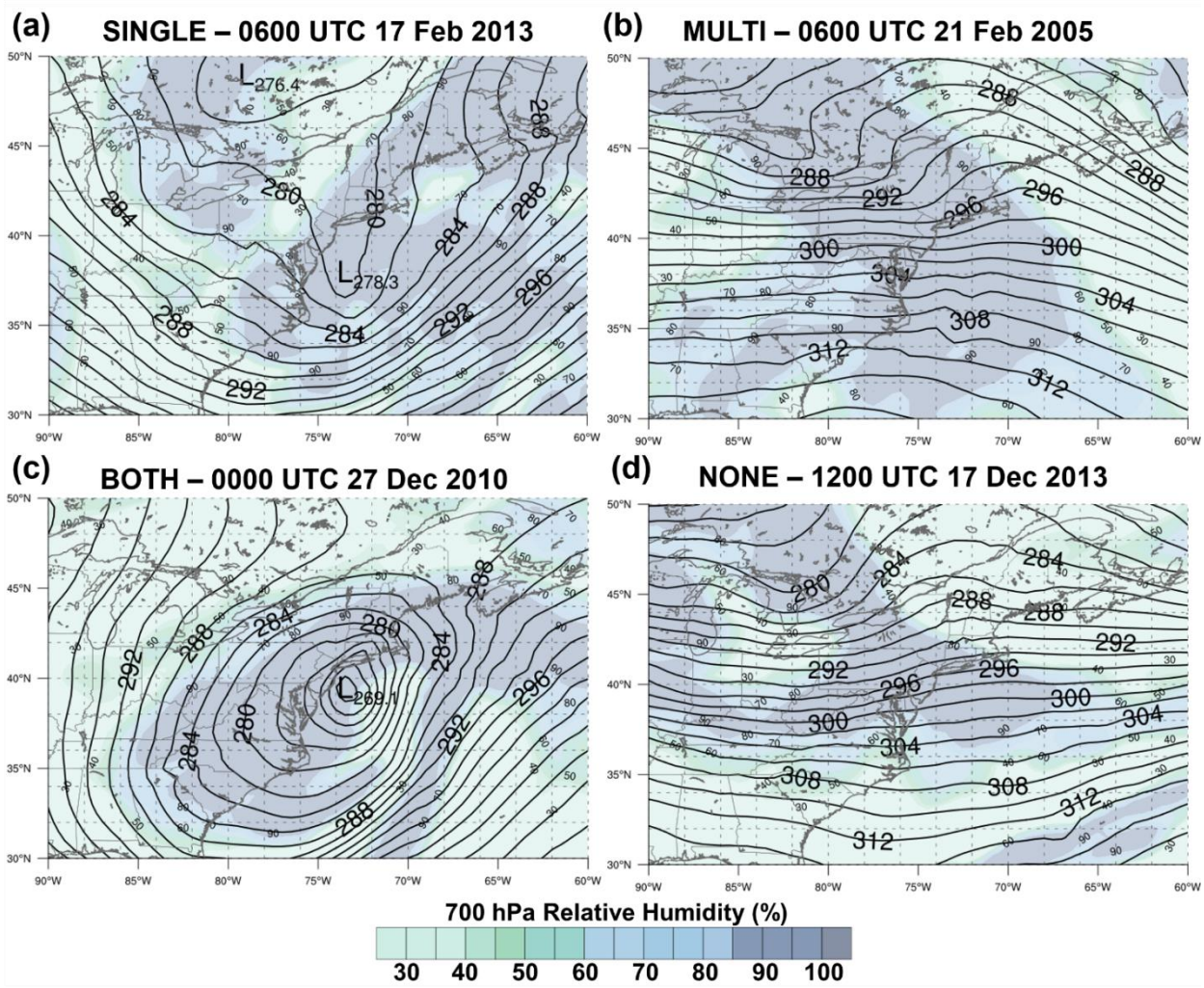

Figure 3.27. As in Figure 3.26 but for 700-hPa geopotential height (contoured every 4 dam) and 700-hPa relative humidity (shaded according to scale every 5%).

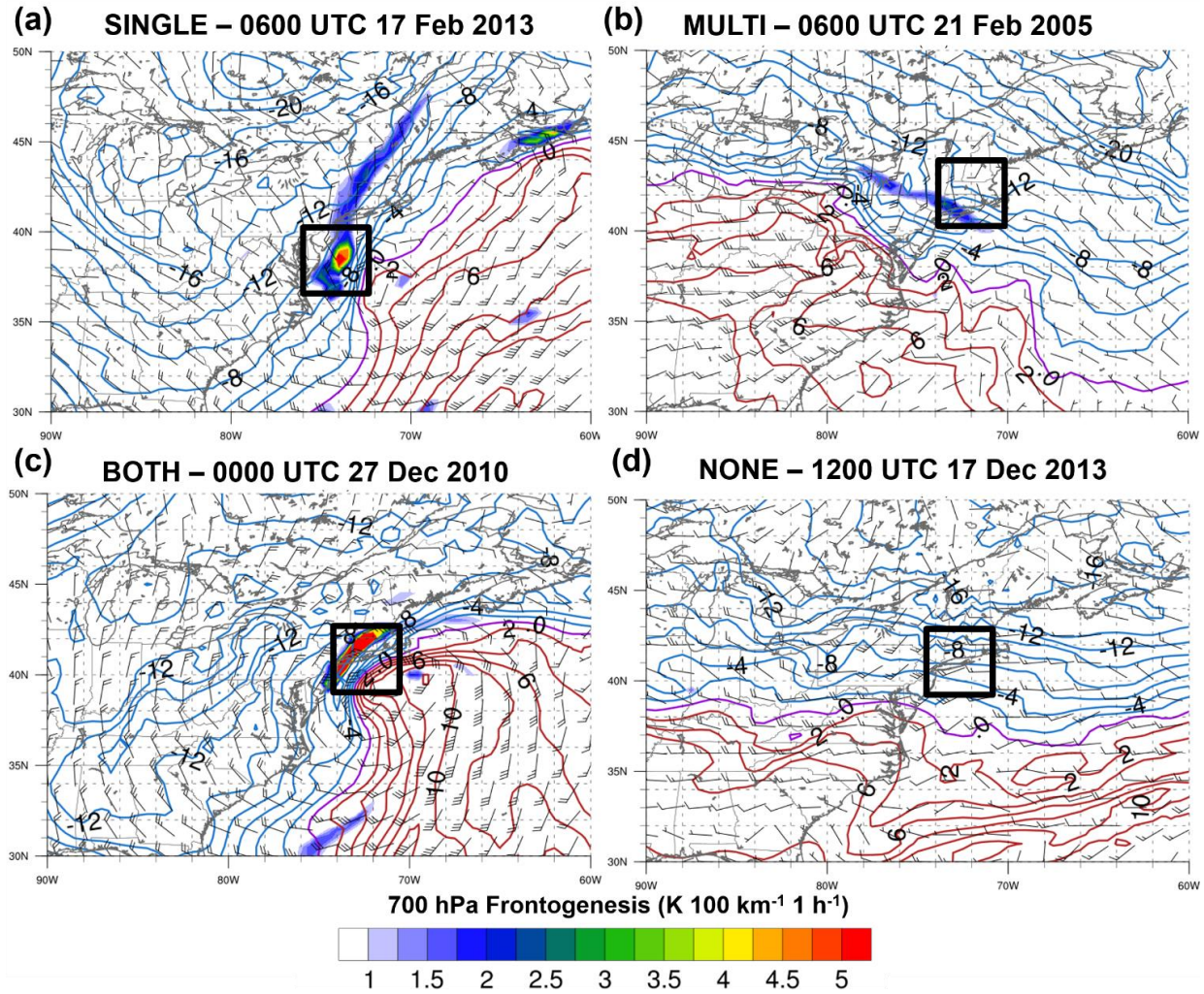

Figure 3.28. As in Figure 3.26 but for 700-hPa frontogenesis (shaded, K 100 km^{-1} 1 h^{-1}), 850-hPa temperature (°C), and 850-hPa winds (barbed). The black boxes indicate the banded or non-banded precipitation region.

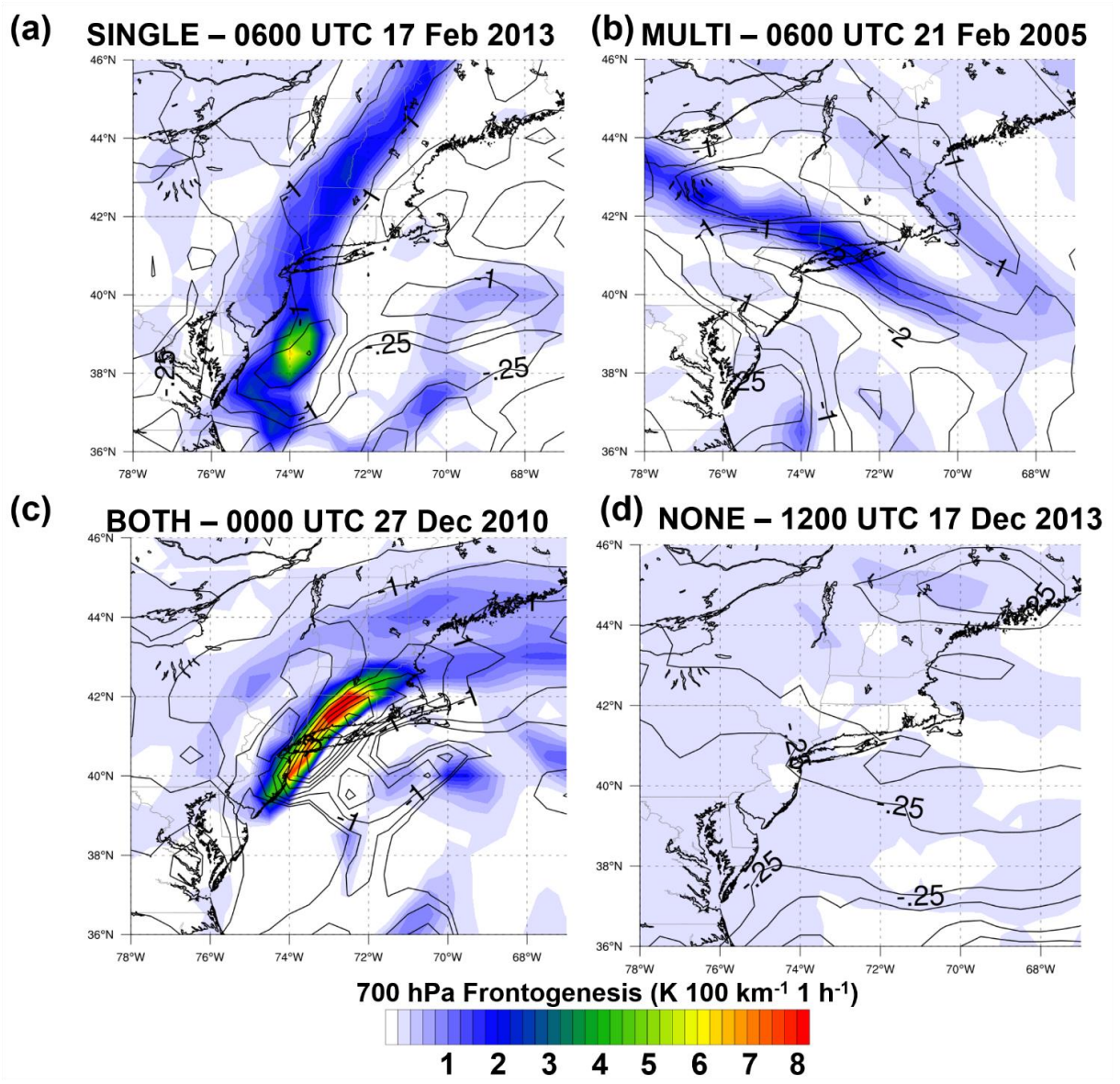

Figure 3.29. As in Figure 3.26 but for 700-hPa frontogenesis (shaded, K 100 km^{-1} 1 h^{-1}) and 700-600-hPa average saturation equivalent potential vorticity (PVU, negative values only contoured every 0.25).

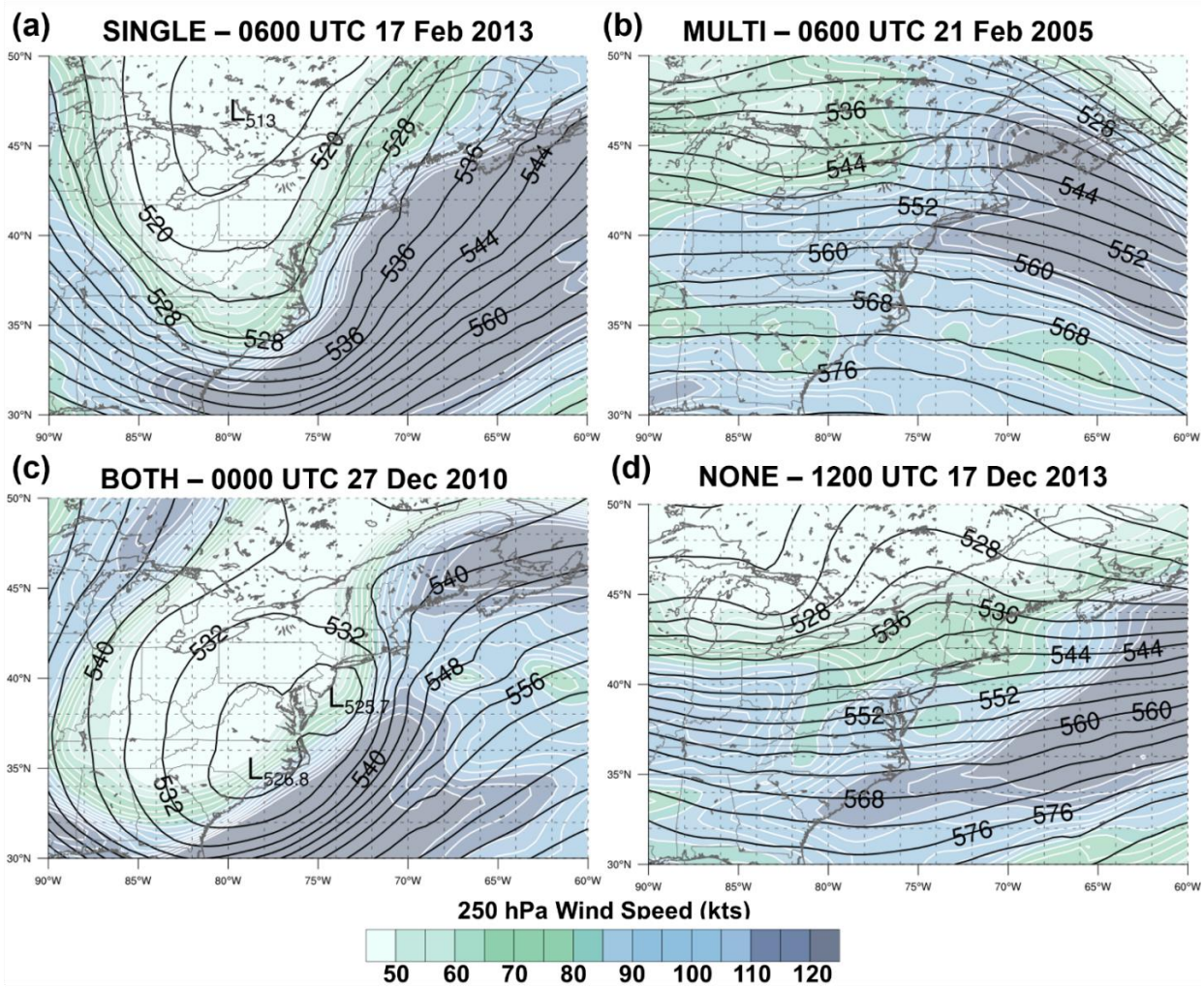

Figure 3.30. As in Figure 3.26 but for 500-hPa geopotential height (contoured every 4 dam) and 250-hPa wind speed (shaded according to scale every 5 kts).

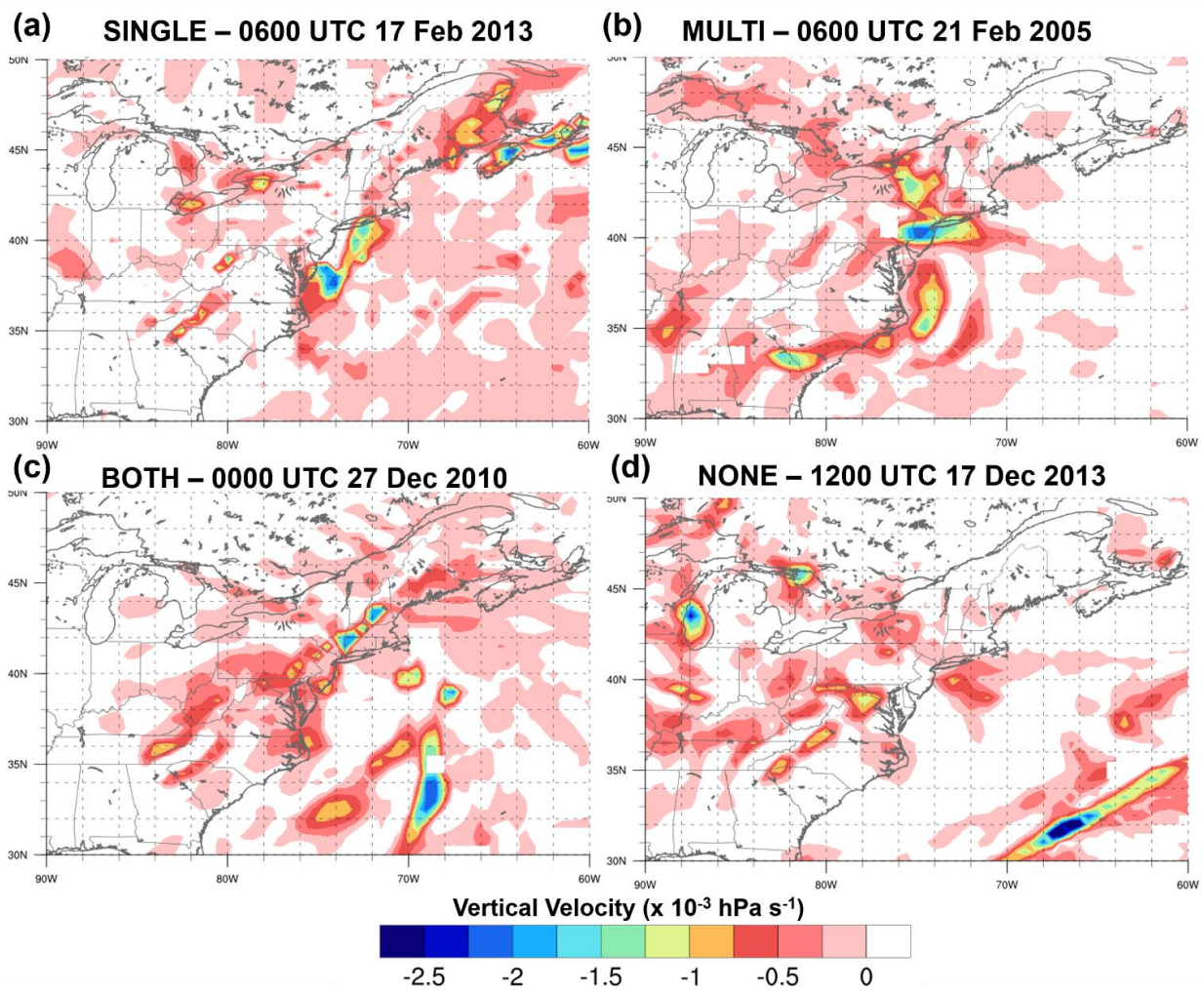

Figure 3.31. As in Figure 3.26 but for vertical velocity (shaded according to scale every 0.5 x 10^{-3} hPa s^{-1}).

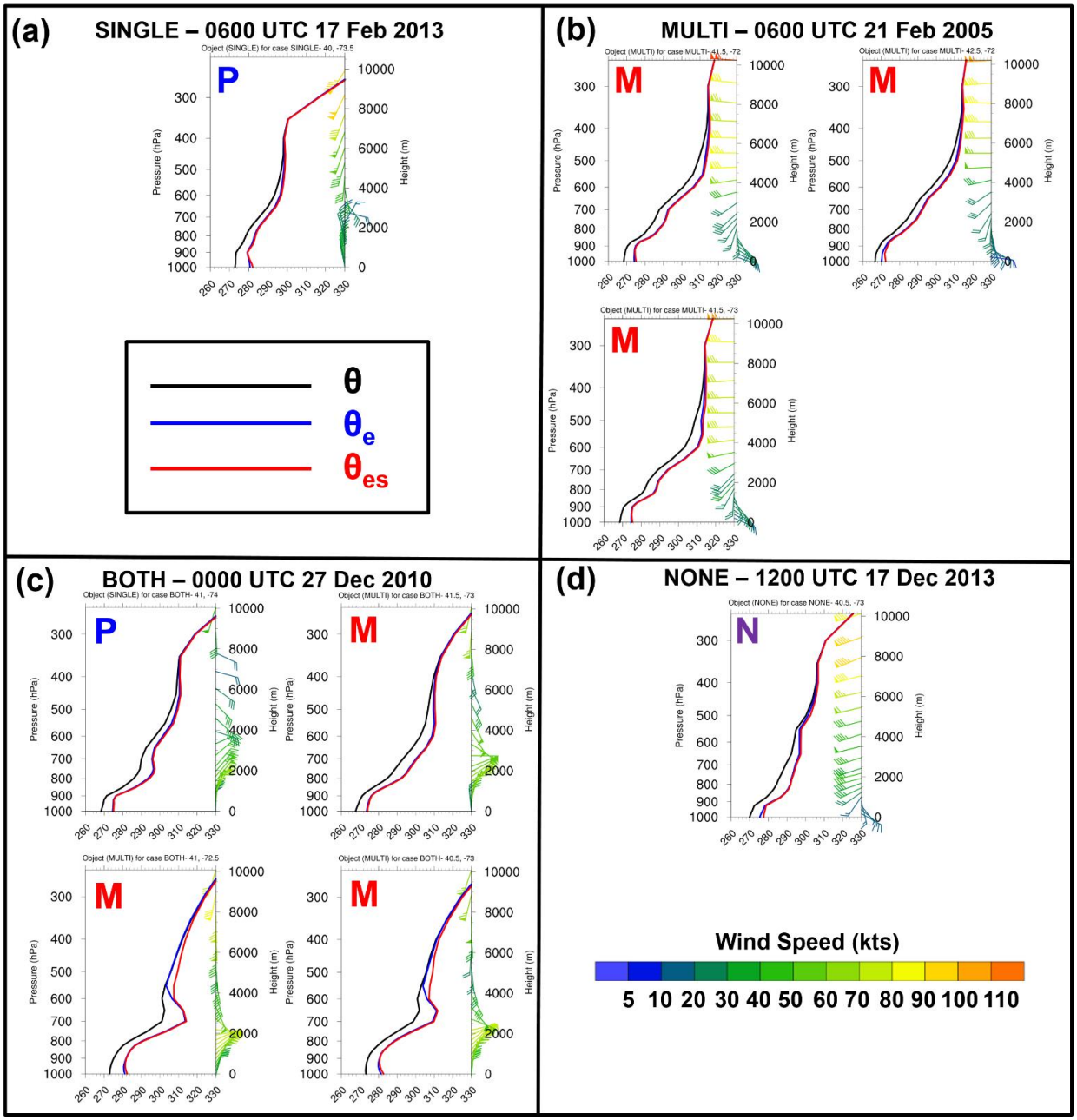

Figure 3.32. Profiles from the markers shown in Figure 3.25 of potential temperature (K, black line), equivalent potential temperature (K, blue line), saturation equivalent potential temperature (K, red line) and wind speed and direction (kts, barbs shaded according to scale). For multiple profiles per event, the "P" refers to a primary band, "M" to a multi-band and "N" to non-banded. The latitude and longitude are also provided of each profile.

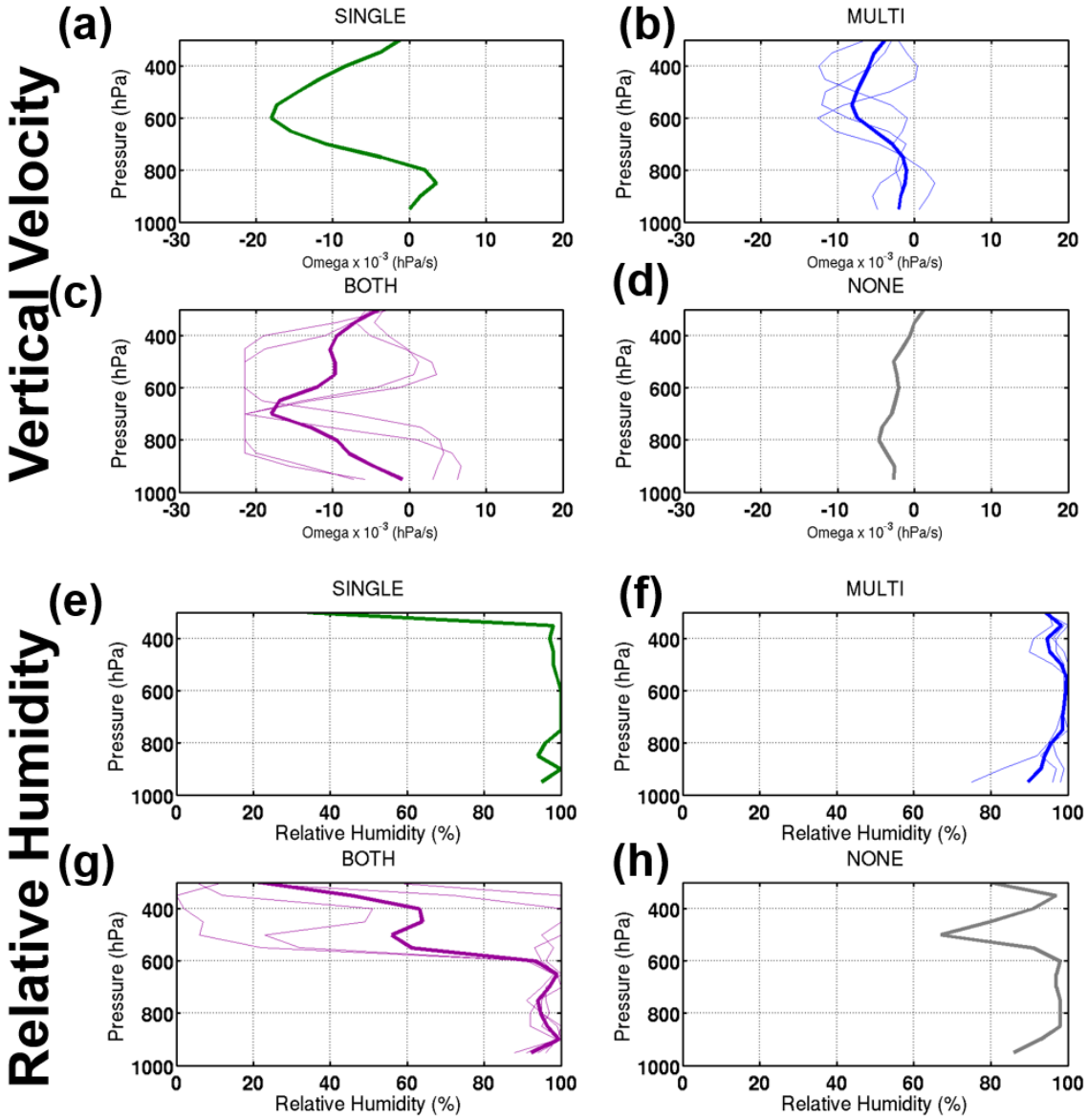

Figure 3.33. Vertical profiles from each example case of (a,e,i) SINGLE, (b,f,j) MULTI, (c,g,k) BOTH, and (d,h,l) NONE with the mean profile in bold for (a–d) vertical velocity (x 10^{-3} hPa s^{-1}), and (e–h) relative humidity (%).

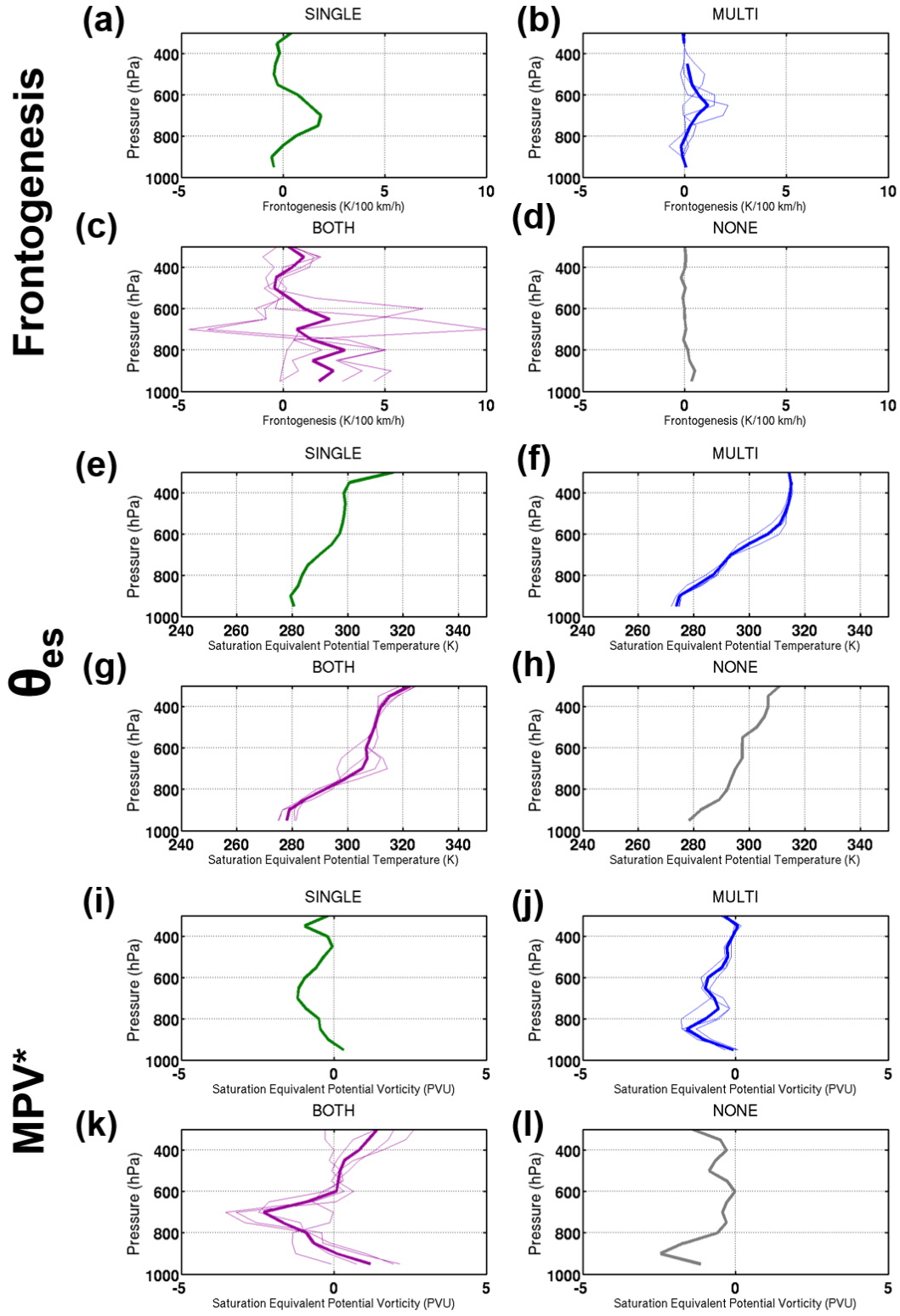

Figure 3.34. As in Figure 3.33 but for (a–d) frontogenesis (K 100 km^{-1} h^{-1}), (e–h) saturation equivalent potential temperature (K), (i–l) saturation equivalent potential vorticity (PVU).

Chapter 4:

The Thermodynamic and Microphysical Evolution of an Intense Snowband during the Northeast U.S. Blizzard of 8–9 February 2013

4.1 Introduction

An extratropical cyclone on 8–9 February 2013 produced 0.3–0.6 m (1–2 ft) of snow across New York City and Long Island and over 0.9 m (3 ft) of snow in central Connecticut (Fig. 4.1a). Hurricane-force winds occurred along the coast from Massachusetts to Maine, including an observed gust of 34 m s^{-1} at Boston Logan International Airport. After the storm, a federal state of emergency was declared for Connecticut and a federal disaster declaration was issued for Connecticut and Long Island. Much of the heavy snow fell within a mesoscale snowband within the comma head of the cyclone with 7.5–10 cm h^{-1} (3–4 in h^{-1}) snow rates reported within the band and radar reflectivities exceeding 55 dBZ (Picca et al. 2014).

Over the Northeast United States there are mesoscale snowbands within the comma head of ~85% of extratropical cyclones during the winter months (Novak et al. 2004). Well-defined primary bands have been identified as forming north of the surface cyclone center in the region of enhanced midlevel (~700 hPa) frontogenesis and reduced stability (Novak et al. 2004, 2010). For single band formation, Novak et al. (2010) found that development occurred along the northern edge of an upper-level potential vorticity (PV) hook, where there are likely either weakly stable or conditionally unstable conditions.

Theoretical and modeling studies have shown that latent heat release is important in the formation and evolution of banded precipitation. Latent heat release on the warm side of a frontal boundary acts to concentrate vertical circulations into a narrow updraft or band (Emanuel 1985; Thorpe and Emanuel 1985). Novak et al. (2009) found that PV generation within the band from the latent heat release decreased mid-level heights northwest of the band and led to larger convergence, tightened the temperature gradient, and increased frontogenesis at this level. During band maturity, the stability gradually increased as conditional instability was released.

Band dissipation occurred when mid-level frontogenesis weakened when a new diabatic PV anomaly formed a few hundred kilometers to the east of the band, thus reducing the mid-level flow deformation over the original band.

Snowbands can exhibit rapid transitions in ice habit and degree of riming due to the magnitude of vertical motions within different thermal environments. Stark et al. (2013) examined the microphysical evolution (including snow crystal habit and degree of riming) of two snowbands crossing Long Island, NY using vertically-pointing radar data and surface observations. Their study highlighted the rapid ascent on the warm frontogenetical side of the band, resulting in light to moderate riming and dendritic ice growth, while on the cold side of the band there was less riming and fewer dendrites (more plates). Colle et al. (2014) examined snow characteristics and environments centered around 12 cyclones over three winter seasons for developing and mature East Coast cyclones. Within some of the bands, they found that the heaviest riming occurred closest to the cyclone center with convective cells aloft and strong vertical motions around 800 hPa. The recent field campaign over the Midwest U.S., the Profiling of Winter Storms (PLOWS; Market et al. 2012; Rauber et al. 2014), sampled 17 storms in the 2009-10 winter season and also found cells of vertical motion of 1–2 m s^{-1} aloft (Rosenow et al. 2014). Similarly, Kumjian et al. (2014) studied cloud-top generating cells in Colorado and found that the updrafts could maintain supercooled liquid water in the presence of ice crystals.

Picca et al. (2014) used base (0.5°) radar reflectivity and dual-polarization products from the WSR-88D radar at KOKX (cf. Fig. 4.1b) to document the rapid transitions between snow and sleet as the snowband on 8–9 February moved northward across Long Island. The relatively high (~55 dBZ) reflectivity values around the time of the maximum intensity were attributed to large hydrometeors that likely formed through wet-growth processes within strong updrafts. The environment around the band cooled, but a narrow region of above-freezing temperatures (> 0°C) remained coincident with the band and was responsible for a persistent mixture of rimed snow and sleet. The band reflectivities appeared to weaken to 35 dBZ between 0300 and 0400 UTC 9 February, but surface reports of intense snowfall rates (4–8 cm h^{-1}) were maintained. The decreased reflectivity values were attributed to smaller cold-type hydrometeors after the environment aloft cooled. For the same storm, Griffin et al. (2014) identified additional features using dual-polarization radar, such as the downward excursion of the melting layer, which they hypothesized was either from melting and evaporative cooling or a localized updraft that

produced larger rimed particles with higher fall speeds. They also noted several polarimetric artifacts, such as depolarization streaks indicative of electrification during the band's maximum intensity.

While many studies have highlighted mesoscale snowbands within the comma head of extratropical cyclones (e.g., Sanders and Bosart 1985; Wolfsberg et al. 1986; Nicosia and Grumm 1999; Novak et al. 2004; Evans and Jurewicz 2009), their focus has been on the structure and frontogenetical forcing associated with the band, not its detailed microphysical characteristics and thermodynamic budget. The blizzard of 8–9 February 2013 exhibited rapid changes in snow habit and degree of riming, which allows one to build upon previous work on the thermodynamical evolution and microphysics within the comma head of winter storms. The snowbands from these past studies over the Northeast U.S. occurred within an entirely sub-freezing thermal environment. In addition, the two previous case studies of primary snowband microphysical observations completed by Stark et al. (2013) were not discussed in terms of the thermodynamic evolution of the bands related to observations nor had dual-polarization radar data available. A more comprehensive temperature budget and model sensitivity tests are needed to elucidate the role of various thermodynamic processes on the maintenance or destruction of the mixed phase environment of the band.

The microphysical evolution can be compared with the previous knowledge of cyclone-relative dominant snow habits (Colle et al. 2014). Dual-polarization technology provides temporally consistent products to compare with sporadic in-situ observations of snow habit and has been used to determine the precipitation type in winter storms (e.g., Trapp et al. 2001; Andrić et al. 2013; Thompson et al. 2014). Picca et al. (2014) provided some polarimetric observations of the 8-9 February 2013 snowband event, but they were not put in context with the full band structural and thermodynamic evolution. Griffin et al. (2014) provided more polarimetric and microphysical insight for the event, but the linkages to the thermodynamic evolution were limited, since the Rapid Refresh (RAP) model that they used failed to accurately capture the vertical temperature structure (i.e. warm layer) around the band.

The purpose of this case study is to answer the following questions:

- What was the thermodynamic evolution of the band, and what were the dominant processes that led to the temperature changes at low-levels?

- How did the thermodynamic evolution impact the microphysics and snowfall rates?

This case contains 5 events classified as both a single band and multi-bands (BOTH) associated with a mature (MAT) cyclone occurring between 1800 UTC 8 Feb – 1200 UTC 9 Feb, however this case is analyzed with special attention given to the single band, A case study of robust multi-bands follows in Chapter 5 for comparison. The rest of this chapter is structured as follows. Section 4.2 discusses the datasets and methodology of this study. Section 4.3 provides an overview of the event from a large-scale perspective. Section 4.4 provides details on the microphysical evolution of the snowband based on observations. Section 4.5 highlights the thermodynamical evolution of the band and the environment within which it evolved. Section 6 examines the temperature evolution with analysis of air parcel trajectories, quantitative comparison of terms of the thermodynamic equation, and sensitivity tests. The chapter concludes with a summary and discussion of future work.

4.2 Datasets and methodology

a. Observational datasets

The KOKX dual-polarization radar was used to observe the apparent intensity and location of the band. In addition to reflectivity factor at horizontal polarization (Z_H), co-polar correlation coefficient (ρ_{hv}) and differential reflectivity (Z_{DR}) were used to discern regions of liquid, frozen, and mixed-phase hydrometeors, as summarized by Kumjian (2013). The diversity of how the scattering of each particle contributes to the horizontal and vertical return signals is measured by ρ_{hv}. For example, spherical particles and uniform particles would result in $\rho_{hv} \sim 1$. Variability of hydrometeor type, shape and/or orientations can decrease ρ_{hv}. Melting particles result in lower ρ_{hv} values because the liquid water may accentuate irregular features. Z_{DR} is the logarithmic ratio of the reflectivity factor at horizontal polarization to the reflectivity factor at vertical polarization and is sensitive to the shape, density and orientation of particles. Z_{DR} is larger for rain than most ice and dry snow, even for the same shape and orientation, because of the higher density of liquid water. The Level-II radar data was converted to NetCDF format using the National Center for Atmospheric Research (NCAR) Research Applications Laboratory

(RAL) radial radar software package, Radx (http://www.ral.ucar.edu/projects/titan/docs/radial_formats/radx.html) and displayed using NCAR Command Language (NCL) version 6.1.2.

Ground observations of snow habit, degree of riming, snow water equivalent and snowfall rate were taken at Stony Brook University (SBNY in Fig. 4.1b), about 20 km west of KOKX using the methodology presented in Colle et al. (2014) and a stereomicroscope in a cold shed. Satellite data were obtained from the Geostationary Operational Environmental Satellite-13 (GOES-13) via the National Oceanic and Atmospheric Administration (NOAA) National Climatic Data Center (NCDC) Comprehensive Large Array Data Stewardship System (CLASS) and displayed using the Integrated Data Viewer (IDV; Murray et al. 2003). The 13-km Rapid Refresh (RAP; Benjamin et al. 2009) hourly gridded analyses, conventional surface observations, and radiosonde observations from KOKX and Chatham, MA (KCHH on Fig. 4.1b) were used for model verification on the synoptic scale discussed in Section 4.2b.

b. Model setup

The Weather Research and Forecasting (WRF) model version 3.4.1 (Skamarock et al. 2008) was used for a 48-h simulation initialized ~17 h prior to band formation at 0000 UTC 8 February 2013. This lead time is within the range (15–21 h) employed by Novak and Colle (2012) for three East Coast banding cases. The simulation was run using the 6-hourly 0.5° Global Forecast System (GFS) data from the 0000 UTC 8 February forecast cycle as the initial and boundary conditions with four one-way nested domains from 36-km down to 1.33-km horizontal grid spacing centered over the band location (Fig. 4.2c). There were 40 levels in the vertical, with the model top set to 100 hPa. The $1/12^{th}$ degree sea surface temperature data from 0000 UTC 8 Feb was used to initialize the simulation and obtained from the National Centers for Environmental Prediction (NCEP). Snow cover was initialized from the 0.5° GFS 0000 UTC 8 Feb analysis file. The Mellor-Yamada-Janjic planetary boundary layer (PBL) scheme (Janjic 1994) and the Unified Noah Land Surface Model (NOAH LSM; Tewari et al. 2004) were used. The Betts-Miller-Janjic cumulus parameterization (Betts 1986) was applied in the 36 and 12-km domains only, while the Thompson microphysical parameterization scheme was used in all domains (Thompson et al. 2004; Thompson et al. 2008). These physics options followed from

previous work on simulating snowbands in the region using the WRF model (Stark 2012), with the non-spherical ice assumption within the Thompson microphysical parameterization scheme shown to produce realistic simulated reflectivity structures. The 1.33-km domain was output at a temporal frequency of 15 minutes in order to complete the microphysical and thermodynamic analyses found in Sections 4.4 and 4.5.

Additional runs were conducted to obtain the most representative simulation by varying the initial and boundary conditions between the 0000, 0600, and 1200 UTC 8 February 2013 NCEP North American Model (NAM) forecast, GFS analyses and forecasts, and 3-hourly RAP analysis gridded data while keeping the physics options constant. The results were compared with available observational data (e.g., KOKX radar reflectivity, KOKX and KCHH soundings, various ASOS station data, etc.). Most simulations resulted in larger position and magnitude errors of the snowband than using the GFS forecast data starting at 0000 UTC 8 February (not shown), and some of this is linked to larger position and magnitude errors of the cyclone southeast of Long Island. Thus, the 0000 UTC 8 February 2013 GFS forecast initial and boundary conditions were used for the WRF simulation discussed in subsequent sections. This simulation exhibited some error, including with the structure of the snowband, but is sufficiently accurate in the band processes to serve the goals of this study.

4.3 Large-Scale overview

The 8–9 February 2013 cyclone developed when a 500-hPa shortwave trough over the Carolinas strengthened and phased with a larger-amplitude northern stream trough that originated from the Great Lakes region. The original cyclone weakened over the Great Lakes, while cyclogenesis occurred just east of the mid-Atlantic coast as in Miller type-B (Miller 1946) (Fig. 4.2a). The low off of the East Coast deepened approximately 29 hPa in 24 h from 0600–0600 UTC 8–9 Feb according to the NOAA Weather Prediction Center (WPC) 3-hourly surface analyses. The coastal low developed as the poleward exit region of a 300-hPa jet core ≥ 110 kts (~55 m s^{-1}) interacted with a low-level baroclinic zone from 0600 UTC 8 Feb to 0000 UTC 9 Feb. The surface cyclone continued to be situated under the equatorward entrance region of a 300-hPa jet core (≥ 130 kts) as it deepened further (Fig. 4.2c), and the cyclone occluded as it entered the Gulf of Maine (not shown).

The WRF simulation was verified using available observations and gridded analysis data from the RAP. The WRF realistically simulated the structure and evolution of the mid-level shortwave trough and the interaction with the northern stream trough. This is demonstrated by the similar storm structure between the observed infrared imagery (Figs. 4.3a,c,e) and the simulated cloud top temperatures (Figs. 4.3b,d,f) at 1800 UTC 8 Feb, 0000 UTC 9 Feb, and 0600 UTC 9 Feb. The simulation reproduced the central pressure of the cyclone to within ±2 hPa of the WPC analyzed mean sea level pressure (MSLP) valid at the same time during the critical 12-h time period relevant to the snowband (1800 UTC 8 – 0600 UTC 9 Feb), whereas the RAP analyses were 2-8 hPa too weak throughout the same time period (not shown). The simulated cyclone track was similar to the observed with the exception of a ~200 km southward shift around 0600 UTC 9 Feb (forecast hour 33) (Figs. 4.2b,c).

4.4 Observed and simulated snowband evolution

a. Phase 1: North-south-oriented mixed-phase transition zone

Picca et al. (2014) and Griffin et al. (2014) used observations from a dual-polarization radar to highlight some of the evolution of this event. We expanded on their analysis of the band life cycle separated into three phases defined by the observed changes in the radar and surface observations. We define phase 1 from 2000 UTC to 2300 UTC on 8 February. Phase 1 was associated with a west-east-oriented mixed-phase transition zone that separated the snow to the north of Long Island, NY with the rain to the south. This was characterized by $\rho_{hv} < 0.95$ and Z_{DR} ~1.0 dB from rain and mixed-phase precipitation along the southern coast and to the south of Long Island, while the snowband along central Long Island and to the north was characterized by ρ_{hv} ~1 and Z_{DR} ~0 dB (Figs. 4.4a,d,g), which is associated with hydrometeors with low effective density, such as aggregated snowflakes with little riming. A northwest-southeast cross section (A to A' on Fig. 4.4i) at 2129 UTC 8 Feb shows the melting signature located approximately 20 km southeast of SBNY, given by low values of ρ_{hv} (< 0.90) and large Z_{DR} values (> 1.5 dB) below ~1.5 km ASL, which suggests a mixture of hydrometeors, mainly snow melting into rain (Figs. 4.5a,d,g). Also noted is the height of the 25 dB*Z* contour to 4.5 km near the snowband. Surface observations taken around 2000 UTC 8 Feb at SBNY near the western edge of the snowband

included large aggregates of mainly colder-type crystals including sideplanes and plates (Fig. 4.6), with an average snow-to-liquid ratio (SLR) of 10:1 and snowfall rates of 4.0–8.5 cm h^{-1} (1.6–3.3 in h^{-1}) within this phase.

The WRF output valid at 2100 UTC 8 Feb (21 h) simulated an east-west-oriented precipitation band north of the 850-hPa low center (Fig. 4.7a). A northwest-southeast cross section (B to B' on Fig. 4.7a) shows that the WRF realistically simulated the depth of the higher reflectivity values (~40 dBZ) to around 800 hPa (~1.9 km ASL) near SBNY and the simulated cloud depth extended to just above 500 hPa (~5.44 km ASL) (Fig. 4.7c). The simulated microphysical output reveals a broad area of snow mixing ratios exceeding 1.5 g kg^{-1} above 700 hPa coincident with the band (Fig. 4.7e), as well as snow to the north of SBNY and rain mixing ratios exceeding 0.35 g kg^{-1} to the south (Fig. 4.7e). There is a graupel maximum of 0.30 g kg^{-1} from the surface to 950 hPa above and ~20 km south of Long Island within the colder lower-level air, indicating either heavy riming resulting in snow converting to graupel or refreezing taking place in the model. The Thompson scheme cannot produce sleet, so rain water refreezes to graupel (Thompson et al. 2008). Model-derived snow depth and liquid equivalent are output from the NOAH LSM which inputs the precipitation rate and fraction of frozen precipitation (FOFP) from the Thompson scheme. The NOAH LSM classifies all precipitation as snow if FOFP > 0.5 or as freezing rain if the air temperature is > 0°C but the ground temperature is < 0°C. The NOAH LSM also accounts for melting and compaction of existing snow with a time-varying and temperature-dependent snow density used in calculating the snow depth (Ek et al. 2003; Tewari et al. 2004). The simulated snow depth values were used to calculate the snowfall rates within each phase. The simulated SLR values were calculated using the hourly change in liquid equivalent snow on the ground and the snow depth. During phase 1, simulated snowfall rates at SBNY were 5.1 cm h^{-1} (2.0 in h^{-1}). Table 4.1 provides a comparison between the observed and simulated snow depth and liquid equivalent within each phase and SLR values averaged throughout each phase. Each phase included at least three observed measurements. Simulated snowfall amounts during phase 1 were 5.0 cm (2.0 in) less than observed, but liquid equivalent values were 0.5 cm (0.2 in) larger than observed.

b. Phase 2: Heavy riming and extreme hydrometeor diversity

The snowband evolved from a broad region of smaller bands with enhanced reflectivities (Fig. 4.4a) into a primary snowband that pivoted to a north-south orientation as the cyclone moved east (Fig. 4.4b). Phase 2 (2300 UTC 8 Feb - 0200 UTC 9 Feb) was a period of heavy riming and extreme hydrometeor diversity and was the peak of intensity of the snowband extending from south of Long Island northward into central Connecticut. Reflectivity reached 57.5 dB*Z* at 0042 UTC in a region of ρ_{hv} ~ 0.85 and Z_{DR} > 3 dB (Figs. 4.4b,e,h). This is near the time lightning was observed ~30 km east of KOKX (D. Stark, NOAA/NWS Upton, NY, 2013, personal communication), which is consistent with electrification implied by the depolarization streaks observed around this time reported in Griffin et al. (2014). A cross section shows Z_H ~ 40 dB*Z*, ρ_{hv} < 0.90, and Z_{DR} ~ 1.5 dB in the vicinity of SBNY extending to a height of 1.5 km, which is an indication of the hydrometeor diversity at low-levels of the atmosphere (Figs. 4.5b,e,h). Surface microphysical observations at SBNY indicate that phase 2 coincided with heavy riming and sleet (Fig. 4.6), an average SLR of 6.8:1, and snowfall rates of 1.5–7.6 cm h^{-1} (0.6–3.0 in h^{-1}). During this phase, 10–20 % of observed hydrometeors were classified as miscellaneous ice. Picca et al. (2014) provided an image of ice crystals that experienced heavy riming (their Fig. 8a) possibly due to wet-growth processes within the strong updrafts within a moisture-rich environment with temperatures near 0°C, which supports the same hypothesis proposed by Griffin et al. (2014).

The simulated band at 0100 UTC (25 h) is displaced ~30 km to the west of the observed band (Figs. 4.8a, 4b), and the WRF produced another band of higher reflectivities just southeast of Long Island that was not observed. The simulated snowband in the vicinity of SBNY along section B-B' shows a core of higher reflectivities coincident with ~3 m s^{-1} upward-directed circulation vectors (Fig. 4.8c,d), and a horizontal width of the simulated band (< 100 km) comparable to what was observed (Fig. 4.5b). A cross section (B-B' in Fig. 4.8a) shows an amplifying thermal wave in the saturation equivalent potential temperature (θ_{es}) field, with the warm axis coincident with an isolated pocket of air > 0°C from 900–700 hPa located above SBNY (Figs. 4.8b,d), while it was < 0°C just southeast of Long Island to support graupel mixing ratios of ~0.25 g kg^{-1} (Fig. 4.8b). Meanwhile, farther south over the ocean the temperatures ranged from 0–8°C coincident with rain water mixing ratio values ≥ 0.25 g kg^{-1}. The heavy snow over central Long Island fell into the 200-hPa-thick layer of air > 0°C, with some melting to produce rain water mixing ratios < 0.25 g kg^{-1} (Fig. 4.8e). Over SBNY, the rain refroze in a

shallow layer of air < 0°C air between the surface and 900 hPa, producing graupel mixing ratios ≥ 0.30 g kg^{-1} collocated with snow mixing ratios ≥ 1.25 g kg^{-1} (Figs. 4.8d,e). During phase 2, simulated snowfall rates at SBNY were 5.2 cm h^{-1} (2.0 in h^{-1}) and simulated snowfall amounts were 5.3 cm (2.1 in) larger than observations (Table 4.1).

c. Phase 3: Transition to colder, less-dense snow aggregates

The large hydrometeor diversity and 50+ dB*Z* reflectivity signature abruptly ceased around 0230 UTC 9 Feb and was replaced with more homogeneous snow aggregates and a signature more consistent with snowbands that have been studied in the past (e.g., Novak et al. 2008, 2009, 2010). The reflectivity values decreased to ~30 dB*Z* within 1 h and the snowband persisted until approximately 0800 UTC 9 Feb. This change in observed microphysics constitutes phase 3 (0200 – 0800 UTC 9 Feb). Figure 4.4 (c,f,i) shows the persistent band at 0340 UTC 9 Feb with the ρ_{hv} and Z_{DR} fields both showing more uniform values along western Long Island into south-central Connecticut, but given the relatively large coverage of reflectivity values > 30 dB*Z*, heavy snow was still falling across the region. The cross section shows that this transition had occurred throughout the lower atmosphere (Figs. 4.5c,f,i). Surface observations of ice habit and riming during phase 3 at SBNY show a transition to colder-type crystals with less riming (Fig. 4.6) while the heavy snow persisted and the SLR increased again to 9.4:1 with snowfall rates of 6.5–6.7 cm h^{-1} [2.6 in h^{-1}].

The simulated snowband at 0400 UTC (28 h) showed a similar marked decrease in reflectivity in the horizontal (Fig. 4.9a) and cross section B-B' (Fig. 4.9a), which was greater than observed by < 5 dB*Z*. Meanwhile, the simulated precipitation to the east of the snowband over southeastern Massachusetts was stronger than observed. The vertical profile of temperature over SBNY also cooled by as much as 6°C between 1–2 km. Section 4.6 will examine the reasons for the ~500-m-deep layer above 0 °C between 1–2 km (900–700 hPa) during the second phase and its abrupt cooling during phase 3. The observed transition to colder, less-dense snow aggregates (Figs. 4.4c, 4.5c) is comparable to the simulated transition to all-snow and cessation of rain and graupel (Fig. 4.9e) and is thus evident in the simulated reflectivity values around 0400 UTC (Figs. 4.9a,c). Specifically, the rain and graupel mixing ratios and cloud water decreased to < 0.10 g kg^{-1} and the snow decreased to between 0.50–0.90 g kg^{-1} (Figs. 4.9b,d,e).

During phase 3, the simulated snowfall rate at SBNY was 2.4 cm h^{-1} (0.9 in h^{-1}) and the simulated change in snow depth was 36.3 cm (11.2 in) less than observations (Table 4.1). This discrepancy is due to the simulated band dissipating ~3 h sooner than the observed band within phase 3 at 0500 UTC 9 Feb. As such, the simulated snow depth and liquid equivalent amounts were comparable to what was observed during both phases 1 and 2 and any analysis of the simulation within phase 3 will be conducted prior to 0500 UTC 9 Feb.

4.5 Thermodynamic evolution

a. Phase 1: North-south-oriented mixed-phase transition zone

Phase 1 (2000-2300 UTC 8 February) occurred when the simulated band was situated along and parallel to Long Island (Figs. 4.7a,b) near where 850-hPa frontogenesis was approximately 0.1 K $(100\ km)^{-1}\ h^{-1}$ (Fig. 4.7f). The band was located in a stable environment above 900-hPa. South and east of the band were multiple narrow snowbands (Figs. 4.7a,c), but their discussion is beyond the scope of this study.

The 900-hPa thermal structure at 2100 UTC 8 Feb showed evidence of cold air to the north of the surface cyclone center with easterly winds north of Long Island into southern New England (Fig. 4.7b). During this phase there was warm advection over southern Long Island and confluence of the flow due to 900-hPa easterly winds decelerating from 75 kts to 50 kts over ~50 km. At 2100 UTC, a north-south temperature gradient was simulated at 900 hPa with simulated mixing ratios of mostly snow to the north and rain to the south of Long Island, both of which exceed 0.25 g kg^{-1} (Fig. 4.7b). A cross section from B-B' taken through the different thermal environments near SBNY shows that a sub-freezing layer extended from 800-500 hPa, an above-freezing layer from 925–800 hPa, a low-level sub-freezing layer from 975–925 hPa, and a near-surface shallow above-freezing layer extended from the surface to ~975 hPa (Fig. 4.7d).

b. Phase 2: Heavy riming and extreme hydrometeor diversity

The band exhibited the greatest reflectivity (57.5 dB*Z*) in the proximity of SBNY during phase 2 (2300 8 Feb to 0200 UTC 9 Feb) (Fig. 4.4b). The area of maximum 850-hPa

frontogenesis of 0.8 K (100 km)$^{-1}$ h^{-1} was ~60 km southeast of the north-south-oriented snowband (Fig. 4.8f). The band coincided with a region of weak conditional stability at 0100 UTC 9 Feb near 600 hPa (Fig. 4.8d), which is similar to the stability of a snowband studied in Novak et al. (2009).

During phase 2, the 900-hPa temperatures decreased over a fairly broad area around Long Island as winds at this level started to back to the northeast (Fig. 4.8b). However, there was a narrow north-south-oriented swath of 900-hPa air > 0°C maintained over Long Island collocated with the snowband > 45 dB*Z* (Fig. 4.8b). The depth of the air > 0ºC above SBNY extends from 900-700 hPa, as shown in cross section B-B' (Fig. 4.8a), while the temperature of the environments to the northwest and southeast of Long Island were < 0ºC (Figs. 4.8b,d). At this time there was an amplified signal in the θ_{es} field, a strong vertical circulation associated with the snowband, and the pocket of air above 0°C was located below the mid-level subsidence (~750 hPa).

c. Phase 3: Transition to colder, less-dense snow aggregates

By 0300 UTC 9 Feb (start of phase 3) the 850-hPa frontogenesis at 0400 UTC weakened to 0.5 K (100 km)$^{-1}$ h^{-1} and the snowband persisted in the simulation but decreased in intensity to 30–25 dB*Z* (Fig. 4.9a). There was still ascent in the band environment around 750 hPa (Fig. 4.9c,d), but the immediate band environment exhibited increased stability (Fig. 4.9d). The strongest ascent over SBNY during this phase decreased to < 40 cm s^{-1} and was confined to regions west of SBNY above 2 km (Fig. 4.9c,d). The 900-hPa temperature around Long Island continued to decrease as winds backed more to the north-northeast (Fig. 4.9b). The vertical profile of temperature over SBNY also cooled by as much as 6°C between 1–2 km compared with the temperature of the band environment during the previous phase (Figs. 4.8d, 4.9d). The next section will examine the reason for the ~500 m deep layer above 0°C between 1–2 km (900–700 hPa) during phase 2 and what led to its abrupt cooling.

4.6 Examination of thermodynamic environment

a. Trajectory analysis

In order to diagnose the thermodynamic processes responsible for the warm layer along the band between 900–700 hPa between 2300–0200 UTC 8–9 Feb, backwards trajectories were calculated along Long Island from three points starting at 0200 UTC (Fig. 4.10a). Two trajectories were located to the west and east of the snowband, and one within the temperatures above 0°C at 900 hPa within the band. Although only three trajectories are shown, tens of others were launched in order to find a set of representative trajectories. Backwards trajectories using 15-minute output from the model were calculated using Read/Interpolate/Plot (RIP) version 4.6 (Stoelinga 2009). Previous work by Novak et al. (2009) used trajectories terminating in a snowband environment to discern the role of the dry slot in destabilizing the environment for snowband development and found that the diabatic heating of the snowband itself acted to stabilize the immediate band environment. A recent study by Fuhrmann and Konrad (2013) employed trajectory analysis to understand the large-scale evolution of air parcels pertaining to cool season extratropical cyclones. Their results indicated that diabatic warming and cooling from precipitation processes contribute significantly to the vertical temperature profile intercepted by trajectories.

Figure 4.10a shows the potential temperature evolution for the three trajectories ending at 0200 UTC 9 February. The eastern trajectory likely followed the cold conveyor belt as it remained at a nearly constant height (~500 m ASL) and it is much cooler than the other trajectories by approximately 10 K (Fig. 4.10b). The western and central trajectories followed similar paths, originating from the northeast of the developing cyclone and rotating in counter-clockwise while undergoing ascent and descent of 0.1 m s^{-1} and -0.25 m s^{-1} for the central trajectory versus 0.03 m s^{-1} and -0.19 m s^{-1} for the western trajectory before arriving at their final locations at 0200 UTC; however, the central trajectory is about 4 K warmer than the western trajectory at the same terminal height. The central trajectory underwent ascent between 2300 UTC and 0100 UTC and during that time the water vapor mixing ratio decreased while the snow and cloud water mixing ratios increased presumably from deposition and condensation, resulting in a 4 K warming of the parcel's potential temperature (Figs. 4.10b,c). The central trajectory underwent descent (-0.25 m s^{-1}) between 0100–0200 UTC coincident and just to the west of the snowband (Fig. 4.8a), and entered an environment where melting and evaporation likely occurred with a parcel relative humidity of 84% and temperature of 2.5°C by 0130 UTC (not

shown). Both melting and evaporative processes contributed roughly 7 K of cooling by 0200 UTC of the environment along the course of both the central and western trajectories. Overall, the final potential temperature of the environment of the central trajectory was 4 K warmer than that of the western trajectory because the latent heating allowed for the temperature to increase more before both environments diabatically cooled by ~7 K.

b. Evaluation of the thermodynamic equation within the band environment

Another way to quantify the thermodynamic changes is to calculate a potential temperature budget as in Eq. 4.1.

$$\frac{\partial \theta}{\partial t} = -\left(u\frac{\partial \theta}{\partial x} + v\frac{\partial \theta}{\partial y}\right) - \omega\frac{\partial \theta}{\partial P} + Diabatic \qquad \text{Eq. 4.1}$$

Novak et al. (2009) used this method (their Eq. 2) to analyze the static stability around the snowband. Our study looks at the spatial structure of the terms during two representative times during the evolution of the band during phases 2 and 3. The left-hand term is the total change over a 15 minute interval. The first term on the right-hand-side is horizontal advection. The middle term is the vertical advection, which also accounts for adiabatic changes. The term labeled as '*Diabatic'* is the temperature tendency output from the microphysical parameterization scheme, the radiative schemes, and the planetary boundary layer scheme. The results for the calculation are provided in the following cross section from C to C' (Fig. 4.10a) in Figure 4.11. Figure 4.11 shows the contribution from each term at 0030 UTC 9 Feb, which is just before the θ pattern amplified by 0100 UTC 9 Feb. This amplified pattern in the isentropes from moist ascent and compensating subsidence has been shown in another snowband environment in Novak et al. (2008) (their Figs. 4.12b,d).

The tendency terms are first discussed for what led to the ridge in the isentropes near the eastern edge of the snowband (30 km southeast of SBNY). During this time there is a positive contribution from the horizontal advection term within the environment between 950–800 hPa southeast of SBNY (10.0 x 10^{-3} K s^{-1}), but the negative contribution from the vertical advection term is approximately 2.5 times larger (-23.4 x 10^{-3} K s^{-1}), likely resulting from strong ascent (Figs. 11b,c). The ascent at this time was frontogenetically-forced and extends from 800–650

hPa (Fig. 4.11c). Condensation, deposition, and freezing are likely occurring within the environment to allow the diabatic term to contribute a maximum of 9.8 x 10^{-3} K s^{-1} (Fig. 4.11d). This positive contribution occurs within a much smaller areal extent near the ridge in the isentropes around 650 hPa than both the horizontal and vertical advection terms. The result is a net cooling of 1.9 x 10^{-3} K s^{-1}, which is attributed mainly to vertical advection (Fig. 4.11a). The temperature tendency is now applied to the developing low-level warm anomaly over SBNY, as denoted by an apparent thermal trough in the isentropes. The contribution from subsidence (5.2 x 10^{-3} K s^{-1}) covers a larger area and is greater than that of diabatic cooling effects (-1.4 x 10^{-3} K s^{-1}), such as the melting of snow. The horizontal advection term in this region is contributing to cooling (-3.3 x 10^{-3} K s^{-1}) from 975–900 hPa. The net result is a warming of 2.2 x 10^{-3} K s^{-1}, which is coincident with the warm layer that favored melting and wet-growth processes of hydrometeors discussed in previous sections. To reconcile the results of the evaluation of the thermodynamic equation with those of the trajectory analysis, it is evident that both diabatic effects and subsidence maintained the layer of temperatures above 0°C. The environment warmed by moist air rising through the band that released latent heat via condensation, deposition and freezing and then rapidly subsided via the descending branch of the frontogenetical circulation along the western edge of the snowband.

Analyzing the contributions from each term of the equation for times during phase 3 (0400 UTC 9 Feb in Fig. 4.12) of the snowband lifecycle reveals that the vertical advection term weakened to -8.6 x 10^{-3} K s^{-1} within the thermal ridge to the east of SBNY and 4.4 x 10^{-3} K s^{-1} in the thermal trough in the isentropes (Fig. 4.12c). This is likely due to decreased mid-level frontogenesis, which allowed the contributions from diabatic cooling from melting and evaporation (-2.1 x 10^{-3} K s^{-1}) and horizontal cold advection (-3.1 x 10^{-3} K s^{-1}) to dominate and result in the overall cooling of the column (-2.1 x 10^{-3} K s^{-1}), relaxing the amplified signal in the θ field. This supports the cessation of mixed-phase processes and the transition to less dense, albeit still heavy snow.

c. Sensitivity tests to phase changes within the band

To better understand the role of diabatic processes in the evolution of the thermal environment and resulting microphysics, two sensitivity experiments were conducted and

compared with the control run (CTRL) discussed in the previous sections. The first simulation was to identify the role of latent cooling that occurred within the band environment. A simulation was run in which the temperature tendency contributions from evaporation, sublimation, and melting after 2000 UTC 8 Feb 9 Feb (20 h) were not included (no latent cooling; NOLC). The hypothesis is that the snowband environment will be warmer and produce different microphysical results because there will be no evaporative cooling or cooling by melting acting to erode the above-freezing layer between 1–2 km ASL. Studies have highlighted the importance of melting on transitioning precipitation type (e.g. Kain et al. 2000; Lackmann et al. 2002; Market et al. 2006) but that process is not isolated from sublimation and evaporative cooling in this paper in order to study the general aggregate effects in the snowband environment.

The second experimental simulation was similar to the first except that the processes of freezing, deposition and condensation were isolated. The contributions to the temperature tendency calculation from freezing (including riming), deposition, and condensation were turned off after 2000 UTC so that the thermal environment would only respond to advection, diabatic cooling, and adiabatic vertical motion (no latent heating; NOLH). The snowband environment is expected to be cooler and produce less mixed-phase hydrometeors, especially during phase 2 between 2300–0200 UTC.

1) NO LATENT COOLING SIMULATION

The main difference between the NOLC simulation and the CTRL simulation was the persistence and magnitude of the layer of air above 0 °C between 900–700 hPa (0.5–2.0 km ASL). At 2100 UTC 8 Feb (1 h into experiment) the cross section B to B’ (Figs. 4.7a, 4.8a, 4.9a) for the NOLC simulation shows only slight (± 2°C) temperature differences from the CTRL simulation (Fig. 4.13a). A distinct northwest-southeast transition from snow to rain resembles the CTRL simulation (Fig. 4.13b). During phase 2 (Figs. 4.13c,d), the magnitude of the above-freezing layer is > 4°C larger in NOLC than CTRL from 950–750 hPa. This environment supports a deeper layer of simulated rain water mixing ratios reaching the surface southeast of SBNY. The layer above 0 °C persists through 0400 UTC, which altered phase 3 by likely melting most of the simulated snow resulting in less concentrations (0.15 g kg^{-1}) than the CTRL simulation (0.50 g kg^{-1}) reaching the surface at SBNY (Figs. 4.13e,f, 4.9e). The NOLC

experiment provided evidence that the warm layer that had allowed for hydrometeor diversity was partly removed by the combination of cooling processes of melting, evaporation, and sublimation. An additional sensitivity test that removed the contribution just from evaporation more closely resembled the CTRL simulation (not shown), which suggests that melting was the most important diabatic process contributing to cooling the band environment.

2) NO LATENT HEATING SIMULATION

Figure 4.14 shows the effect of the warming diabatic processes including freezing, condensation, and deposition in the NOLH simulation on the evolution of the thermodynamic environment in the vicinity of the simulated band. Phase 1 is similar to that of the CTRL simulation with a northwest-southeast-oriented transition zone from snow to rain (Figs. 4.14a,b). Phase 2 in the NOLH simulation lacks any amplified pattern in the θ_{es} field, since there is little mid-level frontogenesis, which corresponds with the idea that there is a large diabatic component driving frontogenesis (not shown). The environment of the entire domain is much cooler than that of the CTRL simulation and, most importantly, the entire environment aloft extending ~40 km south of SBNY is cold enough to support snow (Figs. 4.14c,d). This environment continues to support snow throughout the beginning of phase 3, but the lack of strong vertical motion from the more stable environment results in less snow and the cessation of the band earlier than the CTRL simulation. The diabatic processes associated with the band itself were critical to the development and maintenance of the band, which supports the conclusions of Novak et al. (2009).

Given the results from the NOLH and the NOLC experiments, a combination of the heating within the updraft just upwind of the observed snowband, the weaker compensating downward motion from weaker ascent, and cooling by melting altered the environment of the snowband near SBNY. Diabatic heating was important in maintaining the thermal gradient that drove the ageostrophic frontogenetical vertical circulation that led to a layer above 0°C from near the surface to ~700 hPa. This thermal environment led to hydrometeors undergoing mixed-phase microphysical growth processes that ultimately resulted in diverse ground observations of snow habits and ice particles. Diabatic cooling was important in the evolution of the band from a mixed-phased environment to one with a vertical temperature environment over SBNY that

supported all snow by phase 3. The importance of diabatic effects to changing precipitation type addressed in this study agrees with previous studies (e.g., Kain et al. 2000; Lackmann et al. 2002). The results support that the simulated band occurrence, intensity and precipitation type were very sensitive to diabatic effects.

4.7 Conclusions

The Northeast U.S. snowstorm of 8–9 February 2013 produced an intense snowband that exhibited reflectivity values that were around 20 dBZ higher than has been documented with previous snowband research (e.g., Novak et al. 2004, 2009, 2010; Stark et al. 2013). The dual-polarization radar observations provided insight into the general identification of hydrometeors and mixed-phase transition zones which were verified using ground observations of snow habit, degree of riming, and SLR at Stony Brook University (SBNY). Building upon Picca et al. (2014) and Griffin et al. (2014), the WRF model was used to simulate the event to determine (1) the evolution of forcing and stability of the snowband, (2) the thermodynamic evolution of the band and (3) how the evolution impacted the microphysics and snowfall rates.

The snowband occurred in three distinct phases. Phase 1 was classified by heavy snow with rates of 4.0–8.5 cm s^{-1} (1.6–3.3 in h^{-1}) to the north of a north-south transition zone that was apparent across Long Island, NY. The band developed in a region of weak 850-hPa frontogenesis ~0.1 K $(100\ km)^{-1}$ h^{-1} and in a region of weak stability. At 2100 UTC during this phase, a distinct northwest-southeast separation between sub-freezing and above-freezing air was apparent throughout the low-to-mid levels in the band environment.

Phase 2 was classified by the largest hydrometeor diversity and was the period during which the highest base reflectivity value of 57.5 dBZ was measured coincident with snow falling at the ground. The band was located near a region of strong frontogenesis (> 0.8 K $(100\ km)^{-1}$ h^{-1}) in a weakly stable environment. During this phase, the SLR decreased from 13:1 to 4:1 and the snowfall rates decreased to 1.5–7.6 cm h^{-1} (0.6–3.0 in h^{-1}), including increased percentages of observed sleet and unidentifiable ice. Further investigation determined that an approximately 200-hPa layer of temperatures above 0°C was collocated with the snowband, just downwind of a strong frontogenetically-induced updraft. The strong updraft led to high snow mixing ratios aloft which may have never fully melted while descending through the warm layer as well as

hydrometeors possibly growing via wet-growth processes in the ~0°C environment.

During phase 3 the environment cooled enough to support snow throughout the snowband environment. This was in part due to the diabatic cooling effects of melting snow into the layer above 0°C which, coupled with the weakened vertical motion from decreased mid-level frontogenesis (< 0.5 K (100 km)$^{-1}$ h^{-1}), was able to cool the column over SBNY. Observed SLR increased to 9.6:1 with snowfall rates of 6.5–6.7 cm h^{-1} (2.6 in h^{-1}).

This study discussed the thermodynamic evolution of the band which showed that diabatic processes, especially condensational heating and cooling by melting, affect the evolution of the band's observed microphysics, but vertical advections induced by a strong frontogenetical circulation are also important. This case is interesting because the snowband formed in an environment with low-to-midlevel mixed-phase processes that were dynamic with time. The trajectory analysis and evaluation of the thermodynamic equation provided evidence that the frontogenetically-enhanced vertical motion during the band's most intense phase 2 was important because without it, the environment may have cooled a lot sooner to support an all-snow event instead of the complex hydrometeors that were observed during that time period. Further evidence was provided by the sensitivity tests that showed that latent heating was critical to the maintenance of an environment of decreased stability and narrow updrafts which agreed with the findings of Novak et al. (2009). In addition to the large-scale horizontal temperature advection, diabatic cooling was important to ultimately cool the band environment to support less-dense snow aggregates. The diabatic effects occurring within the band environment were shown to affect the simulated band occurrence, intensity and precipitation type which ultimately changes the storm total snowfall amounts.

Future work focusing on the relative magnitudes of adiabatic expansion/compression versus diabatic processes, which are sometimes assumed to equally oppose one another, for a greater number of snowband cases would be enlightening. Additional modeling work could be done to explore the effects of using different microphysical parameterization schemes as well as other model physics variations for this case and other cases on the structure of simulated bands.

Table 4.1. A summary of observed and simulated snow depth, liquid equivalent, and snow-to liquid ratio (SLR) values at SBNY for each of the three phases of the snowband (1) 2000 UTC 8 Feb – 2300 UTC 8 Feb, (2) 2300 UTC 8 Feb – 0200 UTC 9 Feb, (3) 0200 UTC 9 Feb – 0800 UTC 9 Feb. Snow depth values are not cumulative and represent the value from the beginning to end of each phase. SLR values are given in fractional form.

	Observed Snow Depth (cm) [in]	**WRF Simulated Snow Depth (cm) [in]**	**Observed Liquid Equivalent (cm) [in]**	**WRF Simulated Liquid Equivalent (cm) [in]**	**Observed SLR**	**WRF Simulated SLR**
Phase 1	20.3 [8.0]	15.3 [6.0]	2.0 [0.8]	2.5 [1.0]	10.0	6.1
Phase 2	10.2 [4.0]	15.5 [6.1]	1.5 [0.6]	2.3 [0.9]	6.8	6.7
Phase 3	40.6 [16.0]	12.2 [4.8]	4.3 [1.7]	1.5 [0.6]	9.4	8.1

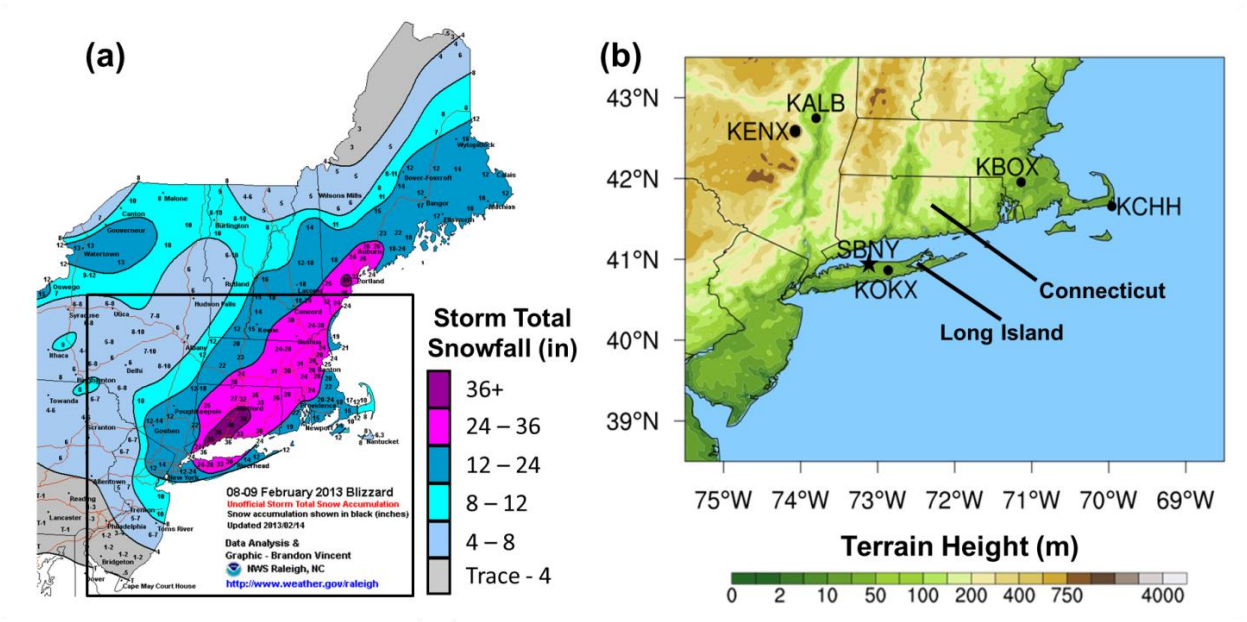

Figure 4.1. (a) Storm total snowfall accumulation for 8–9 February 2013 adapted from Brandon Vincent of NWS Raleigh, NC. (b) Topographic map showing the locations of Stony Brook University (SBNY), KOKX dual polarized radar and upper-air site (KOKX), Chatham, MA upper-air site (KCHH), KBOX dual polarized radar site, Albany, NY upper-air site (KALB) and Albany, NY dual polarized radar site (KENX).

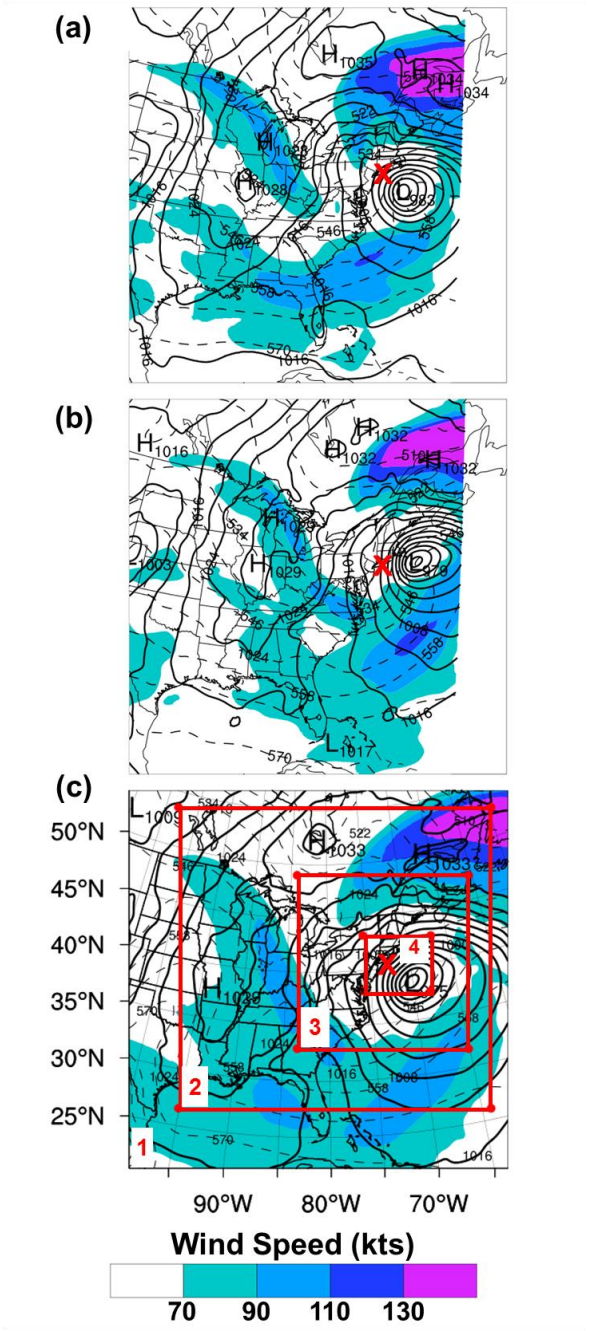

Figure 4.2. 13-km RAP analysis of MSLP (solid, contoured every 4 hPa), 1000-500-hPa thickness (dashed, contoured every 6 dam), and 300-hPa wind speed (shaded every 20 kts) at (a) 0000 UTC 9 Feb and (b) 0600 UTC 9 Feb. (c) As in (b) but for 30-h WRF forecast valid at (c) 0600 UTC 9 Feb 2013. The red boxes indicate the three one-way nested domains within the outer domain (outer map outline) with horizontal grid spacing of 36, 12, 4, and 1.33 km, respectively. The red "x" marks the approximate location of SBNY and the snowband.

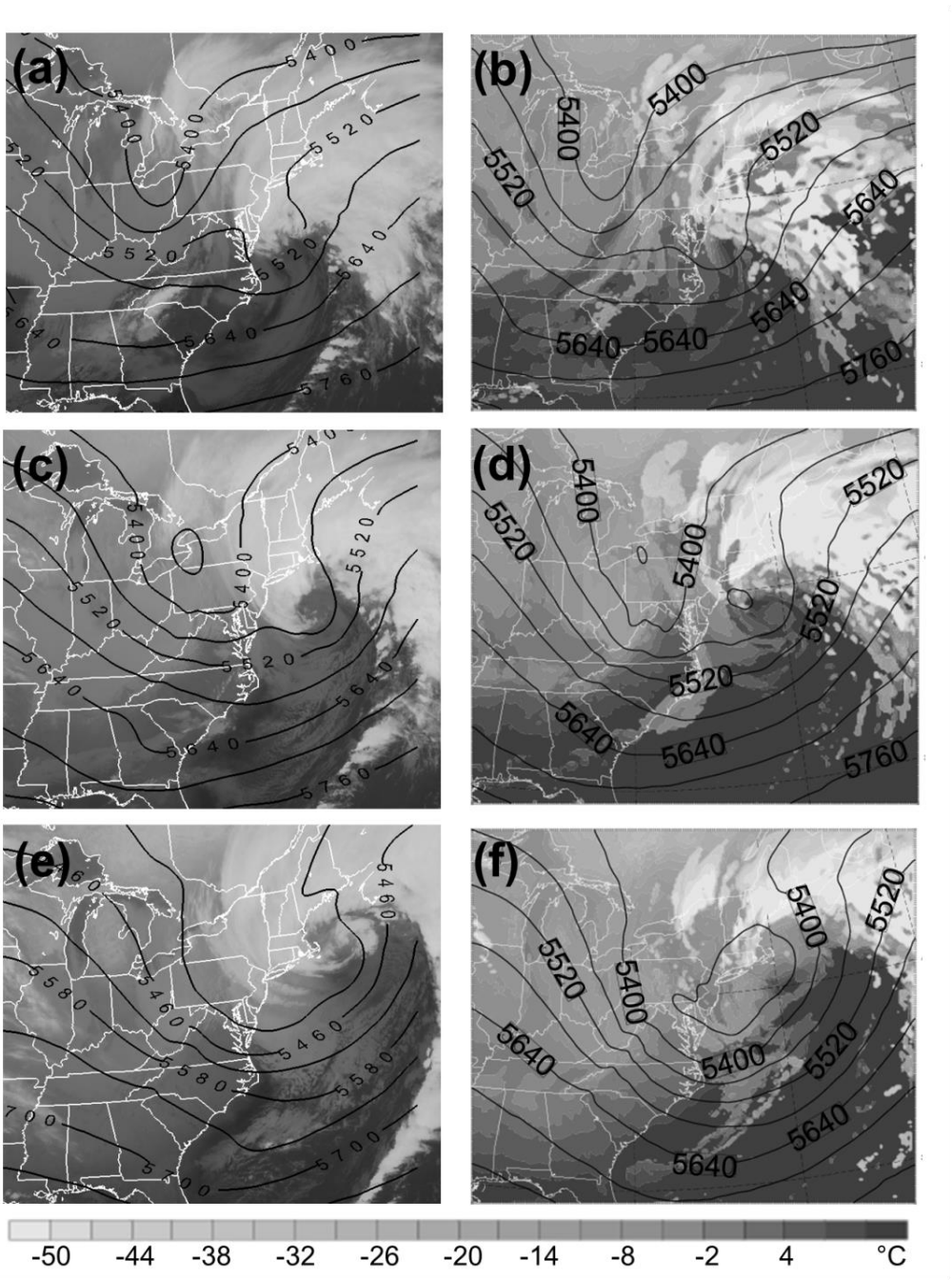

Figure 4.3. Geostationary Operational Environmental Satellite-13 (GOES-13) infrared satellite brightness temperature (K, shaded) and 13-km RAP analysis of 500-hPa geopotential height (solid black contoured every 60 m) at (a) 1800 UTC 8 Feb 2013, (c) 0000 UTC 9 Feb 2013, (e) 0600 UTC 9 Feb 2013. WRF simulated cloud top temperature (°C, shaded according to scale) and 500-hPa geopotential height contoured every 60 m at (b) 1800 UTC 8 Feb 2013, (d) 0000 UTC 9 Feb 2013, and (f) 0600 UTC 9 Feb 2013.

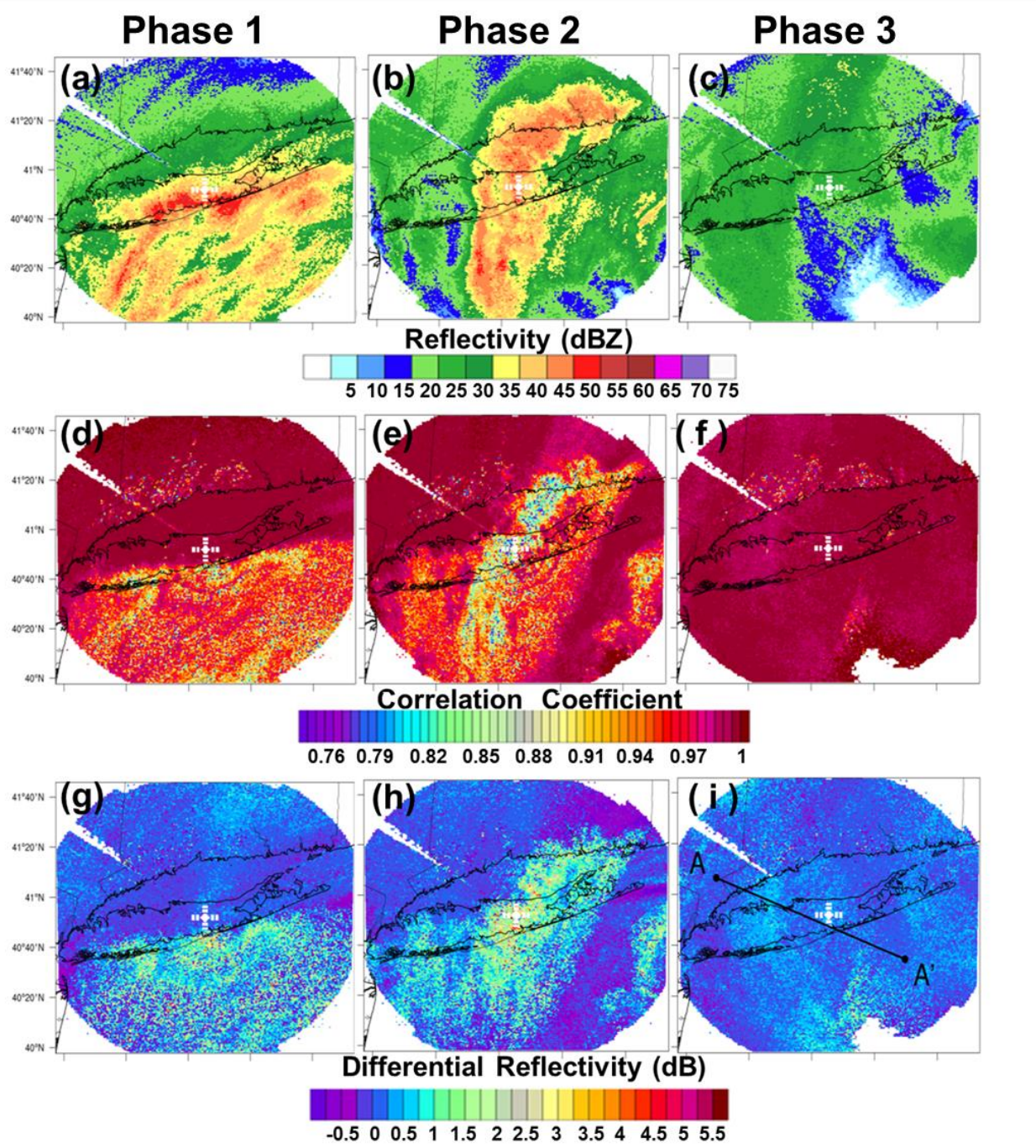

Figure 4.4. KOKX 0.5° Plan Position Indicators (PPIs) of (a, b, c) reflectivity (dBZ, shaded according to scale), (d, e, f) correlation coefficient (shaded according to scale), and (g, h, i) differential reflectivity (dB, shaded according to scale) for (a, d, g) 2129 UTC 8 Feb, (b, e, h) 0042UTC 9 Feb, and (c, f, i) 0340 UTC 9 Feb.

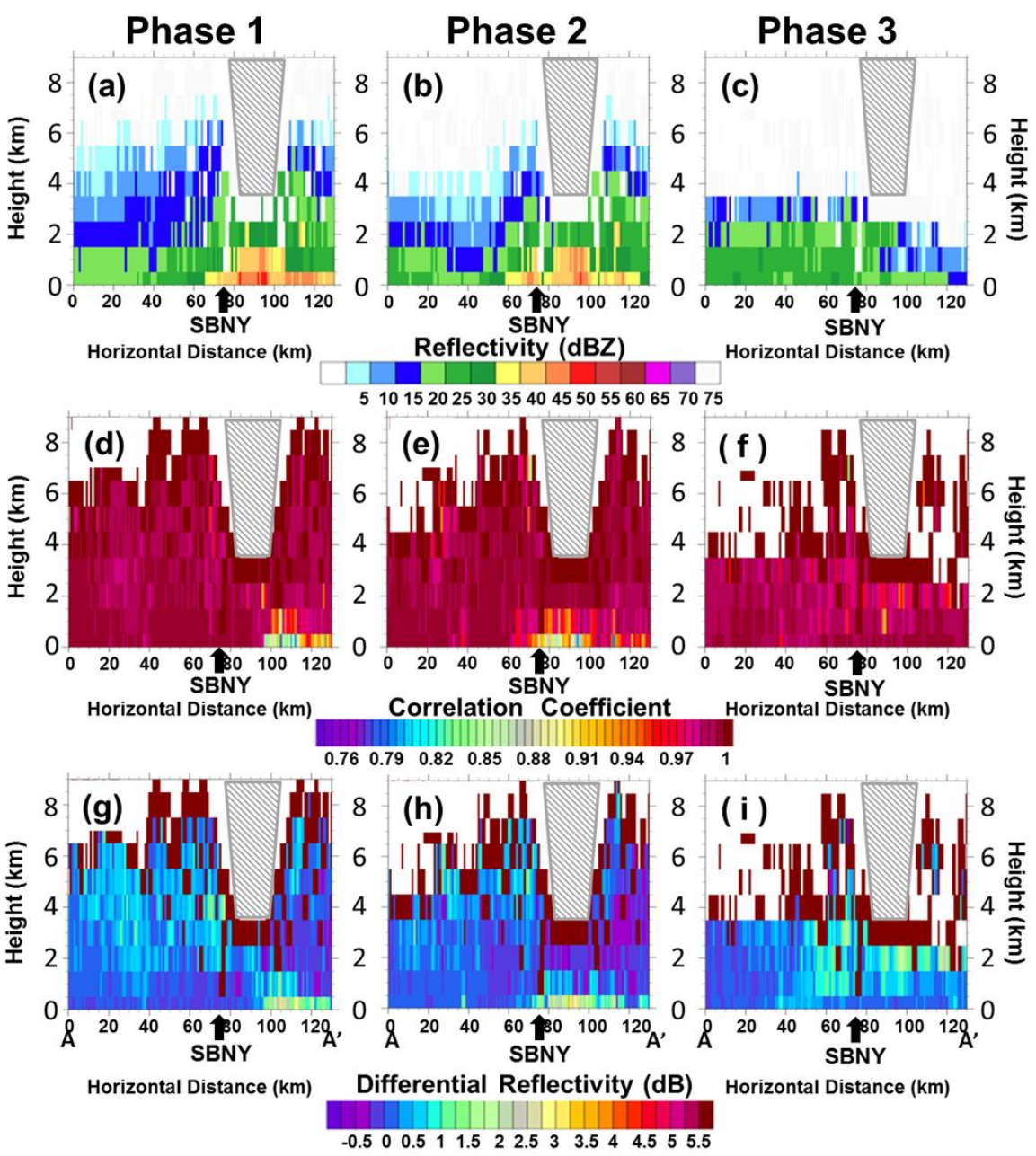

Figure 4.5. Northwest-southeast cross section from A to A' as shown in Fig. 4.4i of (a, b, c) reflectivity (shaded every 5 dBZ), (d, e, f) correlation coefficient (ρ_{hv}), and (g, h, i) differential reflectivity (dB, shaded according to scale) for (a, d, g) 2129 UTC 8 Feb, (b, e, h) 0042 UTC 9 Feb, and (c, f, i) 0340 UTC 9 Feb 2013. The approximate location of Stony Brook University (SBNY) is denoted by the arrow and the cone of silence is hatched.

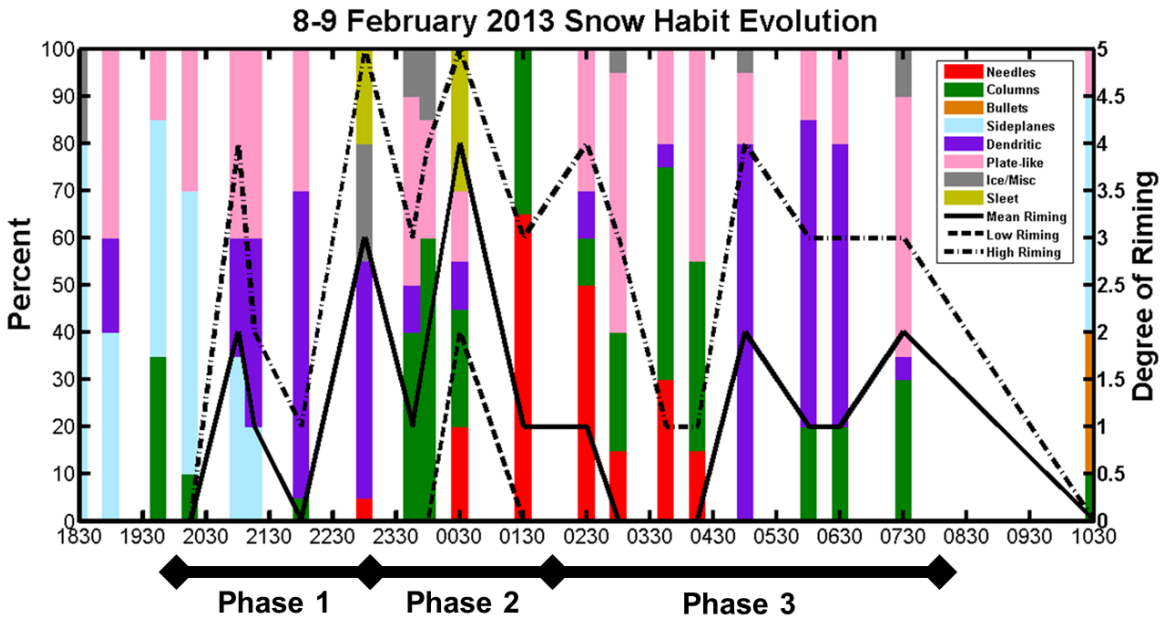

Figure 4.6. Field observations at SBNY of the microphysical evolution of ice habit (shaded vertical bars), riming (mean: solid, low: dashed, high: dotted-dash) from 1830 UTC 8 Feb – 1030 UTC 9 Feb 2013. The time of each observed phase is indicated along the bottom of the image.

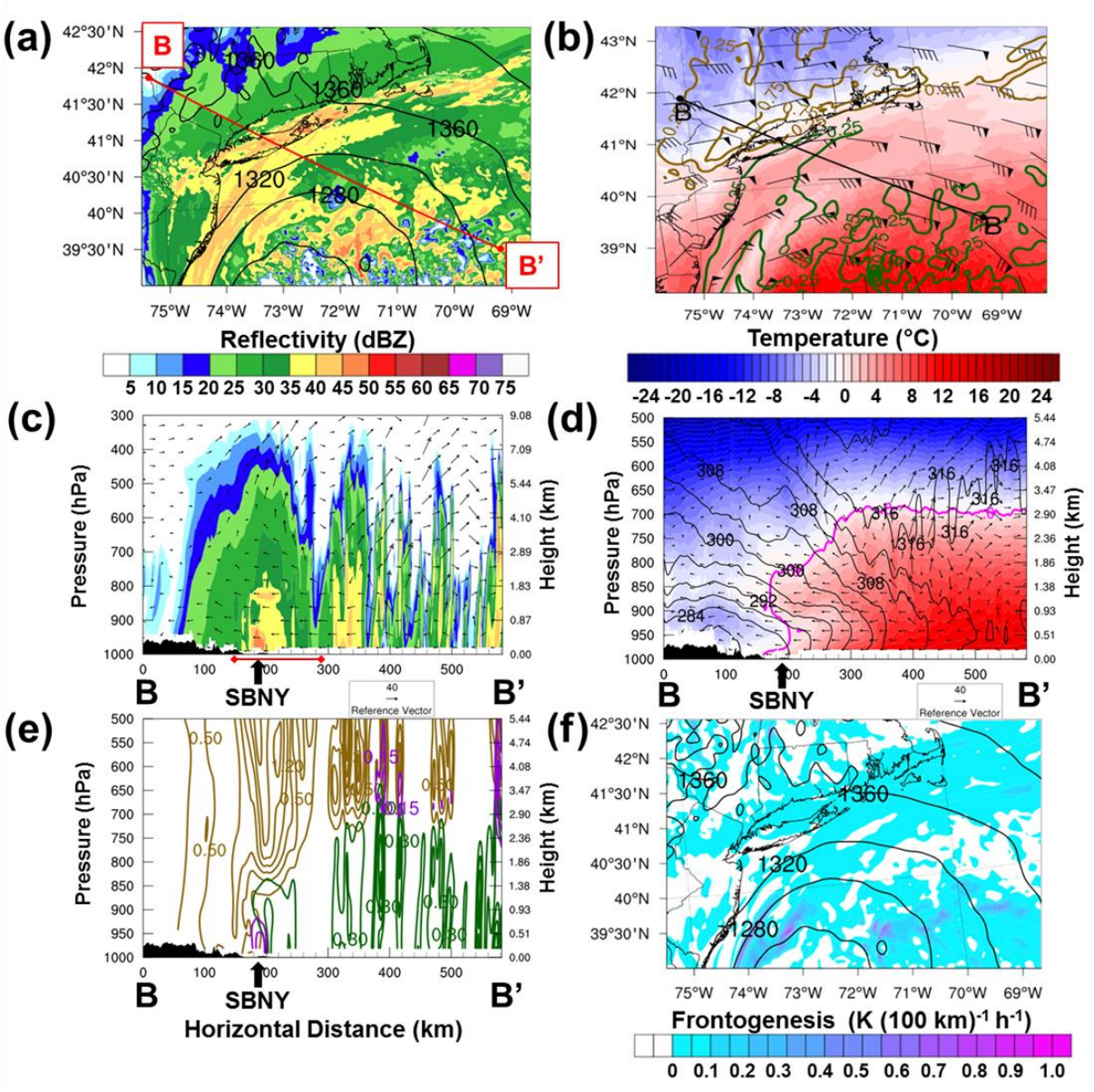

Figure 4.7. 21-h WRF forecast valid at 2100 UTC 8 Feb for (a) simulated reflectivity at approximately 500 m ASL (dBZ, shaded according to scale) and 850-hPa geopotential height (m, black solid contours every 40 m), (b) simulated 900-hPa temperature (°C, shaded every 1°C according to scale), horizontal wind (kts, barbed vectors), snow mixing ratio (g kg^{-1}, gold contours from 0.25 g kg^{-1} by 0.5 g kg^{-1}), rain mixing ratio (g kg^{-1}, green contours using the same contour interval as snow), graupel mixing ratio (g kg^{-1}, purple contours), (c) cross-section from B to B' as shown within Fig. 7a of simulated reflectivity (dBZ, shaded according to scale) and circulation vectors (arrows were scaled such that the reference vector corresponds to 0.4 m s^{-1}) with the approximate bounds of A–A' given in red, (d) cross-section of temperature (°C, shaded every 1°C according to scale), saturation equivalent potential temperature (K, contoured every 4 K), and circulation vectors, (e) snow mixing ratio (g kg^{-1}, gold contours from 0.15 g kg^{-1} by 0.35g kg^{-1}), rain mixing ratio (g kg^{-1}, green contours every 0.15 g kg^{-1}), graupel mixing ratio (g kg^{-1}, purple contours using the same contour interval as rain), and (f) simulated 850-hPa

frontogenesis (K (100 km)$^{-1}$ h^{-1}, shaded according to scale) and 850-hPa geopotential height (m, black contours every 40 m). The approximate location of SBNY is given in the cross-sections and the terrain is shaded.

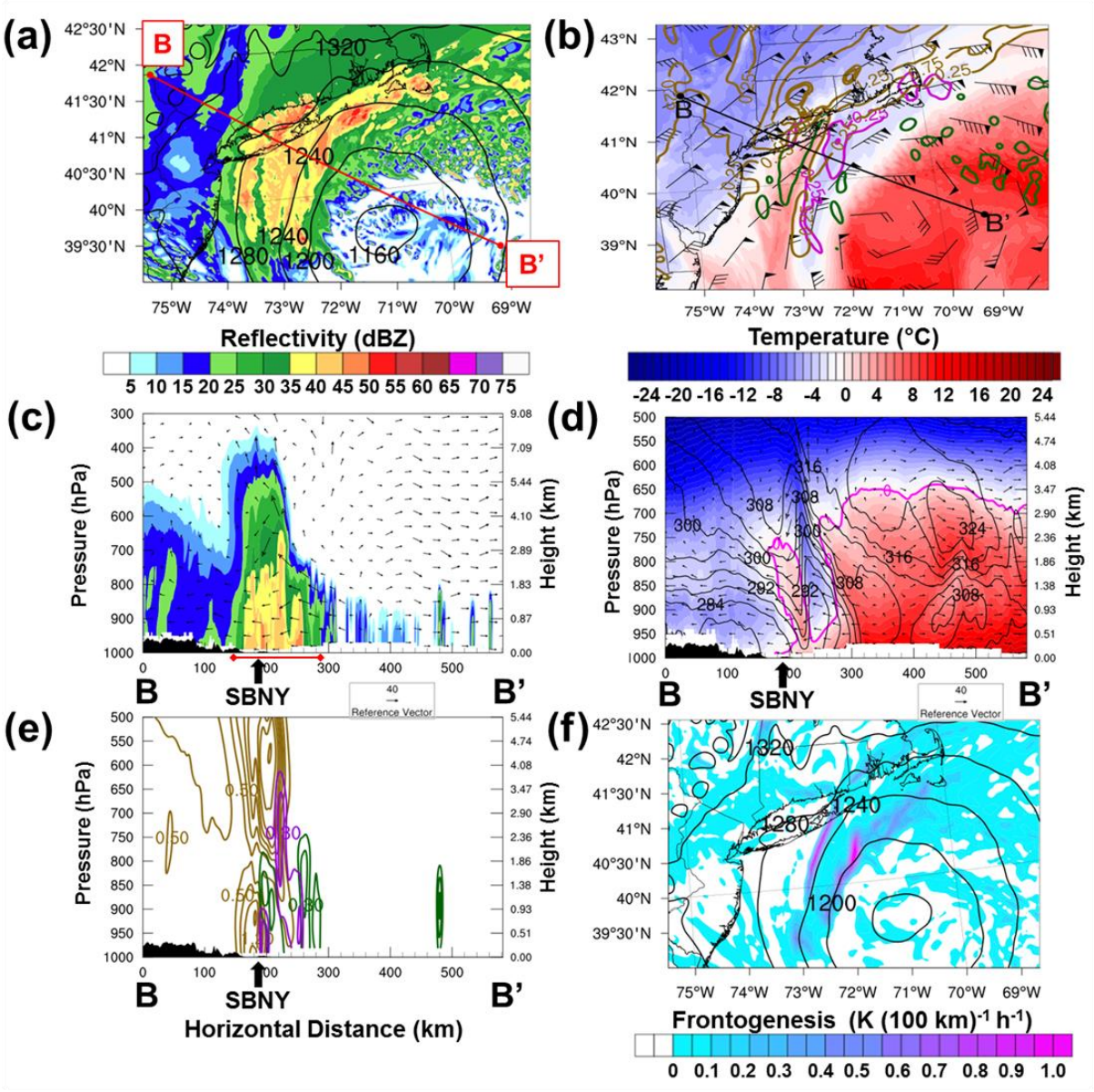

Figure 4.8. As in Fig. 4.7 but for the 25-h forecast valid at 0100 UTC 9 Feb.

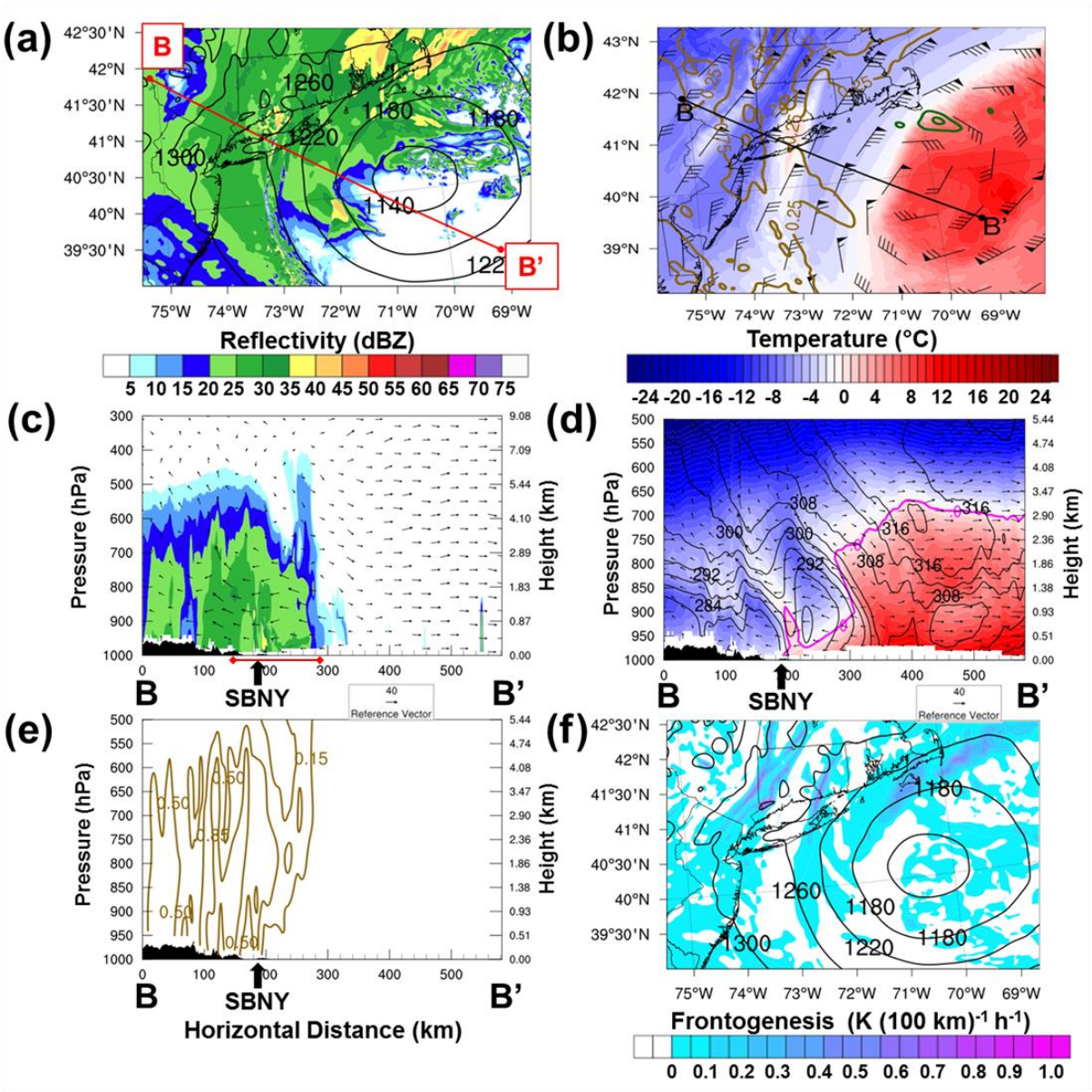

Figure 4.9. As in Figs. 4.7 and 4.8 but for the 28-h forecast valid at 0400 UTC 9 Feb.

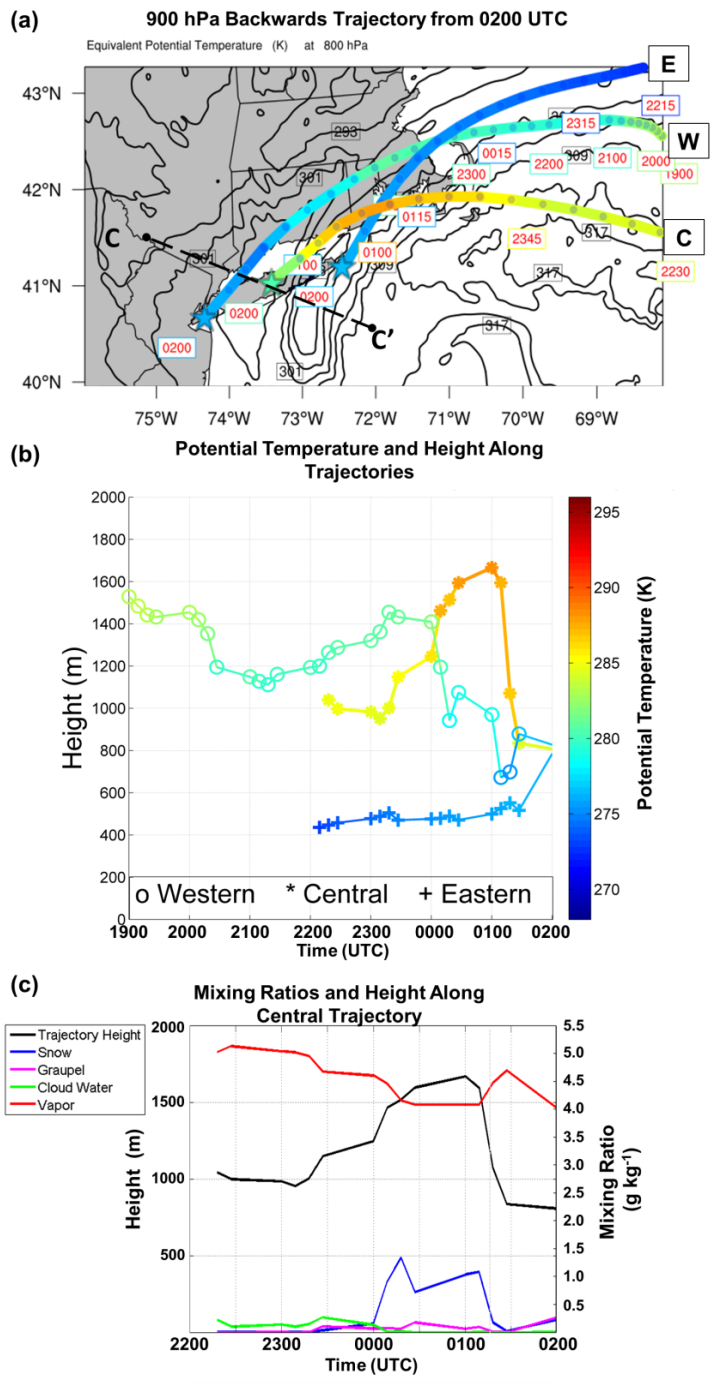

Figure 4.10. (a) Potential temperature along backwards trajectories launched from three distinct points (indicated by stars) to the west (W), east (E) and central (C) to the snowband from 900-hPa at 0200 UTC 9 Feb with 0200 UTC 800-hPa equivalent potential temperature (K) contoured and times along the trajectory path labeled (UTC). (b) Potential temperature with height and time for each of the three trajectories. (c) Height and mixing ratio with time along the central trajectory only.

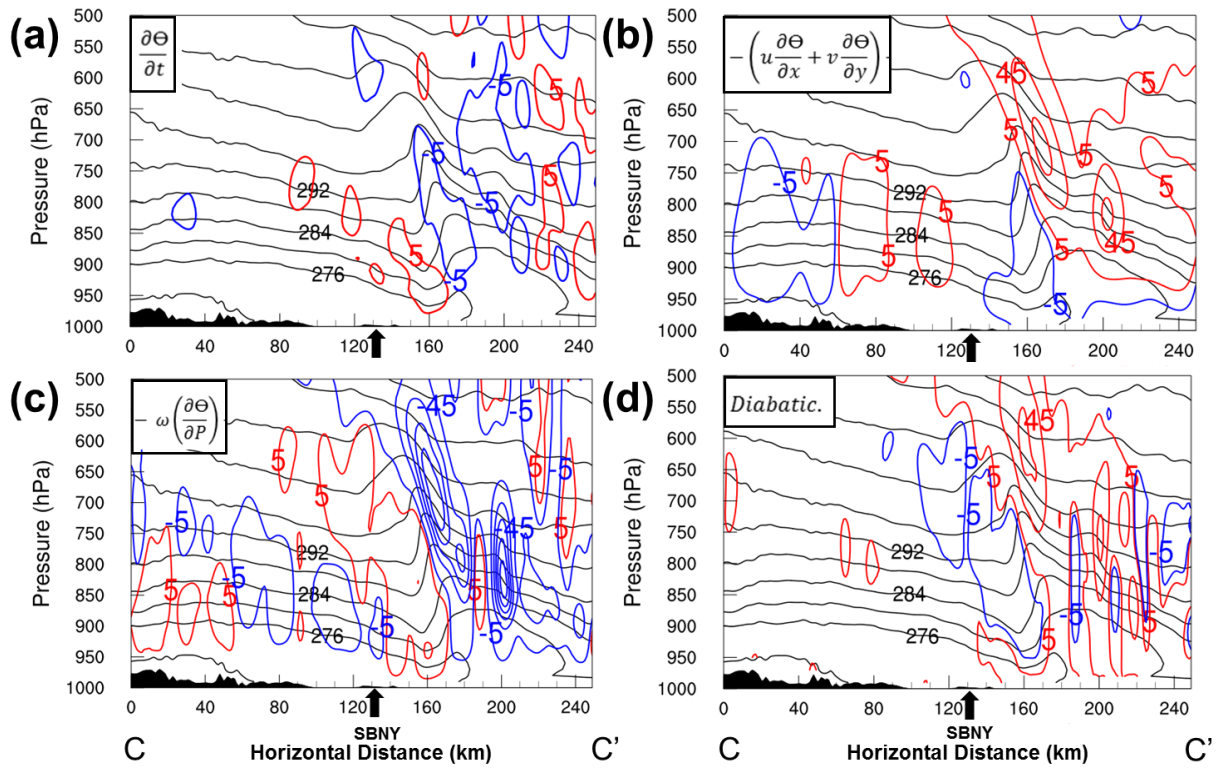

Figure 4.11. Cross-section from C to C' shown in Fig. 4.10a of potential temperature and the thermodynamic equation for the 24.5-h forecast valid at 0030 UTC 9 Feb separated by terms (a) the total change in potential temperature over 15 minutes, (b) the horizontal advection term, (c) the vertical advection term, and (d) the diabatic term that includes contributions from the microphysical scheme, radiative processes, and planetary boundary layer scheme. Positive values are contoured in red lines and negative values are contoured in blue lines. All terms are contoured from 5 x 10^{-4} K s^{-1} every 40 x 10^{-4} K s^{-1}. The approximate location of SBNY is indicated by the arrows.

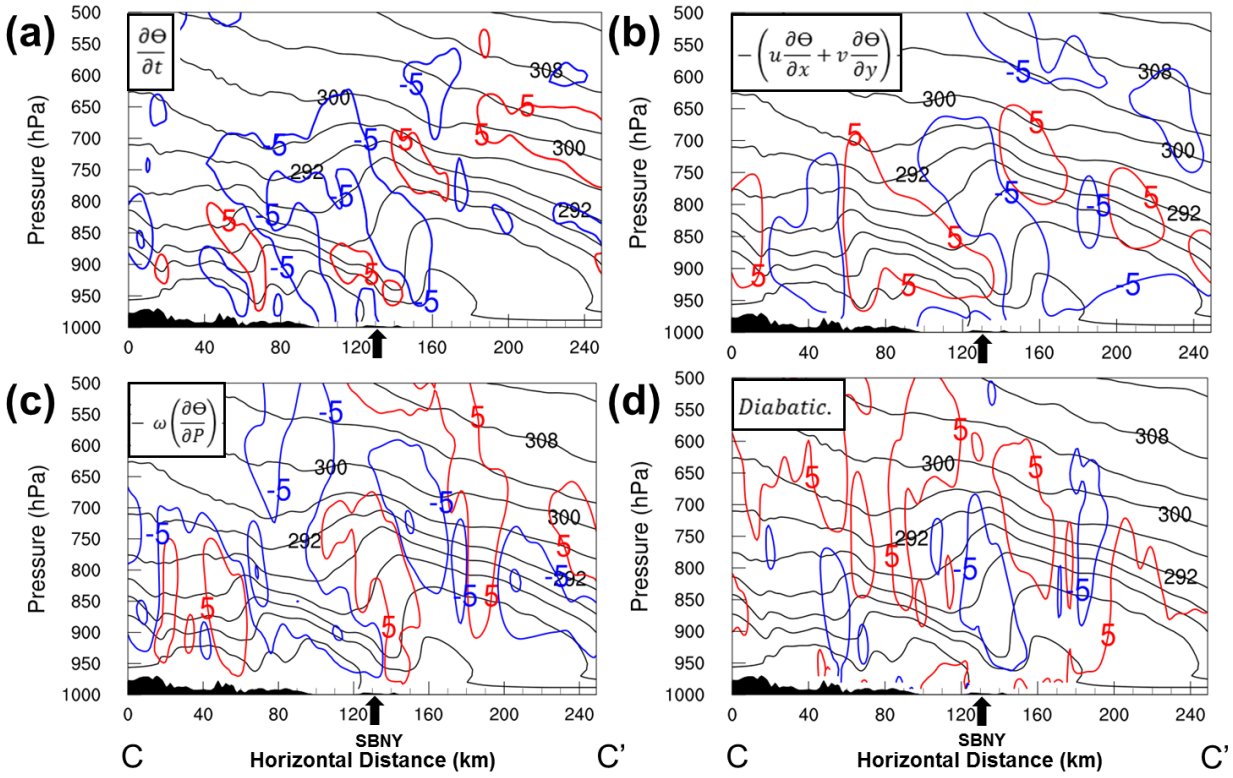

Figure 4.12. As in Fig. 4.11 but for the forecast hour 28 valid at 0400 UTC 9 Feb.

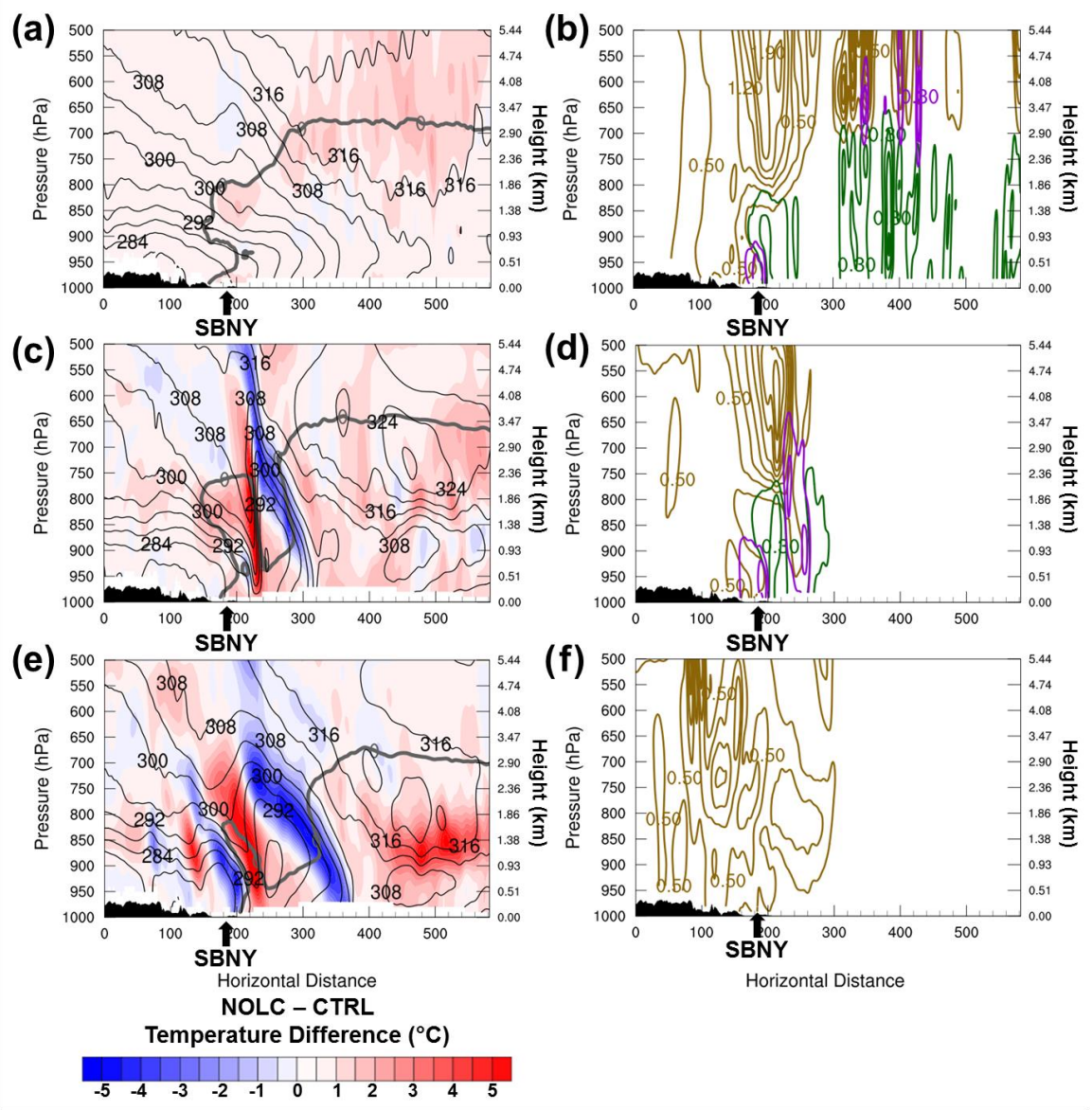

Figure 4.13. NOLC experimental simulation with the cooling contribution to the temperature tendency from melting, evaporation, and sublimation turned off starting at forecast hour 20 (2000 UTC 8 Feb 2013) showing (a, c, e) NOLC saturation equivalent potential temperature (K, black contours), NOLC 0°C (grey contour) and NOLC – CTRL temperature difference (°C, shaded every 0.5°C according to scale) and (b, d, f) NOLC snow mixing ratio (g kg^{-1}, gold contours from 0.15 g kg^{-1} by 0.35 g kg^{-1}), rain mixing ratio (g kg^{-1}, green contours every 0.15 g kg^{-1}), graupel mixing ratio (g kg^{-1}, purple contours every 0.15 g kg^{-1}) with results shown for (a, b) 2100 UTC, (c, d) 0100 UTC, and (e, f) 0400 UTC.

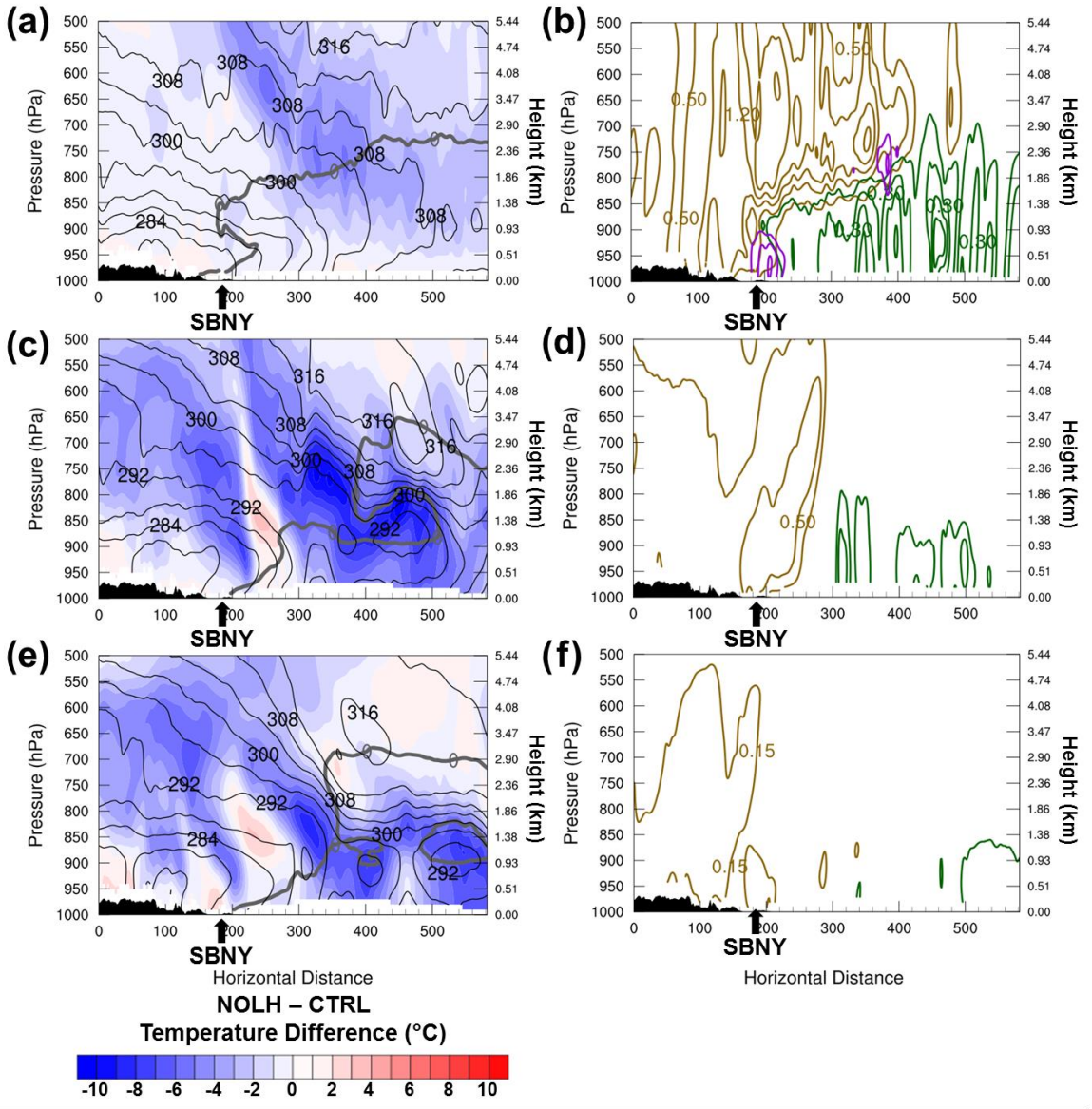

Figure 4.14. NOLH experimental simulation with the warming contribution to the temperature tendency from freezing, condensation, and deposition turned off starting at forecast hour 20 (2000 UTC 8 Feb 2013) showing (a, c, e) NOLH saturation equivalent potential temperature (K, black contours), NOLH 0°C (grey contour) and NOLH – CTRL temperature difference (°C, shaded every 1°C according to scale) and (b, d, f) NOLH snow mixing ratio (g kg^{-1}, gold contours from 0.15 g kg^{-1} by 0.35g kg^{-1}), rain mixing ratio (g kg^{-1}, green contours every 0.15 g kg^{-1}), graupel mixing ratio (g kg^{-1}, purple contours every 0.15 g kg^{-1}) with results shown for (a, b) 2100 UTC, (c, d) 0100 UTC, and (e, f) 0400 UTC.

Chapter 5:

Evolution of Single and Multi-banding during the 26–27 December 2010 Northeast U.S. Winter Storm

5.1 Introduction

The comma head of an extratropical cyclone can have both a single band and multi-bands. It is useful to investigate a case in detail to better understand the evolution of multi-bands and primary bands (e.g., Sanders and Bosart 1985a,b, Novak et al. 2008, Ganetis and Colle 2015). The 26–27 Dec 2010 event or the "Boxing Day Blizzard of 2010" is an exemplary case of both a primary band and multi-bands forming and maturing within the comma head of a Northeast U.S. winter storm. This chapter explores the following mechanisms that may be responsible for the genesis and maintenance of these multi-bands, including shear-induced circulations, frontogenetical forcing, and gravity waves. The lifecycle of both a strong primary band and a few robust multi-bands are analyzed to compare and contrast their thermodynamic evolutions.

Storms exhibiting both single and multi-bands (BOTH) were discussed in Chapters 2 and 3. The case of 26–27 Dec 2010 is also classified as a mature (MAT) cyclone with an apparent occlusion around the time of peak banding (0000–0300 UTC 27 Dec) with multi-band movement described as perpendicular to the long axis of the bands, or radial (RAD), while the primary band remained quasi-stationary after pivoting from the northeast quadrant into the northwest quadrant. The composites for BOTH cases within MAT cyclones showed that more amplified mid-to-upper-level height fields indicative of stronger cyclones with enhanced low-to-mid-level frontogenesis could lead to both types of bands. Theoretical work has shown that multiple bands could result from a vertical circulation breaking down into multiple circulations in a more unstable environment (Xu 1989, 1992). However, as illustrated in Chapter 3, the stability environment for BOTH cases in the northwest quadrant showed that both types of bands can occur in the presence of vertical and slantwise stable conditions. The analysis in that chapter may

have been unable to differentiate the environmental banding ingredients between the primary band and the multi-bands given the spatial and temporal coarseness of the CFSR and CFSv2 data (0.5° available every 6 h). This motivates additional analysis using a high-resolution mesoscale model. For example, the genesis of pre-existing convection by shear-induced turbulence and the potential for upscale growth into multi-bands or the role of gravity waves cannot be explored with 0.5° data. Recently, Rauber et al. (2017) found evidence of finescale wave activity at mid-levels along a sloping warm frontal zone that resulted in multiple bands of snowfall using the NCAR HIAPER Cloud Radar flown at an altitude at 12.8 km.

This chapter examines the formation and maintenance mechanisms of multi-bands within a detailed case study. The specific questions that will be examined are as follows:

- Do multi-bands form with similar ingredients as single bands, namely from frontogenetical circulations in an environment of weak slantwise stability?
- Do shear instabilities and gravity waves help generate multi-bands?
- Can multi-bands persist and amplify through diabatic heating and potential vorticity generation?

The Weather Research and Forecasting (WRF) model is used in conjunction with conventional observations to investigate the genesis, maturity, and decay of multi-bands in the case of 26–27 Dec 2010. Section 5.2 provides an overview of the model setup, verification methods, and tools used to analyze the banding environment. The synoptic and mesoscale evolution of this case is discussed in Section 5.3. Section 5.4 presents the lifecycle of the multi-bands and the single band that occurred in three distinct phases. The examination of the thermodynamic evolution of the primary band contrasted with that of the multi-bands is presented in Section 5.5. Section 5.6 summarizes what is found regarding multi-banding in this case study and is put into context with what was discussed in Chapter 3 and compared to what is known from previous studies of single banded snowfall.

5.2 Data and methods

a. Observations

Level II radar data from the KOKX WSR-88D (Fig. 5.1) is used in addition to the regional composite radar data discussed in Chapter 3. Level II data is converted into NetCDF format using the National Center for Atmospheric Research (NCAR) Research Applications Laboratory (RAL) radial radar software package, Radx (http://www.ral.ucar.edu/projects/titan/docs/radial_formats/radx.html) for reflectivity at constant elevation angle as well as vertical azimuth display (VAD) wind profiles. Upper-air profiles were used from KOKX and KCHH (Fig. 5.1) for analysis and verification of model output. The 0.5° latitude-longitude grid spacing NCEP Climate Forecast System Reanalysis (CFSR; Saha et al. 2010) was also used to subjectively verify the model output for such large-scale features as 500-hPa and 700-hPa trough placement and timing.

b. WRF model setup

The Weather Research and Forecasting (WRF-ARW) v. 3.6.1 was used to simulate the 26–27 Dec 2010 case using four one-way nested domains of 12, 4, 1.33, 0.44 km grid spacing with 40 vertical levels (Fig. 5.2c). Twenty-four experiments were conducted to test which configuration produced the most realistic results. These included four different initial and lateral boundary conditions comprised of the National Oceanic and Atmospheric Administration (NOAA) National Centers for Environmental Prediction (NCEP) Global Forecast System (GFS), North American Model (NAM), the Rapid Update Cycle (RUC; Benjamin et al. 2004) and the North American Regional Reanalysis (NARR; Mesinger et al. 2006). Two different planetary boundary layer (PBL) schemes that were tested included the Yonsei University (YSU; Hong et al. 2006) and the Mellor-Yamada-Janjic (MYJ; Janjic et al. 1994) scheme that employed non-local and local vertical mixing, respectively. Three different microphysical parameterization schemes tested included the Thompson (THOM; Thompson et al. 2008) single-moment, the Morrison double-moment (MORR; Morrison et al. 2009), and the WRF Single Moment 6-class (WSM6; Hong and Lim 2006) schemes.

1) VARIATIONS IN SIMULATED BAND STRUCTURE

This case exhibited a large, single band located in a fixed location over New Jersey to the northwest of several smaller, multi-bands that formed offshore of Long Island and moved towards the single band. The 24 simulations were assessed by whether or not they contained a period of a simulated single band coincident with smaller, multi-bands (Fig. 5.4). Five simulations initialized with the NAM and 1 initialized with the GFS did not simulate the single band either by not meeting the structure (L > 200 km of ≥ 5 dBZ over adjacent precipitation) or duration (> 1 h) criteria (Fig. 5.5). Ten out of 24 simulations did not simulate multi-bands successfully, defined as < 2 bands with L < 200 km with similar orientation and spacing with a duration of each band > 1 h (Fig. 5.5). All simulations using the NAM for initial and lateral boundary conditions did not contain multi-bands (Fig. 5.5). A qualitative assessment of the single and multi-bands structure and evolution as compared to observations found that the 32-km NARR as initial and lateral boundary conditions combined with YSU PBL scheme and MORR double-moment microphysical parameterization scheme yielded higher fidelity of simulated multi-bands compared to observations which was subjectively assessed (Figs. 5.4, 5.5). The simulation that produced the worst, or lack of, banded structure was the NAM-initialized simulation with the YSU PBL scheme and MORR microphysical parameterization scheme.

2) ANALYSIS OF BANDING INGREDIENTS

The environments produced within the 24 simulations are compared in order to identify differences that are resulting in the highly varied precipitation structures. The differences in simulated banding structure cannot easily be traced back to environmental differences. There are subtle differences in vertical profiles at KOKX of thermal and moisture variables among the simulations, all of which are similar to the observed profile (Fig. 5.6). This suggests that simulated bands may result from differences in other parameters, such as forcing mechanisms, rather than available stability and moisture. The comparison of 700-hPa frontogenesis from each simulation showed that the location of the frontogenesis maxima is closely related to band location (Fig. 5.7). For simulations resulting in widespread, disorganized convection, frontogenesis values were large near the primary band over NJ and multi-banding region 200-km offshore (Fig. 5.7). For simulations with higher reflectivity values offshore with a weaker single band, frontogenesis values are higher in the multi-banding region offshore and weaker to the

northwest collocated with the absence of the single band (Fig. 5.7). The simulations with the best primary band and multi-bands had larger values of frontogenesis near the primary band with spaced-out, weaker values in the multi-banding region.

Cross sections through the primary band and into the multi-banding environment are analyzed for the "best" and "worst" simulations, i.e., the NARR_YSU_MORR and the NAM_YSU_MORR simulations (Figs. 5.8, 5.9). The "best" simulation shows multi-bands on the warm side of a sloping frontal zone in an environment of 850–800-hPa frontogenetical forcing and CSI (Fig. 5.8). The "worst" simulation did not contain multi-bands, but the same region was also associated with a sloping frontal zone with height but ~10 K km^{-1} h^{-1} larger values of frontogenesis maximized about 50-hPa lower at 850 hPa but ~10 K km^{-1} h^{-1} weaker frontogenesis in the primary band region (Fig. 5.9). The "worst" simulation also is more stable from the surface to 500-hPa in the primary band region than the "best" simulation which shows weakened stability between 600–400 hPa (Figs. 5.8, 5.9). This analysis suggests that the single band and multi-bands result from a sloping frontal zone with decreased mid-level stability and frontogenetical ascent of near-equal magnitudes in both the primary band and multi-band environments.

The evolution of banding ingredients of moisture, frontogenetical forcing, and CSI are assessed through time series calculations averaged within ~200 km^2 boxes from 800–500 hPa of the primary band and multi-band region for all 24 simulations (Fig. 5.10). The primary band environment exhibited little variation in relative humidity (> 80%), but the relative humidity within the multi-band environment trended closely with initial condition used (Figs. 5.10b,c). The NARR-initialized simulations showed a reduction in relative humidity in the multi-banding region to ~60% by 0000 UTC 27 Dec near the time of the observed dry intrusion, with a few GFS- and RUC-initialized simulations capturing this moisture reduction 2–5 h later (Fig. 5.10b). The simulations that had more widespread precipitation that lacked banded structure maintained > 80% relative humidity values throughout the time period (Fig. 5.10b). Frontogenesis values within the primary band environment varied little, but ~0 K 100 km^{-1} h^{-1} was found with some GFS- and NAM-initialized simulations that failed to capture the primary band (Fig. 5.10d). This is consistent with what was discussed with the NONE classification in Chapter 3, as having frontogenesis be a required banding ingredient in order to concentrate the precipitation into bands. Frontogenesis within the multi-banding environment was either too large (most RUC-

initialized simulations) or too weak (most NAM-initialized simulations) (Fig. 5.10e). The simulations that resolved multi-bands exhibited a short duration of enhanced frontogenesis after 0000 UTC 27 Dec (Fig. 5.10e). The primary band environment was associated with CSI after 0000 UTC 27 Dec for all simulations except for the NAM-initialized simulations, which had the "worst" simulation that was too stable (Fig. 5.10f). The multi-banded region exhibited weak CSI after 0200 UTC 27 Dec (Fig. 5.10g).

3) SELECTION OF REPRESENTATIVE SIMULATION

The 32-km NARR as initial and lateral boundary conditions combined with YSU PBL scheme and MORR double-moment microphysical parameterization was subjectively assessed as being the most representative simulation when comparing simulated band structure and evolution to observations (Fig. 5.4). Additional examination of the banded environment when compared with a poor simulation showed that subtle differences in forcing and stability resulted in a more representative simulation. The primary band environment and multi-band environment were assessed to be resulting from a sloping frontal zone with weakened stability above levels of maximum frontogenetical forcing. Variations in magnitude and location of the frontogenesis maxima and the degree of stability within the other simulations produced less accurate banded structures compared to observations. As such, the NARR-YSU-MORR simulation was determined to be the "best" and was chosen for additional analysis within this case study. Table 5.1 outlines the physics and other attributes of this simulation that will be used in the following sections.

5.3 Case overview

A series of snowbands produced 12–32 inches (30.5–81.2 cm) of storm total snowfall with rates approaching 3 in h^{-1} (7.62 cm h^{-1}) and wind gusts up to 70 mph (60.8 kts) in the NYC metropolitan area from 1500 UTC 26 – 1200 UTC 27 Dec 2010. A deep, cutoff 500-hPa trough was located over West Virginia to North Carolina with an amplified coupled 250-hPa jet located off the Delmarva coast at 1800 UTC 26 Dec (Fig. 5.11a). A closed 700-hPa low was situated over Virginia with ~26 m s^{-1} (50 kt) flow off the Atlantic bringing air with a higher moisture

content (i.e., higher equivalent potential temperature, θ_e) towards the north and west of the 985-hPa surface low (Figs. 5.11b–d). The associated low pressure system developed in the Gulf of Mexico and matured as it moved up the U.S. Eastern Seaboard deepening to 964 hPa off the coast of Cape Cod by 1200 UTC 27 Dec (Fig. 5.3). While south of Long Island during the region's banded snowfall between 1800 UTC 26 – 0600 UTC 27 Dec, the system exhibited a comma head structure with a well-defined dry intrusion slightly east of the deeper comma head clouds that was reproduced in the simulation (Figs. 5.2, 5.12).

By 0000 UTC 27 Dec, the 500-hPa cutoff trough continued to deepen as it moved eastward towards the coast, with the left exit region of the 250-hPa jet core providing additional means for the cyclone to deepen to 979 hPa (Figs. 5.13a,d). The closed 700-hPa low was nearly vertically-stacked with the surface low offshore with cyclonic flow advecting higher θ_e air into the northwest quadrant of the system where the primary band was located at this time (Figs. 5.13b,d). The 850-hPa baroclinic zone exhibits the tightest gradient along the poleward edge of the higher 700-hPa θ_e air, with lower values of θe to the east indicative of the dry intrusion (Figs. 5.13c,d). By 0300 UTC 27 Dec, the time during which robust multi-bands and a single band were present in the simulation, the system is vertically-stacked from the 975-hPa surface low to the 500-hPa closed low (Figs. 5.14a,b,d). The dry intrusion is present in the 700-hPa θ_e east of higher θ_e values extending into the northwest quadrant collocated with the 850-hPa (> 10°C 100 km^{-1}) baroclinic zone (Figs. 5.14c,d). At 0600 UTC 27 Dec, the vertically-stacked 971 hPa surface through 500-hPa low tracked to the northeast where it ceased to intensify (not shown).

5.4 Observed and simulated multi-bands

Snowbands evolved as three distinct phases related to primary and multi-band genesis and maturity provided in Table 5.2. The WRF simulation produced realistic results of the evolution of the precipitation banding within this case and these three main phases. However, the model is ~2 hours slow with the band evolution, and thus a 2 h later forecast hour (FH) is used to compare with the observed structures. Phase 1 occurred from 1500 UTC 26 Dec – 2100 UTC 27 Dec (FH 11–17, 1700–2300 UTC 26 Dec) and consisted of primary band genesis south of Long Island and then it pivoted to its quasi-stationary position over NJ during its maturity by 2100 UTC 26 Dec (FH 17, 2300 UTC 26 Dec). Figures 5.15a,b show the simulated primary band

located ~75 km eastward of the observed primary band with similar size and intensity. Phase 2 occurred from 2100-0300 UTC (FH 17–23, 2300–0500 UTC), and it consisted of primary band maturity as well as multiple band genesis as cells south of Long Island growing into multiple bands with lengths ≥ 50 km. Figures 5.15c,d show the primary band remaining quasi-stationary from the previous phase and several multi-bands to its east across Long Island, NY and offshore. The simulated multi-bands had comparable intensities as observed but the simulated widths were about ~10 km smaller than the observed multi-bands. Phase 3 occurred from 0300–0600 UTC (FH 23–24, 0500–0600 UTC) and contained the decay of all bands as the parent low pressure system weakened via occlusion and moved away towards the northeast. Figures 5.15e,f show the weakening of multi-bands in the region before the primary band begins to decay.

The multi-bands formed at a quasi-stationary location ~100 km offshore south of Long Island. The bands moved from their genesis location towards the northwest where some merged with the primary band between 2200 26 Dec and 0500 UTC 27 Dec. Hovmöller diagrams of the observed and simulated reflectivity data perpendicular to the band movement highlight the movement of the bands (Figs. 5.16a,c,e). The observed multi-bands formed around 2100 UTC 26 Dec and moved following the 700-hPa flow towards the quasi-stationary single band over NJ by 0300 UTC 27 Dec (Fig. 5.16b). The formation and movement of multi-bands were simulated by the 1.33-km and 444-m WRF simulations with band genesis around 0100 UTC 27 Dec and aggregation with the primary band around 0400 UTC 27 Dec (Figs. 5.16d,f). The largest domain with 4-km and 12-km grid spacing did not simulate individual multi-bands, but rather a broad region of enhanced precipitation with no separation into bands (not shown). The 1.33-km domain will be used in the analysis in the following section in lieu of the 444-m results as both domains produced very similar primary bands and multi-bands (not shown). The simulated bands from the 444-m domain were similar in size, shape, and intensity to those of the 1.33-km domain, but did produce more small (< 5 km width) cells offshore east of the multi-band genesis region than the 1.33-km domain (not shown).

5.5 Evolution of single and multi-bands

a. Primary band

1) BAND GENESIS

The primary band formed on the northern side of a rapidly developing cyclone at approximately 1430 UTC 26 Dec in an area of weak low-to-mid-level baroclinicity (Fig. 5.17). At this time, the band resulted from weak ascent along the warm side of the developing baroclinic zone (Fig. 5.18). Once formed, the primary band intensifies while the cyclone rapidly deepened off the East Coast and the band pivoted to a nearly quasi-stationary location over western Long Island and New Jersey by 1800 UTC 26 Dec (Figs. 5.15b).

Prior to reaching its maximum intensity and the formation of multi-bands at 2200 UTC 26 Dec, the primary band was located in a 700-hPa trough extending northward from the closed low to the south, on the cold side of a 8 K 100 km^{-1} 850-hPa temperature gradient, and near a 700-hPa equivalent potential temperature gradient of ~10 K 100 km^{-1} (Figs. 5.19a–c). A cross section through the primary band indicates an intensifying sloping frontogenesis maximum into the cold air from 900 hPa to 650 hPa, with ascent in a layer of weak stability between 650 hPa and 300 hPa (Figs. 5.20a,b).

2) BAND MATURITY

The primary band reached peak intensity and organization during Phase 2 from 0100 UTC – 0500 UTC Dec 2010. By 0200 UTC, the 974-hPa low had intensified by ~10 hPa but remained quasi-stationary since 2200 UTC 26 Dec (Figs. 5.19c, 5.21c). This coincided with an increasing moisture gradient ~150 km off the southern shore of Long Island resulting from the dry air intrusion at 700-hPa (Figs. 5.19c, 5.21c). A cross section through this environment showed that near the southeastern point, a layer of conditional instability is present between 750–600 hPa likely due to this dry intrusion (Fig. 5.22a).

A cross section through the primary band at 0200 UTC 27 Dec revealed that the band had remained in an environment with a 850–650-hPa frontogenesis maximum and ascent along the warm side maximized in a region of weak conditional stability between 550 and 450 hPa (Fig. 5.23). The single band is associated with an amplified pattern in θ_e^* at 700 hPa which was also seen with the primary band within the 8–9 Feb 2013 case in Chapter 4. This is attributed to upward vertical motion of cooler and drier air and downward vertical motion of diabatically

warmer and moister air within the band circulation. A backwards trajectory launched from the 800 hPa within the primary band at 0200 UTC warmed by 2 K as it descended 200 m attributed to deposition given by the decreasing vapor mixing ratio by 0.1 g kg^{-1} and increase in snow mixing ratio by 0.3 g kg^{-1} (Figs. 5.24b,c).

3) BAND DECAY

The period of band decay during Phase 3 after 0500 UTC 27 Dec was determined by the time when the maximum reflectivity associated with the primary band decreased by 5 dB*Z* and started to lose a linear structure (Fig. 5.25d). The environment became less favorable for the maintenance of the primary band, including a weakening of the low-to-mid-level baroclinic zone in the northwest quadrant of the cyclone while intensifying in the southwest quadrant (Figs. 5.25b,c, 5.26b). After 0500 UTC, the 800–700-hPa averaged frontogenesis values within the primary band was remaining steady around 20 K 100 km^{-1} h^{-1} but both environment became increasingly stable to vertical motions indicated by the 650–700-hPa layer difference of θ_e^* > 2 K likely because of the stabilization of the frontogenetical circulation (Figs. 5.27,a,b). The environment also exhibited near zero vertical motion with weak (~0 K s^{-1}) diabatic tendency in the 550-600-hPa layer (Figs. 5.27c,d).

b. Multi-bands

1) BAND GENESIS

The genesis and organization of multi-bands underwent a more complex evolution than the primary band. Between 1900–2200 UTC 26 Dec, the multi-bands genesis region ~200 km southeast of the primary band was free from precipitating structures (i.e., bands or cells) following the passage and pivot of the primary band and the beginning of a dry intrusion by the cyclonically-wrapping mid-level flow (Figs. 5.15b, 5.19, 5.20a). At 2200 UTC, a stable layer is found between 900 and 700 hPa (Figs. 5.20b,d). This stable layer coincides with large values of frontogenesis and diabatic heating, which favored convective cell genesis within the multi-band development region ~200 km southeast of the primary band (Figs. 5.20b,c).

The genesis of these precursor cells resulted from a combination of enhanced low-level convergence along a baroclinic zone, weak conditional stability, and shear-induced instability. One particular multi-band was manually traced every 15 minutes back to its antecedent cell in order to examine how the cells were triggered and grew upscale into bands. This upscale growth has been shown to occur from the latent heat release within a layer of weak stability within cumulus clouds that grow upscale into rain bands oriented parallel to the along-band shear and across-band baroclinicity through a feedback process discussed by Jascourt et al. (1988).

At 2215 UTC 26 Dec, ~30 min prior to the formation of a cell, relatively strong (30 kts) of 950–700-hPa vertical wind shear with nearly 180° of directional shear coincides with enhanced convergence (15×10^{-4} s^{-1}) along a near-surface frontal zone with frontogenesis values exceeding 45 K 100 km^{-1} h^{-1} (Fig. 5.28). The pre-cell environment showed moderate diabatic heating (10 K s^{-1}) resulting in the diabatic generation of positive potential vorticity (PV) (Figs. 5.28e,f). This is likely due to condensation of vapor into cloud water that is not yet precipitating (not shown).By 2245 UTC, a cell formed likely from strong (> 75 K 100 km^{-1} h^{-1}) surface to 950-hPa frontogenesis, capped at 800 hPa with its ~1 m s^{-1} updraft maximized around 900 hPa (Figs. 5.29a–d). Collocated with the cell, a PV dipole of both positive and negative PV is present centered around the updraft at 900 hPa (Figs. 5.29d–f). The PV dipoles may arise from pre-existing shear-generated vorticity in the presence of a moist updraft that leads to the diabatic conversion of latent vorticity to relative vorticity, the combination of which results in the horizontal orientation of the PV maximum and minimum (Chagnon and Gray 2009). Considering the PV dipole and cell exist below the maximum in directional and speed shear (30–35 kts) from 700–900 hPa suggests that the PV dipole is resulting from these processes (Figs. 5.29f, 5.30).

Antecedent multi-band cells were still being triggered offshore at 0000 UTC 27 Dec. At this time, the multi-band development region was collocated with an enhanced 850-hPa temperature gradient (~8 K 100 km^{-1}) and the western boundary of the mid-level dry intrusion (Figs. 5.13c,d). A cross section through the same multi-band precursor cell at 0000 UTC 27 Dec shows a 850–700 hPa frontogenesis maxima of 30 K 100 km^{-1} h^{-1} with 1.6×10^{-3} s^{-1} 850-hPa convergence and a ~1 m s^{-1} updraft at 750 hPa (Figs. 5.31b,d). The cell extends to 750 hPa with a positive diabatic heating tendency (~4×10^{-3} K s^{-1}) below likely from 750-800 hPa condensation because temperatures are > 0°C (Figs. 5.31c,e). A horizontal PV dipole is still centered on the updraft at 750 hPa (Fig. 5.31f). By 0100 UTC, some cells have grown upscale

into bands and their corresponding PV dipoles have also acquired a linear structure (Fig. 5.32a). This is due to this region coinciding with large values of 700-hPa total deformation (> 50 x 10^{-5} s^{-1}) along the 900–700-hPa vertical wind shear vector (Fig. 5.32).

Gravity waves are hypothesized to be a potential triggering mechanism of multi-band genesis. Recent work by Hoban et al. (2017) suggests that gravity waves may travel faster than the bands themselves, suggesting that they may be responsible for lifting air parcels to saturation and the resultant precipitation may travel slower (e.g., at the advective or steering speed) than the waves. Analysis of the band speeds was comparable to the speed of potential vorticity anomalies, both of which were approximately the 10 m s^{-1} steering flow of the 700-hPa wind (not shown). The PV dipoles and multi-bands are wave-like in appearance and emanate from convection forming along a frontal zone, initially capped by a stable layer (Figs. 5.25a, 5.26d, 5.27d).

The precursor cells continued to grow upscale into multi-bands during Phase 2 between 0100–0500 UTC. At 0200 UTC 27 Dec, the multi-bands genesis region ~200 km off the southern shore of Long Island discussed in Section 5.5a continued to generate convection at the boundary between high 700-hPa θ_e air and the dry intrusion as individual bands moved towards the northwest following the 700-hPa steering flow (Figs. 5.24a,c,d). This region coincided with fractured frontogenesis maxima between the surface and 600 hPa in an environment of conditional instability between 700 and 600 hPa (Figs. 5.22a,b).

2) BAND MATURITY

The multi-bands continued to grow larger in scale with time and became elongated into bands. All multi-bands that formed during Phase 2 coincided with PV dipoles implying consistent shear and upward motion in the model-resolved bands that may have helped maintain the bands. These features were oriented parallel to the 900–700-hPa wind shear and moved in the same direction as the 700-hPa wind (Figs. 5.21a, 5.32a). A cross section through a mature multi-band at 0200 UTC showed that the horizontal PV dipole is centered on the ~1.5 m s^{-1} updraft indicating that the environmental shear is large between 500–800 hPa (Figs. 5.33d,f). Without the vertical wind shear, there would be no dipole structure like is seen in the environment of the primary band from 500–700 hPa (Fig. 5.23e).

The mature multi-bands did not weaken as they moved from the band genesis region to

the northwest towards the primary band following the 700-hPa flow. Localized diabatic heating can reduce stability (i.e. vertical potential temperature gradients) above the level of maximum heating within a band environment which can increase horizontal convergence with localized height falls and intensify a band by intensifying the upward vertical motions (Novak et al. 2009). A cross section through a mature multi-band at 0200 UTC 27 Dec shows that there is a diabatic heating maxima at approximately 650-hPa with reduced absolute stability and conditional stability apparent from that level to 525-hPa (Figs. 5.33a,c). The 650-hPa diabatic heating maximum coincides with a maximum of convergence values 1.5 x 10^{-3} s^{-1} between 750–650 hPa and an updraft of 1.6 m s^{-1} (Figs. 5.33d,e).

3) BAND DECAY

The period of band decay during Phase 3 after 0500 UTC 27 Dec was determined by the time the multi-bands in the region to the east of the primary band were losing their linear structure. The environment became less favorable for the maintenance of the multi-bands for the same reasons as mentioned in Section 5.5a. After 0500 UTC, there were still measurable values of frontogenesis but the environment had stabilized likely from the frontogenetical circulation (Figs. 5.27,a,b). The multi-band environment also exhibited near zero vertical motion with weak (~0 K s^{-1}) diabatic tendency in the 550–600-hPa layer (Figs. 5.27c,d). The cyclone continued to track towards the northeast while stagnating in intensity at around 972 hPa (Fig. 5.3).

5.6 Summary and discussion

A high-resolution mesoscale model is used to explore the evolution of single and multi-bands in the case of 26–27 Dec 2010. The single band that formed in this case is similar to those that form in the northwest quadrants of mature cyclones such that it is associated with a frontogenesis maximum sloping into the cold air with height with maximum ascent on the warm side, concentrating the ageostrophic circulation in a layer of decreased stability (Novak et al. 2009, 2010).

The multi-bands form in response to the combination of shear-induced circulations and mid-level convergence in a conditionally unstable environment in a region of a large horizontal

moisture gradient attributed to the dry intrusion. The time during multi-band genesis coincides with larger positive 500–900-hPa shear values (50 kts) than the primary band (-40 kts) development time prior to 0000 UTC 27 Dec (Fig. 5.27e). Due to the highly-sheared environment producing relative vorticity, a moist updraft can effectively convert latent vorticity to relative vorticity, producing a horizontal potential vorticity (PV) dipole (Raymond and Jiang 1990; Raymond 1992; Chagnon and Gray 2009). The multi-bands were associated with these linear PV dipoles centered on each updraft of a cell that grows upscale and deformed into band by the 700-hPa wind. These cells are located in the boundary layer and are different than the cloud-top generating cells of Rosenow et al. (2014) that were found to produce bands in the comma head of continental cyclones. The multi-bands and the horizontal PV dipoles were wave-like in appearance and are found along a sloping, stable frontal boundary. Such structures were not present for the primary band. The multi-bands move from their genesis location by the 700-hPa steering flow allowing for the formation of new bands with consistent spacing, unlike the single band that remains fixed to a 700-hPa frontogenesis maximum. The movement following the cross-band wind and orientation parallel to the along-band wind shear in the convective layer is consistent with what was found by Jascourt et al. (1988) with multiple rainbands. Latent heating and cooling within the multi-bands is shown to increase their intensity and duration by contributing to localized height falls that likely enhance horizontal convergence and upward vertical motions. This was also true for the primary band in this chapter as well as the primary band shown in Novak et al. (2009), but on a weaker and larger spatial scale compared to the multi-bands.

There were some notable differences between the stability evolutions of the primary band and multi-bands. Although both types of bands formed in a sloping frontal zone in the comma head to the northwest of a surface cyclone, the multi-bands formed along the boundary between the higher 700-hPa θ_e air in the comma head associated with the cyclonically-turning branch of the warm conveyor belt and the dry intrusion. As a result, this multi-banded region was collocated with CI than the primary band environment between 850–500-hPa. This supports the theory by Xu (1992) that states that a single band may form within more stable conditions, but multiple bands require instability.

The forcing responsible for the primary band and multi-bands is found to be different. Layer-averaged frontogenesis values are consistently weaker for the analyzed multi-band than

the primary band by at most 10 K 100 km^{-1} h^{-1} but is largest during band genesis suggesting that frontogenesis may play a brief role in the initial genesis of the multi-bands but is not responsible for the maintenance of these bands (Fig. 5.27a). This corresponds with the case of Shields et al. (1991) that showed intermittent thermally direct circulations induced by geostrophic imbalance caused by frontogenesis that resulted in multiple snowbands. After the multi-bands reached maturity at 0200 UTC 27 Dec, the multi-band environment was comparable to that of the primary band. Prior to 0200 UTC, the differences in the initial environments suggest that multi-bands formed through different processes, such as the shear-enhanced convection. As the multi-bands mature, the environment becomes more similar to the primary band until their decay.

The analysis of the environment of the multi-bands in this case study adds to what is discussed in Chapter 3. Specifically, that for BOTH cases like this case, multi-bands would be expected to form on the warm side of a low-to-mid-level baroclinic zone in the northwest of a surface low pressure center but closer to the low than the primary band. Multi-bands form different mechanisms but grow to resemble the primary band environment as they are steered toward and merge with the primary band. Therefore, this reinforces the difficulty in separating the environments of individual band types within BOTH cases, especially with 0.5° data.

Future work could analyze the mechanisms associated with multi-bands in similar cases within the dataset provided in Chapters 2 and 3 such as 5–6 Dec 2003, 11–12 Feb 2006, and 2–3 March 2010 with the goal of comparing the band and PV structures to those seen in this case. Another avenue to explore the role of the moist updraft in converting latent vorticity to relative vorticity in the highly-sheared multi-band genesis environment would be to run this case simulation with diabatic contributions turned off. If this latent vorticity component is not important to the formation of the PV dipoles, then the PV and multi-band structures would remain the same as the control simulation presented in this chapter. Otherwise, it is expected that the PV dipoles would not form and therefore the multi-bands may not result but rather widespread scattered cellular convection would dominate due to the available instability (Chagnon and Gray 2009).

Table 5.1. WRF model setup for most representative simulation of the case study of 26–27 Dec 2010.

Initial / Lateral Boundary Conditions	NARR
Simulation Times	0600–0600 UTC 26–27 Dec 2010
Microphysics Scheme	Morrison 2-moment
Planetary Boundary Layer Scheme	YSU
Horizontal Grid Spacing	12, 4, 1.33, 0.44 km
Number of vertical levels	40
Time steps	36, 12, 4, 1 s
Cumulus Parameterization Scheme	BMJ, none, none, none
Longwave Radiation Scheme	RRTM
Shortwave Radiation Scheme	Dudhia
Land surface scheme	Noah-MP

Table 5.2. Observed and simulated phases of both single and multi-bands in the 26–27 Dec 2010 case.

Phase	Description	Observed Times	Simulated Times
1	Primary band genesis and pivot	15–21 UTC 26 Dec	FH 11–17 17–23 UTC 26 Dec
2	Primary band maturity and multi-band genesis and maturity	21 UTC 26 – 03 UTC 27 Dec	FH 17–23 23 UTC 26 – 05 UTC 27 Dec
3	Band decay	03–06 UTC 27 Dec	FH 23–24 05–06 UTC 27 Dec

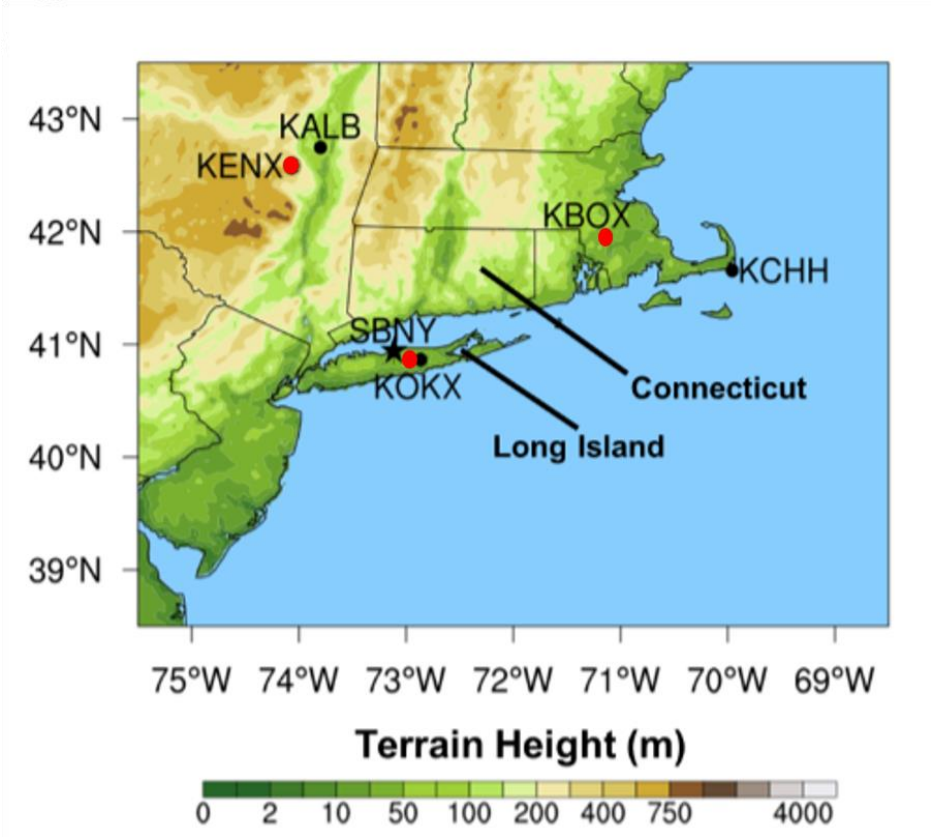

Figure 5.1. Map showing location of radar (red markers) and upper-air locations (black markers) used in this study.

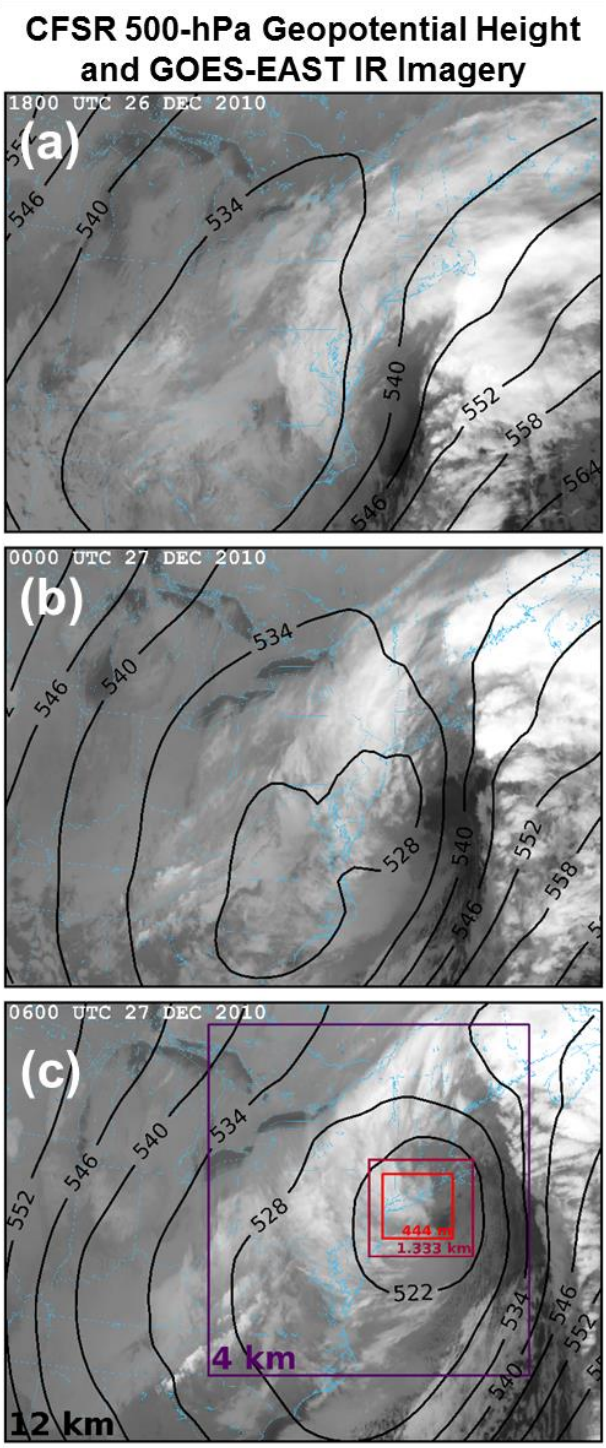

Figure 5.2. GOES-EAST Infrared (IR) satellite imagery (shaded) with 500-hPa geopotential heights (contoured every 4 dam) from the CFSR for (a) 1800 UTC 26 Dec, (b) 0000 UTC 27 Dec, (c) 0600 UTC 27 Dec. The four nested domains (12, 4, 1.33, 0.44 km) used in the WRF modeling are shown in panel c.

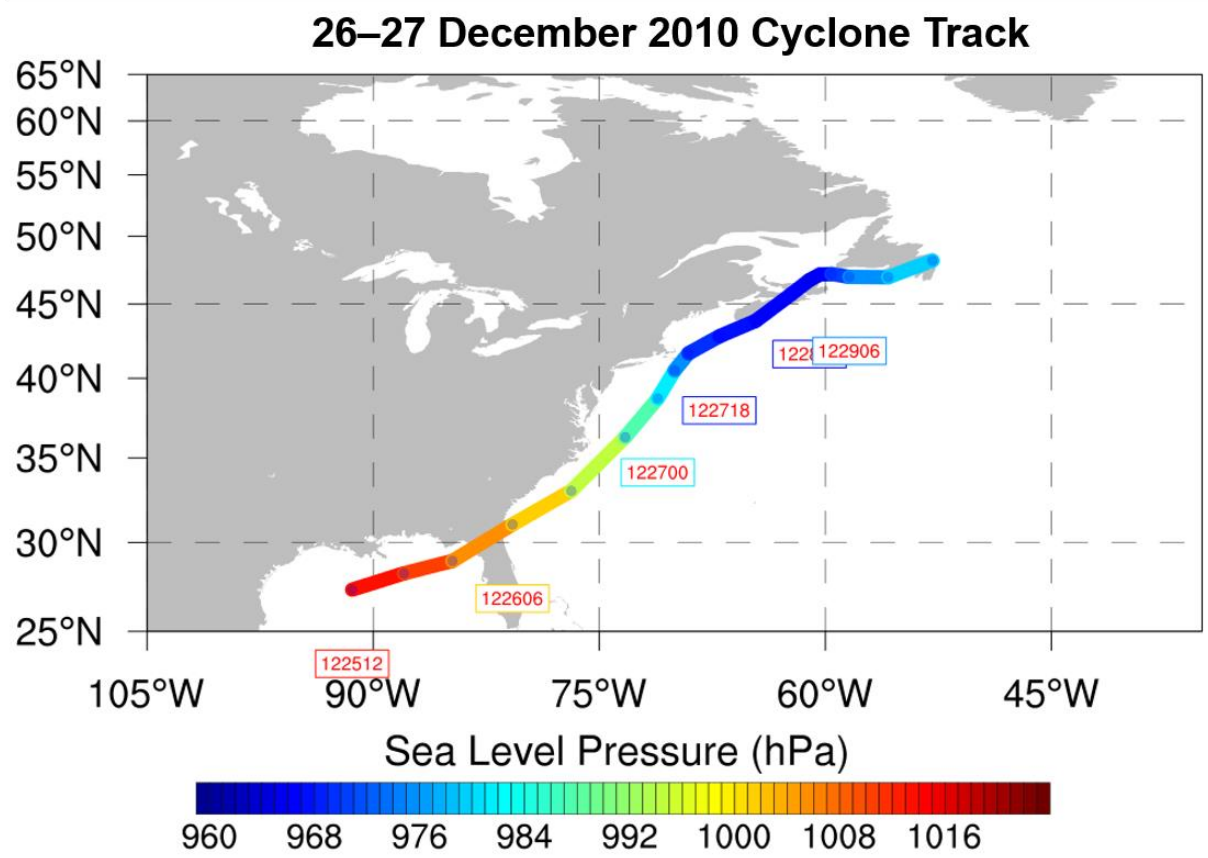

Figure 5.3. Sea level pressure (hPa, shaded according to scale) along the cyclone track of the 26–27 Dec 2010 NEUS winter storm.

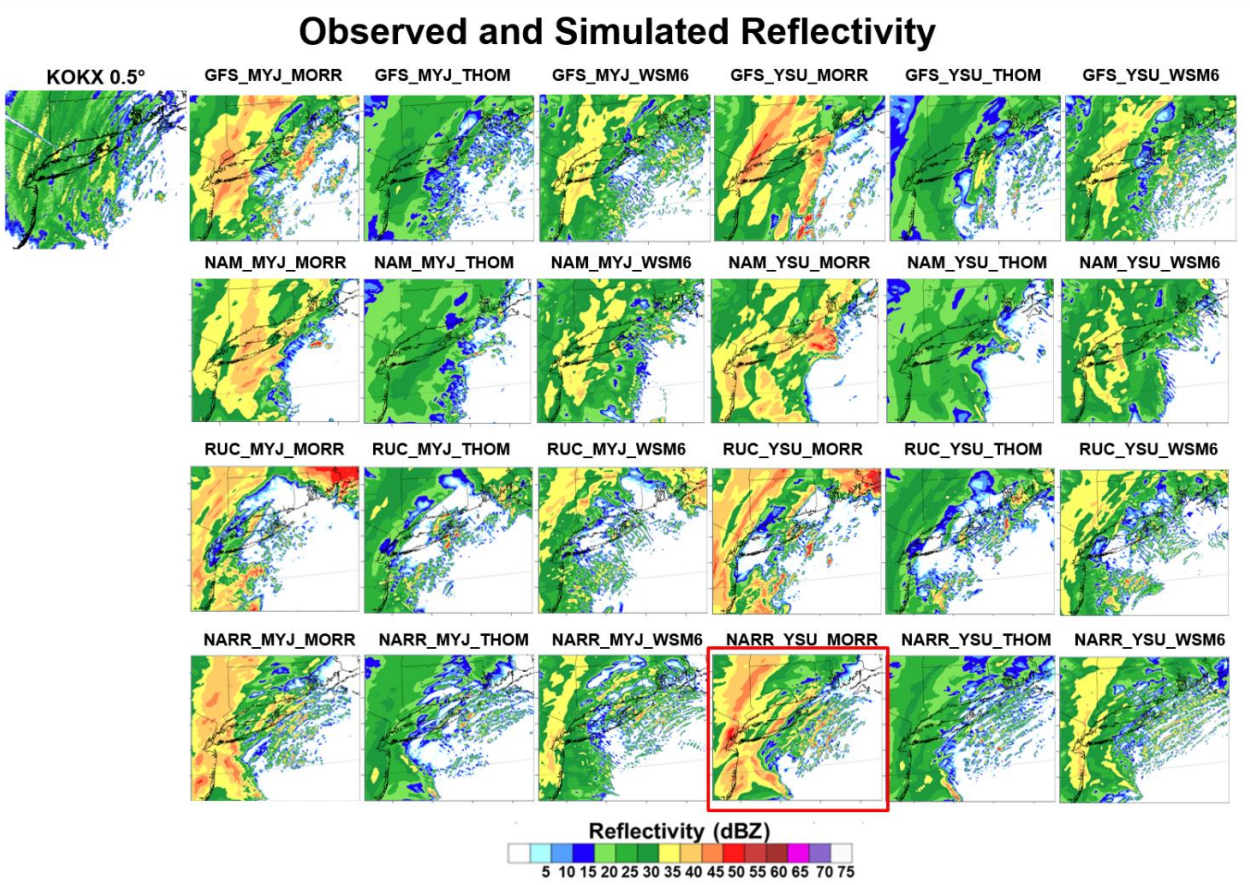

Figure 5.4. Observed and simulated reflectivity showing the range of position and intensity of the primary band. The 24 simulations shown were comprised of 4 separate initial and lateral boundary conditions, 2 planetary boundary layer schemes, and 3 microphysical parameterization schemes. Each row corresponds to a single initial condition. The columns represent the same combination of planetary boundary layer and microphysical parameterization schemes. The most representative simulation used in this case study is highlighted by a red box.

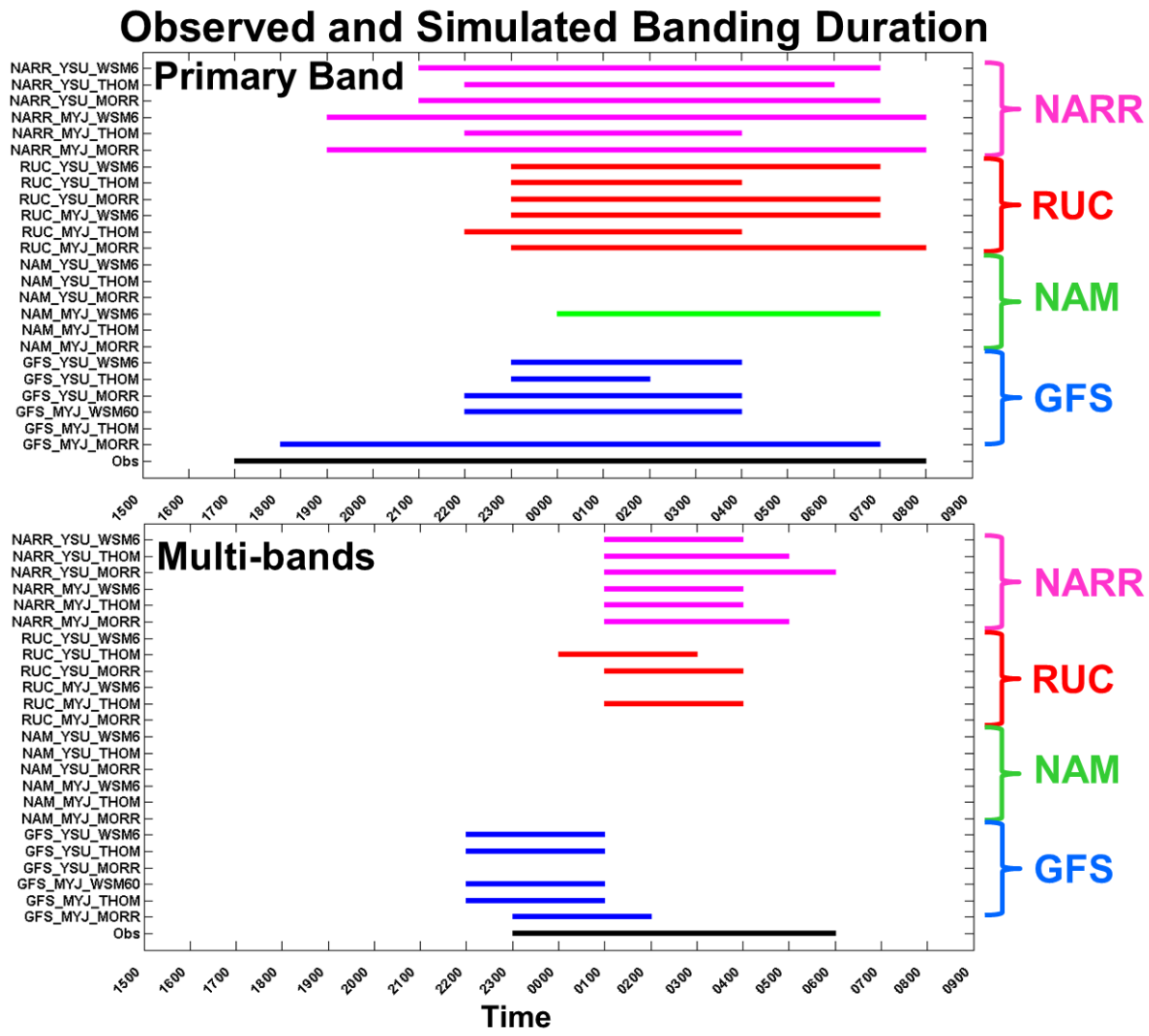

Figure 5.5. Comparison of observed and simulated (top panel) primary band and (bottom panel) multi-band duration. The observed timing and duration is indicated by the black line. The 24 simulations are colored by initial and lateral boundary conditions of NARR (pink), RUC (red), NAM (green), GFS (blue).

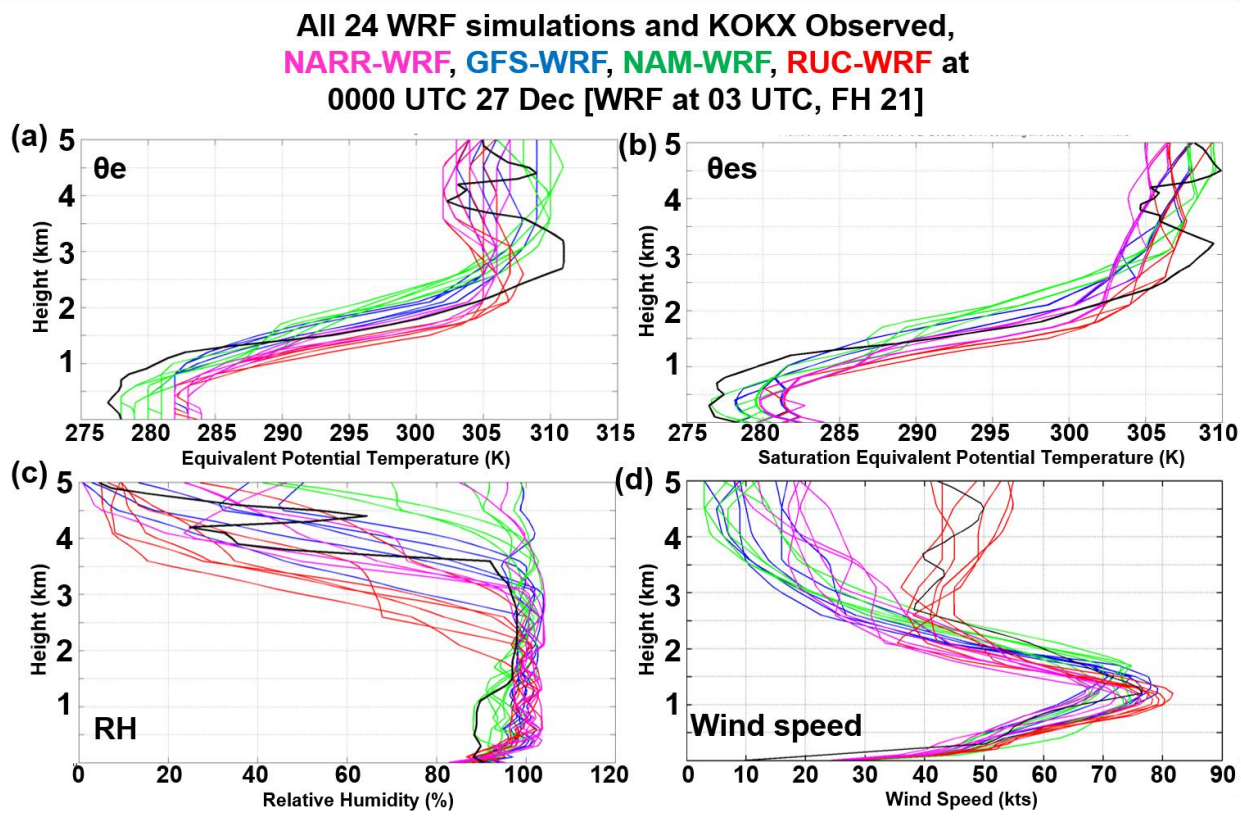

Figure 5.6. Observed profiles (black) of (a) equivalent potential temperature (K), (b) saturation equivalent potential temperature (K), (c) relative humidity (%), and (d) wind speed (kts) at 0000 UTC 27 Dec. Simulated profiles are colored by initial condition of NARR (pink), RUC (red), NAM (green), GFS (blue).NAM (green), GFS (blue) and are valid at 0300 UTC 27 Dec 2010 (FH 21).

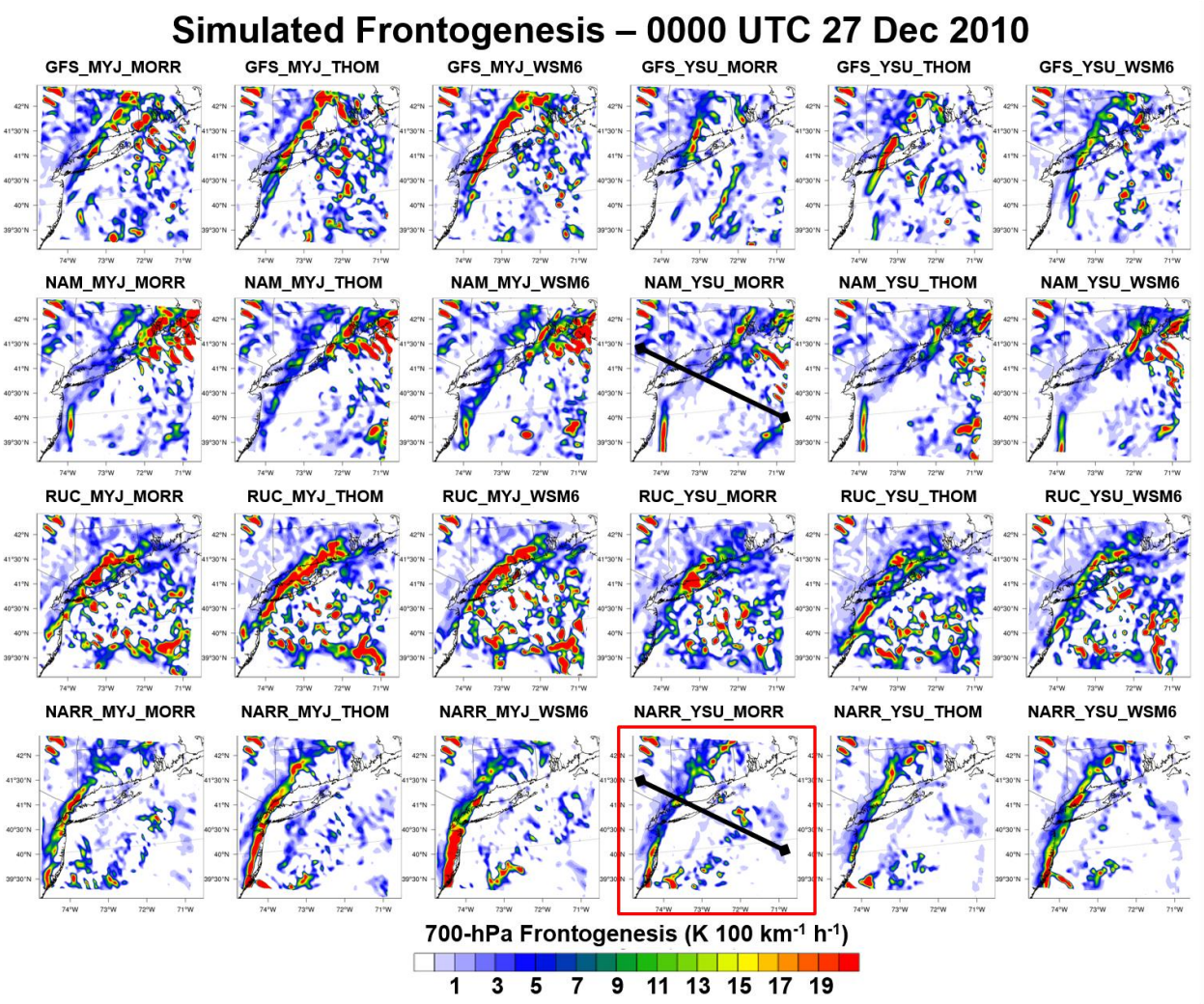

Figure 5.7. As in Figure 5.4 for 700-hPa frontogenesis (K 100 km^{-1} h^{-1}, shaded according to scale) from each of the 1.33-km WRF simulations.

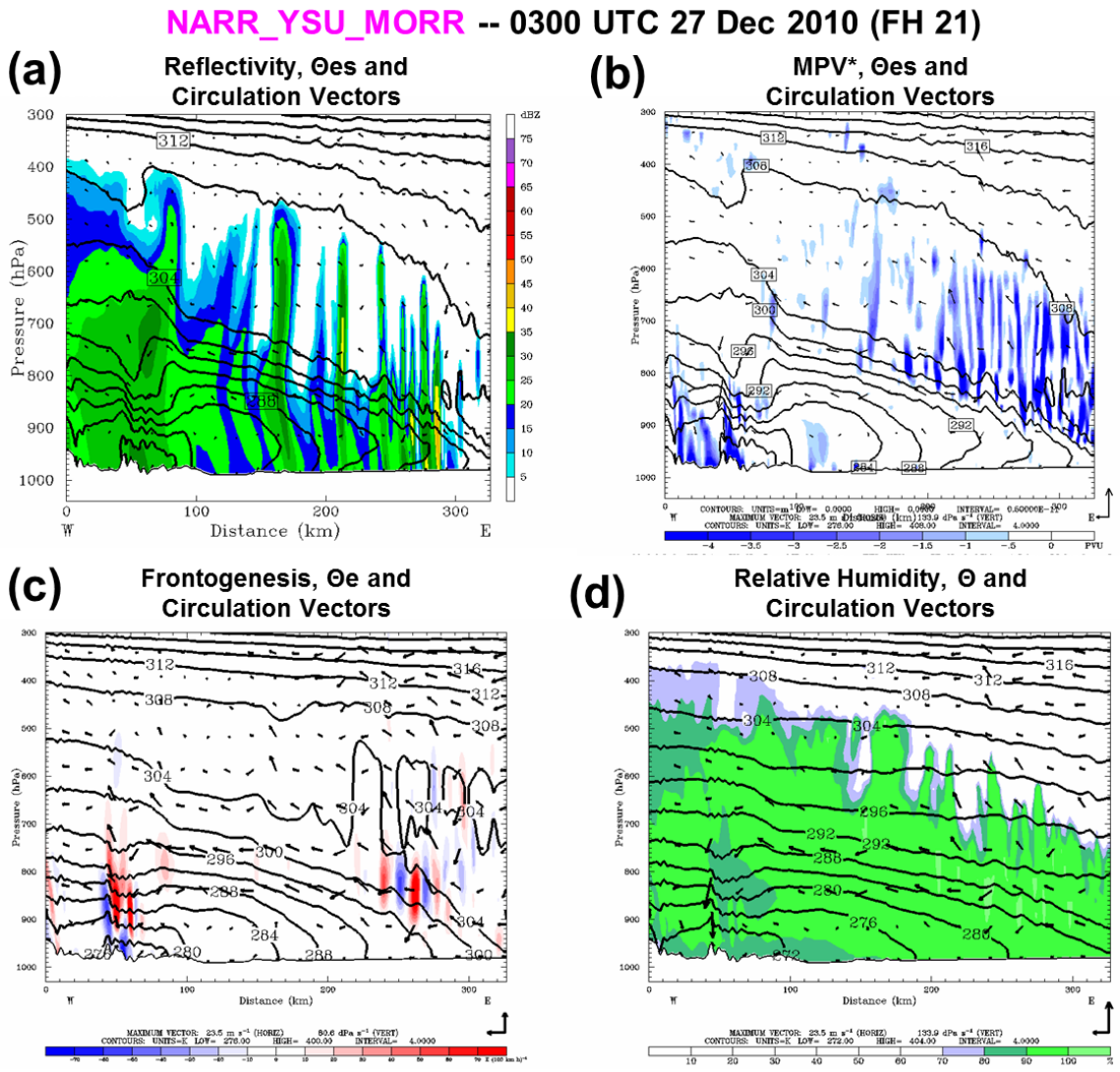

Figure 5.8. NARR_YSU_MORR / "best simulation" 1.33-km domain NW-SE cross section (Fig. 5.7) of (a) reflectivity (shaded, dBZ), saturation equivalent potential temperature (black contours, K), and circulation (vectors, m s^{-1}), (b) saturation moist potential vorticity (shaded, PVU), saturation equivalent potential temperature (black contours, K) and circulation (vectors, m s^{-1}), (c) frontogenesis (shaded, K 100 km^{-1} h^{-1}), equivalent potential temperature (black contours, K), circulation (vectors, m s^{-1}), and (d) relative humidity (shaded, %), potential temperature (black contours, K), and circulation (vectors, m s^{-1}) for 21-hour forecast verifying 0300 UTC 27 Dec.

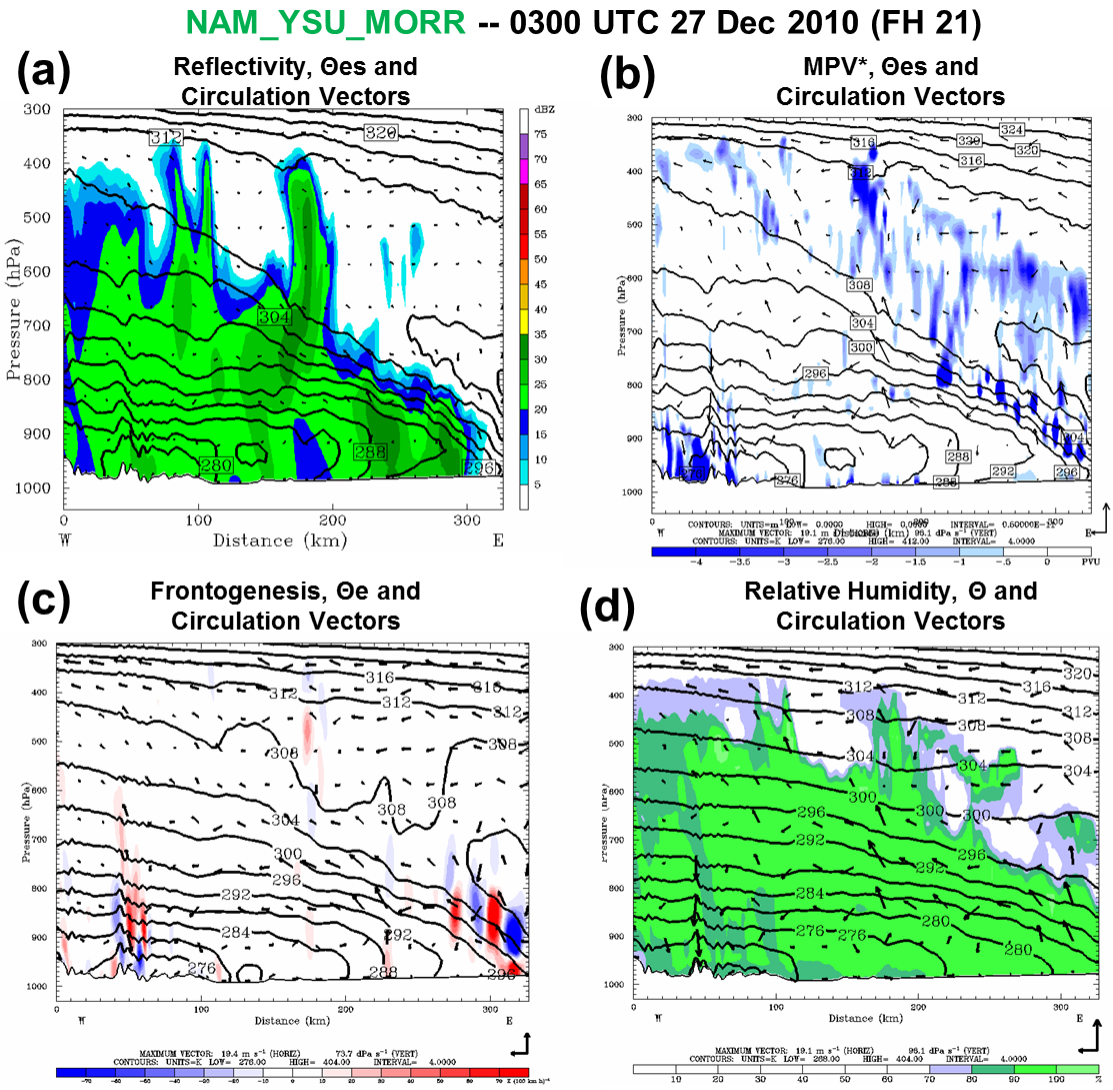

Figure 5.9. As in Fig. 5.8 but for NAM_YSU_MORR / "worst simulation".

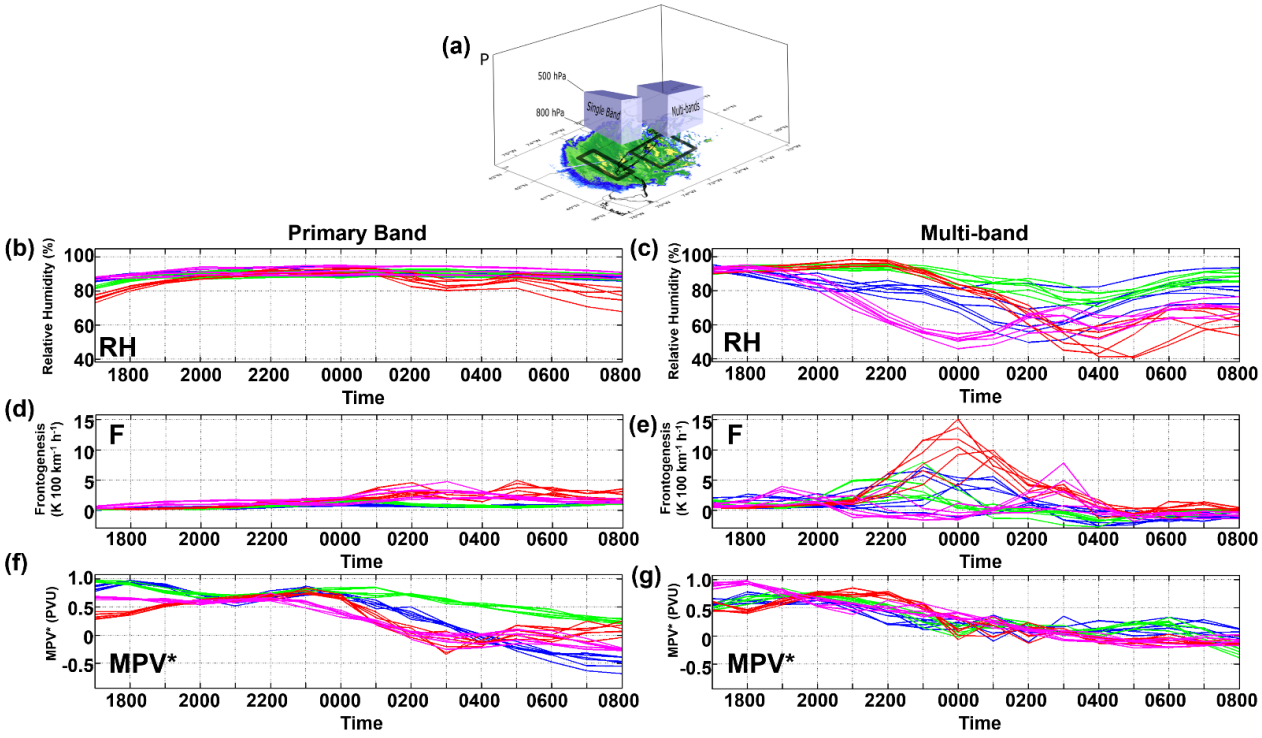

Figure 5.10. (a) 3-dimensional boxed regions for the primary band and multi-band time series calculations in panels b–g calculated from 800-hPa to 500-hPa from the 1.33-km WRF configuration simulations. Primary band time series calculations are provided in the left column and multi-band time series calculations are in the right column. Time series of (b,c) relative humidity (%), (d,e) frontogenesis (K 100 km^{-1} h^{-1}), (f,g) saturation equivalent potential vorticity (PVU).

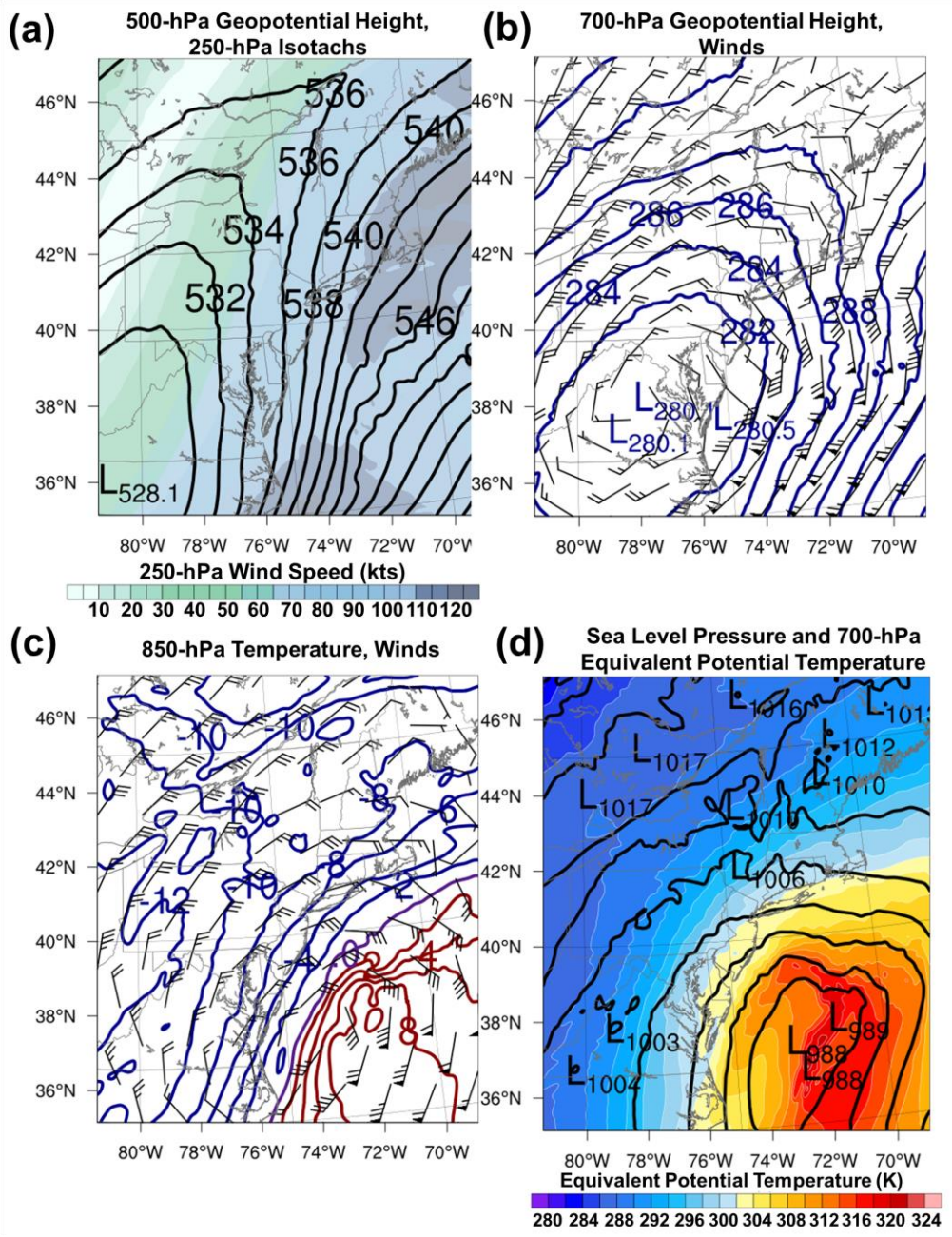

Figure 5.11. WRF 4-km domain output valid at 1800 UTC 26 Dec for (a) 500-hPa geopotential heights (dam, contoured) and 250-hPa isotachs (kts, shaded according to scale), (b) 700-hPa geopotential height (dam, contoured) and winds (kts, barbed), (c) 850-hPa temperature (°C, contoured) and winds (kts, barbed), and (d) SLP (hPa, contoured) and 700-hPa equivalent potential temperature (K, shaded according to scale).

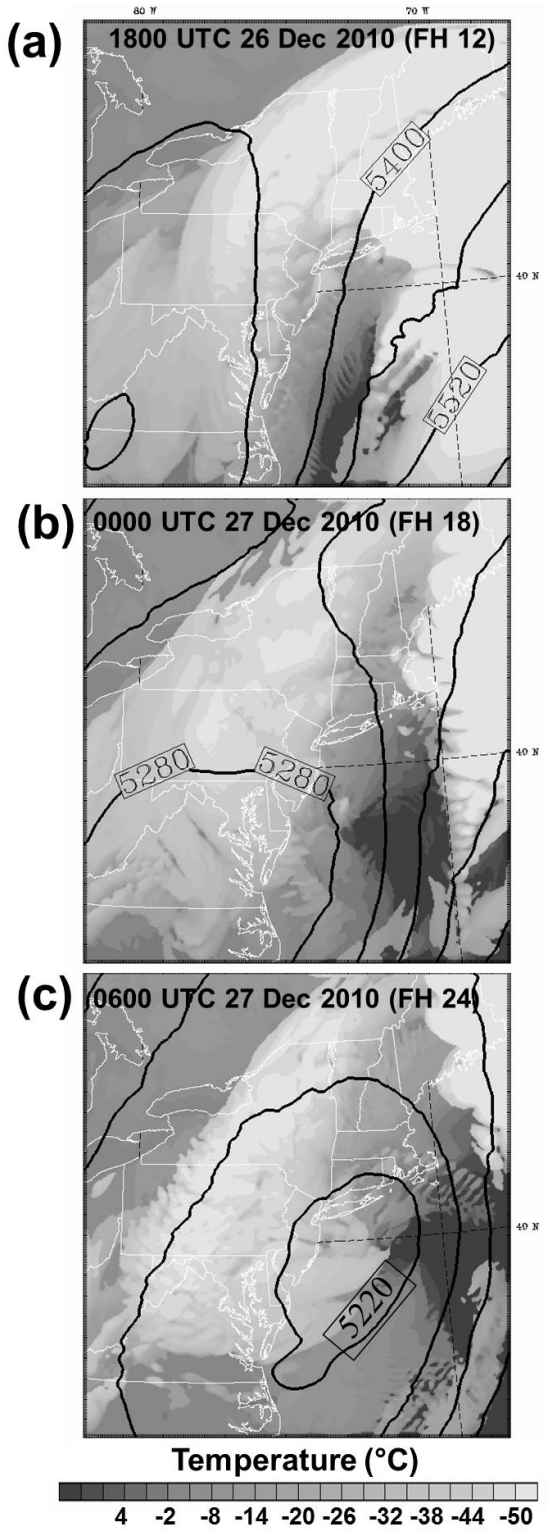

Figure 5.12. NARR-YSU-MORR simulated 4-km cloud top temperature (°C, shaded according to scale) and 500-hPa geopotential height (contoured every 60 m) valid at (a) 1800 UTC 26 Dec (FH 12), (b) 0000 UTC 27 Dec (FH 18), and (c) 0600 UTC 27 Dec (FH 24).

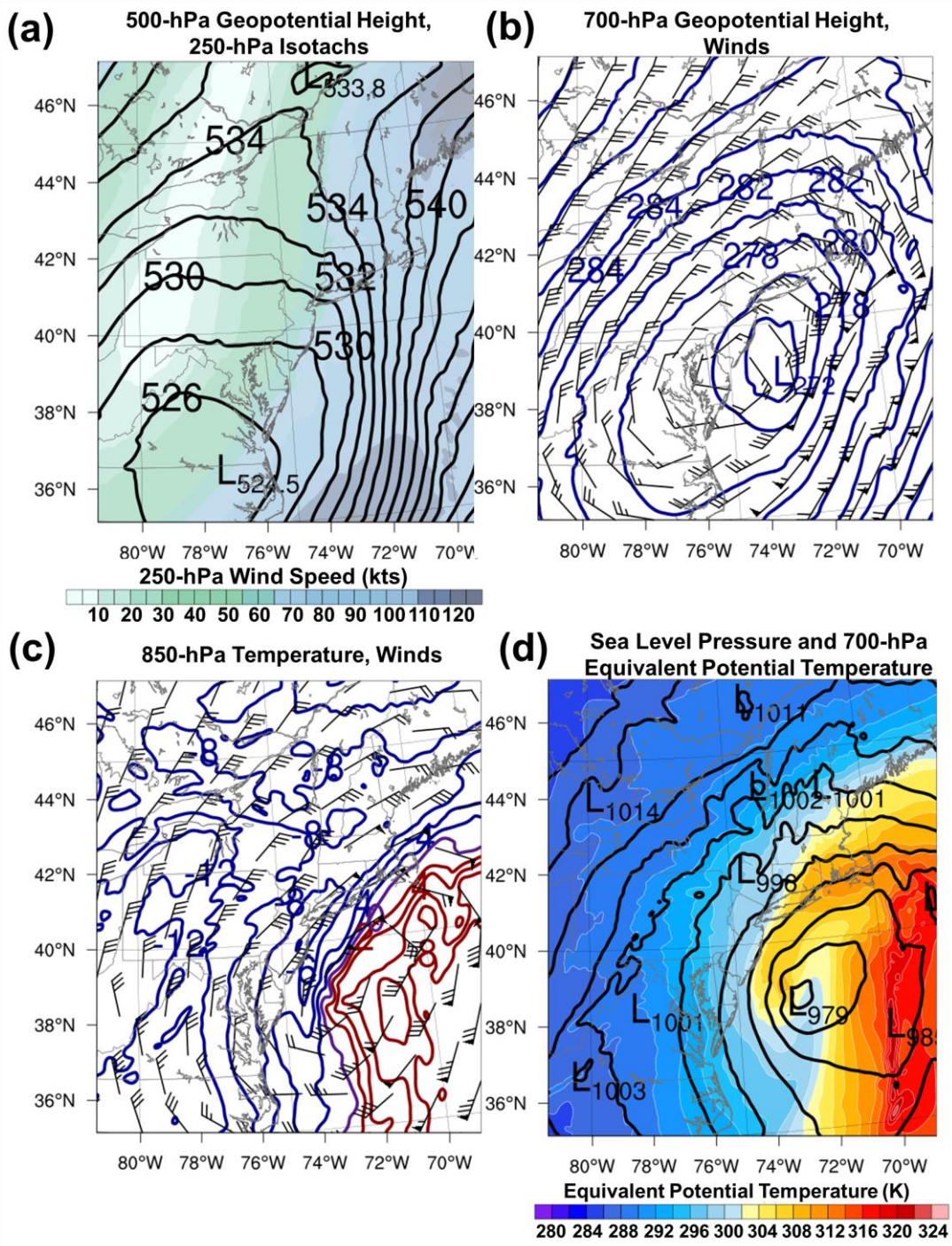

Figure 5.13. As in Figure 5.11 but valid at 0000 UTC 27 Dec.

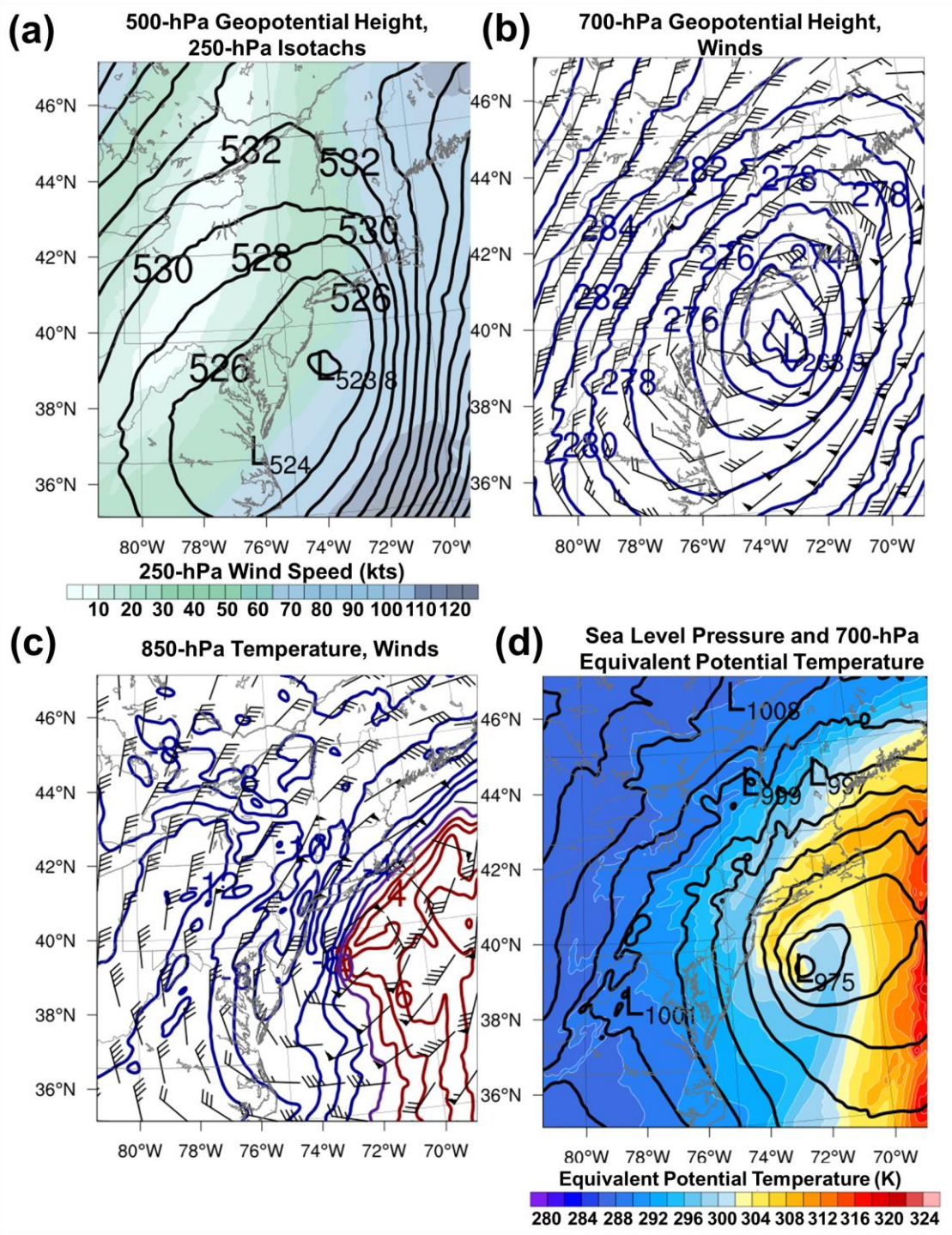

Figure 5.14. As in Figure 5.11 but valid at 0300 UTC 27 Dec.

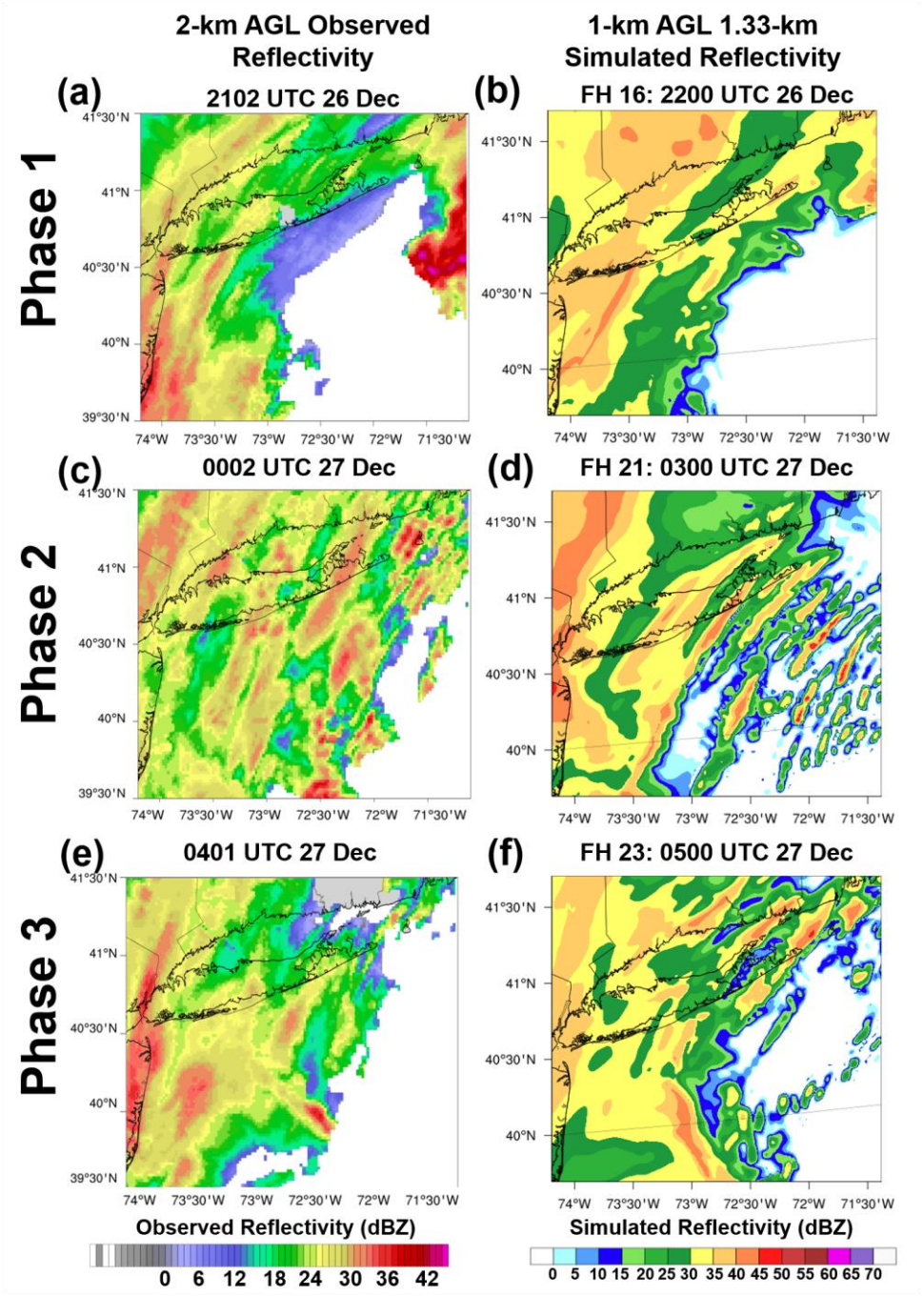

Figure 5.15. Observed 2-km AGL reflectivity (a,c,e) and 1-km AGL simulated reflectivity from the 1.33-km domain (b,d,f) showing Phase 1 (a,b), Phase 2 (c,d) and Phase 3 (e,f) of the precipitation banding within the 26–27 Dec 2010 case.

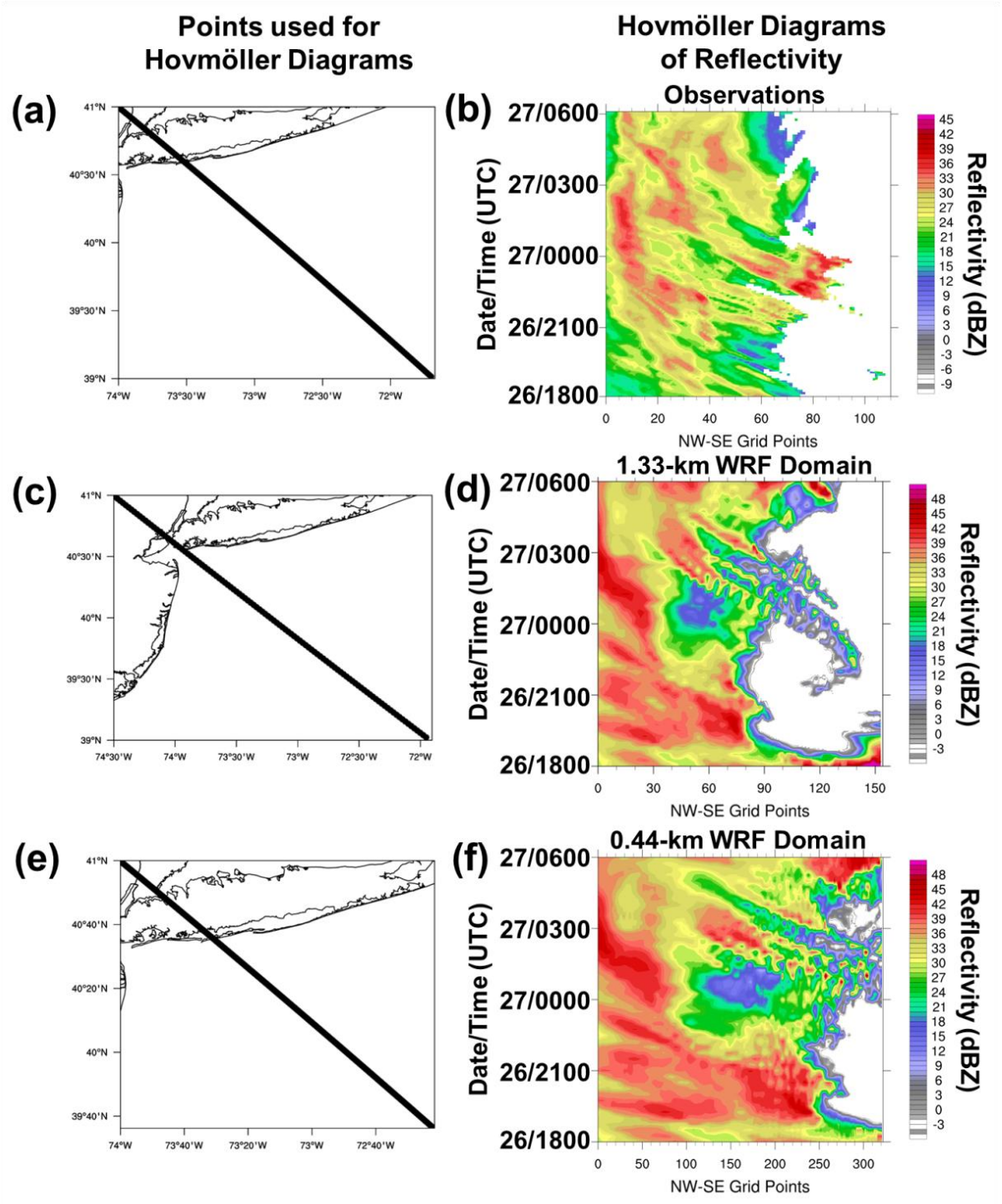

Figure 5.16. Points oriented NW-SE approximately perpendicular to the bands for the (a) 2-km observed, (c) 1.33-km WRF domain, and (e) 0.44-km WRF domain used to construct hovmöller diagrams of reflectivity from 1800 UTC 26 Dec – 0600 UTC 27 Dec (b,d,f).

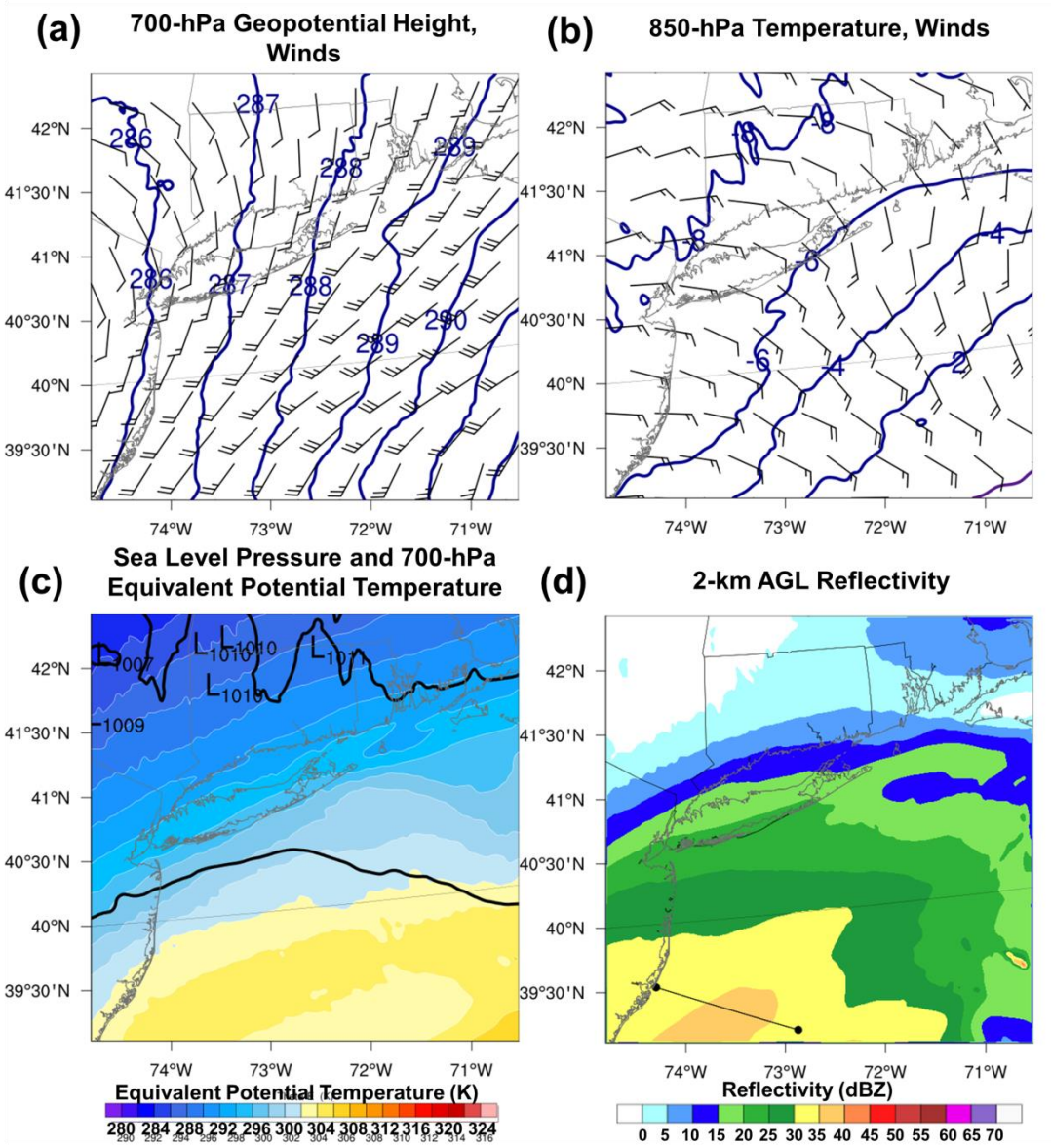

Figure 5.17. WRF 1.33-km output valid at 1430 UTC 26 Dec for (a) 700-hPa geopotential height (dam, contoured) and winds (kts, barbed), (b) 850-hPa temperature (°C, contoured) and winds (kts, barbed), (d) SLP (hPa, contoured) and 700-hPa equivalent potential temperature (K, shaded according to scale), and (d) 2-km AGL simulated reflectivity (dBZ, shaded according to scale). The cross section location used in Figure 5.18 is provided in (d).

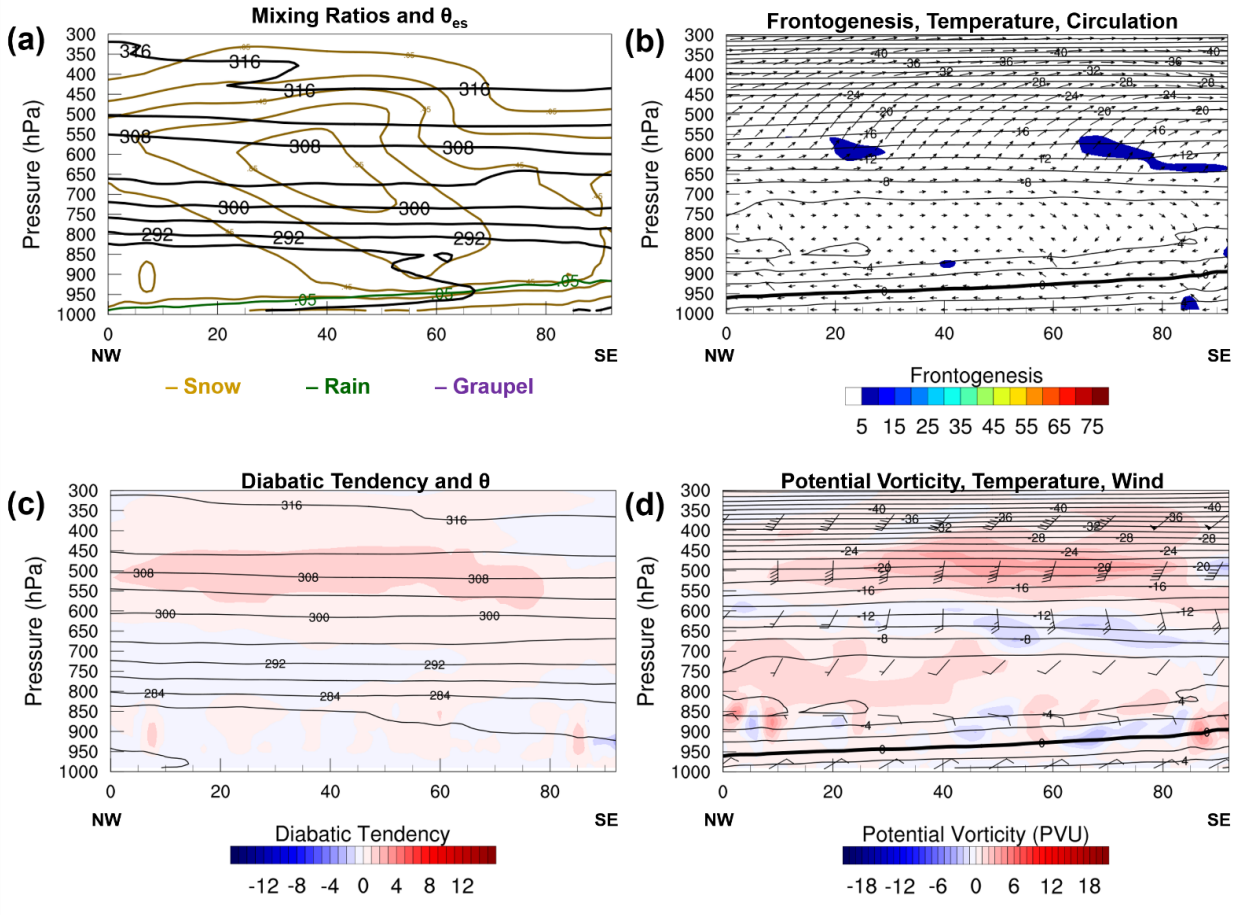

Figure 5.18. Cross sections from the point shown in Figure 5.17d of (a) snow mixing ratio (contoured in gold every 0.2 g kg^{-1}), graupel mixing ratio (contoured in purple every 0.1 g kg^{-1}), and rain mixing ratio (contoured in green every 0.1 g kg^{-1}) and θ_{es} (K, contoured), (b) frontogenesis (K 100 km^{-1} h^{-1}, shaded), temperature (°C, contoured), and upward vertical motion (m s^{-1}, contoured), (c) diabatic tendency (x 10^{-3} K s^{-1}, shaded) and θ, and (d) potential vorticity (PVU, shaded) and temperature (°C, contoured) valid at 1430 UTC 26 Dec.

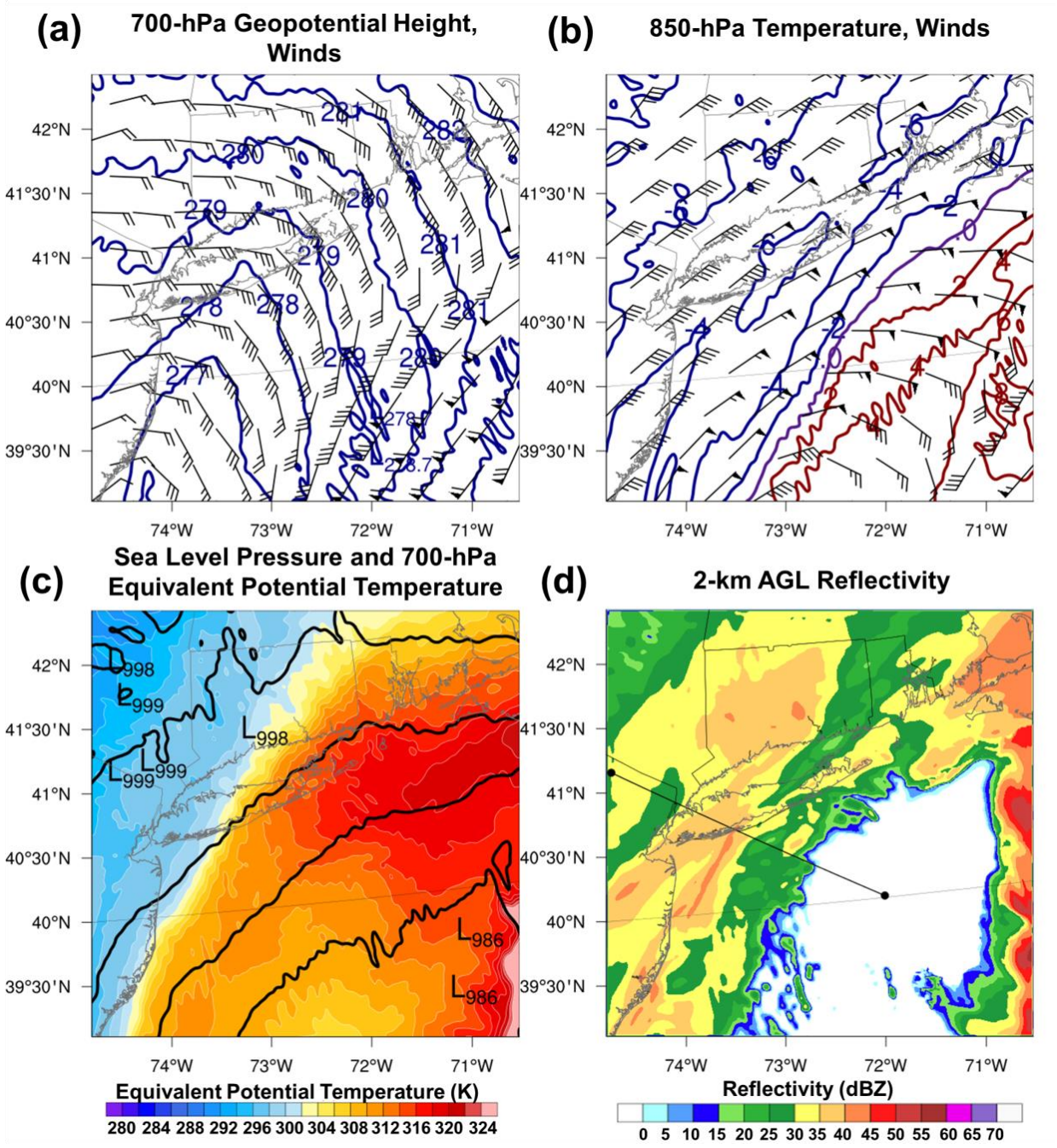

Figure 5.19. As in Figure 5.17 valid at 2200 UTC 26 Dec. The cross section location used in Figure 5.20 is provided in (d).

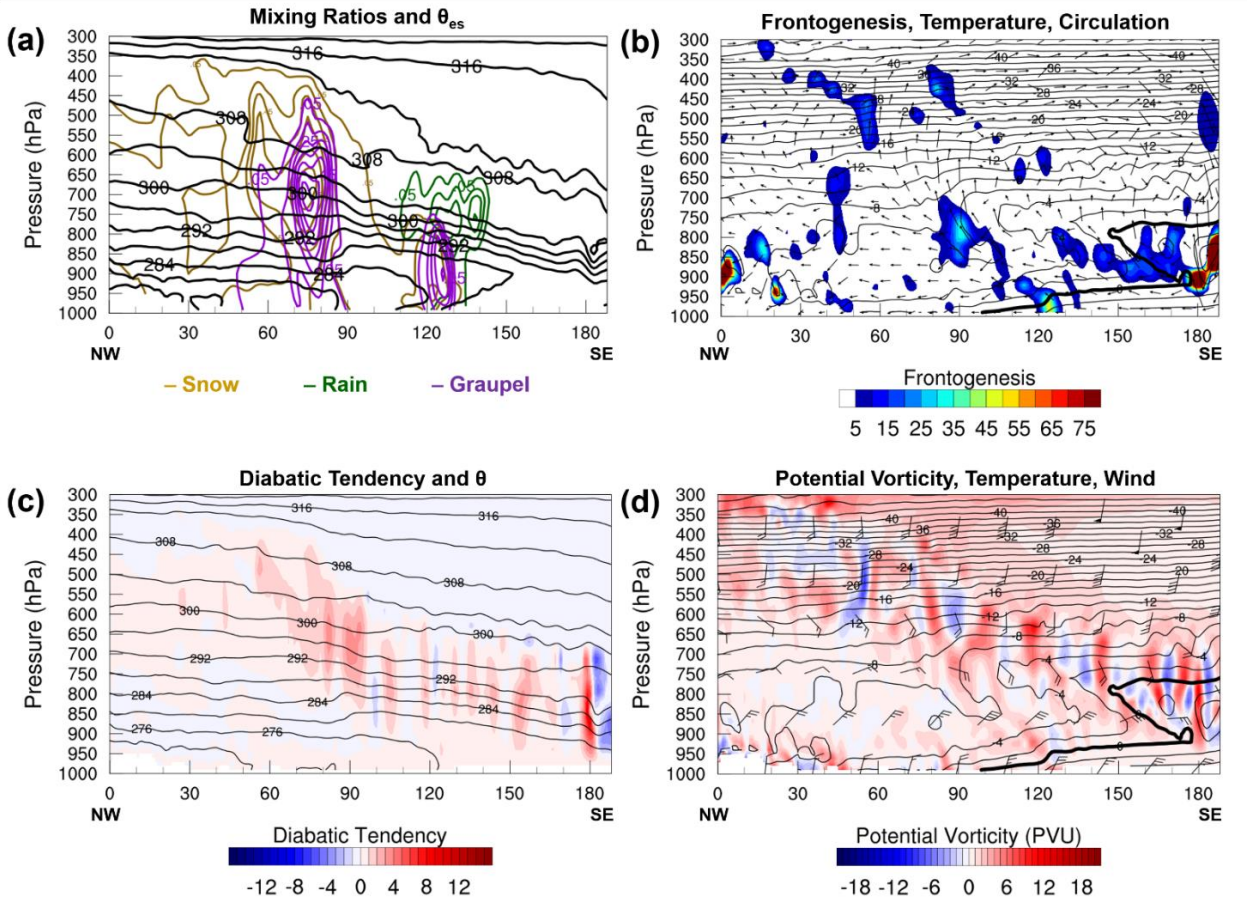

Figure 5.20. As in Figure 5.18 valid at 2200 UTC 26 Dec for the cross section shown in Figure 5.19d.

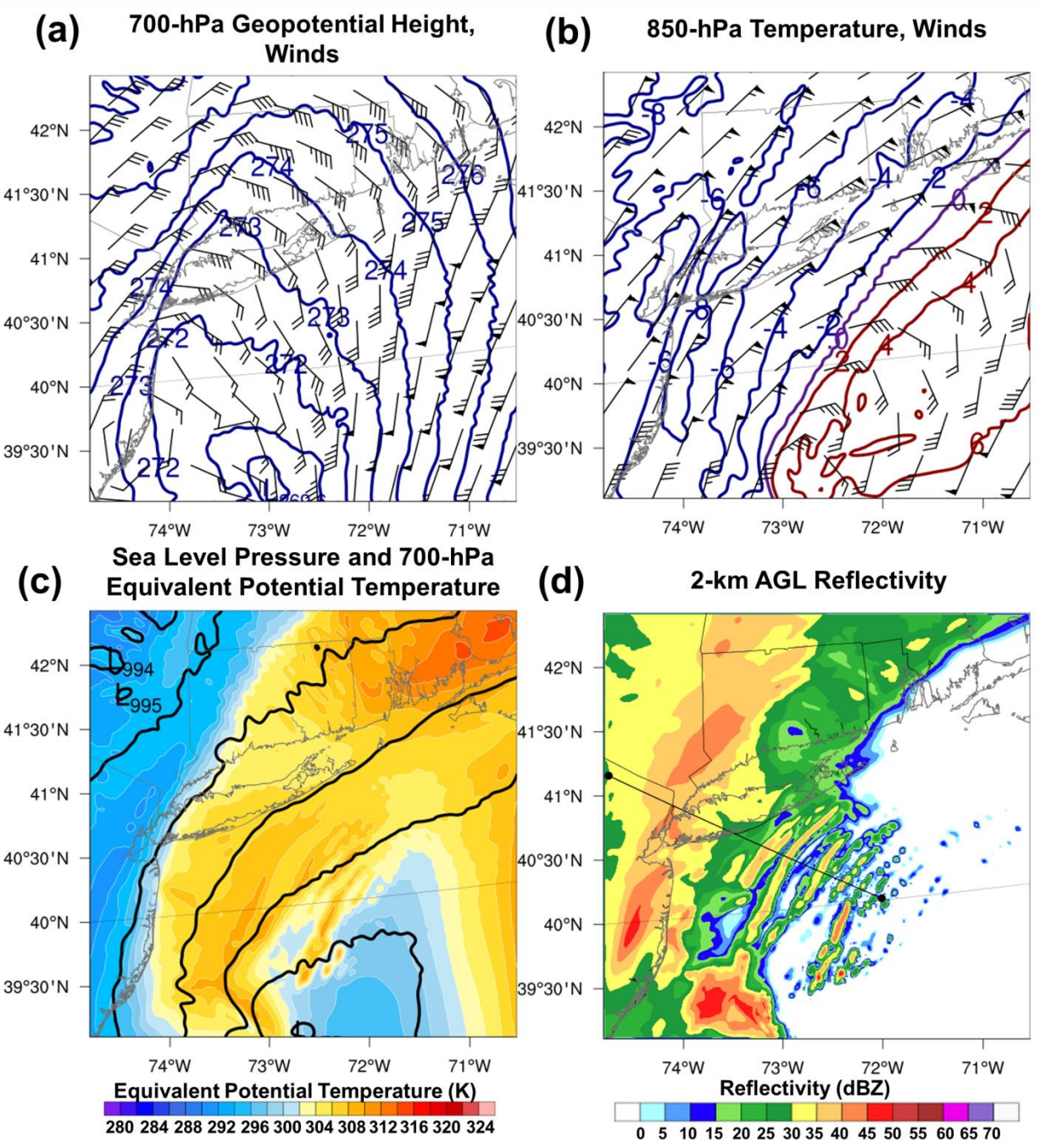

Figure 5.21. As in Figure 5.17 but valid at 0200 UTC 27 Dec. The cross section locations used in Figure 5.22 are shown in (d).

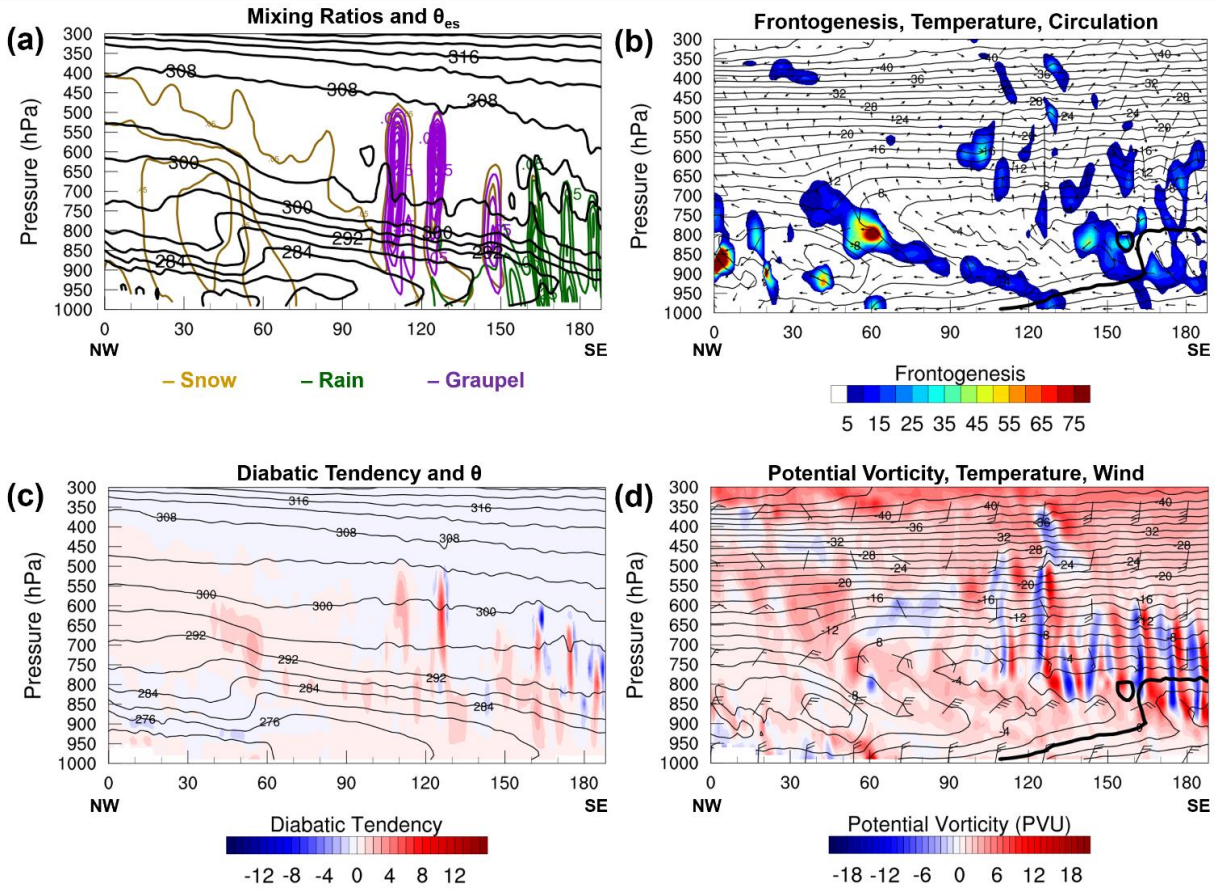

Figure 5.22. As in Figure 5.18 valid at 0200 UTC 27 Dec for the cross section shown in Figure 5.21d.

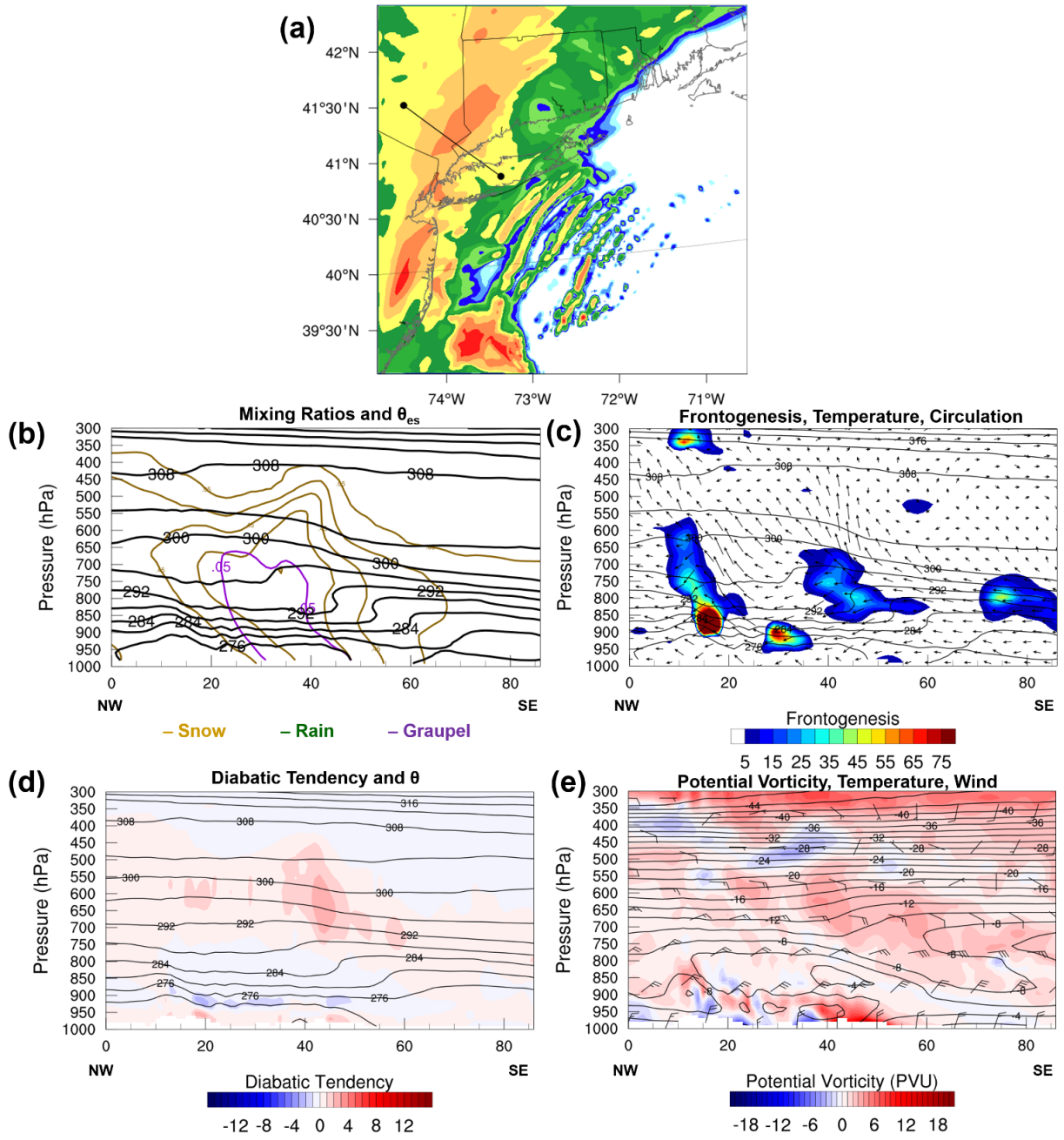

Figure 5.23. (a) NW to SE cross section location through the primary band of (b) snow mixing ratio (contoured in gold every 0.2 g kg^{-1}), graupel mixing ratio (contoured in purple every 0.1 g kg^{-1}), and rain mixing ratio (contoured in green every 0.1 g kg^{-1}) and θ_e^* (K, contoured), (c) frontogenesis (K 100 km^{-1} h^{-1}, shaded), θ_e^* (K, contoured) and circulation vectors (arrows), (d) diabatic tendency (K s^{-1}, shaded) and θ (K, contoured), and (e) potential vorticity (PVU, shaded), temperature (°C, contoured) and horizontal wind (kts, barbed) valid at 0200 UTC 27 Dec.

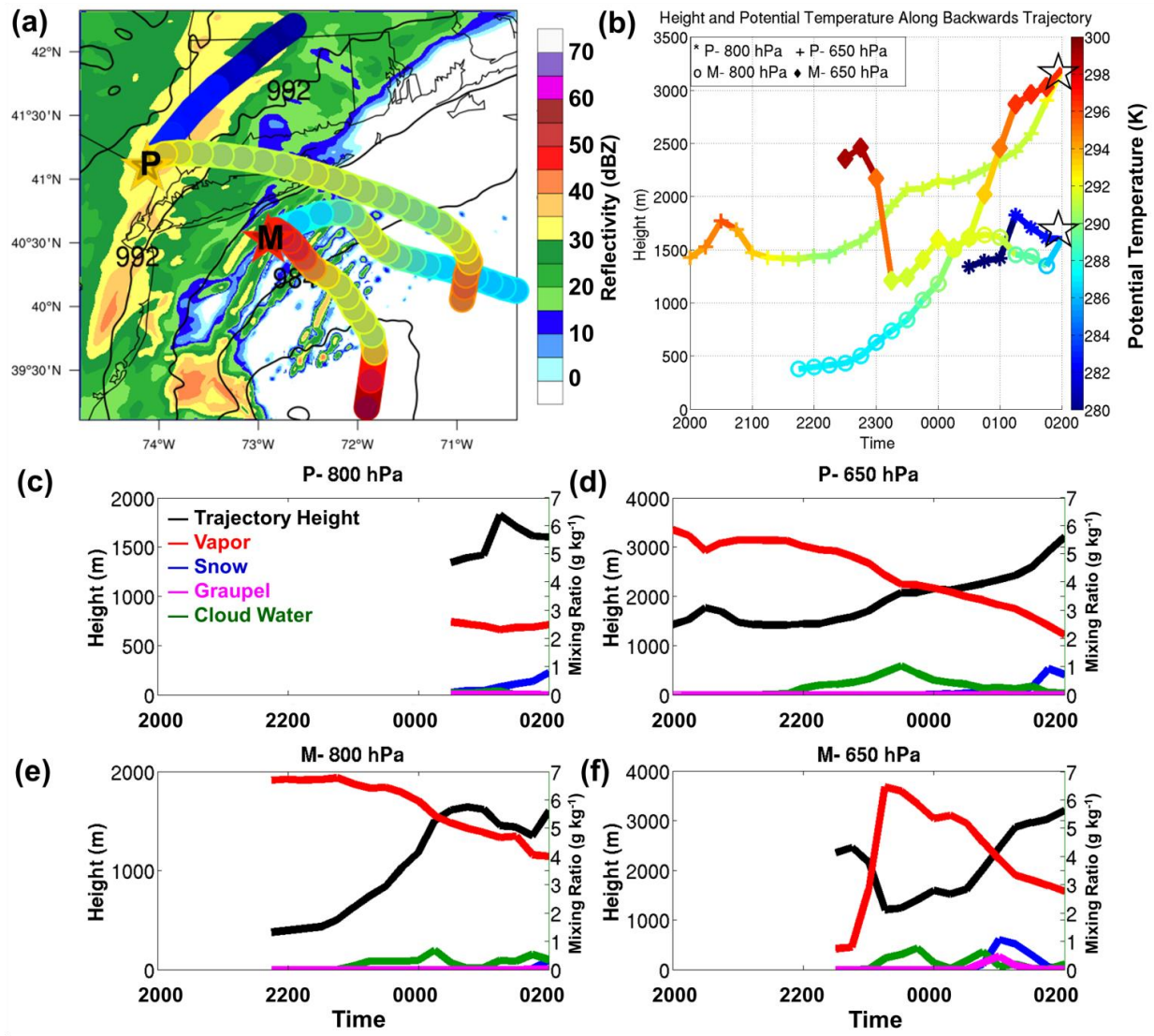

Figure 5.24. (a) Backwards trajectories launched from 0200 UTC 27 Dec within the primary band (P) and multi-band (M) from 800 hPa and 650 hPa. Potential temperature along each trajectory is shaded according to the scale provided. Trajectories are overlaid on sea level pressure (hPa, contoured) and 2-km AGL reflectivity (dBZ, shaded according to scale) valid at 0200 UTC 27 Dec. (b) Potential temperature and height along each trajectory for the primary band terminating at 800-hPa (asterisk) and 650-hPa (plus sign) and the multi-band terminating at 800-hPa (circle) and 650-hPa (diamond). (c–f) Height (black) and vapor mixing ratio (g kg^{-1}, red), snow mixing ratio (g kg^{-1}, blue), graupel mixing ratio (g kg^{-1}, magenta), and cloud water mixing ratio (g kg^{-1}, green) along the trajectory terminating in the (c) primary band at 800 hPa, (d) primary band at 650 hPa, (e) multi-band at 800 hPa, (f) multi-band at 650 hPa.

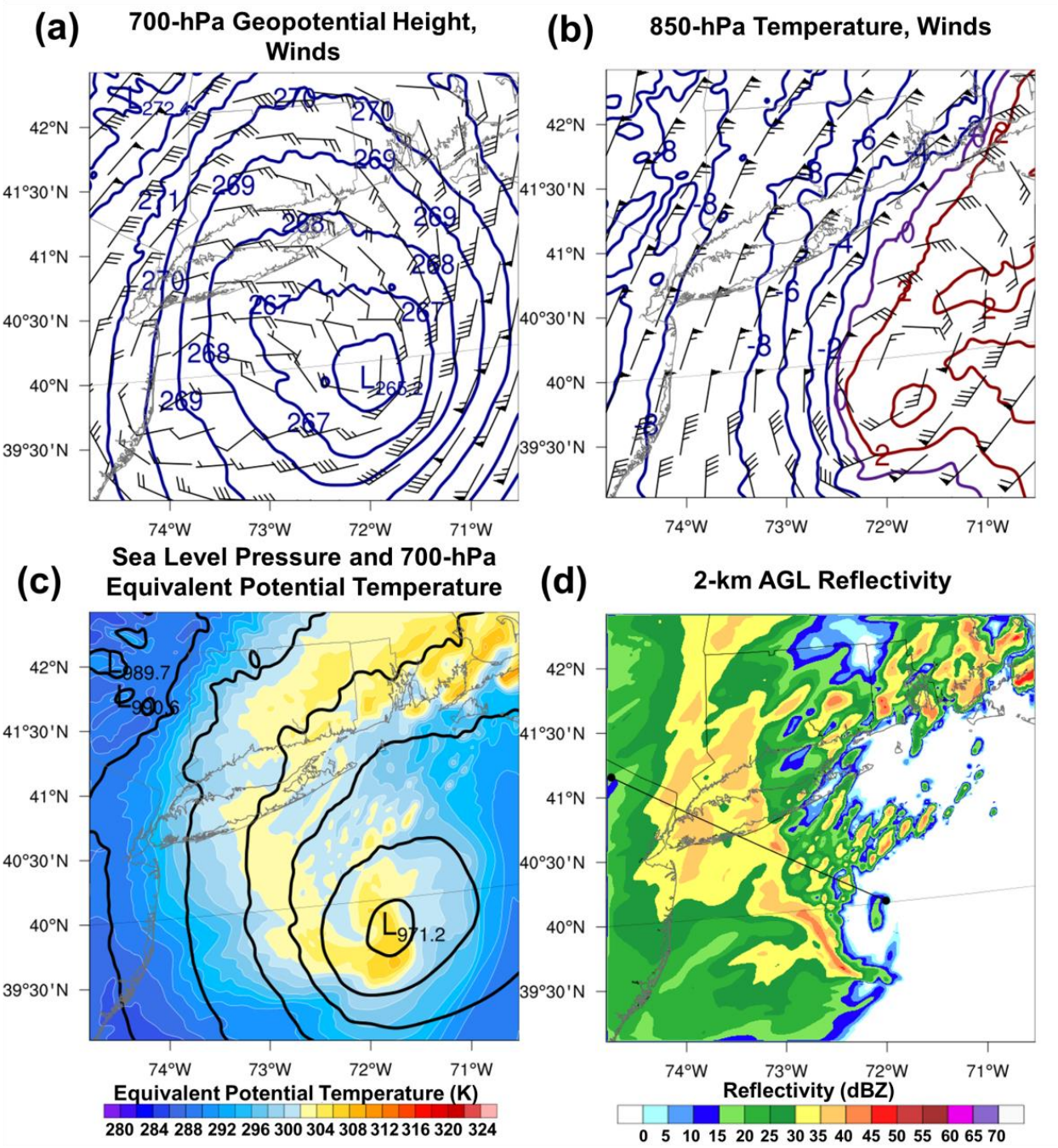

Figure 5.25. As in Figure 5.17 but for 0600 UTC 27 Dec and showing the cross section points in (d) used in Figure 5.26.

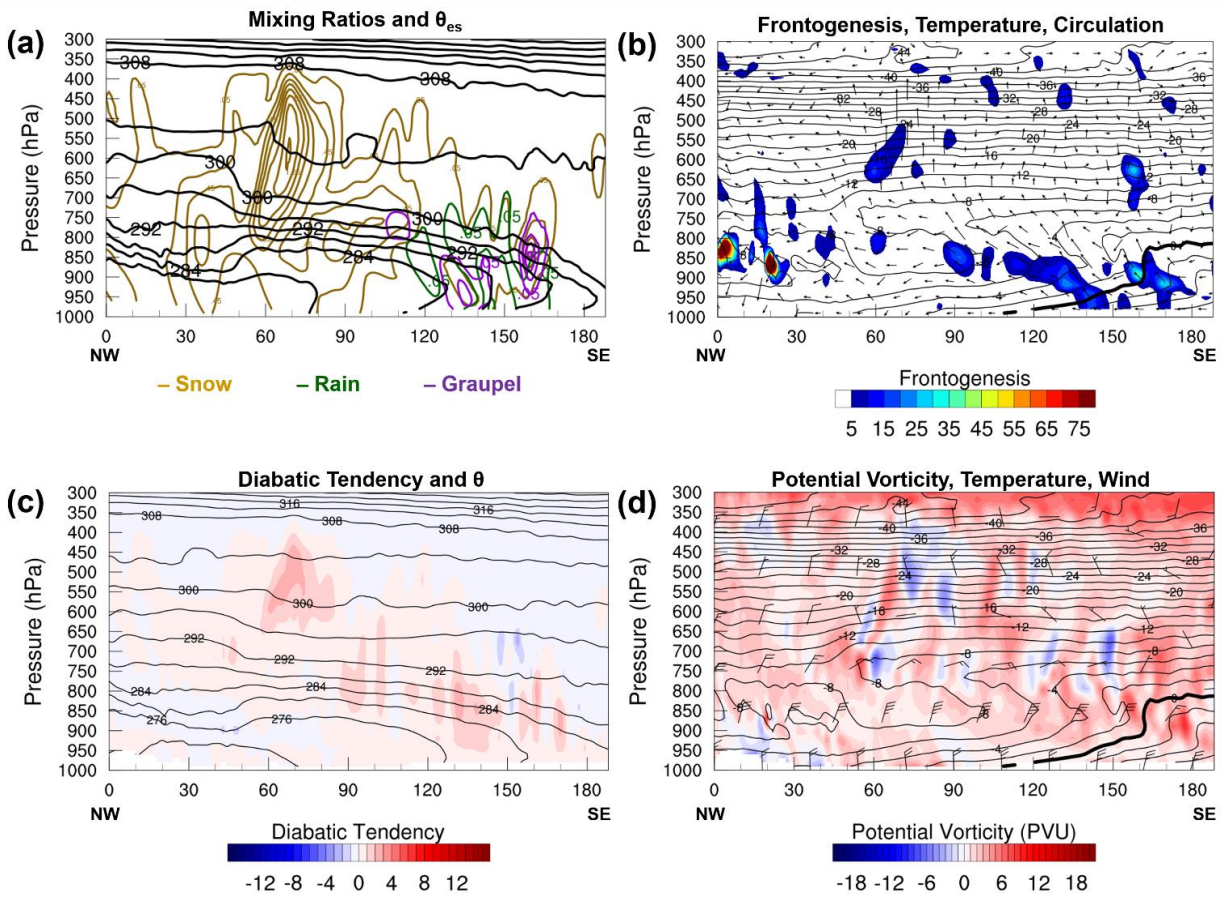

Figure 5.26. As in Figure 5.18 valid at 0600 UTC 27 Dec for the cross section shown in Figure 5.22d.

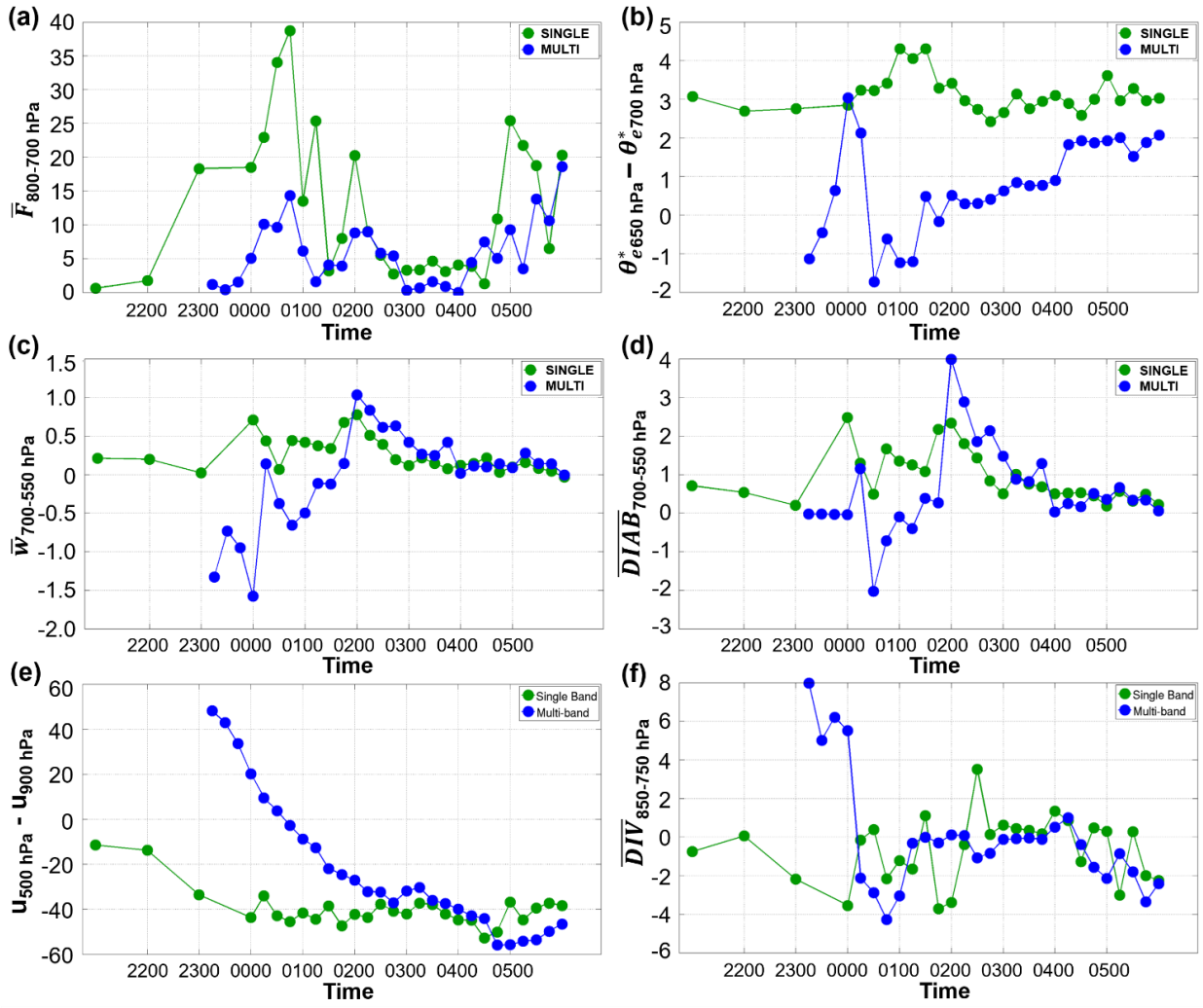

Figure. 5.27. Time series from data taken from profiles through the center of the single band (green) and multi-band (blue) for (a) 2-D frontogenesis averaged in the 800–700-hPa layer (K 100 km^{-1} h^{-1}), (b) difference in saturation equivalent potential temperature (K) in the 50-hPa layer from 650 hPa to 700 hPa, (c) vertical motion averaged in the 700–550-hPa layer (m s^{-1}), and (d) diabatic tendency averaged in the 700–550-hPa layer (x 10^{-3} K s^{-1}), (d) wind shear from 900 hPa to 500 hPa (kts), (e) divergence averaged in the 850–750 hPa layer (x 10^{-4} s^{-1}).

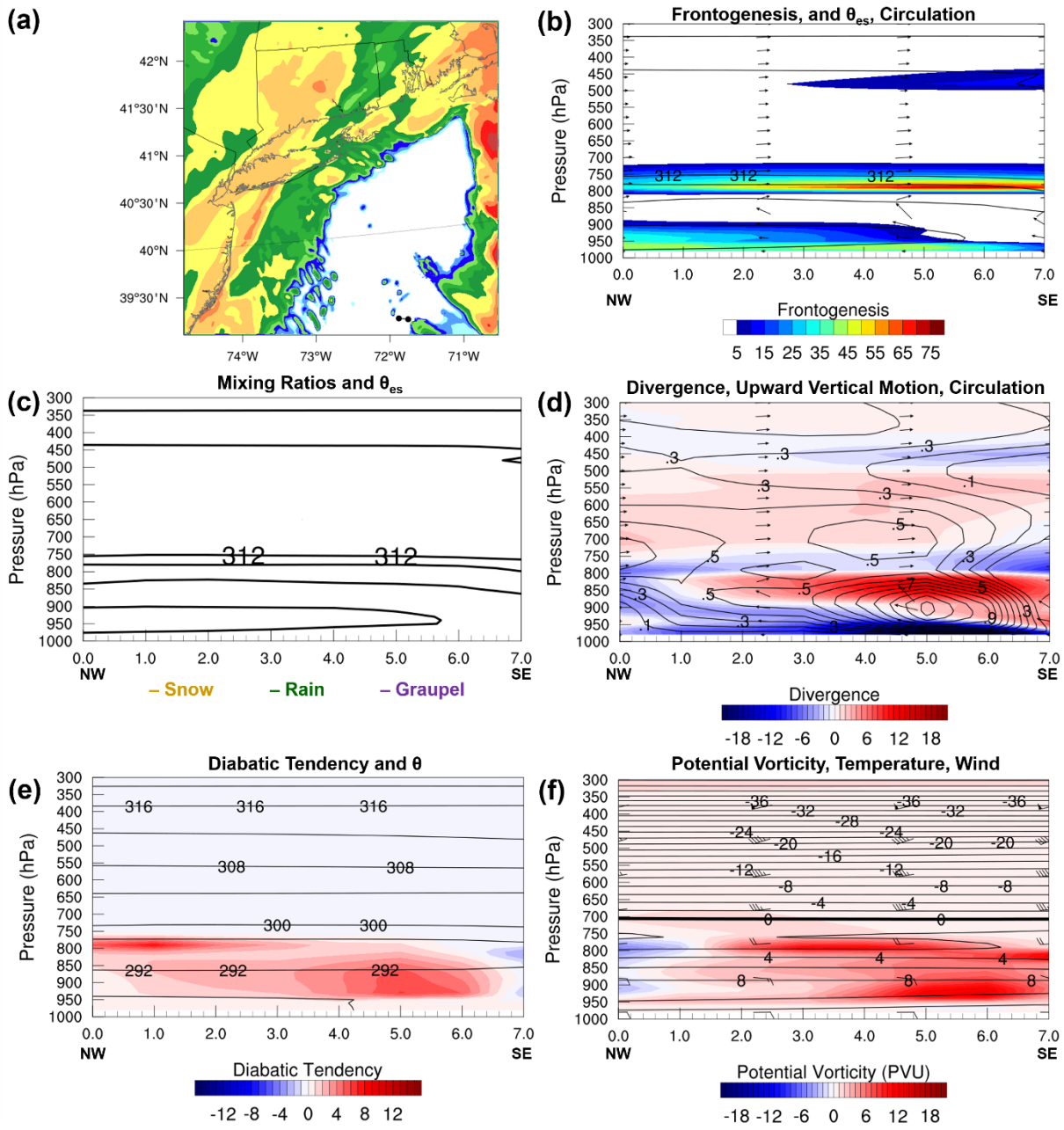

Figure 5.28. (a) Cross sections points through a precursor cell to a multi-band of (b) frontogenesis (K 100 km^{-1} h^{-1}, shaded), θ_{es} (K, contoured), and circulation vectors, (c) snow mixing ratio (contoured in gold every 0.2 g kg^{-1}), graupel mixing ratio (contoured in purple every 0.1 g kg^{-1}), and rain mixing ratio (contoured in green every 0.1 g kg^{-1}) and θ_{es} (K, contoured), (d) divergence (x 10^{-4} s^{-1}, shaded) and upward vertical motion (m s^{-1}, contoured), (e) diabatic tendency (x 10^{-3} K s^{-1}, shaded) and θ (K, contoured), and (f) potential vorticity (PVU, shaded) and temperature (°C, contoured) valid at 2215 UTC 26 Dec.

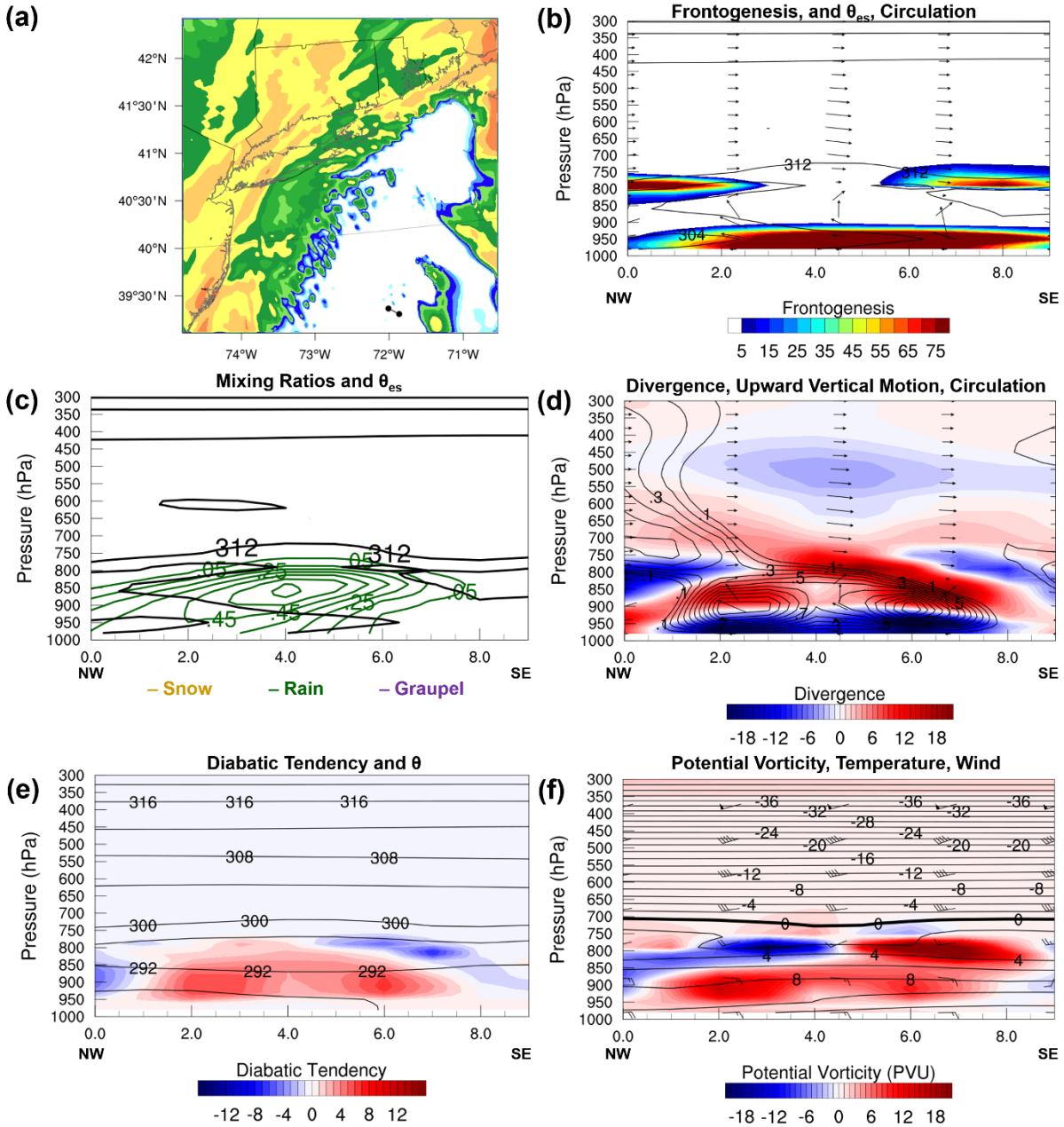

Figure 5.29. As in Figure 5.28 valid at 2245 UTC 26 Dec.

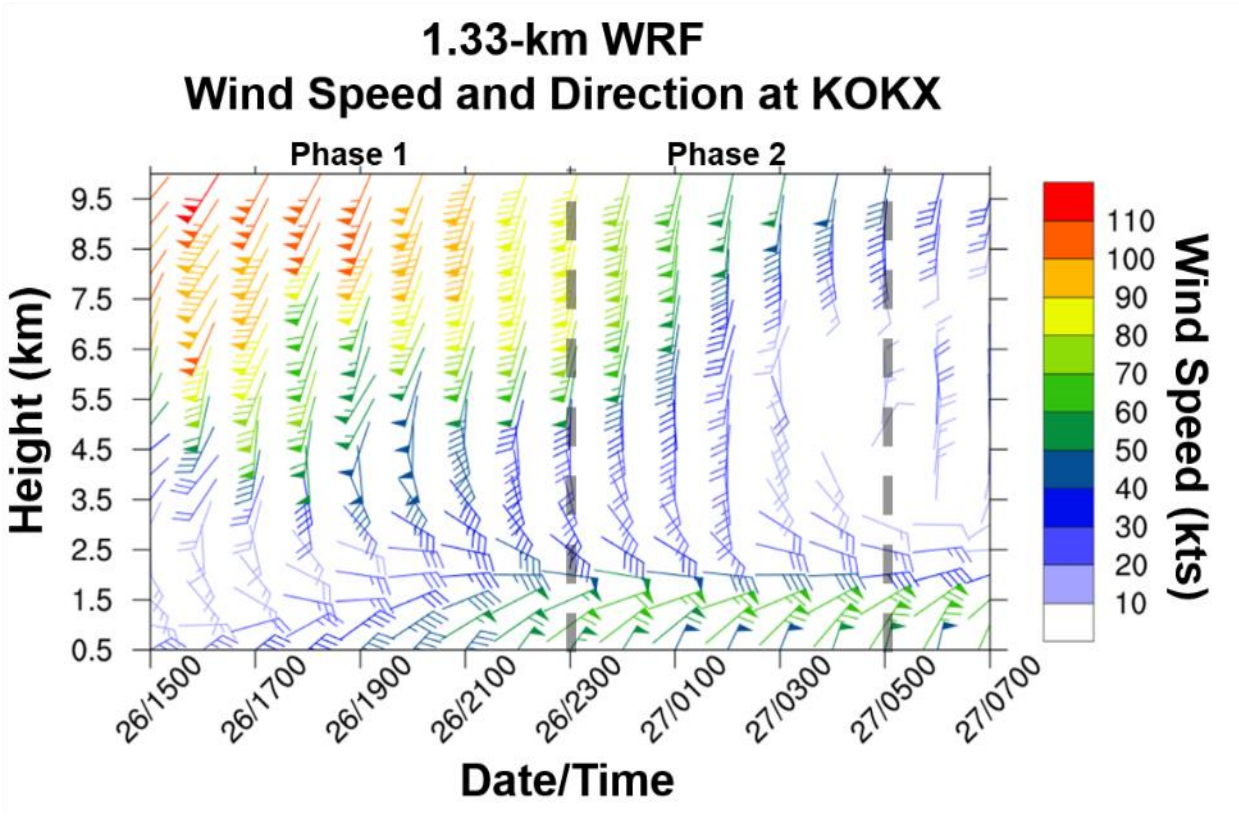

Figure 5.30. Time series of vertical wind profiles at KOKX (Fig. 5.1) showing wind speed (kts, shaded) and direction (barbs). The demarcation between phases 1–3 are indicated with the vertical dashed bars.

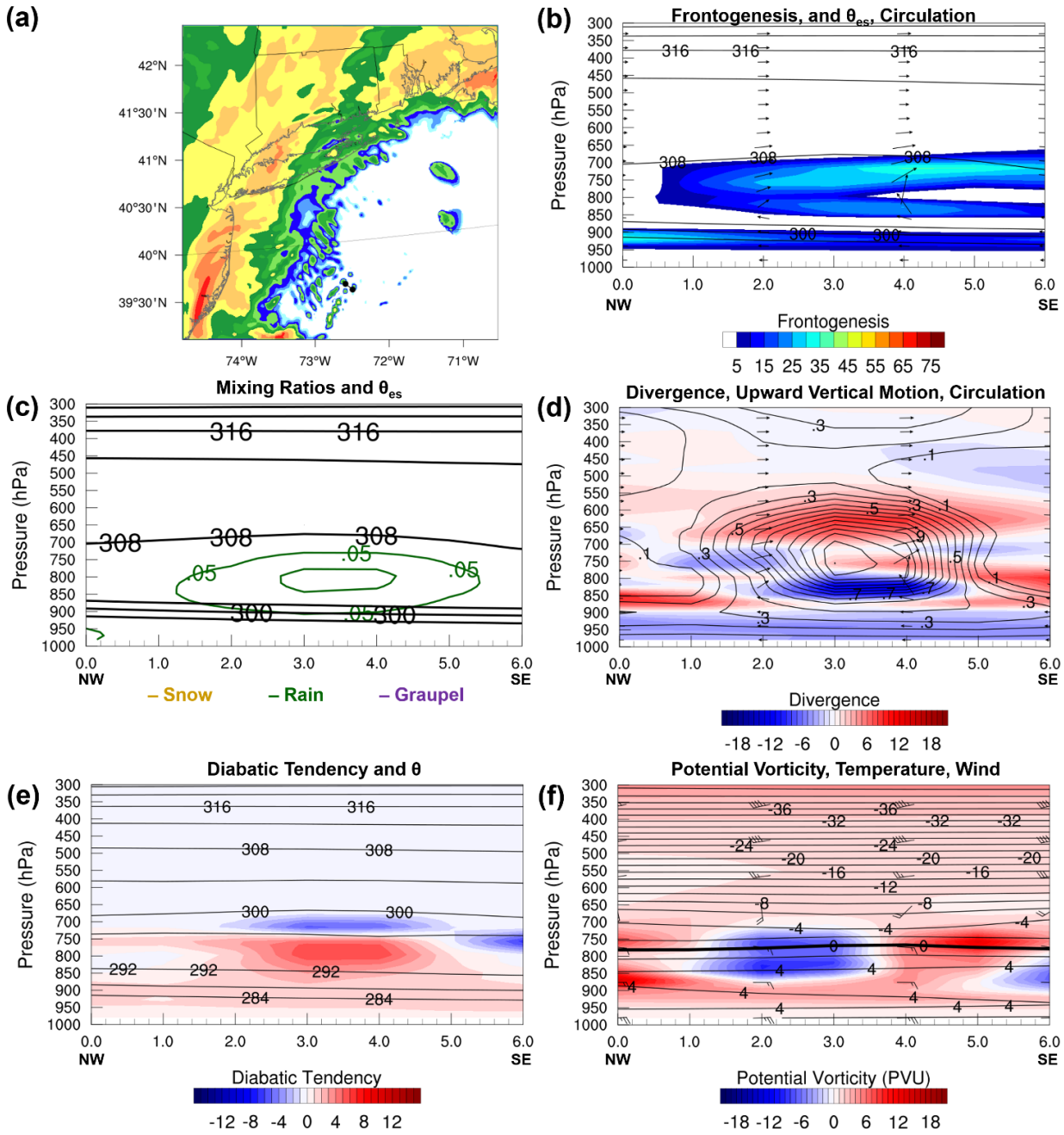

Figure 5.31. As in Figure 5.28 valid at 0000 UTC 27 Dec.

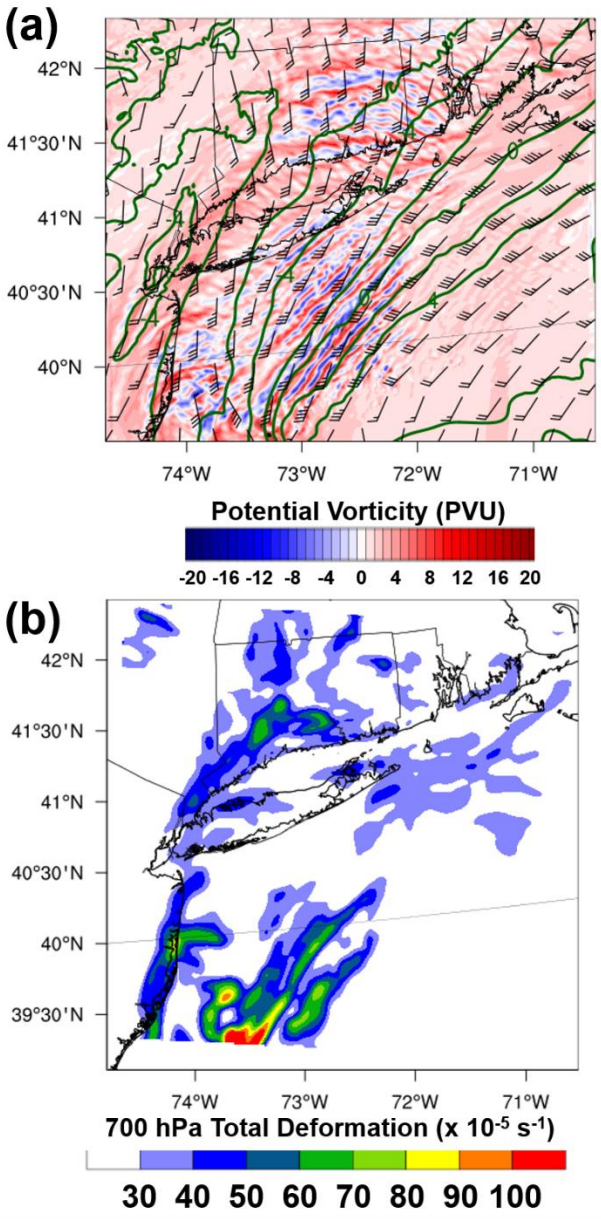

Figure 5.32. (a) 700-hPa potential vorticity (PVU, shaded), 850-hPa temperatures (ºC, contoured), and 700–900-hPa wind shear (kts, barbs), (b) 700-hPa total deformation, the sum of shear and stretching deformation (x 10^{-5} s^{-1}, shaded according to scale) valid at 0100 UTC 27 Dec.

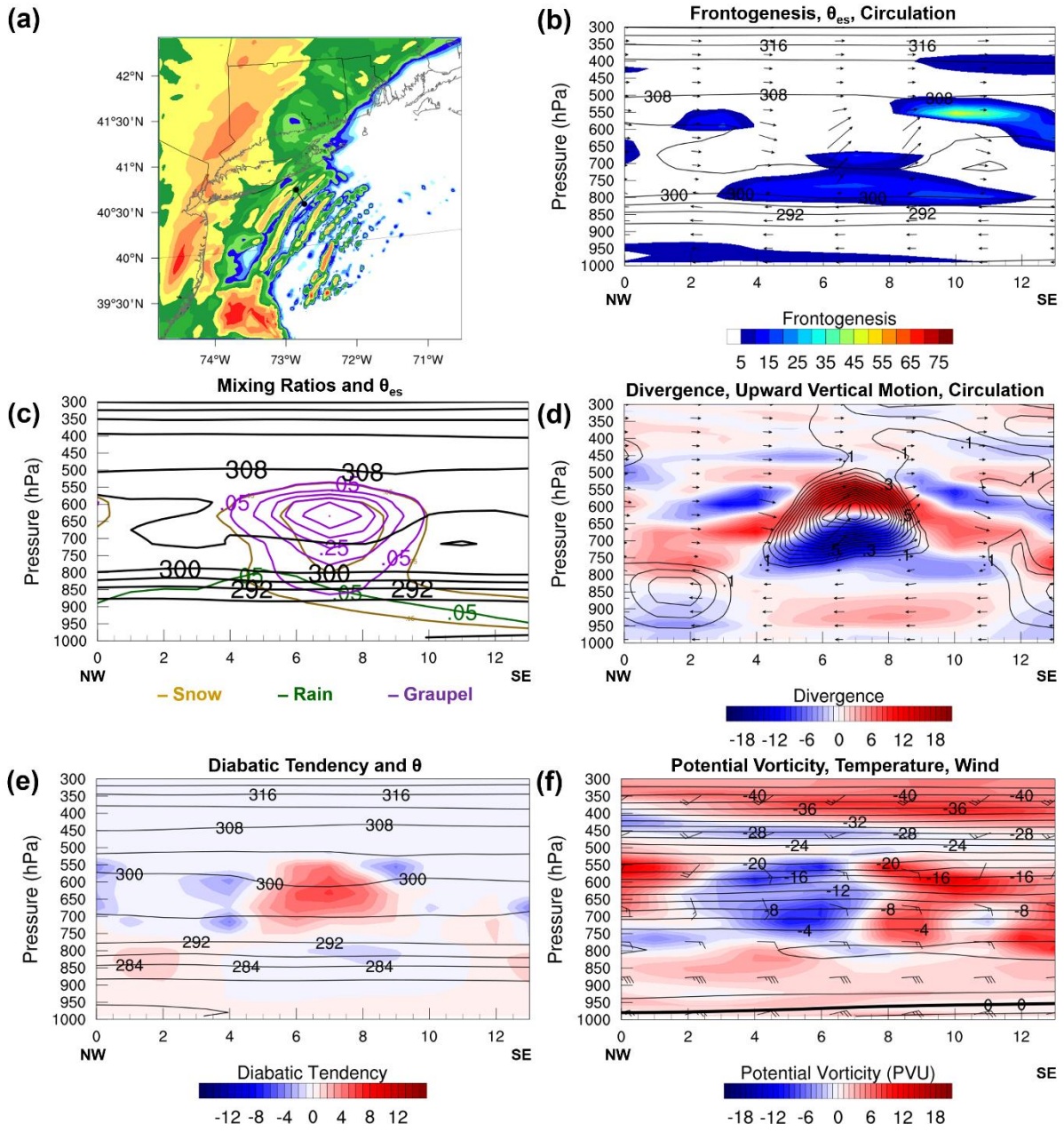

Figure 5.33. As in Figure 5.28 but valid at 0200 UTC 27 Dec and from the multi-band cross section shown in (a).

Chapter 6:

Conclusions and Future Work

This dissertation uses radar observations, reanalyses, and high-resolution model simulations to explore the thermodynamic evolution of single and multi-bands in Northeast U.S. (NEUS) extratropical cyclones. Since the majority of mesoscale banding studies investigate single bands, a climatology of multi-bands with or without the accompaniment of a single band is created. The goals of this study are to compare environmental banding ingredients for multi-bands to that of single bands and non-banded, stratiform precipitation. The mesoscale processes that can result in bands such as frontogenesis and shear-induced circulations are examined using high-resolution case studies. This study investigates the diabatic processes within the band environment and the effect of such processes as latent heating on band intensity and longevity. The following sections will highlight some of the major findings and additional research avenues.

6.1 Conclusions

a. Climatology of multi-bands in Northeast U.S. winter storms

A combination of objective and subjective approaches for the classification of bands of 110 NEUS winter storms from 1996–2016 are conducted. The dataset was comprised of extratropical cyclones that produced ≥ 1.00 in (2.54 cm) liquid equivalent snowfall in the NYC metropolitan area. Regional composite 2-km AGL radar reflectivity data from six coastal NEUS radars were used to identify and classify bands using the Method for Object-based Diagnostic Evaluation (MODE), specifically into primary bands ($L \geq 200$ km) and mid-sized bands ($L < 200$ km) both with aspect ratios (ratio of width to length) ≤ 0.5. The identified bands were then classified within one of six regions of a cyclone within a sounding domain into one of four categories at a 6-hourly analysis time: single band only (SINGLE), multi-bands only (MULTI),

both single and multi-bands (BOTH), and non-banded (NONE). This resulted in 193 classified events with the most common categories being BOTH (107) and NONE (46), followed by MULTI (35) and SINGLE (5).

Additional information was used to further sub-classify the categories by their association with a developing (DEV) or mature (MAT) cyclone and the type of geographic-centric band movement exhibited as being either radially moving (perpendicular to long axis, RAD) or laterally moving (parallel to long axis, LAT). This analysis was done for the 193 6-hourly events. DEV cyclones most often exhibited BOTH (48%) in the northeast quadrant, NONE (32%) in the eastern quadrants, and MULTI (20%) in the northeast quadrant. DEV cyclones were predominantly associated with LAT moving bands (69%) that were clustered in the northeast quadrant. MAT cyclones most often exhibited BOTH (48%) in the northwest quadrant, MULTI (17%) in the northeast quadrant, NONE (17%) in the eastern quadrants, and SINGLE (5%) in the northwest quadrant. MAT cyclones were predominantly associated with RAD moving bands (87%) that occurred most frequently in the northwest quadrant of the cyclone. Of the BOTH classification, 65% of DEV events exhibited LAT movement in the northeast quadrant and 91% of MAT events exhibited RAD movement in the northwest quadrant. Therefore, a conceptual model for BOTH events for either DEV or MAT cyclones is presented in Figure 6.1 which shows the preferential location of bands relative to cyclone stage consistent with the single band analysis of Novak et al. (2010) and Schultz and Vaughan (2010).

b. Analysis of band environments

The observed soundings, CFSR, and CFSv2 analyses were used to compare environmental variables of the known important single banding ingredients of lift, instability and moisture for the different banding classifications. On average, frontogenesis is stronger for SINGLE and BOTH events compared to MULTI and NONE, with more events exceeding 2 K 100 km^{-1} h^{-1}. However, MULTI and BOTH typically exhibit a 200-hPa layer of conditional symmetric instability (CSI) more often than conditional instability (CI). Previous studies suggest that CSI is the dominant instability responsible for multiple bands from analysis of one case or synoptic situation (e.g., Shields et al. 1991, Xu 1992) to three cases (Nicosia and Grumm 1999) whereas Novak et al. (2010) found that CI occurred more often than CSI for dozens of single

band cases within mature cyclones. Furthermore, Schultz and Schumacher (1999) found that CSI is not a guaranteed instability that is always associated with banding. CI might be important for multi-bands within BOTH events but a relationship is not clear for MULTI events which requires additional investigation. NONE events show shallow near-surface layers of CSI, but even if the instability is present it might not be released without air being lifted via frontogenesis and therefore is non-banded. There was no significant difference the third banding ingredient, moisture, among the classifications likely due to the common location in the near-saturated environment of the cyclone comma head.

Cyclone-relative composites allowed for the spatial examination and comparison of the environments of the four classifications for DEV and MAT cyclones. Generally, the strongest cyclones with the largest low-to-midlevel (i.e., 850–700 hPa) temperature gradients exhibited bands. SINGLE, MULTI, BOTH were associated with larger low-level temperature gradients with deeper cyclones, more amplified mid-level troughs, and stronger upper-level jets than non-banded (NONE) cases. For SINGLE, MULTI, and BOTH, the strength of the surface low and mid-level trough may indicate how much warmer and higher moisture content (indicated by higher values of 700-hPa θ_e) may reach the northern quadrants of the cyclone where increased baroclinicity with the colder, drier to the north of the surface low may result in frontal ascent. For both DEV and MAT cyclones, MULTI was associated with a larger spatial extent of the mid-level warm, moist air reaching the northern quadrants of the cyclone interacting with stronger baroclinic zones than the SINGLE bands that are concentrated in the northwest quadrant consistent with the findings of Novak et al. (2004).

c. Thermodynamic evolution of multi-bands and single bands

Two detailed case studies were conducted using high-resolution mesoscale model simulations of bands within NEUS winter storms. The first case was of an intense single band in the comma head of the 8–9 Feb 2013 storm. The observed microphysical evolution was assessed using dual-polarization radar observations that provided insight into the general identification of hydrometeors and mixed-phase transition zones which were verified using ground observations of snow habit, degree of riming, and SLR at Stony Brook University (SBNY). The WRF model was used to simulate the event to determine (1) the evolution of forcing and stability of the

snowband, (2) the thermodynamic evolution of the band and (3) how the evolution impacted the microphysics and snowfall rates.

The thermodynamic analysis of the band showed that diabatic processes, especially condensational heating and cooling by melting, affect the evolution of the band's observed microphysics, but vertical advections induced by a strong frontogenetical circulation also impact observed microphysics. The trajectory analysis and evaluation of the thermodynamic equation provided evidence that the frontogenetically-forced vertical motion during the band's most intense phase was important because without it, the environment may have cooled a lot sooner to support an all-snow event instead of the complex hydrometeors including heavily rimed aggregates and large sleet that were observed during that time period. Further evidence was provided by the sensitivity tests that showed that latent heating was critical to the maintenance of an environment of decreased stability and narrow updrafts which agreed with the findings of Novak et al. (2009). In addition to the large-scale horizontal temperature advection, diabatic cooling was important to ultimately cool the band environment to support less-dense snow aggregates. The diabatic effects occurring within the band environment were shown to affect the simulated band occurrence, intensity, and precipitation type which ultimately changed the storm total snowfall amounts.

The second case study was of a case of both single and multi-banding in the comma head of the 26–27 Dec 2010 storm. The environments of the single and multi-bands exhibited some key differences. Firstly, the single band formed along a 700-hPa frontal zone but the multi-bands grew upscale from cells ~200 km southeast of the single band in the northwest quadrant of a mature cyclone. The cells were triggered by enhanced small-scale 850-hPa frontogenesis maxima in an environment of considerable 800–900-hPa vertical wind shear, which allowed for the conversion of latent vorticity to relative vorticity once a moist updraft formed. The cell then grew upscale and elongated into bands parallel to the 900–500-hPa wind shear in a deformation zone and steered by the 700-hPa wind. Secondly, although both types of bands formed in a sloping frontal zone in the comma head to the northwest of a surface cyclone, the multi-bands formed along the boundary between the higher 700-hPa θ_e air in the comma head associated with the cyclonically-turning branch of the warm conveyor belt and the dry intrusion. As a result, this multi-banded region was collocated with weaker conditional stability than the single band environment between 850–500-hPa. Therefore a single band may form within more stable

conditions, but multiple bands require weaker stability (Shields et al. 1991; Xu 1992; Nicosia and Grumm 1999).

There is consistency among the primary bands in the two case studies with the conceptual diagram presented by Novak et al. (2010) of mature single bands in the northwest quadrant of mature cyclones. They found that single bands form in a region of enhanced mid-level frontogenesis from an ageostrophic thermally direct circulation that is enhanced by weak conditional stability. Multi-bands in the presence of a primary band in a similar environment in the northwest quadrant of a mature cyclone have been added to this conceptual model in Figure 6.2 based on the two case studies and the 64 BOTH events within MAT cyclones. The multi-bands occur to the southeast of the primary band in a region of CI. Analysis of multi-bands occurring with or without a primary band in the northeast quadrant requires additional analysis and therefore no conceptual diagram of banding ingredients is provided.

d. Contributions to mesoscale snowband research

This dissertation reassessed conventional knowledge of banding types in a climatology of NEUS winter storms and provided case studies of the thermodynamic evolutions of two storms exhibiting intense single bands and one with robust multi-bands. The research contributed to the existing body of mesoscale snowband research as follows:

- The first automatic climatology of multi-bands is created from observations.
- Single bands rarely exist without also being accompanied by multi-bands from observations from 110 NEUS winter storms.
- The first high-resolution simulation of multi-bands from a real data case for NEUS winter storms is examined.
- According to observations and reanalysis data, multi-bands accompanying a single band to the northwest of a mature cyclone are most often associated with an environment of conditional instability whereas the single band is associated with conditional symmetric instability.
- From a simulation, multi-bands can form from upscale growth of convective cells in an environment of enhanced vertical wind shear, like has been shown for rainbands.

Most existing climatologies of snowbands did not include multi-bands (i.e., Kenyon et al. 2013, Baxter and Schumacher 2017) or contained a similar multi-bands classification but did not include them in any environmental analysis (Novak et al. 2004). Therefore, this thesis is unique in that it employed automatic methods that improved upon previous subjective methodology that allowed for both the identification and examination of small-scale multi-bands.

The second bullet challenges what was shown by Novak et al. (2004) regarding his percentage of events that exhibit single bands versus multi-bands, 55% and 33%, respectively. In this study, only 3% of events exhibited a single band but 55% of events exhibited a single band accompanied by multi-bands. Only 18% of events were of solely multi-bands. This discrepancy may be a result of the 5-dBZ binning of the reflectivity field that Novak et al. (2004) subjectively used, rather than utilizing a dynamic threshold that automatically defined bands within the reflectivity.

Theoretical work by Xu (1992) suggests that multiple bands result from increasingly unstable environments. Specifically that single bands could exist in more stable environments but unstable environments were required in order to have vertical circulations supporting multi-bands. The analysis in this study suggests that multi-bands may form in a variety of environments, some of which are stable to vertical motions but unstable to slantwise motions. The case study of 26–27 Dec 2010 agrees with Xu (1992) whereby multi-bands formed within a region of conditional instability southeast of a single band that was quasi-stationary within a more stable environment.

Previous studies have cited the limitation of observational data as a limiting factor in analysis of small-scale multi-bands (e.g., Jascourt et al. 1988, Shields et al. 1991). This study utilized a high-resolution (~1-km grid spacing) mesoscale model to create a dataset in order to analyze multi-bands forming to the east of a primary band in the comma head of a mature cyclone. This simulation put multi-bands and primary bands occurring in the BOTH classification of MAT cyclones into the context of previous research of single bands (Novak et al. 2010) in that multi-bands can form in an environment of weaker forcing but greater instability and become deformed and elongated by the vertical wind shear while moving with the ambient steering flow. This analysis also showed that multi-bands can form from upscale growth of convective cells along a sloping frontal zone in an environment of enhanced vertical wind shear,

like has been shown for rainbands (Jascourt et al. 1988). In order to generalize these results, analysis of more cases would be necessary.

6.2 Future work

a. Observations of multi-bands in Northeast U.S. snowstorms

This dissertation heavily relied upon conventional observations (i.e., WSR-88D radars, radiosonde profiles) and reanalysis data. The ~5-min radar data were from radars that were fixed relative to the moving and evolving bands within the extratropical cyclones being sampled. While the 6 coastal radars in the Northeast U.S. provided a good amount of spatial coverage, there were several cases in the dataset where bands were forming offshore (east-southeast of the range of the eastern-most radars). The radiosonde observations were also fixed in space and time, launched from 6 locations every 12-h. It was determined that 6-h reanalysis data be used in place of observed soundings to increase the temporal coverage within individual storms. More often than not, bands occurred outside of the 2 h window (±1 h) around a reanalysis time (i.e., 0000, 0600, 1200 UTC, etc.). In order to increase the number of banded events in this climatology, more environmental data is necessary. For example, additional data could include satellite-derived soundings.

An intensive field campaign with airborne dual-polarization radars and dropsondes would be an ideal way to create a dataset of a few cases over a couple winter seasons in order to study the evolution of multi-bands. Rauber et al. (2017) used the High-Performance Instrumented Airborne Platform for Environmental Research (HIAPER) Cloud Radar to examine the detailed reflectivity and spectral width indicative of turbulence through various banded and non-banded structures within a single NEUS snowstorm. The individual circulations resulting in multi-bands may be able to be sampled to examine microphysical evidence of shear, a stable layer, etc. and compare with that of single bands. Another mobile observation platform could be mobile Doppler radars. A Doppler on wheels (DOW) was used by Kristovich et al. (2017) in their investigation of lake effect snowstorms over Lake Ontario. A combination of Range Height Indicator (fixed in the horizontal while scanning all elevations in the vertical) and Plan Position Indicator (fixed elevation while scanning all horizontal angles) scans would be able to create a 3-

dimensional observational dataset of the fine-scale bands of NEUS winter storms.

Perhaps a more cost-effective data-collecting method would be utilizing additional static, ground-based instrumentation. While the dataset was new and not utilized for this dissertation, the snowflake images from the Multi-Angle Snowflake Camera (MASC) at Stony Brook University provide high-resolution imagery showing snowflake crystal habit and degree of riming. When data has been collected for more storms in the coming seasons, results can be compared to that of Colle et al. (2014) of crystal habit and related to banding type as determined from this study. The addition of new radar technology at Stony Brook University may (i.e., K-band radar) may also provide additional datasets to analyze the complex structures observed in different banding types within storms that pass over Long Island.

b. Additional modeling experiments analyzing the thermodynamic evolution of multi-bands

The case study of 8–9 Feb 2013 provided in Chapter 4 used the ability to tune the microphysical parameterization scheme in order to isolate the contributions of individual processes to diabatic heating or cooling of a band environment in order to assess their relative importance to the evolution of a single band. Such an exercise in isolating the diabatic effects in the multi-band case study of 26–27 Dec 2010 would provide additional insight into multi-band evolution, specifically testing whether the diabatic warming within the band results in enhanced convergence resultant vertical circulations that increase the longevity of each band. This could be assessed by turning off diabatic warming once the multi-bands have formed around FH 19, i.e., 0100 UTC 27 Dec 2010 from a 0600 UTC 27 Dec 2010 initialized run. The diabatic heating through deposition or condensation could be isolated together or individually in the experiment.

The NEUS domain is situated along a storm track in the winter with cold, dry continental air northeast of the warm, moist maritime air enhanced by the nearby Gulf Stream. With the Gulf Stream acting as an offshore reservoir of heat and moisture allowing for explosive cyclogenesis with strong banded signatures, an experiment could be designed to test the level of sensitivity of banded structure with varying surface temperatures (SSTs). This type of experiment has been conducted to test the sensitivity of latent heat release with regards to cyclogenesis (Stoelinga 1996; Willison et al. 2015). Of particular interest is if the presence of warm core rings or eddies from the Gulf Stream can be related to enhance convection and banding activity in the northwest

quadrant of a mature cyclone. Further investigation of the concept of analyzing the effect of sea surface temperatures on the resulting banding activity could employ a coupled ocean-atmospheric model. The Model for Prediction Across Scales (MPAS, Skamarock et al. 2012) would be a good tool to produce a realistic coupled system that in which the depth and temperature of the ocean boundary layer could be modified in a number of experiments.

c. Predictability of multi-bands

The ability of a mesoscale model in simulating multi-bands needs to be assessed for more cases. Chapter 5 discussed a system of 24 differently-configured WRF simulations employing 4 different initial and lateral boundary conditions (NARR, NAM, GFS, RUC), 2 planetary boundary layer schemes (YSU, MYJ), and 3 microphysical parametrization schemes (Morrison, Thompson, WSM6) in a single case study. Out of those 24 simulations, there was only one simulation that resolved the primary and multi-bands with minimal error in structure and duration. The variation in simulated bands was associated with most simulations being too stable with weak frontogenetical forcing for ascent in the single band or multi-bands environments. Additional work could be done analyzing the spatial verification statistics of the simulated bands. The Model Evaluation Tools (MET) could be employed to quantify errors in spatial quantities such as reflectivity or even environmental parameters. Using the MODE tool was preliminarily applied to three WRF simulations from the case study as a proof of concept (Fig. 6.3). Such verification methods can rapidly identify snowbands in model simulations which can be readily applied to a large number of cases. Preliminary results of 24 simulations for 3 additional cases showed that the variance in the results of the structure and intensity of simulated bands is not isolated to the one case study in Chapter 5.

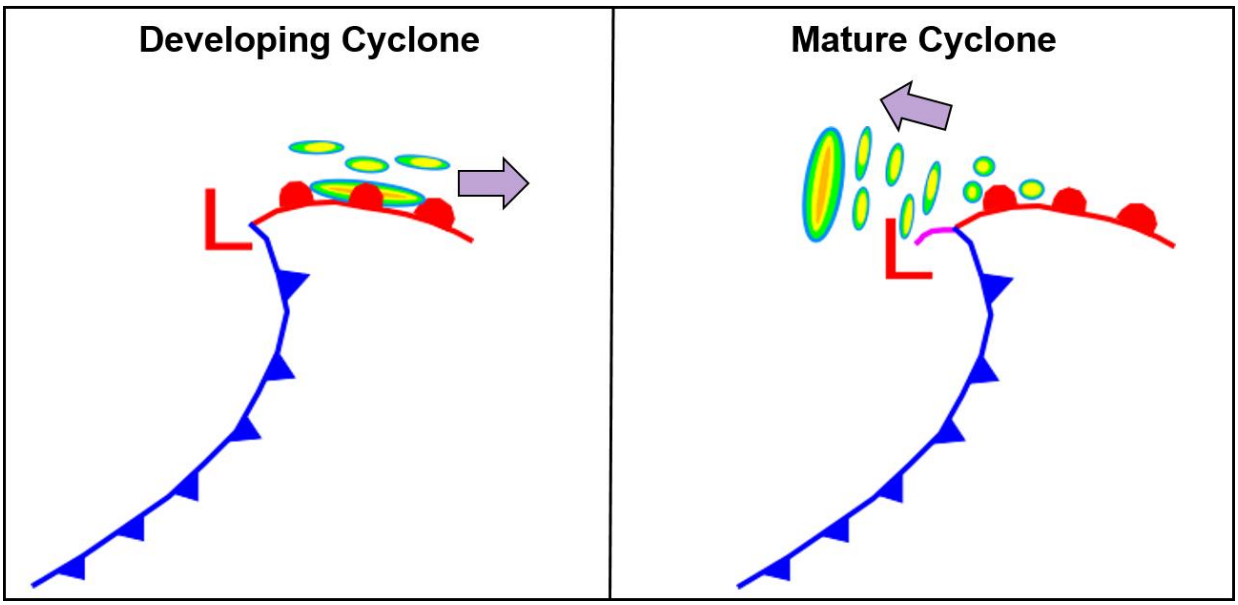

Figure 6.1. Idealized location of the primary and multi-bands of the BOTH classification for (left panel) DEV cyclones and (right panel) MAT cyclones. The purple arrow indicates the predominant LAT or RAD movement for DEV and MAT, respectively. Adapted from Fig. 17 of Schultz and Vaughan (2010).

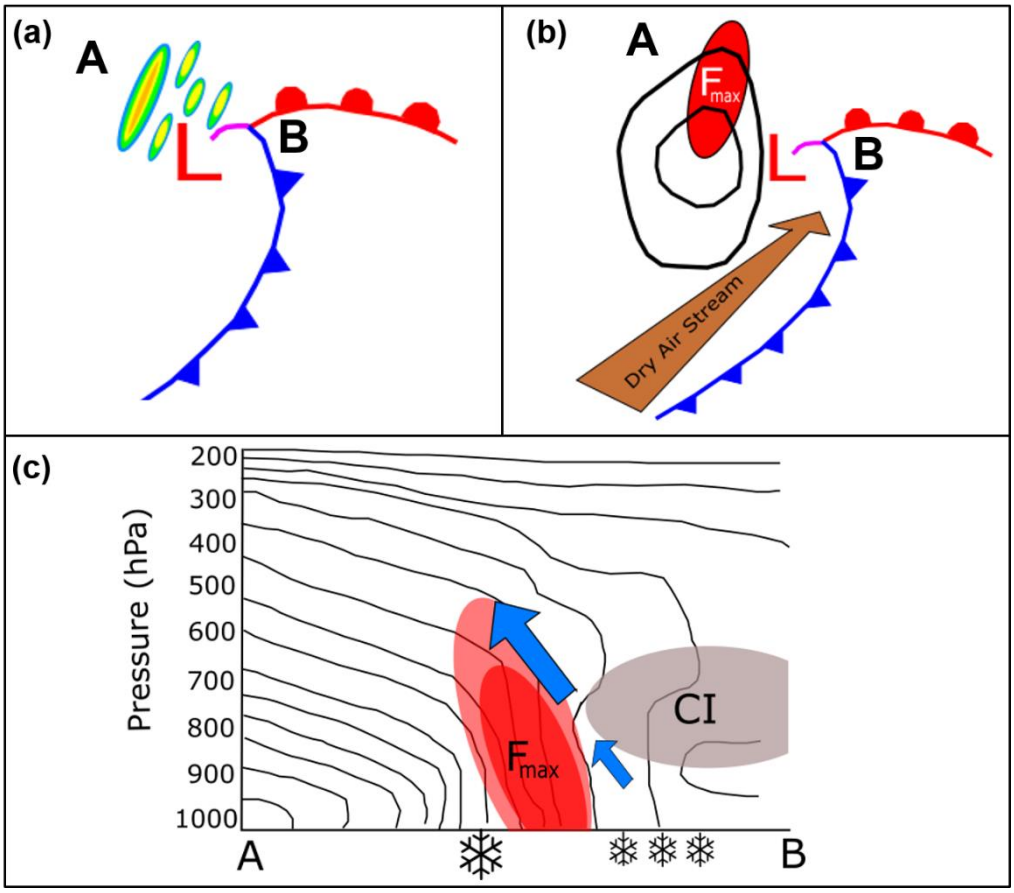

Figure 6.2. Adapted from Novak et al. (2010; Their Figs. 15c,d) showing a schematic depiction of both a single band and multi-bands (BOTH) in the northwest quadrant of a mature (MAT) cyclone from analysis of the case study of 26–27 Dec 2010. (a) Plan-view schematic of the bands relative to the cyclone and locations of the cross section end points used in (c). (b) As in (a) but showing the key banding ingredients of the 700-hPa trough (black lines), frontogenesis maximum (red oval), and dry air stream (brown arrow). (c) Cross section showing isentropes (black lines), frontal ascent maxima (blue arrows), sloping frontogenesis maximum (red oval), and a region of conditional instability (CI; gray oval). The location of the single band is indicated by the large snowflake symbol and the location of the multi-bands is indicated by the smaller snowflake symbols.

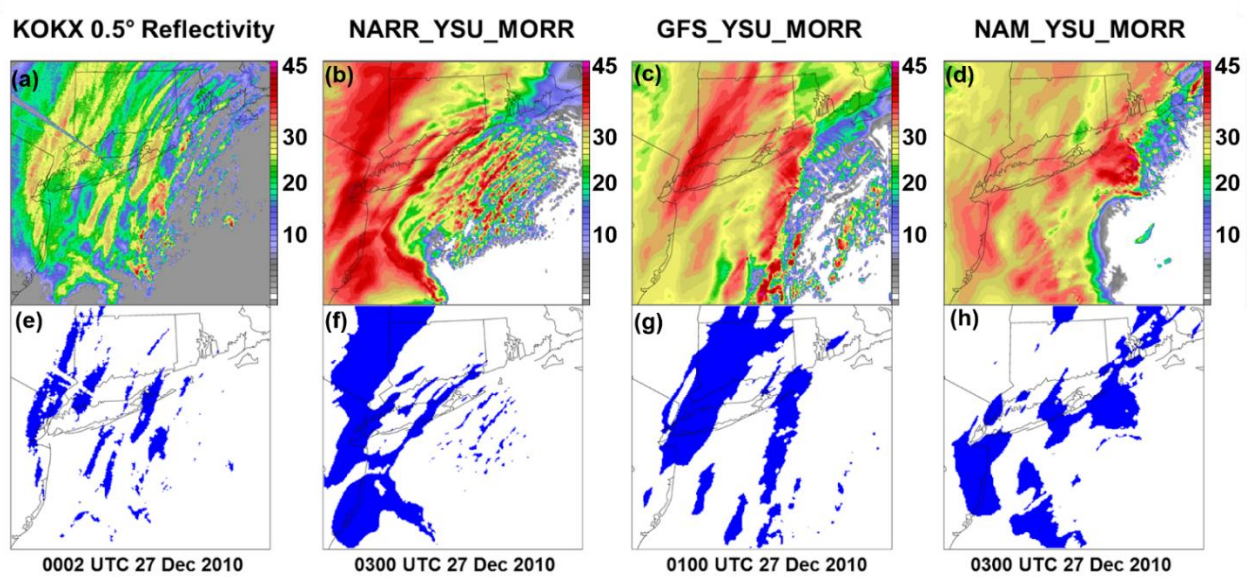

Figure 6.3. Comparison of MODE identified bands from observations and three separate WRF simulations. (a–d) Observed and simulated reflectivity (dB*Z*, shaded according to scale). (e–h) Objects output from MODE.

References

Andrić, J., M. R. Kumjian, D. S. Zrnić, J. M. Straka, and V. M. Melnikov, 2013: Polarimetric signatures above the melting layer in winter storms: An observational and modeling study. *J. Appl. Meteor. Climatol.*, **52**, 682–700.

Baxter, M. and P. Schumacher, 2017: Distribution of single-banded snowfall in Central United States cyclones. *Wea. Forecasting*, **32**, 533–554.

Benjamin, S. G., G. A. Grell, J. M. Brown, T. G. Smirnova, and R. Bleck, 2004: Mesoscale weather prediction with the RUC hybrid isentropic-terrain-following coordinate model. *Mon. Wea. Rev.*, **132**, 473–494.

Benjamin, S.G., W.R. Moninger, S.S. Weygandt, M. Hu, D. Devenyi, J.M. Brown, T. Smirnova, J. Olson, C. Alexander, K. Brundage, G. Grell, S. Peckham, T. L. Smith, S.R. Sahm, B. Jamison, 2009: Technical review of Rapid Refresh/RUC project, NOAA/ESRL/GSD Internal Review, 168 pp.

Betts, A. K., 1986: A new convective adjustment scheme. Part I: Observational and theoretical basis. *Quart. J. Roy. Meteor. Soc.*, **112**, 677–691.

Bjerknes, J., and H. Solberg, 1922: Life cycle of cyclones and the polar front theory of atmospheric circulation. *Geofys. Publ.*, **3**, 3–18.

Brown, B.G., R. Bullock, J. Halley Gotway, D. Ahijevych, C. Davis, E. Gilleland, and L. Holland, 2007: Application of the MODE object-based verification tool for the evaluation of model precipitation fields. *AMS 22nd Conference on Weather Analysis and Forecasting and 18th Conference on Numerical Weather Prediction*, 25–29 June, Park City, Utah, Amer. Meteor. Soc.

Bryan, G., 2014: Recommendations for WRF simulations with horizontal grid spacing between 100 m and 1 km. *15th WRF Users' Workshop*. Boulder, CO. NCAR. [Available online at http://www2.mmm.ucar.edu/wrf/users/workshops/WS2014/ppts/4.1.pdf.]

Bullock, R. G., B. G. Brown, and T. L. Fowler, 2016: Method for object-based diagnostic evaluation. NCAR Tech.Note. NCAR/TN-532+STR, 84 pp, doi:10.5065/D61V5CBS.

Chagnon, J. M., and S. L. Gray, 2009: Horizontal potential vorticity dipoles on the convective storm scale. *Quart. J. Roy. Meteor. Soc.*, **135**, 1392–1408.

Charles, M. E., and B. A. Colle, 2009: Verification of extratropical cyclones within the NCEP operational models. Part I: analysis errors and short-term NAM and GFS forecasts. *Wea. Forecasting*, **24**, 1173–1190.

Clark, J. H. E., R. P. James, and R. H. Grumm, 2002: A reexamination of the mechanisms responsible for banded precipitation. *Mon. Wea. Rev.*, **130**, 3074–3086.

Colle, B. A., and S. E. Yuter, 2007: The impact of coastal boundaries and small hills on the precipitation distribution across Southern Connecticut and Long Island, New York. *Mon. Wea. Rev.*, **135**, 933–954.

Colle, B. A., D. Stark, and S. E. Yuter, 2014: Surface microphysical observations within East Coast winter storms on Long Island, NY. *Mon. Wea. Rev.*, **142**, 3126–3146.

Colle, B. A., Z. Zhang, K. A. Lombardo, E. Chang, P. Liu, and M. Zhang, 2013: Historical evaluation and future prediction of Eastern North American and Western Atlantic extratropical cyclones in the CMIP5 models during the cool season. *J. Climate*, **26**, 6882–6903.

Corbin, N. A., 2016: Northern California's Central Valley spatial precipitation patterns associated with atmospheric rivers under different environmental conditions, M.S. Thesis, Dept. of Marine, Earth, Atmospheric Sciences, North Carolina State University, 227 pp.

Cotton, W. R., G. Bryan, and S. C. van den Heever, 2011: Chapter 10 - The mesoscale structure of extratropical cyclones and middle and high clouds. *International Geophysics*, G. B. W. Cotton, and H. S. van den, Eds., Academic Press, 527–672.

Cronce, M., R. M. Rauber, K. R. Knupp, B. F. Jewett, J. T. Walters, and D. Phillips, 2007: Vertical motions in precipitation bands in three winter cyclones. *J. Appl. Meteor. Climatol.*, **46**, 1523–1543.

Cunningham, J. G., and S. E. Yuter, 2014: Instability characteristics of radar-derived mesoscale organization modes within cool-season precipitation near Portland, Oregon. *Mon. Wea. Rev.*, **142**, 1738–1757.

Davis, C.A., B.G. Brown, and R.G. Bullock, 2006a: Object-based verification of precipitation forecasts, Part I: Methodology and application to mesoscale rain areas. *Mon. Wea. Rev.*, **134**, 1772–1784.

Davis, C.A., B.G. Brown, and R.G. Bullock, 2006b: Object-based verification of precipitation forecasts, Part II: Application to convective rain systems. *Mon. Wea. Rev.*, **134**, 1785–1795.

Dee, D. P., and Coauthors, 2011: The ERA-Interim reanalysis: configuration and performance of the data assimilation system. *Q.J.R. Meteorol. Soc*., **137**: 553–597.

desJardins, M. L., K. F. Brill, and S. S. Schotz, 1991: Use of GEMPAK on UNIX workstations. *Proc. Seventh Int. Conf. on Interactive Information and Processing Systems for Meteorology, Oceanography, and Hydrology*, New Orleans, LA, Amer. Meteor. Soc., 449–453.

Developmental Testbed Center, 2015: MET: Version 5.1 Model Evaluation Tools Users Guide. 317 pp. [Available online at http://www.dtcenter.org/met/users/docs/overview.php.]

Dudhia, J., 1996: A multi-layer soil temperature model for MM5. The Sixth PSU/NCAR Mesoscale Model Users' Workshop.

Ek, M. B., K. E. Mitchell, Y. Lin, E. Rogers, P. Grunmann, V. Koren, G. Gayno, and J. D. Tarpley, 2003: Implementation of Noah land surface model advances in the National Centers for Environmental Prediction operational mesoscale Eta model. *J. Geophys. Res.*, **108**, 8851, doi:10.1029/2002JD003296.

Emanuel, K. A., 1985: Frontal circulations in the presence of small moist symmetric stability. *J. Atmos. Sci.*, **42**, 1062–1071.

Evans, M., and M. L. Jurewicz, 2009: Correlations between analyses and forecasts of banded heavy snow ingredients and observed snowfall. *Wea. Forecasting*, **24**, 337–350.

Fairman Jr, J. G., D. M. Schultz, D. J. Kirshbaum, S. L. Gray, and A. I. Barrett: Climatology of banded precipitation over the contiguous united states. *Mon. Wea. Rev.*, **144**, 4553–4568.

Fuhrmann, C. M., and C. E. Konrad, 2013: A trajectory approach to analyzing the ingredients associated with heavy winter storms in Central North Carolina. *Wea. Forecasting*, **28**, 647–667.

Ganetis, S., and B. Colle, 2015: The thermodynamic and microphysical evolution of an intense snowband during the Northeast U.S. blizzard of 8-9 February 2013. *Mon. Wea. Rev.*, **143**, 4104–4125.

Gao, S., X. Wang, and Y. Zhou, 2004: Generation of generalized moist potential vorticity in a frictionless and moist adiabatic flow. *Geophys. Res. Lett.*, **31**, L12113.

Gosselin, J. P., C. M. Gravelle, C. E. Graves, J. P. Gagan, F. H. Glass, 2011: Composite analysis of heavy snow events within the Springfield and St. Louis, Missouri National Weather Service county warning areas. *National Wea. Digest*, **35**, 57–81.

Griffin, E. M., T. J. Schuur, A. V. Ryzhkov, H. D. Reeves, and J. C. Picca, 2014: A polarimetric and microphysical investigation of the Northeast blizzard of 8–9 February 2013. *Wea. Forecasting*, **29**, 1271–1294.

Hoban, N. P., 2016: Observed characteristics of mesoscale banding in Coastal Northeast U.S. snow storms, M.S. Thesis, Dept. of Marine, Earth, Atmospheric Sciences, North Carolina State University, 66 pp.

Hoban, N. P., S. E. Yuter, L. Tomkins, S. A. Ganetis, M. A. Miller, L. Lovell, S. R. Rhodes, E. Scott, and B. A. Colle, 2017: Observed characteristics of mesoscale banding in Coastal Northeast U.S. snow storms. *28th Conference on Weather Analysis and Forecasting / 24th Conference on Numerical Weather Prediction*. Seattle, WA, Amer. Meteor. Soc.

Hobbs, P. V., 1978: Organization and structure of clouds and precipitation on the mesoscale and microscale in cyclonic storms. *Rev. of Geophys. and Space Phys.*, **16**, 741–755.

Hodges, K. I., 1995: Feature tracking on the unit sphere. *Mon. Wea. Rev.*, **123**, 3458–3465.

Hong, S.–Y., and J.–O. J. Lim, 2006: The WRF single–moment 6–class microphysics scheme (WSM6). *J. Korean Meteor. Soc*., **42**, 129–151.

Hong, S.–Y., Y. Noh, J. Dudhia, 2006: A new vertical diffusion package with an explicit treatment of entrainment processes. *Mon. Wea. Rev.*, **134**, 2318–2341.

Houze, R. A., P. V. Hobbs, K. R. Biswas, and W. M. Davis, 1976: Mesoscale rainbands in extratropical cyclones. *Mon. Wea. Rev.*, **104**, 868–878.

Janjic, Z. I., 1994: The step-mountain eta coordinate model: further developments of the convection, viscous sublayer and turbulence closure schemes, *Mon. Wea. Rev.*, **122**, 927–945.

Janjic, Z. I., 2000: Comments on "Development and evaluation of a convection scheme for use in climate models", *J. Atmos. Sci.*, **57**, p. 3686.

Jascourt, S. D., S. S. Lindstrom, C. J. Seman, and D. D. Houghton, 1988: An observation of banded convective development in the presence of weak symmetric stability. *Mon. Wea. Rev.*, **116**, 175–191.

Jurewicz, M. L., and M. S. Evans, 2004: A Comparison of two banded, heavy snowstorms with very different synoptic settings. *Wea. Forecasting*, **19**, 1011–1028.

Kain, J. S., S. M. Goss, and M. E. Baldwin, 2000: The melting effect as a factor in precipitation-type forecasting. *Wea. Forecasting*, **15**, 700–714.

Kain, J. S., 2004: The Kain–Fritsch convective parameterization: An update. *J. Appl. Meteor. Climatol.*, **43**, 170–181.

Kalnay, E., and Coauthors, 1996: The NCEP/NCAR 40-year reanalysis project. *Bull. Amer. Meteor. Soc.*, **77**, 437–471.

Kawashima, M., 2016: The role of vertically propagating gravity waves forced by melting-induced cooling in the formation and evolution of wide cold-frontal rainbands. *J. Atmos. Sci.*, **73**, 2803-2836.

Kenyon, J. S., 2013: The motion of mesoscale snowbands in Northeast U.S. winter storms, M.S. Thesis, Dept. of Atmos. and Environmental Sci., University at Albany, State University of New York, 108 pp.

Kenyon, J. S., L. F. Bosart, D. Keyser, and M. S. Evans, 2013: The motion of mesoscale snowbands in Northeast U.S. winter storms. *15th Conference on Mesoscale Processes.* Portland, OR, Amer. Meteor. Soc.

Keyser, D. and R.A. Anthes, 1982: The influence of planetary boundary layer physics on frontal structure in the Hoskins-Bretherton horizontal shear model. *J. Atmos. Sci.*, **39**, 1783–1802.

Kocin, P. J., and L. W. Uccellini, 2004: *Northeast snowstorms. Volume I: Overview.* Meteor. Monogr. No. 54, Amer. Meteor. Soc., 270 pp.

Kocin, P., L. W. Uccellini, J. Alpert, B. Ballish, D. Bright, R. Grumm, and G. Manikin, 2011: The blizzard of 25-27 December 2010: Forecast assessment. NOAA/NCEP event review. [Available online at http://www.wpc.ncep.noaa.gov/winter_storm_summaries/event_reviews/2010/December25_27_2010_Blizzard.pdf.]

Krekeler, J., 2013: Great Lakes to Northeast major winter storm. NOAA/NCEP/WPC event review. [Available online at http://www.wpc.ncep.noaa.gov/winter_storm_summaries/event_reviews/2013/Great_Lakes_Northeast_Winter_Storm_Feb2013.pdf.]

Kristovich, D. A. R., and Coauthors, 2017: The Ontario winter lake-effect systems field campaign: scientific and educational adventures to further our knowledge and prediction of lake-effect storms. *Bull. Amer. Meteor. Soc.,* **98**, 315-332.

Kumjian, M. R., 2013: Principles and applications of dual-polarization weather radar. Part I: Description of the polarimetric radar variables. *J. Oper. Meteor.,* **1**, 226–242.

Kumjian, M. R., S. A. Rutledge, R. M. Rasmussen, P. C. Kennedy, and M. Dixon, 2014: High-resolution polarimetric radar observations of snow-generating cells. *J. Appl. Meteor. Climatol.*, **53**, 1636-1658.

Lackmann, G. M., K. Keeter, L. G. Lee, and M. B. Ek, 2002: Model representation of freezing and melting precipitation: Implications for winter weather forecasting. *Wea. Forecasting*, **17**, 1016-1033.

Lawson, J. R., and W. A. Gallus, 2016: Adapting the SAL method to evaluate reflectivity forecasts of summer precipitation in the central United States. *Atmos. Sci. Lett.*, **17**, 524-530.

Lawson, J., D. M. Schultz, G. Vaughan, and D. J. Kirshbaum, 2013: Multiple bands near fronts in VHF wind-profiling radar and radiosonde data. *Atmos. Sci. Lett.*, **14**, 146-152.

Magono, C. and C. W. Lee, 1966: Meteorological Classification of Natural Snow Crystals. *J. of the Faculty of Science*, Hokkaido University.

Market, P. S., R. W. Przybylinski, and S. M. Rochette, 2006: The role of sublimational cooling in a late-season Midwestern snow event. *Wea. Forecasting*, **21**, 364-382.

Market, P.S., K. Crandall, and R. Rauber, 2012: High-resolution rawinsonde observations of the cold-sector precipitation regions in transient mid-latitude extratropical cyclones. *Natl. Wea. Dig*., **36**, 3–8.

Markowski, P., and Y. Richardson, 2010: *Mesoscale meteorology in Midlatitudes*. Wiley-Blackwell, 424 pp.

Martínez-Alvarado, O., and R. S. Plant, 2014: Parametrized diabatic processes in numerical simulations of an extratropical cyclone. *Quart. J. Roy. Meteor. Soc.*, **140**, 1742-1755.

McCann, D. W., 1995: Three-dimensional computations of equivalent potential vorticity. *Wea. Forecasting*, **10**, 798–802.

Mesinger, F., and Coauthors, 2006: North American Regional Reanalysis. *Bull. Amer. Meteor. Soc.*, **87**, 343–360.

Miller, J. E., 1946: Cyclogenesis in the Atlantic coastal region of the United States. *J. Meteor.*, **3**, 31–44.

Mofor, L. A., and C. Lu, 2009: Generalized moist potential vorticity and its application in the analysis of atmospheric flows. *Prog. Nat. Sci.*, **19**, 285-289.

Moore, J. T., F. H. Glass, C. E. Graves, S. M. Rochette, and M. J. Singer, 2003: The environment of warm-season elevated thunderstorms associated with heavy rainfall over the Central United States. *Wea. Forecasting*, **18**, 861-878.

Moore, J. T., C. E. Graves, S. Ng, and J. L. Smith, 2005: A process-oriented methodology toward understanding the organization of an extensive mesoscale snowband: A diagnostic case study of 4–5 December 1999. *Wea. Forecasting*, **20**, 35-50.

Moore, J. T., and T. E. Lambert, 1993: The use of equivalent potential vorticity to diagnose regions of conditional symmetric instability. *Wea. Forecasting*, **8**, 301-308.

Morcrette, C. J., and K. A. Browning, 2006: Formation and release of symmetric instability following Delta-M adjustment. *Quart. J. Roy. Meteor. Soc.*, **132**, 1073-1089.

Morrison, H., G. Thompson, V. Tatarskii, 2009: Impact of cloud microphysics on the development of trailing stratiform precipitation in a simulated squall line: Comparison of one– and two–moment schemes. *Mon. Wea. Rev.*, **137**, 991–1007.

Murray, D., J. McWhirter, S. Wier, and S. Emmerson, 2003: The integrated data viewer: a web-enabled application for scientific analysis and visualization. *19th Intl. Conf. on IIPS for Meteorology, Oceanography and Hydrology*.

The NCAR Command Language (Version 6.1.2) [Software]. (2013). Boulder, Colorado: UCAR/NCAR/CISL/VETS.[Available online at http://dx.doi.org/10.5065/D6WD3XH5.]

Neiman, P. J., M. A. Shapiro, and L. S. Fedor, 1993: The life cycle of an extratropical marine cyclone. Part II: Mesoscale structure and diagnostics. *Mon. Wea. Rev.*, **121**, 2177-2199.

Nicosia, D. J., and R. H. Grumm, 1999: Mesoscale band formation in three major Northeastern United States snowstorms. *Wea. Forecasting*, **14**, 346-368.

Norris, J., G. Vaughan, and D. M. Schultz, 2014: Precipitation banding in idealized baroclinic waves. *Mon. Wea. Rev.* **142**, 3081-3099.

Novak, D., 2009: Evolution and dynamical processes of solitary precipitation bands within the comma-head of Northeast United States cyclones. Dissertation, School of Marine and Atmospheric Sciences, Stony Brook University, 136 pp.

Novak, D. R., L. F. Bosart, D. Keyser, and J. S. Waldstreicher, 2004: An observational study of cold season–banded precipitation in Northeast U.S. cyclones. *Wea. Forecasting*, **19**, 993-1010.

Novak, D. R., and B. A. Colle, 2012: Diagnosing snowband predictability using a multimodel ensemble system. *Wea. Forecasting*, **27**, 565-585.

Novak, D. R., B. A. Colle, and A. R. Aiyyer, 2010: Evolution of mesoscale precipitation band environments within the comma head of Northeast U.S. cyclones. *Mon. Wea. Rev.*, **138**, 2354-2374.

Novak, D. R., B. A. Colle, and R. McTaggart-Cowan, 2009: The role of moist processes in the formation and evolution of mesoscale snowbands within the comma head of Northeast U.S. cyclones. *Mon. Wea. Rev.*, **137**, 2662-2686.

Novak, D. R., B. A. Colle, and S. E. Yuter, 2008: High-resolution observations and model simulations of the life cycle of an intense mesoscale snowband over the Northeastern United States. *Mon. Wea. Rev.*, **136**, 1433–1456.

Parsons, D.B. and P.V. Hobbs, 1983: The mesoscale and microscale structure and organization of clouds and precipitation in midlatitude cyclones. VII: Formation, development, interaction and dissipation of rainbands. *J. Atmos. Sci.*, **40**, 559–579.

Petterssen, S., 1936: Contribution to the theory of frontogenesis. *Geofys. Publ.*, **11**(6), 1–27.

Picca, J. C., D. M. Schultz, B. A. Colle, S. Ganetis, D. R. Novak, and M. Sienkiewicz, 2014: The

value of dual-polarization radar in diagnosing the complex microphysical evolution of an intense snowband. *Bull. Amer. Meteor. Soc.*, **95**, 1825–1834.

Pizzamei, M., S. L. Gray, and K. A. Browning, 2005: Cloud-resolving model simulations of multiply-banded frontal clouds. *Quart. J. Roy. Meteor. Soc.,* **131**, 2617–2637.

Plougonven, R., and F. Zhang, 2014: Internal gravity waves from atmospheric jets and fronts. *Rev. Geophys*., **52**, 33–76.

Pruppacher, H. R., and J. D. Klett, 1997: Microphysics of Clouds and Precipitation. D. Reidel, 714 pp.

Rauber, R. M., and Coauthors, 2013: Stability and charging characteristics of the comma head region of continental winter cyclones. *J. Atmos. Sci.,* **71**, 1559–1582.

Rauber, R. M., and Coauthors, 2014: Finescale radar and airmass structure of the comma head of a continental winter cyclone: The role of three airstreams. *Mon. Wea. Rev.*, **142**, 4207–4229.

Rauber, R. M., and Coauthors, 2017: Finescale structure of a snowstorm over the northeastern united states: A first look at high-resolution HAIPER cloud radar observations. *Bull. Amer. Meteor. Soc.*, **98**, 253–269.

Raymond, D. J., 1992: Nonlinear balance and potential-vorticity thinking at large Rossby number. *Quart. J. Roy. Meteor. Soc.*, **118**, 987–1015.

Raymond, D.J. and H. Jiang, 1990: A theory for long-lived mesoscale convective systems. *J. Atmos. Sci.*, **47**, 3067–3077.

Rosenow, A. A., D. M. Plummer, R. M. Rauber, G. M. McFarquhar, B. F. Jewett, and D. Leon, 2014: Vertical velocity and physical structure of generating cells and convection in the comma head region of continental winter cyclones. *J. Atmos. Sci.*, **71**, 1538–1558.

Rutledge, S. A., and P. Hobbs, 1983: The mesoscale and microscale structure and organization of clouds and precipitation in midlatitude cyclones. VIII: A model for the “seeder-feeder” process in warm-frontal rainbands. *J. Atmos. Sci.*, **40**, 1185–1206.

Saha, S., and Coauthors, 2010: The NCEP climate forecast system reanalysis. *Bull. Amer. Meteor. Soc.,* **91**, 1015–1057.

Saha, S., and Coauthors, 2014: The NCEP climate forecast system version 2. *J. Climate*, **27**, 2185–2208.

Sanders, F., and L. F. Bosart, 1985a: Mesoscale structure in the Megalopolitan snowstorm of 11–12 February 1983. Part I: frontogenetical forcing and symmetric instability. *J. Atmos. Sci.*, **42**, 1050–1061.

Sanders, F., and L. F. Bosart, 1985b: Mesoscale structure in the Megalopolitan snowstorm, 11–12 February 1983. Part II: doppler radar study of the New England snowband. *J. Atmos. Sci.*, **42**, 1398–1407.

Schultz, D. M., and J. A. Knox, 2007: Banded convection caused by frontogenesis in a conditionally, symmetrically, and inertially unstable environment. *Mon. Wea. Rev.,* **135**, 2095–2110.

Schultz, D. M., and P. N. Schumacher, 1999: The use and misuse of conditional symmetric instability. *Mon. Wea. Rev.,* **127**, 2709–2732.

Schultz, D. M., and G. Vaughan, 2010: Occluded fronts and the occlusion process: A fresh look at conventional wisdom. *Bull. Amer. Meteor. Soc.*, **92**, 443–466.

Schultz, D. M., D. S. Arndt, D. J. Stensrud, and J. W. Hanna, 2004: Snowbands during the cold-air outbreak of 23 January 2003. *Mon. Wea. Rev.*, **132**, 827–842.

Schumacher, R. S., D. M. Schultz, and J. A. Knox, 2010: Convective snowbands downstream of the Rocky Mountains in an environment with conditional, dry symmetric, and inertial instabilities. *Mon. Wea. Rev.*, **138**, 4416–4438.

Shapiro, M. A., and D. Keyser, 1990: Fronts, jet streams and the tropopause. Extratropical cyclones: The Erik Palmén memorial volume, C.W.Newton and E. O. Holopainen, Eds., *Amer. Meteor. Soc.*, pp. 167–191.

Shields, M. T., R. M. Rauber, and M. K. Ramamurthy, 1991: Dynamical forcing and mesoscale organization of precipitation bands in a Midwest winter cyclonic storm. *Mon. Wea. Rev.*, **119**, 936–964.

Skamarock, W. C., and Coauthors, 2008: A description of the Advanced Research WRF version 3. NCAR Tech. Note NCAR/TN-475+STR, 113 pp, doi:10.5065/D68S4MVH.

Skamarock, W. C., J. B. Klemp, M. G. Duda, L. D. Fowler, S.-H. Park, and T. D. Ringler, 2012:

A multiscale nonhydrostatic atmospheric model using centroidal Voronoi tesselations and C-grid staggering. *Mon. Wea. Rev.*, **140**, 3090–3105.

Soltow, M., 2011: December 25-27, 2010, Winter storm, Eastern United States. NOAA/NCEP/WPC event review. [Available online at http://www.wpc.ncep.noaa.gov/winter_storm_summaries/event_reviews/2010/Eastern_US_WinterStorm_December_2010.pdf.]

Stark, D., 2012: Field observations and modeling of the microphysics within winter storms over Long Island, NY. M.S. thesis, School of Marine and Atmospheric Sciences, Stony Brook University, 132 pp.

Stark, D., B. A. Colle, and S. E. Yuter, 2013: Observed microphysical evolution for two East Coast winter storms and the associated snow bands. *Mon. Wea. Rev.*, **141**, 2037–2057.

Stoelinga, M. T., 2009: A users' guide to RIP Version 4.5: A program for visualizing mesoscale model output. NCAR on-line document, [Available online at http://www2.mmm.ucar.edu/wrf/docs/ripug.htm.]

Tewari, M., F. Chen, W. Wang, J. Dudhia, M. A. LeMone, K. Mitchell, M. Ek, G. Gayno, J. Wegiel, and R. H. Cuenca, 2004: Implementation and verification of the unified NOAH land surface model in the WRF model. *20th Conf. on Weather Analysis and Forecasting/16th Conf. on Numerical Weather Prediction*, Seattle, WA, pp. 11–15.

Thompson, G., R. M. Rasmussen, and K. Manning, 2004: Explicit forecasts of winter precipitation using an improved bulk microphysics scheme. Part I: Description and sensitivity analysis. *Mon. Wea. Rev.*, **132**, 519–542.

Thompson, G., P. R. Field, R. M. Rasmussen, and W. D. Hall, 2008: Explicit forecasts of winter precipitation using an improved bulk microphysics scheme. Part II: Implementation of a new snow parameterization. *Mon. Wea. Rev.*, **136**, 5095–5115.

Thompson, E. J., S. A. Rutledge, B. Dolan, V. Chandrasekar, and B. L. Cheong, 2014: A dual-polarization radar hydrometeor classification algorithm for winter precipitation. *J. Atmos. Oceanic Technol.*, **31**, 1457–1481.

Thorpe, A. J., and K. A. Emanuel, 1985: Frontogenesis in the presence of small stability to slantwise convection. *J. Atmos. Sci.*, **42**, 1809–1824.

Trapp, J. R., D. M. Schultz, A. V. Ryzhkov, and R. L. Holle, 2001: Multiscale structure and

evolution of an Oklahoma winter precipitation event. *Mon. Wea. Rev.*, **129**, 486–501.

Uccellini, L. W., and S. E. Koch, 1987: The synoptic setting and possible energy sources for mesoscale wave disturbances. *Mon. Wea. Rev.*, **115**, 721–729.

Vaughan, G. et al., Cloud banding and winds in intense European cyclones: Results from the DIAMET project, *Bull. Amer. Meteor. Soc.*, **96**, 249–265.

Wei, J., and F. Zhang, 2013: Mesoscale gravity waves in moist baroclinic jet–front systems. *J. Atmos. Sci.*, **71**, 929–952.

Wilks, D.S., 2011: *Statistical methods in the atmospheric sciences*, 3rd Ed. International Geophysics Series, Vol. 100, Academic Press, 704 pp.

Willison, J., W. A. Robinson, and G. M. Lackmann, 2015: North Atlantic storm-track sensitivity to warming increases with model resolution. *J. Climate*, **28**, 4513–4524.

Wolfsberg, D. G., K. A. Emanuel, and R. E. Passarelli, 1986: Band formation in a New England winter storm. *Mon. Wea. Rev.*, **114**, 1552–1569.

Xu, Q., 1986: Conditional symmetric instability and mesoscale rainbands. *Quart. J. Roy. Meteor. Soc.*, **112**, 315–334.

Xu, Q., 1989: Extended Sawyer–Eliassen equation for frontal circulations in the presence of small viscous moist symmetric stability. *J. Atmos. Sci.*, **46**, 2671–2683.

Xu, Q., 1992: Formation and evolution of frontal rainbands and geostrophic potential vorticity anomalies. *J. Atmos. Sci.*, **49**, 629–648.

Appendix:

Table of Event Classifications

Table A.1. The case number, case start date (YYYYMMDD), event time (YYYYMMDDHH), event classification (SINGLE, MULTI, BOTH, NONE), cyclone stage (DEV, MAT) band movement (LAT, RAD), and sounding site (by WMO ID number) for the 193 classified events from 110 cases of NEUS storms from Oct–Apr 1996–2016.

Case Number	Case Start Date	Event Time	Event Classification	Cyclone Stage	Band Movement	Sounding Site for Event
1	19960102	1996010218	NONE	DEV	NONE	72501
2	19960110	1996011006	BOTH	DEV	RAD	74494
2	19960110	1996011012	MULTI	DEV	RAD	74389
3	19960112	1996011218	NONE	MAT	NONE	72501
4	19970111	1997011112	BOTH	DEV	RAD	72501
5	19970127	1997012806	NONE	MAT	NONE	72501
6	19970216	1997021706	NONE	DEV	NONE	72501
7	19970310	1997031012	NONE	MAT	NONE	74494
8	19970331	1997040100	BOTH	MAT	RAD	74389
9	19971227	1997122800	NONE	DEV	NONE	74494
10	19990306	1999030618	MULTI	DEV	LAT	74389
11	20000113	2000011312	SINGLE	MAT	LAT	74494
12	20000125	2000012518	BOTH	MAT	RAD	72518
13	20000130	2000013106	BOTH	MAT	RAD	74494
14	20000316	2000031706	NONE	DEV	NONE	74389
15	20001230	2000123018	BOTH	MAT	RAD	72518
15	20001230	2000123100	SINGLE	MAT	RAD	72518
16	20010119	2001011912	MULTI	DEV	LAT	72501
16	20010119	2001011918	BOTH	DEV	LAT	74389
16	20010119	2001012000	BOTH	DEV	LAT	74494
17	20010205	2001020518	BOTH	MAT	RAD	72501
17	20010205	2001020600	BOTH	MAT	RAD	72501
17	20010205	2001020606	BOTH	MAT	RAD	72501
18	20011208	2001120900	BOTH	DEV	LAT	72518
18	20011208	2001120906	BOTH	DEV	LAT	74494
18	20011208	2001120912	BOTH	DEV	LAT	74389
19	20020107	2002010700	NONE	MAT	NONE	72501
20	20020119	2002011918	MULTI	DEV	LAT	72501

20	20020119	2002012000	BOTH	DEV	LAT	72501
20	20020119	2002012006	BOTH	DEV	LAT	74494
21	20021127	2002112706	BOTH	DEV	LAT	72501
21	20021127	2002112712	BOTH	DEV	LAT	72501
22	20021205	2002120512	MULTI	DEV	LAT	72501
22	20021205	2002120518	BOTH	DEV	LAT	72501
22	20021205	2002120600	BOTH	MAT	LAT	72501
23	20021224	2002122506	MULTI	DEV	LAT	72501
23	20021224	2002122512	NONE	DEV	NONE	72501
23	20021224	2002122518	NONE	MAT	NONE	72518
23	20021224	2002122600	BOTH	MAT	RAD	72518
24	20030207	2003020712	BOTH	DEV	LAT	72501
24	20030207	2003020718	BOTH	MAT	RAD	74494
25	20030217	2003021718	BOTH	DEV	RAD	72501
25	20030217	2003021800	MULTI	MAT	RAD	72501
26	20030306	2003030612	NONE	DEV	NONE	72501
26	20030306	2003030618	BOTH	DEV	LAT	74494
27	20030407	2003040718	BOTH	DEV	RAD	72501
28	20031205	2003120518	BOTH	MAT	RAD	72501
28	20031205	2003120600	BOTH	MAT	RAD	72501
28	20031205	2003120606	MULTI	MAT	RAD	74494
29	20031214	2003121500	MULTI	MAT	RAD	74389
30	20040102	2004010212	NONE	DEV	NONE	72501
31	20040112	2004011206	NONE	MAT	NONE	72501
32	20040114	2004011506	NONE	DEV	NONE	72501
33	20040117	2004011806	NONE	MAT	NONE	72501
34	20040127	2004012806	NONE	MAT	NONE	72501
35	20040206	2004020612	NONE	DEV	NONE	72501
36	20040217	2004021806	MULTI	DEV	RAD	72501
37	20040316	2004031618	BOTH	DEV	RAD	72518
38	20040319	2004031912	BOTH	MAT	RAD	72501
39	20050122	2005012218	MULTI	DEV	RAD	72501
39	20050122	2005012300	BOTH	MAT	RAD	74494
39	20050122	2005012306	BOTH	MAT	RAD	74389
40	20050220	2005022106	MULTI	DEV	LAT	72501
40	20050220	2005022112	MULTI	DEV	LAT	72501
41	20050224	2005022418	MULTI	DEV	LAT	72402
41	20050224	2005022500	BOTH	DEV	RAD	72501
41	20050224	2005022506	BOTH	DEV	RAD	72501

42	20050228	2005030100	BOTH	DEV	RAD	72501
43	20050308	2005030812	NONE	MAT	NONE	72501
44	20051204	2005120412	NONE	DEV	NONE	74494
45	20051209	2005120912	NONE	DEV	NONE	72501
45	20051209	2005120918	BOTH	DEV	RAD	74494
46	20060114	2006011506	NONE	MAT	NONE	72501
47	20060211	2006021206	BOTH	MAT	RAD	72501
47	20060211	2006021212	BOTH	MAT	RAD	72501
47	20060211	2006021218	BOTH	MAT	RAD	74494
48	20060309	2006030918	NONE	DEV	NONE	74494
49	20070213	2007021412	NONE	MAT	NONE	74494
50	20070225	2007022606	NONE	MAT	NONE	72501
51	20070319	2007032000	NONE	DEV	NONE	74494
52	20081207	2008120706	NONE	DEV	NONE	72501
53	20081219	2008121918	NONE	DEV	NONE	72501
53	20081219	2008122000	BOTH	MAT	LAT	74389
54	20081231	2008123118	BOTH	MAT	RAD	74494
55	20090111	2009011106	MULTI	DEV	LAT	74494
55	20090111	2009011112	MULTI	DEV	LAT	74389
56	20090128	2009012812	BOTH	DEV	RAD	74494
57	20090203	2009020400	BOTH	MAT	RAD	74389
58	20090218	2009021906	MULTI	DEV	RAD	74389
59	20090228	2009022806	NONE	DEV	NONE	74494
60	20091205	2009120518	BOTH	DEV	LAT	74389
60	20091205	2009120600	MULTI	MAT	LAT	74389
60	20091205	2009120606	BOTH	MAT	RAD	74389
61	20091219	2009122000	BOTH	MAT	RAD	72501
61	20091219	2009122006	BOTH	MAT	RAD	72501
61	20091219	2009122012	BOTH	MAT	RAD	74494
62	20091231	2009123118	NONE	DEV	NONE	74494
63	20100209	2010021100	BOTH	MAT	LAT	72501
64	20100216	2010021606	NONE	MAT	NONE	72501
65	20100225	2010022606	MULTI	MAT	RAD	72501
65	20100225	2010022612	BOTH	MAT	RAD	72501
65	20100225	2010022618	MULTI	MAT	RAD	72501
65	20100225	2010022700	MULTI	MAT	LAT	74389
66	20100302	2010030306	SINGLE	MAT	RAD	72402
66	20100302	2010030312	BOTH	MAT	RAD	72501
66	20100302	2010030318	BOTH	MAT	RAD	74494

67	20101226	2010122618	BOTH	MAT	RAD	72501
67	20101226	2010122700	BOTH	MAT	RAD	72501
67	20101226	2010122706	BOTH	MAT	RAD	72501
68	20110107	2011010718	NONE	MAT	NONE	72501
69	20110112	2011011212	BOTH	MAT	RAD	72501
70	20110125	2011012518	NONE	DEV	NONE	72501
71	20110126	2011012612	NONE	DEV	NONE	72501
71	20110126	2011012618	MULTI	MAT	LAT	72501
71	20110126	2011012700	BOTH	MAT	RAD	72501
71	20110126	2011012706	BOTH	MAT	RAD	72501
72	20110201	2011020118	NONE	DEV	NONE	74494
73	20110202	2011020212	MULTI	MAT	RAD	74389
73	20110202	2011020218	MULTI	MAT	RAD	74389
74	20110221	2011022106	BOTH	DEV	LAT	72501
74	20110221	2011022112	BOTH	DEV	LAT	72501
75	20110227	2011022706	BOTH	DEV	LAT	74494
76	20110323	2011032306	BOTH	MAT	LAT	72501
76	20110323	2011032312	BOTH	MAT	LAT	72501
77	20110331	2011040100	NONE	MAT	NONE	72501
78	20111028	2011102906	BOTH	DEV	LAT	72402
78	20111028	2011102912	BOTH	DEV	RAD	72501
78	20111028	2011102918	BOTH	MAT	RAD	72501
78	20111028	2011103000	BOTH	MAT	RAD	72501
78	20111028	2011103006	BOTH	MAT	RAD	72501
79	20120121	2012012106	BOTH	DEV	LAT	72402
79	20120121	2012012112	BOTH	DEV	LAT	72501
80	20120210	2012021112	BOTH	DEV	LAT	72501
80	20120210	2012021118	BOTH	MAT	RAD	74494
81	20120229	2012022918	NONE	DEV	NONE	72501
82	20121107	2012110712	BOTH	MAT	RAD	72501
82	20121107	2012110718	BOTH	MAT	RAD	72501
82	20121107	2012110800	BOTH	MAT	RAD	72501
82	20121107	2012110806	BOTH	MAT	RAD	72501
83	20121226	2012122700	BOTH	DEV	RAD	74494
83	20121226	2012122706	MULTI	MAT	RAD	74389
83	20121226	2012122712	BOTH	MAT	RAD	74389
83	20121226	2012122718	NONE	MAT	NONE	74389
84	20121229	2012122918	MULTI	MAT	RAD	74389
84	20121229	2012123000	MULTI	MAT	RAD	74494

85	20130116	2013011612	NONE	DEV	NONE	72501
85	20130116	2013011618	MULTI	DEV	LAT	74389
86	20130121	2013012200	BOTH	DEV	LAT	72501
87	20130208	2013020818	BOTH	MAT	RAD	72501
87	20130208	2013020900	BOTH	MAT	RAD	72501
87	20130208	2013020906	BOTH	MAT	RAD	72501
87	20130208	2013020912	BOTH	MAT	RAD	74389
88	20130214	2013121406	BOTH	DEV	RAD	72501
89	20130216	2013021700	BOTH	DEV	LAT	72402
89	20130216	2013021706	SINGLE	MAT	LAT	72501
90	20130306	2013030700	BOTH	MAT	RAD	72402
90	20130306	2013030706	BOTH	MAT	RAD	72501
90	20130306	2013030712	MULTI	MAT	RAD	72501
91	20130318	2013031900	MULTI	DEV	LAT	74494
91	20130318	2013031906	MULTI	MAT	RAD	74494
91	20130318	2013031912	MULTI	MAT	RAD	74389
92	20131210	2013121012	BOTH	DEV	LAT	72501
92	20131210	2013121018	BOTH	DEV	LAT	74494
93	20131215	2013121506	BOTH	MAT	LAT	74389
93	20131215	2013121512	MULTI	MAT	RAD	74389
94	20131217	2013121712	NONE	DEV	NONE	72501
95	20140102	2014010300	BOTH	DEV	LAT	72501
95	20140102	2014010306	SINGLE	MAT	RAD	72501
96	20140110	2014011012	NONE	DEV	NONE	74494
97	20140121	2014012118	BOTH	DEV	RAD	72501
97	20140121	2014012200	BOTH	MAT	RAD	72501
98	20140129	2014012906	BOTH	DEV	LAT	72501
98	20140129	2014012912	BOTH	DEV	RAD	74494
99	20140203	2014020312	NONE	DEV	NONE	72501
100	20140205	2014020518	BOTH	DEV	LAT	74389
101	20140213	2014021400	BOTH	MAT	RAD	74389
101	20140213	2014021406	BOTH	MAT	RAD	72518
102	20140215	2014021518	MULTI	DEV	RAD	74494
102	20140215	2014021600	BOTH	MAT	RAD	74494
103	20140218	2014021812	NONE	DEV	NONE	72501
104	20150124	2015012500	MULTI	DEV	RAD	74494
105	20150126	2015012700	BOTH	MAT	RAD	74494
105	20150126	2015012706	BOTH	MAT	RAD	72501
105	20150126	2015012712	BOTH	MAT	RAD	74494

105	20150126	2015012718	BOTH	MAT	RAD	74389
106	20150202	2015020212	NONE	DEV	NONE	74494
107	20150214	2015021500	NONE	MAT	NONE	74494
108	20150221	2015022212	BOTH	DEV	LAT	74494
109	20150301	2015030200	NONE	DEV	NONE	74494
110	20160122	2016012306	NONE	DEV	NONE	72501
110	20160122	2016012312	BOTH	MAT	RAD	72501
110	20160122	2016012318	BOTH	MAT	RAD	72501
110	20160122	2016012400	BOTH	MAT	RAD	74494